UC Berkeley
UC Berkeley Electronic Theses and Dissertations

Title

Controls on critical zone thickness and hydrologic dynamics at the hillslope scale

Permalink

https://escholarship.org/uc/item/6td3h4s8

Author

Rempe, Daniella Marie

Publication Date

2016

Peer reviewed|Thesis/dissertation

Controls on critical zone thickness and hydrologic dynamics at the hillslope scale

by

Daniella Marie Rempe

A dissertation submitted in partial satisfaction of the

requirements for the degree of

Doctor of Philosophy

in

Earth and Planetary Science

in the

Graduate Division

of the

University of California, Berkeley

Committee in charge:

Professor William E. Dietrich, Chair
Professor Inez Fung
Professor Sally Thompson

Summer 2016

Controls on critical zone thickness and hydrologic dynamics at the hillslope scale

Copyright 2016
by
Daniella Marie Rempe

Abstract

Controls on critical zone thickness and hydrologic dynamics at the hillslope scale

by

Daniella Marie Rempe

Doctor of Philosophy in Earth and Planetary Science

University of California, Berkeley

Professor William E. Dietrich, Chair

The critical zone is defined as the thin outer veneer of Earth's terrestrial surface, extending from the top of the vegetation canopy to the base of weathered bedrock. Very little is known about how the critical zone is structured and how its structure controls the storage, transport, and chemical evolution of the biosphere's most important resource-water. In hilly or mountainous landscapes, the critical zone often includes tens of meters of weathered rock beneath the surface and this weathered rock hosts a dynamic hydrologic system that is virtually unexplored. Below weathered bedrock, lies an unmapped three dimensional fresh bedrock surface, Z_b, that defines the bottom boundary of the critical zone. This dissertation develops novel theory to predict how this fresh bedrock surface is structured across ridge and valley topography and illustrates, through a field study, how that structure influences the routing of water within the landscape. I report, for the first time, how the structure and hydrologic dynamics of the critical zone vary across an entire hillslope, from channel to topographic divide.

Current models for development of the critical zone emphasize top-down processes associated with infiltrating waters and gases, as well as fracturing due to the differential stresses generated by topography. I propose a distinctly different theory, which enables a prediction of the thickness of weathered bedrock across a landscape. I hypothesize that as fresh bedrock, saturated with nearly stagnant fluid, is advected upward into the near-surface through uplift and erosion, channel incision produces a lateral head gradient within the fresh bedrock inducing drainage towards the channel. Drainage of the fresh bedrock causes weathering through drying (i.e. repeated cycles of wetting and drying) and permits the introduction of atmospheric and biotically controlled acids and oxidants such that the boundary between weathered and unweathered bedrock is set by the uppermost elevation of undrained fresh bedrock, Z_b.

At steady-state the rate at which fresh bedrock crosses the Z_b boundary is equal to the channel incision rate (which commonly is less than 1 mm/yr). Hence, this slow drainage of fresh bedrock, progressively allowing weathering to proceed, exerts a "bottom up" control on the advance of the weathering front. The thickness of the weathered zone is calculated as the difference between the predicted topographic surface profile (driven by erosion) and

the predicted groundwater profile (driven by drainage of fresh bedrock). For the steady state, soil-mantled case, a coupled analytical solution arises in which both profiles are driven by channel incision. Lithology of the fresh bedrock influences the thickness of the weathered zone through the saturated hydraulic conductivity of the bedrock. Measurements of rate processes and topography, as well as depth to fresh bedrock at the divide can be used to estimate the saturated hydraulic conductivity and porosity of the fresh bedrock. Two non-dimensional numbers corresponding to the mean hillslope gradient and mean groundwater table gradient emerge and their ratio defines the proportion of the hillslope relief that is unweathered. The model predicts a thickening of the weathered zone upslope and consequently, a progressive upslope increase in the residence time of bedrock in the weathered zone. Despite its simplicity, the model makes testable predictions and is consistent with field data from three sites.

To investigate how the critical zone is structured across a hillslope and how water is routed throughout the critical zone, I conducted an intensive field investigation on a steep (average 30 degree), actively eroding (0.2-0.4 mm/yr), 135 m long soil-mantled hillslope within the Northern California Coast Ranges (referred to as Rivendell). The 4000 m^2 hillslope is located within the 17 km^2 Elder Creek watershed, in the Angelo Coast Range Reserve. The hillslope is forested with up to 60 m tall Douglas fir (*Pseudotsuga menziesii*) and mixed evergreen hardwoods including live oak (*Quercus wislizeni*), madrone (*Arbutus menziesii*), and California bay (*Umbellularia californica*), and is underlain by vertically dipping argillite with sandstone interbeds. The climate is seasonally dry, and characterized by warm, dry summers (May- Sept) and cool, wet winters within which all of the precipitation (1800 mm mean annual precipitation) falls.

A network of 12 wells, as deep as 30 m, were drilled across the hillslope into fresh bedrock and an extensive sensor network of over 750 sensors records soil moisture and rock moisture, and meteorological and groundwater conditions across the site. Streamflow at the base of the hillslope is recorded at a United States Geologic Survey station a short distance upstream. To document the spatial and temporal dynamics of rock moisture, I performed periodic neutron probe surveys within deep wells.

Drilling revealed a 4-25 m thick zone of variably weathered, fractured bedrock underlying, thin (<50 cm) soils. Intensely fractured argillite forms a saprolite in the upper 4 m, below which fracture density, porosity, and mechanical strength decreases with depth. Fresh bedrock at the base of the profile (revealed through large increases in standard penetration resistance and an absence of signs of oxidative weathering) bounds the weathered zone from below. The boundary between unweathered and weathered rock, Z_b, is progressively deeper upslope, forming an upslope thickening wedge of fractured, weathered bedrock that is increasingly weathered upslope.

The seasonal addition of rainfall to this structured weathering profile, leads to the development of three distinct hydrologic zones: a near surface 4-18 m thick zone that remains unsaturated year round, a 4-15 m thick seasonally saturated zone that fluctuates largely within the same elevations year after year, and a zone which remains chronically saturated below an annually repeatable minimum water table position.

A significant consequence of the development of the weathering front into bedrock is that infiltrating rainfall travels through and is stored within weathered rock as rock moisture. Rock moisture is the exchangeable water within unsaturated weathered and fractured bedrock. It has been identified as an important source of moisture to vegetation, but is poorly documented due to its inaccessibility and therefore remains an unaccounted for, but important, component of the hydrologic cycle. Here, for the first time, I directly document the spatial and temporal dynamics of rock moisture throughout the critical zone.

Periodic surveys in deep wells reveal a seasonal cycle of rock moisture addition and depletion across the hillslope. This cycle begins with the first rains that mark the end of the dry season, which advance moisture into the soil and often up to 1 m into the weathered bedrock. Subsequent rains advance a wetting front through the upper 5-12 m of the profile, where increases in rock moisture storage are proportional to the addition of rainfall. In some instances, these early wet season storms generate a small, rapid but short-lived response of the water table.

Once cumulative rainfall has caused the local rock moisture storage to reach a capacity beyond which rock moisture no longer increases, groundwater responds to rainfall. Further incoming water is passed rapidly, via fracture flow, to the groundwater table. This rock moisture storage capacity, which is observed to be approximately the same each year, increases upslope from 85 to 615 mm, corresponding to the upslope increase in weathering of the bedrock. The average rock moisture storage in the chronically unsaturated zone across the hillslope is about 280 mm. The upslope increase in rock moisture storage needed to initiate the seasonal groundwater response leads to the condition where, early in the wet season, runoff is generated from the lower part of the hillslope while the upper part of the hillslope is still gaining moisture.

Once rock moisture is seasonally elevated, all infiltrating precipitation travels vertically through soil, saprolite, and weathered rock (we observe no overland flow or saturated flow within the soil). The timing of the rapid response of the groundwater system ($\sim$ hours) is highly variable for a given depth and does not appear to depend on travel distance to the water table. Additional storms throughout the wet season do not alter the structure or magnitude of rock moisture storage within the hillslope. Rock moisture storage is most significant in the upper 5-12 m and diminishes with depth to a zone where no detectable changes in rock moisture are observed despite the rise and fall of the water table within this zone. Rock moisture may occur as water along fracture surfaces or as water that penetrates the matrix blocks bounding fractures. At depth, the constant saturation of matrix blocks leads to the dominance of fracture flow, which drives the rapid (10^{-5} to 10^{-3} m/s) and significant (up to 11 m in a single storm) rise of the water table. On average, rock moisture changes of only 5% are needed to achieve saturation in the seasonally saturated zone. The dynamic and responsive, fracture dominated groundwater system leads to 97-99% of runoff in Elder Creek occurring during the wet season.

The final storm of the wet season marks the initiation of the slow decline of rock moisture and groundwater within the hillslope throughout the long (>120 days) dry season.

The 30-130 mm of seasonal soil moisture storage is rapidly depleted within the first several weeks following the final storm. Approximately 12 weeks into a typically 18-week dry season, less than 15 mm of soil moisture remains, while up to 120 mm (53 mm average across the hillslope) is stored in the upper 10 m as rock moisture. An annual cycle is repeated each year: drying to a characteristic value and then wetting to a similar rock moisture storage capacity. Because the precipitation exceeds the rock moisture storage capacity even in dry years, the spatial pattern and magnitude of dry season rock moisture are insensitive to the precipitation magnitude and temporal pattern of the immediately preceding wet season, even in a significant drought year (approximately half mean annual precipitation). The drop in groundwater level over the last 2 months of the dry season (equivalent to approximately 5-50 mm) is also similar in different years. Runoff of just 5 mm per month is sufficient to sustain flow in Elder Creek and support salmonid populations.

Rock moisture, a direct consequence of the alteration of bedrock in the near surface, is a virtually unknown and unmapped component of the hydrologic balance. Here, I show that year after year, 30-60% of the incoming precipitation is stored seasonally as rock moisture. Nearly all of that water must be used in transpiration.Hence, rock moisture is a major source of water for vegetation. Because incoming rainfall first restores this moisture content before generating runoff, even in strong drought years, the rock moisture is available, and provides drought resilience. The ecohydrologic function of the critical zone at this site must therefore be divided between 1) near surface rock moisture storage that controls the exchange of gases and solutes and supports dry season transpiration and 2) the fracture dominated seasonally perched groundwater system that routes most precipitation as runoff and controls both peak and low streamflow and aquatic habitat. The dual function of seasonal storage and rapid transmission of water is the defining feature of the rock moisture system.

The rock moisture dynamics documented here explain several previously observed processes at Rivendell. The seasonal build up of rock moisture leads to mixing of waters and damping of the stable isotope signature of storm events. Within the dynamic rock moisture zone, seasonal stimulation of subsurface microbial communities (as expressed in gas composition) occurs and cation exchange processes likely drive the solute chemistry of water recharged to the groundwater and drained as runoff.

Rock moisture is likely important in a wide range of settings. I propose here the possibility that there may be a co-evolution of vegetation and critical zone structure wherein the water extraction by trees accelerates weathering of the bedrock, which increases rock moisture retention. Further field characterization is needed in a range of climates lithologies, and tectonic settings to document the critical zone structure, its rock moisture characteristics, and ecosystem dynamics. Modeling has begun to account for rock moisture dynamics and runoff through fractured bedrock, however, further field investigation will help guide models that predict critical zone development over sufficiently large areas to inform regional hydrologic, climate, and ecologic models.

To hard workers. My parents, Iris and John Rempe, in particular.

Contents

List of Figures

List of Tables

Acknowledgments

I have been overwhelmed by the generosity and support of my advisor, Professor Bill Dietrich, ever since our first meeting in 2009. After a multi-hour conversation about soil as a conveyor belt (complete with an even mix of differential equations and references to characters in fantasy novels) Bill asked about my career goals. I told him I'd ideally like to work at an institution "like UT Austin." Years later, I am indebted to Bill for giving me both the guidance to propel me towards my goals and the space to grow. His genius extends so far beyond his intellect, and I have benefitted immeasurably from his example as a fearless tackler of complex problems, rigorous field scientist, enthusiastic teacher, compassionate leader, patient editor, and humble human being. I am grateful that he entrusted me with the projects that we developed into this dissertation and I am excited to follow the path he has illuminated for me.

I am grateful to my role models and thesis committee members, Professors Inez Fung and Sally Thompson, who, through their insight and feedback, tremendously shaped the direction of my research and my development as a scientist. Their anecdotes became the mantras that kept me afloat when I was drowning in rich data and self doubt, and their challenging questions shifted my perspective on the impact of my work. I also thank my qualifying exam committee members, Professors Roland Burgmann, Jim Hunt, and Jim Bishop, for an enriching and challenging qualifying exam experience and their support throughout graduate school.

My dissertation research was motivated by a highly interdisciplinary project that began as Keck Hydrowatch and grew into the Eel River Critical Zone Observatory. I'd like to extend my sincere thanks to the many people that contributed to my dissertation research in various capacities through these projects. Jim Bishop, Todd Dawson and Jill Banfield were generous with their time and ideas, and I cherished the time spent with them in the field and in group meetings. Their insight consistently steered my research in fruitful directions. In particular, I am grateful to Mary Power for continually inspiring me, through science and song, to look around and appreciate interactions at scales that I'm not used to thinking about.

This dissertation relied on often frustrating fieldwork that thankfully turned my smart and perceptive colleagues into treasured friends. I would like to thank Jasper Oshun, Percy Link, Hyojin Kim and Kevin Simonin who, early on, shared in the trials and tribulations of field experiments and engaged me in thoughtful discussions that benefited and motivated my dissertation research. My CZO comrades, Jesse Hahm, Sky Lovill, Chris Wong, Michail Vrettas, Jill Marshall, and David Dralle provided dependable field support and frequent and invaluable feedback on my sometimes zany ideas. I am also grateful to the countless undergraduate Berkeley students, including but not limited to Colleen Murphy, Sami Cargill, Ben Purcell, Jon Weiner, Hunter Philson, Shawn Lee, Stephan Ferencz, Sara Beroff, Jasmine Mason, and Colin McNeece who endured long field days and sometimes smelly car rides to help collect the data that appears in this dissertation. Without the logistical and technical support of Collin Bode, Peter Steel,

Chapter 1

Introduction

1.1   Introduction

The critical zone is the interface between the atmosphere and the terrestrial earth. On landscapes developed in bedrock this zone commonly extends from the canopy top down to fresh bedrock underlying hillslopes (National Science Foundation, Program solicitation 12-575, 2012) (Figure 1.1). At present little is known about the structure and character of the subsurface part of the critical zone due to its inaccessibility and heterogeneity. A key currency that passes across the critical zone is water. The critical zone perspective suggests that we need to look below the soil to understand hydrologic processes in the critical zone. Intensive hydrologic field studies have pointed to the importance of hillslope runoff routed through weathered, and often fractured, bedrock (Wilson and Dietrich 1987, Montgomery et al., 1997, Asano et al. 2002, Blumstock et al., 2015, Frisbee et al. 2011, Haria and Shand, 2004, Kosugi et al. 2006, 2011, Katsuyama et al., 2010, Rademacher et al. 2005, Soulsby et al. 2007, and Hale and McDonnell, 2016). The invisibility and inaccessibility of the components of the critical zone below the soil has made it difficult to fully grasp how hydrologic processes work at depth. Valuable local field studies, conducted prior to the conceptualization of the critical zone, report on perceived patterns of the structure and depth of weathering across landscapes (Ruxton and Berry, 1957, Budel, 1957, Shengwen et al., 2009) and some studies associate this subsurface hillslope structure with specific hydrologic processes (Manning et al., 2007, Katsura et al., 2008, Marechal et al., 2009). Nearly all of these studies necessarily extrapolate from a limited and difficult to create observational base and from these observations, generate a conceptual model for the hydrologic dynamics (e.g. Bonnell, 1993, Legout et al., 2006, Banks et al., 2009). Very few document the critical zone subsurface structure from channel up hillslopes to the ridge divide (e.g. Anderson et al., 2002). However, hillslope and landscape scale investigations of critical zone structure are needed to explore how critical zone properties drive hydrologic processes and inform the theoretical and numerical models that route water from hillslopes to channels (e.g. Fan and Bras, 1998, Troch et al., 2002, 2003, Ebel et al., 2008).

Ultimately, critical zone science aims to predict the structure and function of the critical zone at landscape scales. To achieve this, field studies must describe the critical zone structure, document physical, chemical and biological processes, interrogate the mechanistic relationships between structure and function, and do so across the full range of pertinent scales - vertically down to the fresh bedrock, and laterally across full hillslope. This is not an easy task, but critical zone science is advancing, for example, five distinct theories have been proposed to predict the depth to fresh bedrock across landscape scales (Brantley et al., 2013, Rempe and Dietrich, 2014, St. Clair et al., 2015, Rasmussen et al., 2011, Braun, submitted). At present, these theories have limited observations to which their predictions can be compared (e.g. Pavich et al., 1986), and none predicts the structure or properties of the weathered material above the fresh bedrock, and thus the consequences for critical zone functions including the partitioning of water.

In this dissertation, I provide a detailed description of the critical zone and its hydro-

logic pathways, at the hillslope scale, and propose a theoretical model that can be used to predict the structure of the critical zone across a landscape. The thesis is divided into two parts. In Part I, I describe the theoretical model and in Part II, I describe the results of field observations.

In Part I, I propose a mechanism connecting the evolution of surface topography to the evolution of the bottom boundary of the critical zone and provide a quantitative and testable model to predict the variation in critical zone thickness along a hillslope profile. Specifically, the model predicts that, in landscapes underlain by bedrock, progressive channel incision will lead to slow drainage of groundwater in bedrock and this drainage initiates weathering. This model specifically predicts a fresh bedrock slope underlying the weathered mantle hillslope that may be less steep than the surface topography, thus leading to an upslope thickening zone of weathered bedrock.

In Part II, I explore the implications of the structure of the critical zone on hydrologic processes through direct field observations made within the Eel River Critical Zone Observatory (formerly Keck Hydrowatch). I report the results of an intensive effort to characterize the structure of the critical zone, across a hillslope unit from channel to drainage divide, and document how water influences ecohydrologic processes. Part II is organized as follows: Chapter 3 introduces the site and the methods used in the following chapters, Chapter 4-6 describe results, and Chapter 7 is a discussion and conclusion of the results presented in Chapters 4-6. More specifically, in Chapter 4, I describe the features of an upward thickening critical zone structure that emerged from drilling and hydrologic monitoring. In Chapter 5, I describe long term hydrologic monitoring results and identify the role of rock moisture, the exchangeable water held in weathered rock, on supplying moisture to vegetation. In Chapter 6, I explore how runoff is generated within the critical zone. In the final chapter, Chapter 7, I summarize the hydrologic field monitoring results.
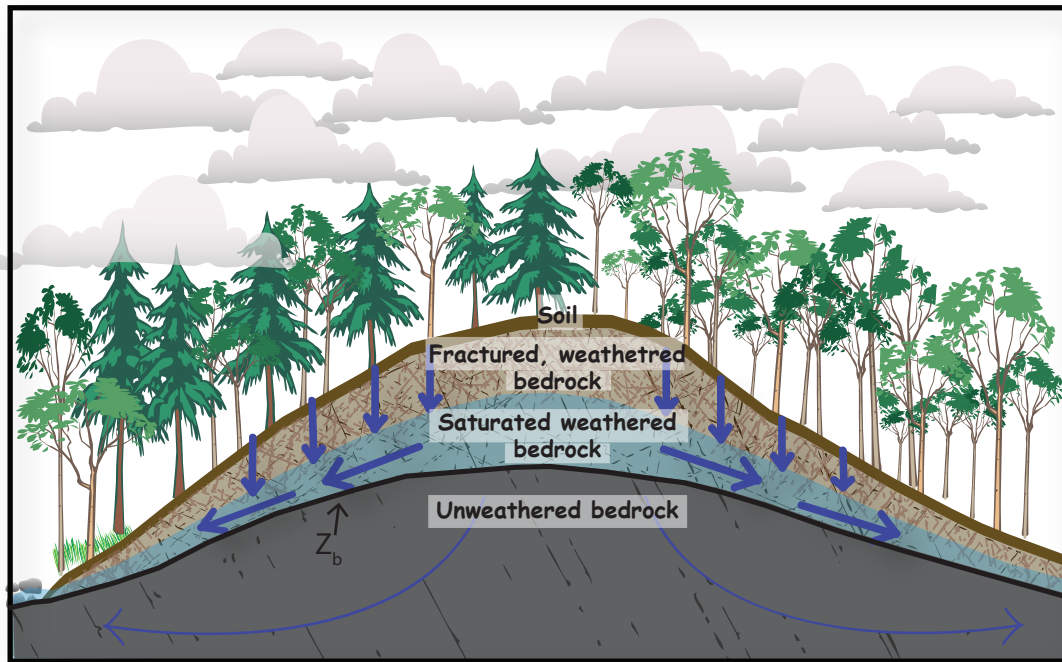
Figure 1.1: The critical zone can be defined as Earth's terrestrial boundary layer that extends from the top of the canopy to the depth of weathering in the subsurface. The extent of alteration of bedrock diminishes with depth and at some depth, below the critical zone, lies unweathered bedrock. Above this interface, called Z_b, the critical zone is comprised of weathered, fractured bedrock and soil that actively participates in the hydrologic cycle. Blue shading represents a seasonal groundwater table, and blue arrows represent flowpaths of water. Vertical arrows in the near surface depict the dominantly vertical flow that occurs in the unsaturated zone, downslope oriented arrows within the saturated zone reflect the downslope transport of groundwater towards the stream, and the deep curved arrows represent the pattern of very slow groundwater flow through nearly impermeable fresh bedrock. This illustration is inspired by the Rivendell field site within the Eel River Critical Zone Observatory. Note that the representation of trees suggests an aspect dependence. Our study site, Rivendell, is mostly on the left side (North facing) of this cartoon where dark green conical shaped needle trees predominate. On the south facing broad leaf trees dominate.

Bibliography

[1] S.P. Anderson, W.E. Dietrich, and G.H. Brimhall. Weathering profiles, mass-balance analysis, and rates of solute loss: Linkages between weathering and erosion in a small, steep catchment. *Geological Society of America Bulletin*, 114(9):1143, 2002.

[2] Suzanne Prestrud Anderson, William E Dietrich, David R Montgomery, et al. Subsurface flow paths in a steep, unchanneled catchment. *Water Resources Research*, 33(12):2637–2653, 1997.

[3] Yuko Asano, Taro Uchida, and Nobuhito Ohte. Residence times and flow paths of water in steep unchannelled catchments, Tanakami, Japan. *Journal of Hydrology*, 261(1):173–192, 2002.

[4] E.W. Banks, C.T. Simmons, A.J. Love, et al. Fractured bedrock and saprolite hydrogeologic controls on groundwater/surface-water interaction: a conceptual model (Australia). *Hydrogeology Journal*, 17(8):1969–1989, 2009.

[5] M Blumstock, D Tetzlaff, IA Malcolm, G Nuetzmann, and C Soulsby. Baseflow dynamics: Multi-tracer surveys to assess variable groundwater contributions to montane streams under low flows. *Journal of Hydrology*, 527:1021–1033, 2015.

[6] Michael Bonell. Progress in the understanding of runoff generation dynamics in forests. *Journal of Hydrology*, 150(2-4):217–275, 1993.

[7] Susan L Brantley, Molly E Holleran, Lixin Jin, and Ekaterina Bazilevskaya. Probing deep weathering in the Shale Hills Critical Zone Observatory, Pennsylvania (USA): the hypothesis of nested chemical reaction fronts in the subsurface. *Earth Surface Processes and Landforms*, 38(11):1280–1298, 2013.

[8] J. Büdel. Double surfaces of leveling in the humid tropics. *Zeitschrift für Geomorphologie*, 1:223–225, 1957.

[9] J St Clair, S Moon, WS Holbrook, et al. Geophysical imaging reveals topographic stress control of bedrock weathering. *Science*, 350(6260):534–538, 2015.

[10] B.A. Ebel, K. Loague, D.R. Montgomery, and W.E. Dietrich. Physics-based continuous simulation of long-term near-surface hydrologic response for the Coos Bay experimental catchment. *Water Resources Research*, 44(7):W07417, 2008.

[11] National Science Foundation. National Science Foundation, Program solicitation 12-575. 2012.

[12] Marty D Frisbee, Fred M Phillips, Andrew R Campbell, Fengjing Liu, and Steve A Sanchez. Streamflow generation in a large, alpine watershed in the southern Rocky Mountains of Colorado: Is streamflow generation simply the aggregation of hillslope runoff responses? *Water Resources Research*, 47(6), 2011.

[13] V Cody Hale, Jeffrey J McDonnell, Michael K Stewart, et al. Effect of bedrock permeability on stream base flow mean transit time scaling relationships: 2. Process study of storage and release. *Water Resources Research*, 2016.

[14] Atul H Haria and Paul Shand. Evidence for deep sub-surface flow routing in forested upland Wales: implications for contaminant transport and stream flow generation. *Hydrology and Earth System Sciences Discussions*, 8(3):334–344, 2004.

[15] Shin'ya Katsura, Ken'ichirou Kosugi, Tasuku Mizutani, Suemi Okunaka, and Takahisa Mizuyama. Effects of bedrock groundwater on spatial and temporal variations in soil mantle groundwater in a steep granitic headwater catchment. *Water Resources Research*, 44(9):n/a–n/a, September 2008.

[16] M Katsuyama, M Tani, and S Nishimoto. Connection between streamwater mean residence time and bedrock groundwater recharge/discharge dynamics in weathered granite catchments. *Hydrological Processes*, 24(16):2287–2299, 2010.

[17] K Kosugi, M Fujimoto, S Katsura, and H Kato. Localized bedrock aquifer distribution explains discharge from a headwater catchment. *Water Resources . . .*, 2011.

[18] Ken'ichirou Kosugi, Shin'ya Katsura, Masanori Katsuyama, and Takahisa Mizuyama. Water flow processes in weathered granitic bedrock and their effects on runoff generation in a small headwater catchment. *Water Resources Research*, 42(2):n/a–n/a, February 2006.

[19] Cédric Legout, Jérome Molenat, Luc Aquilina, et al. Solute transfer in the unsaturated zone-groundwater continuum of a headwater catchment. *Journal of Hydrology*, 332(3):427–441, 2007.

[20] Andrew H Manning and Jonathan Saul Caine. Groundwater noble gas, age, and temperature signatures in an Alpine watershed: Valuable tools in conceptual model development. *Water resources research*, 43(4), 2007.

[21] Jean-Christophe Maréchal, Murari RR Varma, Jean Riotte, et al. Indirect and direct recharges in a tropical forested watershed: Mule Hole, India. *Journal of Hydrology*, 364(3):272–284, 2009.

[22] MJ Pavich. Regolith residence time and the concept of surface age of the Piedmont "peneplain". *Geomorphology*, 2(1):181–196, 1989.

[23] Shengwen Qi, Zhong Qi Yue, Faquan Wu, and Zhonghua Chang. Deep weathering of a group of thick argillaceous limestone rocks near Three Gorges Reservoir, Central China. *International Journal of Rock Mechanics and Mining Sciences*, 46(5):929–939, 2009.

[24] Laura K Rademacher, Jordan F Clark, David W Clow, and G Bryant Hudson. Old groundwater influence on stream hydrochemistry and catchment response times in a small Sierra Nevada catchment: Sagehen Creek, California. *Water resources research*, 41(2), 2005.

[25] Craig Rasmussen, Peter A Troch, Jon Chorover, et al. An open system framework for integrating critical zone structure and function. *Biogeochemistry*, 102(1-3):15–29, 2011.

[26] Daniella M Rempe and William E Dietrich. A bottom-up control on fresh-bedrock topography under landscapes. *Proceedings of the National Academy of Sciences*, 111(18):6576–6581, 2014.

[27] B.P. Ruxton and L. Berry. Weathering of granite and associated erosional features in Hong Kong. *Geological Society of America Bulletin*, 68(10):1263–1292, 1957.

[28] C Soulsby, D Tetzlaff, N Van den Bedem, et al. Inferring groundwater influences on surface water in montane catchments from hydrochemical surveys of springs and streamwaters. *Journal of Hydrology*, 333(2):199–213, 2007.

[29] Peter Troch, Emiel Van Loon, and Arno Hilberts. Analytical solutions to a hillslope-storage kinematic wave equation for subsurface flow. *Advances in Water Resources*, 25(6):637–649, 2002.

[30] Peter A Troch, Claudio Paniconi, and E Emiel van Loon. Hillslope-storage Boussinesq model for subsurface flow and variable source areas along complex hillslopes: 1. Formulation and characteristic response. *Water Resources Research*, 39(11), 2003.

[31] CJ Wilson and WE Dietrich. The contribution of bedrock groundwater flow to storm runoff and high pore pressure development in hollows. *IAHS-AISH publication*, (165):49–59, 1987.

Part I

A theoretical model for the evolution of the critical zone

In Part I, I describe a theoretical model for the thickness of the hydrologically dynamic weathered bedrock region underlying hillslopes that results from the co-evolution of the topographic surface and the drainage of groundwater within fresh bedrock. In Part II that follows, I describe a field investigation into hydrological consequences of hillslope weathering and the implications of these hydrologic dynamics on ecological processes.

Chapter 2

A bottom-up control to fresh bedrock topography under landscapes

2.1 Introduction

Uplift and erosion of bedrock commonly leads to ridge and valley topography variably mantled with weathered bedrock and soil. Quasi-steady state conditions may develop in which the topography is statistically constant as channels incise, hillslope surfaces erode, and fresh bedrock is uplifted to the surface. As this fresh bedrock rises up, it enters a near-surface zone where weathering irreversibly breaks and alters the rock before it is entrained into the mobile soil mantle and transported to adjacent streams. Variably weathered bedrock occupies the zone between the top of the fresh bedrock and the bottom of the soil. Here we identify Z_b as the elevation of the transition from fresh to weathered bedrock (Figure 2.1).

The transport of sediment and water from hillslopes to stream channels is influenced by the rock property changes that result from weathering. Hence, the depth to and topography of Z_b is an important driver in runoff generation and landscape evolution. Weathering tends to increase bedrock hydraulic conductivity and porosity, allowing infiltrating waters to perch on underlying fresh bedrock and flow laterally to stream channels (Figure 2.1). Field studies that have instrumented the weathered rock zone have shown that this perched groundwater path can deliver most of the stream runoff (1-4) and can be the source of sustained summer baseflow (5). The chemical evolution of hillslope runoff may be strongly dictated by the depth to Z_b and flow paths through the weathered zone (6-8). The weathering of bedrock may also increase moisture retention, which can be exploited by vegetation to sustain transpiration (9,10). Furthermore, water exfiltration from this zone on steep slopes can cause localized elevated pore pressures and landslides (11), and the change in rock mass strength across this boundary due to weathering may localize deep-seated landslides (12, 13).

Collectively, these observations suggest that, aside from the ground surface, the topography of Z_b is the most important boundary controlling surface and near-surface processes, and as such, observation and theory are needed to understand what controls its structure across a landscape. Field studies that have directly documented the depth to fresh bedrock underlying ridge and valley topography (e.g., refs 14,15) are rare and none have depicted the detailed three-dimensional pattern of Z_b relative to surface topography. Nonetheless, the few studies that have mapped Z_b under hillslopes have found a tendency for the weathered zone to be thickest at the ridge top and progressively thin downslope (14-18) (as illustrated in Figure 2.1). Though Pavich (1989) (15) and Feininger (1971) (18) associate this trend with areas of low relief, studies in steep landscapes in the California and Oregon Coast Ranges (5,6) have documented a systematic upslope thickening of the weathered zone as well (Figure 2.S1).

It is commonly assumed that the depth of weathered bedrock is controlled by downward propagating ("top-down") processes driven by the advance of chemically reactive meteoric water into the underlying fresh bedrock (e.g., ref 19). The top-down hypothesis leads to a weathered zone thickness that is set by the relative rates of erosion and the downward propagation of the weathering front. Approaches to addressing this hypothesis

have included reactive transport modeling (e.g., ref 20) and extension of the soil production function (21) to the weathered bedrock zone through a negative feedback between weathered zone thickness and erosion rate (e.g., ref 22). For a convex two dimensional hillslope with a mobile weathered layer composed of soil and weathered bedrock, Lebedeva and Brantley (2013) (20) propose that the downslope steepening of the topographic surface may lead to progressively less water flux normal to the underlying reactive bedrock and consequently, a weathered zone that thins downslope.

An alternative hypothesis for the downslope decrease in depth to Z_b under hillslopes is suggested by field observations of weathering profiles. Some of the earliest quantitative observations of weathering profiles identified the role of groundwater in impeding chemical weathering, and restricting the depth of the weathered zone (e.g., refs 14,16, 23, 24) such as occurs in supergene enrichment processes (25). In fresh bedrock of sufficiently low hydraulic conductivity, nearly stagnant or slowly-moving water will reach chemical equilibrium and chemical weathering reactions will slow or stop (19, 26). Additionally, the chronic saturation of fresh bedrock prevents mechanical breakdown due to swelling and contraction cycles associated with wetting and drying (27). Drainage of this fresh bedrock permits meteoric fluids to enter from above, thus allowing atmospherically and biotically controlled acids and oxidants to enter pore spaces and induce weathering reactions.

These observations suggest a "bottom-up" control on the elevation of fresh bedrock under hillslopes in which drainage of saturated fresh bedrock is the key process. We propose that: 1) fresh bedrock that is advected into the near-surface environment through uplift and erosion arrives saturated with nearly stagnant pore fluid that is in chemical equilibrium with surrounding mineral surfaces; 2) in this environment, channel incision creates a lateral head gradient in the fresh bedrock and induces drainage towards the adjacent channel; and 3) drainage may cause drying and fracturing of the bedrock and permit meteoric water to enter the fresh bedrock, inducing weathering at the rate that the fresh bedrock is drained. For these conditions, we propose that the fresh bedrock drainage profile defines Z_b. The depth to fresh bedrock along a hillslope will depend on both this groundwater drainage control and on the erosion shaping the surface topography. Here we predict the thickness of the weathered bedrock zone by coupling a groundwater flow model with a surface erosion model.

2.2 Model for a bottom-up limit to bedrock weathering

Consider the simplest case described above: a steady state landscape in which hillslope erosion has adjusted to and matches the uplift rate and adjacent channel incision rate, C_o. The landscape is mantled with soil, and a steady state groundwater flow system drains water from the uplifting fresh bedrock to the adjacent channel (Figure 2.1). Assume that uplifted bedrock remains both unweathered and saturated until it reaches the top of the drainage profile to the adjacent channel. After the bedrock is advected above the elevation

of the drainage profile (Figure 1), it desaturates, weathers instantaneously, and develops a significant increase in porosity and permeability such that seasonal groundwater dynamics above Z_b do not influence drainage of the low conductivity, slowly draining bedrock. For a steady state groundwater system, the shape of the drainage profile will be set, then, by the porosity and saturated hydraulic conductivity of the bedrock and the rate of channel incision. In effect, "recharge" to this groundwater system is only accomplished by the upward advection of saturated bedrock from below (Figure 2.1).

The presence of a soil mantle allows us to assume that surface sediment flux is proportional to slope, the divergence of which is the erosion rate. For simplicity, we use the common expression $q_s = -D\rho_s \frac{\partial Z_s}{\partial x}$ where q_s is the sediment transport rate per unit contour length ($MT^{-1}L^{-1}$), Z_s is the local elevation, x is the distance from the hillslope divide, ρ_s is the soil bulk density(ML^{-3}) and D is a rate constant often referred to as the soil diffusivity (L^2T^{-1}) (28). At steady state, uplift and erosion are equal to the channel incision rate, C_o, the soil thickness is constant, and erosion is matched by conversion of bedrock to soil at the rate of $\rho_r C_o$ in which ρ_r is the weathered bedrock bulk density at the base of the soil column. For a constant C_o, the surface topography, Z_s, is a convex up profile given by

$$Z_s(x) = \frac{\rho_r}{\rho_s} \frac{C_o}{2D}(L^2 - x^2) \ [1]$$

where L is the hillslope length (see SI). Weathering of the bedrock in this case reduces the bulk density but does not lead to collapse or consolidation of the weathered bedrock column. The surface topography, Z_s, that results from a non-linear relationship between soil flux and slope (Eq. 2.S1), following Roering et al. (2001) (29), is also used in the analysis that follows however the linear form is shown here for simplicity (see SI).

In the saturated fresh bedrock, the one-dimensional, steady state form of the Boussinesq Equation for groundwater flow (30) is

$$\frac{K}{2}\frac{\partial^2 Z_b{}^2}{\partial x^2} + \varnothing C_o = 0 \tag{2.1}$$

where K is the saturated bedrock hydraulic conductivity (L/T) and recharge is defined as the channel incision rate, C_o, times the saturated drainable pore space, set equal to porosity, (see SI). Assuming strictly horizontal flow, topographic symmetry about the ridge, and that the elevation of the channel is the bottom of the flow system, we arrive at

$$Z_b(x) = \sqrt{\frac{\varnothing C_o}{K}(L^2 - x^2)} \tag{2.2}$$

.

The difference between Eq. 2.1 and Eq. 2.3 gives the thickness of the weathered zone (including soil), H, as a function of position along the slope

$$H(x) = \frac{\rho_r}{\rho_s}\frac{C_o}{2D}(L^2 - x^2) - \sqrt{\frac{\varnothing C_o}{K}(L^2 - x^2)} \qquad (2.3)$$

H(x) always increases towards the divide, so to explore the controls on the weathered zone thickness (and thus the distance from the ground surface to fresh bedrock), we focus on the ridgetop (x=0). At the ridgetop, the non-dimensional ratio of bedrock relief, Z_{b0}, to surface relief, Z_{s0}, is given by

$$\frac{Z_{b0}}{Z_{s0}} = \frac{\sqrt{\frac{\varnothing C_o}{K}}}{\frac{\rho_r LC_o}{p_s 2D}} = \frac{S_w}{S_h} \qquad (2.4)$$

Hence, the proportion of the hillslope underlain by fresh bedrock at the divide, Z_{b0}/Z_{s0} is a function of the ratio of two dimensionless numbers: the numerator is the mean slope of the water table, S_w, and the denominator is the mean slope of the surface topography, Sh (Figure 2.S3). Seven terms must be evaluated to solve Eq. 2.5. The lowering rate, C_o, enters both dimensionless numbers, as C_o sets the pace for both landscape lowering and drainage of the bedrock.

The residence time of material that arrives at the soil bedrock boundary at the ridgetop, T_{r0}, is calculated as the ridgetop weathered thickness divided by the channel incision rate. Thus, from Eq. 2.4, the residence time at the divide is

$$T_{r0} = \frac{H_0}{C_o} = \frac{\rho_r}{\rho_s}\frac{L^2}{2D} - L(\frac{\varnothing}{C_o K})^{0.5} \qquad (2.5)$$

The forms of Eq. 2.4, 2.5, and 2.6 derived using the non-linear relationship between slope and soil flux is given in the SI.

Figure 2.2A shows qualitatively how the topographic profile, $Z_s(x)$ and the bedrock profile, $Z_b(x)$, vary with the two non-dimensional variables corresponding to the mean slope of each profile. Higher mean hillslope gradients (S_h), due to high uplift or incision rates, longer hillslopes and lower soil diffusivity lead to a deeper weathered bedrock zone. A higher average groundwater table slope (S_w), due to high C_o and low $K/\varnothing$ thins the weathered zone by increasing Z_b.

Figure 2.2B plots the dependence of Z_{b0}/Z_{s0} on S_w and S_h. If S_w is calculated to equal or exceed S_h, bedrock is expected at the surface and the model no longer applies. Steep slopes characterized by S_h above 1.0 are typically associated with exposed bedrock at the

surface (31). For fresh bedrock to occupy a significant portion of the hillslope relief, S_w must be similar to S_h, which implies (according to Eq. 2.5)$\frac{K}{\varnothing} \approx (\frac{\rho_s}{\rho_r}\frac{2D}{L})^2(\frac{1}{C_o})$. If S_w is much less than S_h, then effectively Z_b is at the elevation of the adjacent channel bed.

Figure 2.2 C-F show the predicted Z_s and Z_b profiles as well as the calculated residence time for material within the weathered bedrock zone for four cases. C_o is held constant and the effects of varying D (thus changing S_h) and varying $K/\varnothing$ (thus changing S_w) are shown. The resulting S_h and S_w for these four profiles are plotted in Figure 2.2B for both the linear and non-linear soil transport case. For sufficiently steep slopes such that non-linear soil transport processes prevail, the non-linear model (Eq. 2.S1) is used to plot the surface profiles (Profiles resulting from the linear model are shown in Figure 2.S2). In general, the non-linear model reduces the slope and relief of the hillslope, making it more likely that Z_b is some significant portion of the relief. Note that the modeled groundwater table is predicted to intersect the ground surface at the lowest, steepest portion of the hillslope. While this does violate the model assumptions (e.g. soil mantled, no seepage face), this prediction is consistent with common field observations of relatively fresh, saturated bedrock exposed at the lower, steep portions of hillslopes (see Figure 2.S1). The model also predicts a systematic thickening of the weathered bedrock zone towards the divide and, correspondingly, a systematic increase in residence time of material transiting through the weathered bedrock zone. Despite the relatively high incision rate (0.1 mm/yr), the residence time through the weathered bedrock zone is calculated to be on the order of 100,000 to 1 million years.

In Figure 2.2B, we plot field data from three field sites where the Z_b surface was reported and estimates of erosion rates and bulk densities are available: Rivendell (14), Coos Bay (15) and Rondônia (32). The Rondônia site is located in the Rio Branco and Rio Massanagana watersheds near the town of Ariquiemes, Rondônia, Brazil (9 deg 55 min 33 sec S; long. 63 deg 2 min W) and is underlain by gneiss (32). Both the Rivendell and Coos Bay sites are located in the Pacific Northwest United States and are underlain by turbidite sequences of shale and sandstone, with the Rivendell nearly all shale (e.g. argillite (14)) and Coos Bay mostly sandstone (e.g greywacke(15)). In Figure 2.2B, the observed S_w and S_h are plotted for each site, leading to Z_{b0}/Z_{s0} values of 0.5, 0.72 and 0.83 for Rondônia, Rivendell and Coos Bay, respectively. Co at the Rondônia site is estimated to be approximately 0.004 mm/yr (32) and the 500 m hillslope is roughly convex. C_o is estimated to be roughly 0.4 mm/yr at Rivendell (33) and approximately 0.1 mm/yr at Coos Bay (6). The high S_h values for the Rivendell and Coos Bay sites and the apparent role played by periodic landsliding indicate that the non-linear soil transport relationship (Eq. 2.S1) is the more appropriate soil flux relationship for these sites (29).

While S_h can be observed from topographic data, and depends on relatively constrained values of transport parameters, C_o, and bulk densities, S_w defines the lower boundary and varies with both C_o and a material property, $K/\varnothing$, which ranges over several orders of magnitude. The hydraulic conductivity, K, of consolidated rocks is known to range between 10^{-12} to $10^{-2}m/s$ while effective porosity, $\varnothing$, ranges from nearly zero to 50% (30, 34). Observed values of S_w and C_o can be used to estimate $K/\varnothing$ (Figure 2.S4).

For possible values of C_o, (0.001 to 10 mm/yr (35)), Z_b will be above the elevation of an adjacent channel for $K/\varnothing$ between approximately 10^{-13} and $10^{-8}m/s$ (Figure 2.S4). Based on lithologic permeability compilations reported by Freeze and Cherry (1979) (34) and recently supported by field data compiled by Gleeson et al. (2011) (36), this range of $K/\varnothing$ is associated with shales and unfractured metamorphic and igneous rocks (assuming $\varnothing = 0.1$)

The observed persistence of the water table at the Z_b boundary at the end of summer in Rivendell over seven years of monitoring (5), argues strongly for a very low bedrock $K/\varnothing$ value, consistent with the predicted value of $10^{-10}m/s$. The $K/\varnothing$ value predicted for the Coos Bay site is $10^{-11}m/s$ (Figure 2.S4). Ebel et al., (2007) (37) modeled the runoff and groundwater dynamics for a relatively short period at Coos Bay and assigned a $K/\varnothing$ value of $5x10^{-7}m/s$ for the fresh bedrock zone. The groundwater table continually dropped, however, during the modeling period (38) hence the modeled $K/\varnothing$ did not lead to the observed condition of a persistent water table significantly higher than the channel elevation.

Using model parameters for the Coos Bay site (Table S1), Figure 2.3 illustrates the influence of C_o on the relative weathered zone thickness (Z_{b0}/Z_{s0}) and the residence time of material arriving at the soil-weathered bedrock boundary at the ridgetop (T_{r0}). The linear model for $Z_s(x)$ predicts that as channel incision rates and $K/\varnothing$ increase, the weathered zone progressively thickens (Z_{b0}/Z_{s0} decreases) and the material residence time correspondingly increases (Figure 2.3). In contrast, the onset of non-linear soil transport dominance, which generally applies as landscapes steepen (29, 39, 40), significantly slows the rate of increase of the hillslope gradient with increasing channel incision rate. Consequently, because S_w continues to increase with incision, the predicted weathered bedrock zone reaches a maximum value (minimum Z_{b0}/Z_{s0}) and then thins as C_o increases (Figure 2.3A). Increasing $K/\varnothing$ lowers the weathered bedrock zone to the channel elevation (Z_{b0}/Z_{s0} approaches zero) but does not eliminate or shift the value of C_o at which the lowest Z_{b0}/Z_{s0} occurs. The material residence time correspondingly has a maximum value, but it shifts to greater values with decreasing C_o and increasing $K/\varnothing$. While the general pattern illustrated in Figure 2.3 holds, the specific values depend on L, ρ_r/ρ_s , and transport parameterization (D,S_c).

2.3   Discussion

The coupled equations that predict the thickness of the weathered zone (Eq. 2.4), the ratio of fresh bedrock to surface relief (Eq. 2.5), and the residence time of material in the weathered zone at the divide (Eq. 2.6) depend on seven parameters for the linear soil flux case, and eight for the non-linear case. Saturated conductivity and porosity of the fresh bedrock, which are treated here as the ratio $K/\varnothing$, are the most difficult parameters to measure. For the likely range of C_o for which the model has applicability, significant S_w (i.e. Z_b above the elevation of the adjacent channel) only occurs for $K/\varnothing$ between 10^{-13}

and $10^{-8} m/s$ (Figure 2.S4). Hence, our model suggests that bedrock of low conductivity is required for a significant portion of the hillslope relief to remain unweathered. As argued by Hatijema and Mitchell-Bruker (2005) (41) and explored by Gleeson et al. (2008, 2011), (36,42) the tendency for a water table to reflect the local topography increases with decreasing hydraulic conductivity, K. Gleeson and Manning (2008) (43) further suggest that low hydraulic conductivity crystalline rock within hillslope interiors limits the role of regional groundwater flow between watersheds.

Despite a few deep conductive fractures in the bedrock, Z_b may remain elevated well above the channel floor. At the Coos Bay site (Figure 2.S1) for example, Anderson et al. (2002) (6) noted two fractures between 12 and 36 m below the surface at the divide that showed signs of oxidation in otherwise fresh bedrock. Similarly, Gburek and Folmar (1999) (44) noted the occurrence of local weathered and more conductive fractures within fresh sedimentary rocks in a drill hole used for characterizing groundwater dynamics on an unglaciated hill in Pennsylvania. This suggests that even though rare fractures may be seasonally dynamic in transmitting some deeper groundwater flow, Z_b might be maintained well above the channel elevation by the predominance of low conductivity rock matrix and the absence of abundant conductive fractures (see SI).

The boundary condition for $Z_b(x)$ in Eq. 2.2 is that all lateral flow emerges at the channel surface at the base of the hillslope (Figure 2.1). The flux of water per unit length of channel due to drainage of the fresh bedrock is simply $C_o \varnothing L$, which, given very slow incision rates (less than 1 mm/yr) and low porosity (less than 0.1), will be typically less than $10^{-3} m^3/m - yr$. This is an undetectable amount of runoff addition to a channel. Even in a seemingly dry channel, slow flow to the channel may occur

While the model successfully predicts a thickening weathered zone towards the divide, it also predicts a surprising Z_b dependency on tectonics and climate. The depth of weathering and the degree of weathering is not a simple function of erosion rate. One might expect that faster erosion rates would thin a weathering profile, but instead the profile initially thickens with increasing uplift (Figure 2.4) due to the more rapid steepening of the hillslope than the groundwater table. This thickness then decreases once non-linear soil transport prevails. Hence, for the non-linear case, fresh bedrock could be at the surface if erosion rates are slow or fast, and, for the Coos Bay example this requires channel incision rates less than 0.02 mm/yr and greater than 0.4 mm/yr. Residence time, and thus, degree of alteration of the weathered rock zone is correspondingly a parabolic function of incision rate, with shorter residence times and a narrower range of possible residence times with decreasing $K/\varnothing$. Observations in the slowly eroding landscapes of tropical Rondônia, Brazil (32)($Z_{b0}/Z_{s0} = 0.5$) and the humid temperature Appalachian Piedmont (15)($Z_{b0}/Z_{s0} = 0.64 - 0.8$) suggest that the bottom-up limit on Z_b may have broad application beyond areas of rapid uplift.

Neither the elevation profile of Z_b (Eq. 2.3), nor the thickness of the weathered zone (Eq. 2.4) is an explicit function of rainfall or runoff rate but climate may play an important role (see full discussion in SI). Climate influences L (or valley wavelength) (e.g., refs 45, 46), C_o (e.g., ref 47), D (48), and ρ_r/ρ_s due to chemical weathering (e.g., ref 6).

Three-dimensional topographic effects arising from ridge and valley topography and vertical or lateral heterogeneities, especially of $K/\varnothing$, could significantly affect the Z_b profile. The time scale to develop the steady state profile modeled here is possibly several relief replacement times (48, 49). For example, a 50 m high hillslope eroding at 0.1 mm/yr requires at least 500,000 years to reach steady state. C_o is unlikely to be constant over such time scales. Global climate cycles and internal dynamics of stream capture, episodic instabilities (e.g. landslides), variably resistant bedrock, propagating knickpoints, and lateral shifting of the channel will all contribute to non-uniform channel incision, even under relatively constant uplift. Such variations could also lead to perturbations in the Z_b profile, and in the case of lateral channel shifting, dissociation of the Z_b profile from the more rapidly adjusting surface topographic profile. Numerical modeling of unsteady C_o is needed to evaluate the degree to which the Z_b profile is damped in response to perturbations.

2.4 Conclusion

Until hillslope interiors are more accessible, either through geophysical imaging or extensive deep drilling, the relationship between surface topography (Z_s) and the topography of the transition to underlying fresh bedrock (Z_b) will remain essentially unknown. This knowledge gap is important to geomorphic, hydrologic, geochemical, ecological, and atmospheric processes. Our theory suggests that slow groundwater drainage of fresh bedrock creates a bottom-up control on the elevation of Z_b. Consistent with limited field data, the weathered zone is predicted to thicken towards the divide. Z_b can be a significant fraction of the hillslope relief under a specific set of circumstances for a given hillslope length: 1) the underlying fresh bedrock $K/\varnothing$ is less than $10^{-9} m/s$ and fractures are rare and mostly nonconductive; 2) channel incision rate is slow (order 0.1 mm/yr or less) or sufficiently high that non-linear soil transport dominates; 3) dissolution significantly lowers the weathered bedrock bulk density (leaving less to be carried away by soil transport); and 4) soil diffusivity is high. The model is testable because all variables can be determined with current technology of topographic surveying, cosmogenic nuclide measurements of erosion rates, field mapping of Z_b through drilling, and measurements of bulk density, porosity, and saturated hydraulic conductivity. The systematic drilling of ridgetops at well-chosen sites could demonstrate the circumstances where Z_b is below the surface and above the elevation of an adjacent channel and also evaluate if the model predicted $K/\varnothing$ corresponds with the observed rock type. Such work would illuminate the interior structure of hillslopes and allow for the systematic mapping of the fresh bedrock topography under landscapes. Just as high-resolution digital elevation data of topography is revolutionizing earth surface process research, we now need high-resolution maps of the topography of the weathering front, Z_b, under landscapes. This is a shallow frontier in earth surface processes.

2.5 References

1. Linton DL (1955) The problem of tors. The Geographical Journal 121:470–487.

2. Ruxton V BP, Berry L (1959) The basal rock surface on weathered granitic rocks. Proceedings of the Geologists' Association 70:285–290.

3. Mabbutt JA (1961) Basal surface'or "weathering front." Proceedings of the Geologists' Association of London 72:357–358.

4. Witty JH, Graham RC, Hubbert KR, Doolittle JA, Wald JA (2003) Contributions of water supply from the weathered bedrock zone to forest soil quality. Geoderma 114:389–400.

5. Anderson SP et al. (1997) Subsurface flow paths in a steep, unchanneled catchment. Water Resources Research 33:2637–2653.

6. Montgomery DR, Dietrich WE (1988) Where do channels begin? Nature 336:232–234.

7. Pavich MJ (1989) Investigations of the characteristics, origin, and residence time of the upland residual mantle of the Piedmont of Fairfax County, Virginia. US Geological Survey professional paper.

8. Taylor G, Eggleton RA (2001) Regolith geology and geomorphology (Wiley).

9. Maxwell RM, Kollet SJ (2008) Interdependence of groundwater dynamics and land-energy feedbacks under climate change. Nature Geoscience 1:665–669.

10. Anderson SP, Bales RC, Duffy CJ (2008) Critical zone observatories: Building a network to advance interdisciplinary study of Earth surface processes. Mineralogical Magazine 72:7–10.

11. Brantley SL, Lebedeva M (2011) Learning to read the chemistry of regolith to understand the Critical Zone. Annual Review of Earth and Planetary Sciences 39:387–416.

12. Gerrard J (1988) Rocks and landforms (Allen & Unwin Australia).

13. Cotton CA (1942) Climatic accidents in landscape-making (John Wiley & Sons).

14. Büdel J (1957) Double surfaces of leveling in the humid tropics. Zeitschrift für Geomorphologie 1:223–225.

15. Ruxton BP, Berry L (1957) Weathering of granite and associated erosional features in Hong Kong. Geological Society of America Bulletin 68:1263–1292.

16. Thomas MF (1966) Some geomorphological implications of deep weathering patterns in crystalline rocks in Nigeria. Transactions of the Institute of British Geographers:173–193.

17. Brantley SL, White AF (2009) Approaches to modeling weathered regolith. Reviews in Mineralogy and Geochemistry 70:435.

18. Ague JJ, Brimhall GH (1989) Geochemical modeling of steady state fluid flow and chemical reaction during supergene enrichment of porphyry copper deposits. Economic Geology 84:506–528.

19. Mann A (1998) Oxidised gold deposits: Relationships between oxidation and relative position of the water-table. Australian Journal of Earth Sciences 45:97–108.

20. Ruddock E (1967) Residual soils of the Kumasi District in Ghana. Geotechnique 17:359–377.

21. Feininger T (1971) Chemical weathering and glacial erosion of crystalline rocks and the origin of till.

22. Anderson SP, Dietrich WE, Brimhall GH (2002) Weathering profiles, mass-balance analysis, and rates of solute loss: Linkages between weathering and erosion in a small, steep catchment. Geological Society of America Bulletin 114:1143.

23. Rempe D, Oshun J, Dietrich W, Salve R, Fung I (2010) Controls on the weathering front depth on hillslopes underlain by mudstones and sandstones. AGU Fall Meeting Abstracts 1:05.

24. Dietrich WE et al. (2003) Geomorphic transport laws for predicting landscape form and dynamics. GEOPHYSICAL MONOGRAPH-AMERICAN GEOPHYSICAL UNION 135:103–132.

25. Roering JJ, Kirchner JW, Dietrich WE (2001) Hillslope evolution by non-linear, slope-dependent transport: Steady-state morphology and equilibrium adjustment timescales. Journal of Geophysical Research 106:16–499.

26. Bear J (1988) Dynamics of fluids in porous media (Dover publications).

27. Kirkham D (1967) Explanation of paradoxes in Dupuit-Forchheimer seepage theory. Water Resources Research 3:609–622.

28. Freeze RA, Cherry JA (1979) Groundwater., 1979.

29. Portenga EW et al. (2011) Understanding Earth's eroding surface with 10 Be. GSA Today 21.

30. McKean JA, Dietrich WE, Finkel RC, Southon JR, Caffee MW (1993) Quantification of soil production and downslope creep rates from cosmogenic 10Be accumulations on a hillslope profile. Geology 21:343.

31. Maher K (2011) The role of fluid residence time and topographic scales in determining chemical fluxes from landscapes. Earth and Planetary Science Letters 312:48–58.

32. Dietrich WE, Bellugi D, De Asua RR (2001) Validation of the shallow landslide model, SHALSTAB, for forest management. Water Science and Application 2:27.

33. Reneau SL, Dietrich WE (1990) Depositional history of hollows on steep hillslopes, coastal Oregon and Washington. National Geographic Research 6:220–230.

34. Roering JJ, Kirchner JW, Dietrich WE (1999) Evidence for nonlinear, diffusive sediment transport on hillslopes and implications for landscape morphology. Water Resources Research 35:853–870.

35. Heimsath AM, Chappell J, Dietrich WE, Nishiizumi K, Finkel RC (2001) Late Quaternary erosion in southeastern Australia: a field example using cosmogenic nuclides. Quaternary International 83:169–185.

36. Roering JJ, Perron JT, Kirchner JW (2007) Functional relationships between denudation and hillslope form and relief. Earth and Planetary Science Letters 264:245–258.

37. Hilley G, Chamberlain C, Moon S, Porder S, Willett S (2010) Competition between erosion and reaction kinetics in controlling silicate-weathering rates. Earth and Planetary Science Letters 293:191–199.

38. West AJ (2012) Thickness of the chemical weathering zone and implications for erosional and climatic drivers of weathering and for carbon-cycle feedbacks. Geology 40:811–814.

39. Alpers, CN, Brimhall GH (1988) Middle Miocene climatic change in the Atacama Desert, northern Chile: Evidence from supergene mineralization at La Escondida. Geological Society of America Bulletin 100:1640–1656.

40. Fernandes NF, Dietrich WE (1997) Hillslope evolution by diffusive processes: The timescale for equilibrium adjustments. Water Resources Research 33: 1307– 1318.

41.   Meinzer OE (1923) Outline of ground-water hydrology. US Geological Survey Water Supply Paper 494:5.

42.   Hubbert MK (1940) The theory of ground-water motion. The Journal of Geology:785–944.

2.6 Figures
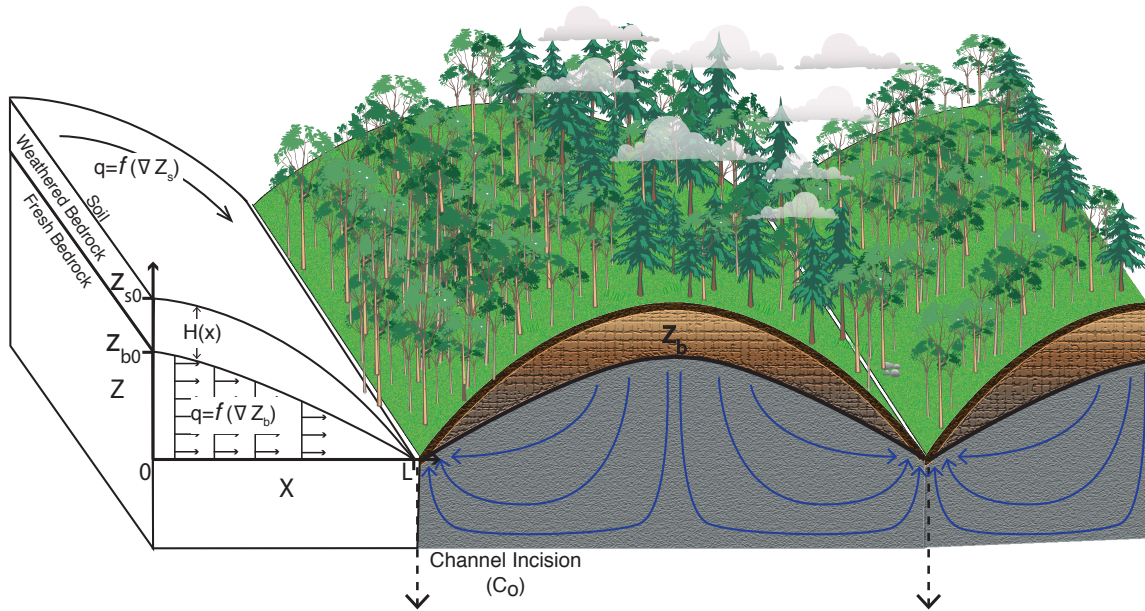
Figure 2.1: Conceptual model showing the elevation of fresh bedrock, Z_b, under ridge and valley topography with a thin soil mantle overlying a weathered bedrock zone that extends to Z_b. Channel incision, at the rate C_o, drives hillslope erosion and drainage of fresh bedrock (flow paths illustrated with blue arrows). The left side of the figure illustrates the model framework and assumptions. At the ridgetop (x=0), the surface elevation is Z_{s0} and the fresh bedrock elevation is Z_{b0}. Groundwater flux, q_w, is horizontal and proportional to the water table gradient, ∇Z_b. Soil transport, q_s is proportional to the surface slope, ∇Z_s. All soil and water leaves the hillslope at L where the hillslope meets the channel. At steady state, the rate of channel incision (C_o) is equal to the uplift rate such that the ground surface, Z_s and surface of the fresh bedrock, Z_b, are stationary.
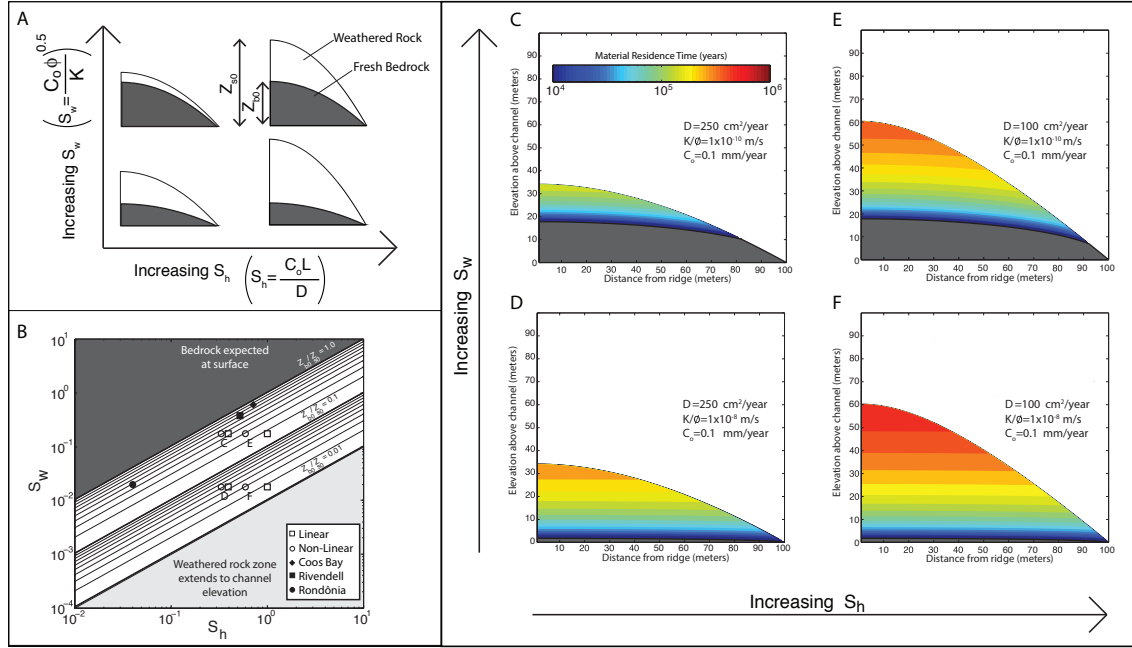
Figure 2.2: Controls on the fresh bedrock profile and thickness of the weathered zone under hillslopes. (A) Conceptual illustration of the dependence of the weathered zone thickness on the mean hillslope gradient, S_h, and mean groundwater table slope, S_w, and thus soil transport and hydraulic properties (all terms defined in the text). (B) The dependence of the ratio of fresh bedrock relief to hillslope relief at the ridgetop, Z_{b0}/Z_{s0}, on S_h and S_w illustrates the parameter space for which the weathered zone is expected to be limited in vertical extent by drainage of fresh bedrock. Observations from three sites (solid symbols) and data associated with the example profiles shown in Figs. 3 C-F (open symbols) are plotted. Open circles represent results of the linear soil flux model (Eq. 2.5) and open squares represent the non-linear model (Eq. 2.S2). The dark gray area indicates where S_w exceeds S_h and thus bedrock is expected at the surface. The light gray area indicates where S_w is so low relative to S_h that Z_{b0} is essentially at the elevation of the channel. (C-F) Four example profiles for a fixed hillslope length (L=100 m) and lowering rate ($C_o = 0.1mm/yr$) demonstrate the influence of soil diffusivity, D, and the ratio of hydraulic conductivity to porosity, $K/\varnothing$, on the thickness and residence time of the weathered bedrock zone. Fresh bedrock is denoted by dark gray. The surface topography was calculated using the non-linear model (29) assuming a critical slope, S_c, of 1.2 (Eq. 2.S1). The corresponding linear profiles are shown in Figure 2.S1.
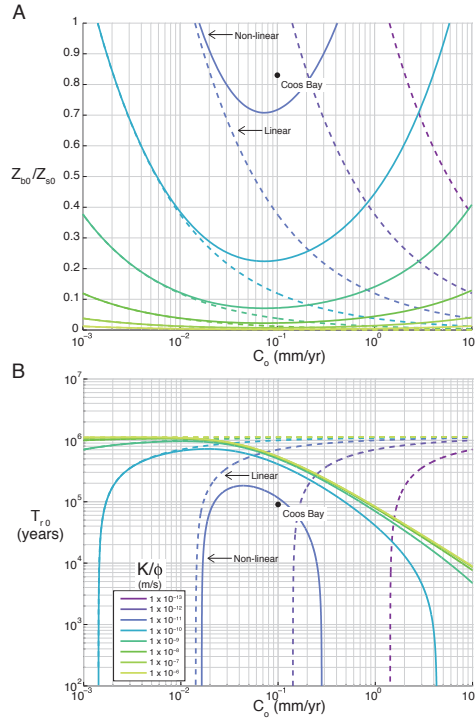
Figure 2.3: Mapping the ratio of saturated hydraulic conductivity to porosity $(K/\varnothing)$, fresh bedrock relief ratio (Z_{b0}/Z_{s0}) and mean residence time (T_{r0}). (A) The influence of channel incision rate, C_o, on the fraction of the total hillslope relief that is unweathered (Z_{b0}/Z_{s0}). (B) The influence of C_o on the residence time of the weathered material that arrives at the soil-bedrock boundary at the ridgetop (T_{r0}). In both (A) and (B), solid lines represent predictions using a non-linear relationship between soil flux and slope (Eq. 2.S2, S3) and dashed lines represent the linear model. Model parameters for Coos Bay were used to generate predictions (Table S1). A range of $K/\varnothing$ is shown to illustrate how the deviation between the linear and non-linear model predictions depend on $K/\varnothing$ such that higher $K/\varnothing$ will produce a thicker weathered zone. Deviations between the two model results are minimal at low C_o but increase with increasing C_o. Whereas the linear model predicts a thickening of the weathered zone (and thus an increase in residence time) with increasing erosion rate, the non-linear model predicts a maximum weathered zone thickness that depends on the bulk density ratio, p_r/ρ_s, hillslope length, L, and critical slope, S_c.

Part II

Field investigation of critical zone hydrologic dynamics

Chapter 3

Site description and methods

3.1   Introduction

Part II describes the results of an intensive investigation focused on characterizing the structure and hydrologic dynamics of the critical zone. The focus of the study is the Rivendell experimental hillsope at the Eel River Critical Zone Observatory within the steep, forested, seasonally dry Northern California Coast Ranges. In the first chapter of Part II (Chapter 3), I introduce the site and methods used in the following chapters. In Chapter 4, I report the results of a drilling investigation aimed at characterizing the critical zone rock weathering profile properties and general hydrologic dynamics. Chapter 5 details the spatial and temporal dynamics of rock moisture, the exchangeable water within weathered and fractured rock, observed within the hillslope. In Chapter 6, I explore the consequences of the spatial structure of the critical zone on groundwater flow and runoff generation. In effect, I introduce the site and methods (Chapter 3), describe the critical zone structure (Chapter 4) and its influence on unsaturated zone (Chapter 5) and saturated zone (Chapter 6) processes. In each chapter, I introduce the research objective and provide a summary of the main findings. I conclude in the final chapter (Chapter 7) with a synthesis of the results outlined in Chapters 4-6.

3.2   Site Description

The study site (39.729 N, 123.644 W) is a steep (average 32 degrees) hillslope affectionately known as "Rivendell." Rivendell is located 150 miles north of San Francisco in Mendocino County, California, and is a small hillslope located within the University of California Angelo Coast Range Reserve (http://angelo.berkeley.edu/). It lies 14 kilometers inland from the Pacific coast, which places the site just outside the coastal fog belt but still within the California Coastal Mountain Range. Rivendell is a 4000 square meter catchment within a hillslope that drains to Elder Creek at 392 m.s.l., a tributary of the South Fork Eel River. Rivendell is located near the mouth of the 17 km^2 Elder Creek watershed. Slightly upstream of Rivendell, along Elder Creek, a United States Geological Survey benchmark real-time gauging station has operated since 1965 (Station 11475560).

As part of the Eel River Critical Zone Observatory, formerly Keck Hydrowatch, over 750 hydrologic and climatic sensors across Rivendell are powered by treetop solar panels and transmit measurements wirelessly across a network of radios and servers within the reserve. To date, over 374 million data points have been collected and stored in the sensor database, with new data available nearly in real-time (http://sensor.berkeley.edu). Instruments record the moisture content of soil and rock at 27 stations, groundwater levels in 12 wells, climatic conditions such as temperature, humidity and solar radiation at 5 stations, and sap flow in over 30 trees across the site. Rivendell is a steep north facing slope and the south slope, which is the headwall of a deep-seated landslide, has a considerably shallower slope of 25 degrees.

Climate

The climate is characterized as Mediterranean, with warm dry summers and cool wet winters. The area receives an annual average of 1800 mm of rain with very little snow, but there is significant variability in total annual precipitation (Link et al., 2014). A 60 year average annual precipitation of 1763 mm was recorded at at nearby Richardson Grove State Park Weather Station. The vast majority of precipitation falls between October through May. Early October daily temperature is about 10 degrees C (which is the average annual temperature); the daily average temperature then drops to nearly 0 degrees C by the end of December before increasing to 20 degrees C in early August (http://angelo.berkeley.edu/). Daily fluctuations in temperature are much larger during the warm summer months than in the winter.

Vegetation

The forest is old growth needleleaf and broadleaf evergreen and relatively dense with a limited understory. Species include Douglas-fir (*Pseudotsuga menziesii*), interior live oak (*Quercus wislizeni*), tanoak (*Notholithocarpus densiflorus*), Pacific madrone (*Arbutus menziesii*), California bay (*Umbellularia californica*) and some relatively younger coast redwood (*Sequoia sempervirens*). Douglas-fir constitutes approximately 40% of tree basal area in the Eel River watershed (Woudenberg et al., 2010) and forms the overstory at the site, with heights up to 55-60 meters. The other species form the lower canopy at approximately 20 meters. Below the lower canopy, there are smaller (5-10 meter) trees of varying type and no dense ground cover. Pacific madrones occur more frequently upslope, but the rest of the trees appear to have a relatively even distribution.

Geologic setting

Most of the site is underlain by nearly vertically dipping argillite, which strikes approximately parallel to the hillslope axis. Along the eastern divide, a sandstone interbed is exposed at the surface (Figure 3.1). Minor interbeds of sandstone in this marine turbidite sequence are common. Kim et al. (2014) report that the major clay minerals are illite, Fe-rich chlorite, kaolinite and mixed layer illite/montmorillonite and the major primary minerals are quartz K-feldspar, plagioclase and chlorite.

The underlying geology, mapped as the Coastal Belt of the Franciscan Formation (McLaughlin et al., 2000), is a record of the accreted terrain of the North American plate margin and consists of slightly metamorphosed marine sedimentary rocks. The Elder Creek watershed falls mostly within the Yager Terrane, however the southwesternmost portion, including the mouth of Elder Creek where Rivendell is located, is mapped within the Coastal Belt Terrane. The Yager terrane is described as well-bedded, little sheared, locally highly folded mudstone rich turbidities with interbeds and lenses of sandstone and conglomerate (Blake et al., 1985). The Yager and Coastal Belt are geochemically similar

(Ernst and McLaughlin, 2012), however structural differences are reported: The Yager Terrane is less severely deformed and has less laumontite veining and no volcanic material, while the Coastal Belt Terrane, is more deformed, has abundant laumontite veining, and does contain volcanic material (Langenheim et al., 2013). The mapped boundary between the two terrances is shown as closely aligned with the ridge forming the southern boundary of the Elder Creek catchment (Langenheim et al., 2013), but this mapping relied primarily on interpretation of photography and topography and must be considered as approximate. Despite the tectonic deformation, the area retains mappable bedding (unlike the Central Belt mélange farther to the east).

The Eel River watershed emerged above sea level in the past 2-4 million years (Lock et al., 2006). Incision rate along Elder Creek during the Holocene was approximately 0.2 mm/yr, while Pleistocene erosion rates associated with wetter conditions approached 0.4 mm/yr (Fuller et al., 2009). Contemporary uplift rates increase from south towards the north from 0.4 mm/yr to >4 mm/yr (Merritts and Bull, 1989). Pleistocene to Holocene erosion rates of $0.07 - 0.35$ mm/yr are measured locally (Fuller et al. 2009). Erosion rates as high as 0.9 mm/yr were measured over the Eel River (Wheatcroft and Summerfeld, 2005). Deep seated landsliding is pervasive and delivers much of the sediment to the channel. Mackey and Roering (2015) proposed that up to 7% of the Elder Creek watershed moved in the past 62 years. Rivendell is a steep north-facing slope with no evidence of deep landsliding. Across the ridge, the south slope, however, forms the headwall of an ancient deep-seated landslide. Rivendell drains directly to the channel but much of Elder Creek is lined by strath terraces which record the active incision into bedrock.

3.3   Prior work at the Rivendell field site

Rivendell was established in 2007 as part of the Keck Hydrowatch project. Since then, projects focused on the spatial and temporal pattern of evapotranspiration of the mixed canopy forest (Link et al., 2014), the source of water to vegetation (Oshun, 2015), controls on the geochemical composition of groundwater (Kim et al., 2012, 2014), streamflow solute concentrations (Kim, 2014, Thurnhoffer, 2015), the extent of the wetted channel in Elder Creek (Lovill, in prep), the subsurface stable isotope composition of pore fluids (Oshun et al., 2015), spatial and temporal patterns of groundwater, soil and rock moisture (Salve et al., 2012), numerical representation of rapid groundwater flow (Vrettas and Fung, 2014) and the development of the weathering front (Rempe and Dietrich, 2014).

Kim et al. (2014) monitored the geochemical composition of groundwater and streamflow at Rivendell at daily frequency in three wells (1,3, and 10) across the hillslope via automated sampling. Kim et al., 2014 found two dominant processes that influence the observed patterns of groundwater chemistry: 1) At high water table positions during the wet season, groundwater is more concentrated than rain water but has relatively low cation and high silica concentrations which are controlled by the fast cation exchange reactions and the probably dissolution of amorphous silica in soils and saprolite (and per-

haps fractured, weathered bedrock) in the near surface where elevated CO_2 concentrations provide a source of protons and 2) At low water table positions during the dry season, groundwater reaches thermodynamic equilibrium with secondary minerals and high base cation concentrations in groundwater are observed. These two "end-member" groundwater compositions are thought to control stream water chemistry in Elder Creek and the spatial and temporal variability of stream chemistry is currently under investigation.

By monitoring sapflow measurements of 26 trees on the Rivendell hillslope, Link et al. (2014) found that the evergreen species on the site exhibit distinct differences in the seasonality of their transpiration rates and that this seasonality is expected to have a significant influence on regional climate. Douglas fir, (*Pseudostuga menziesii*) transpiration peaks in the wet spring and declines significantly during the summer months while other species including Pacific madrone transpire maximally in the mid to late summer when insolation peaks. By comparing transpiration rates to measurements of soil moisture, Link et al., 2014 suggest that the decline in Douglas fir transpiration over the summer months is linked to the sensitivity of Douglas fir stomatal conductance to water availability and vapor pressure deficit, while broadleaf species such as madrone are less sensitive to water stress and maintain greater stomatal conductance during the dry summer. Using an atmospheric modell, Link (2015) demonstrated that a shift in species composition from dominantly broadleaf to dominantly conifer may lead to a near-surface 1.5-2.5 ∘C warming and 2-3 g/kg change in humidity due to the difference in the seasonality of transpiration.

Oshun (2015), investigated the source of water to vegetation through stable isotope (dD and d18O) analysis of weathered bedrock, groundwater, soil, vegetation and rain. Through monitoring of stable isotopes throughout the seasonal cycle over several years, Oshun (2015) show that that the dominant conifer species, Douglas fir, (Pseudostuga menziesii), relies primarily on rock moisture whereas adjacent hardwoods (e.g. Interior live oak Quercus wislizeni) exploit soil moisture. An artificial injection (tracer test) of water below 1.5 m (Oshun, 2015) directly demonstrated the uptake of rock moisture by Douglas Fir in the summer of 2014.

Oshun (2015) found that, despite the rise and fall of the water table, the stable isotope composition of groundwater was relatively invariant, was distinctly different from the stable isotope composition of water taken up by trees (even where groundwater was shallow), and was distinctly different from the composition of water extracted from the rock that the groundwater occupies. By tracking the stable isotope composition of incoming rainfall within the weathering profile (soil, saprolite, and weathered rock) across the hillslope, Oshun et al., (2015) documented a persistent structure of stable isotope pore fluid composition that they suggest reflects the potential evolution of water through the critical zone.

Salve et al., (2012) analyzed the response of soil moisture, rock moisture (a term they introduced that is further explored in Chapter 5) and the groundwater system to rainfall, particularly to the first storms of the season. Their analysis was limited to wells drilled in 2007 (1, 3, 5, 6, 7, 10). They proposed that precipitation travels vertically through the

weathered bedrock along fractures, perches on the dense fresh bedrock, and then flows to the adjacent stream, Elder Creek. The first rains of the season which mark the end of the long dry summer can generate a rock moisture response at depths beyond the soil. Early small storms also cause a rapid but minor water table rise that is short-lived. Subsequent rainfall during the wet season advances a wetting front through fractured and weathered bedrock and recharges a fracture dominated seasonally perched groundwater system which delivers water to the adjacent stream. Salve et al., 2012 suggest that recharge is dominated by flow through fractures, rather than the rock matrix, and document significant seasonal changes in rock moisture, the water stored within fractured bedrock, that exceeded that observed in soil. They observed that rock moisture changes diminished at depth, and that despite the rise and fall of the water table during a large (>200 mm) storm, rock moisture changes were not observed within the water table fluctuation zone suggesting a distinct structure to rock moisture dynamics in the unsaturated and saturated zone.

Vrettas and Fung (2014), motivated to include the processes documented in Salve et al. (2014) in climate models, propose a novel treatment of hydraulic conductivity parameterization that simulates both the rock moisture dynamics and the rapid delivery of water to the groundwater. They showed that by representing the mean hydraulic conductivity (which declines with depth) as a product of effective saturation and a background hydraulic conductivity drawn from a lognormal distribution, they could capture both the rapid groundwater response and the seasonal change in rock moisture content.

3.4   Methods

Drilling

In September 2007 and August 2010, boreholes were drilled into the hillslope using a tractor-mounted rig on and above a dirt access road and a hand-portable system below the road on the steeper portion of the hillslope (Table 3.1). Both systems used a combination of dry augering and standard penetration resistance testing to advance the hole and retrieve samples. During drilling, standard penetration resistance was measured by dropping a 140 lb hammer 30 in. on a 2 in. outside diameter split spoon sampler and recording the number of blows required to penetrate 6 inches. This value was used to calculate the N-value or standard penetration resistance in blows per foot. For penetration smaller than 6 inches, the number of blows was recorded and standard penetration resistance was calculated by dividing the number of blows by the penetration distance and converting this value to blows per foot. Our method differs from the ASTM standard (D1586 − 11) in that N-values were calculated for each individual advance of the sampler as opposed to summed over two 6 inch penetrations and additionally, N-values greater than 100 blows/foot were recorded. Therefore, the N-values or standard penetration resistance can be considered a modified penetration resistance and is referred to as N or penetration resistance herein. The drilled holes were lined with perforated PVC (polyvinyl chloride)

pipes, sealed at the surface with a cement grout, and fitted with submersible pressure transducers and temperature sensors (CS450 and CS451, Campbell Scientific, Inc.) to monitor the height of water in each borehole and water temperature.

These vertical holes were also used to monitor rock-moisture changes using a neutron probe (Model CPN 503DR Hydroprobe). In our surveys, we lowered the probe at 0.3 m intervals throughout the entire unsaturated zone at the time of measurement. The neutron count measured by the neutron probe is sensitive to the volumetric water content of material within approximately 30 cm of the probe and has been shown to be linearly related to volumetric water content. The magnitude of the counts also depends on the casing material, which is uniform for all wells, and diameter, which varies at our site (Table 3.1). While neutron count readings are most sensitive to the presence of hydrogen, variations in soil and rock composition influence the magnitude of counts. Specifically, high absorption capacity elements such as iron, potassium, manganese, boron, and chlorine will decrease neutron counts (Burn 1964, Couchat 1967). In successive measurements over time, water content is the only variable expected to influence changes in neutron counts. While most hydrologic and climatic observations from this investigation (i.e., precipitation, atmospheric temperature, moisture-content changes in shallow profile, water table fluctuations) are from continuous measurements made at a high temporal resolution, neutron probe measurements and downhole temperature and dissolved oxygen profiles are from periodic measurements made at various discrete times. Monitoring equipment is powered by solar panels and data are transmitted to a server via radios. Various power outages and sources of electronic noise were encountered during the period of observation and data from these intervals were not analyzed. Therefore, despite mostly continuous monitoring of all hydrologic and climatic variables, some data are not available for certain discrete periods and are therefore missing or not included in the analyses that follow.

Laboratory Analysis of drilling samples

Samples of soil and rock recovered during drilling were analyzed in hand sample for evidence of weathering. Samples were logged for lithologic characterization (primarily grain size), color, presence of weathering rinds, coatings, or precipitates, presence of roots, extent of fracturing, and friability. Representative samples from each depth where standard penetration testing was conducted were quantitatively analyzed for color through analysis of digital photography. Core samples were photographed under standardized lighting conditions and digital image processing of the photographs provided a quantitative estimate of the RGB and CIELAB color space for each core sample.

Samples for gravimetic moisture content analysis were bagged, placed in a cooler, and transported to a laboratory located within the Angelo Coast Range Reserve within hours of retrieval. Samples were weighed before and after drying at 105 C for 24 hours. Different samples were later taken from storage for measurement of saturated gravimetric moisture content. content. To document moisture content increase upon wetting of matrix blocks, samples of rock matrix were soaked in deionized water for 96 hours and dried by hand

using Kim wipes until no moisture was observed on the Kim wipe and the difference in mass between the soaked sample and the sample dried for 24 hours at 105 C was used to calculate the gravimetric moisture content, $\Theta_{grav} = \frac{m_{wet} - m_{dry}}{m_{dry}}$ where m_{wet} is the mass of the sample prior to oven drying, and m_{dry} is the mass of the sample after drying.

Soil Moisture and Climatalogical Data

Soil moisture was monitored via time domain reflectometers (TDR) across the hillslope. Two types of TDR installation were used to monitor soil moisture (see Salve et al., 2012). Short, 15 cm, TDR (TDR100, Campbell Scientific) were installed directly into soil in small trench faces which were then backfilled (T-series TDR). Long, 30 cm long, TDR (Model CS610_L, Campbell Scientific) were installed in augered holes which were backfilled with native soil (S-series).

Continuous moisture content monitoring of shallow saprolite and weathered rock was accomplished using TDR that were installed using several methods (see Oshun, 2015 and Salve and Rempe, 2013). Three 30 cm long TDR (L5 0.7-1.38 m), (Model CS610_L, Campbell Scientific) were installed into a trench face in highly weathered sandstone saprolite near Well 15. Near the road cut, two 30 cm long TDR (L4, Model CS610_L, Campbell Scientific) were installed directly into fractures located within argillite and sandstone (Salve and Rempe, 2013). Two other 30 cm long TDR (also labeled L4) were installed directly into argillite and sandstone matrix by drilling holes the diamter of the TDR probes and directly pressing the TDR into the matrix.

Precipitation records used in water budget calculations are from the Angelo Meadow Weather Station. Between March 8 2015 and March 25 2015 the Angelo Meadow weather station sensor was down. A modified Angelo Meadow Weather Station rainfall (mm) and cumulative rainfall (mm) dataset was genereated by using the Cahto Peak dataset during the Angelo Meadow Weather Station outage.

Nearby, upstream along Elder Creek, a United States Geological Survey benchmark real-time gauging station has operated since 1965 (Station 11475560) and streamflow data are derived from there. The microclimate of the hillslope was monitored with four raingauges (TE525 Campbell Sci., Inc), (Figure 3.1). Topographic data are derived from LiDAR (light detection and ranging) provided by the National Center for Airborne Laser Mapping (NCALM) in a survey conducted in 2014. Microclimate data were also recorded in an open meadow across Elder Creek from the site (initiated in Fall 2008 using the same system as on the site). The clocks on the control device were synchronized and periodically checked to ensure that timing of measurements along the site were always consistent.

Analysis of groundwater response

During the period of monitoring (2008-2015), we evaluated the hydrologic response to rainfall both within and between seasons. The wells are continuously slotted through-

out the entire penetrated thickness. This allows us to sample and monitor the entire thickness of the seasonally saturated zone without apriori knowldge about its depth. However, we are prevented from identifying the exact depth intervals from which water is derived or from identifying perched water tables within the otherwise unsaturated zone. By constructing wells this way in a fractured bedrock environment, we were able to make observations about the heterogeneity of the hydrologic response across the hillslope without restricting observations to discrete fractures. The timing of groundwater response to rainfall was evaluated by analyzing the groundwater response to individual storm events. A storm was defined as a period that exceeded 2 mm of rain after more than 6 hours of no rain. Analysis of well hydrographs was restricted to unambiguous, single peaked groundwater responses to storms. Several parameters were used to evaluate the groundwater response to storms. Lag to peak was defined as the lag between the centroid of the storm precipitation and the peak groundwater response. The velocity of the initial groundwater response was defined as time between the initiation of rainfall within a given storm and the initial groundwater level rise. The uncertainty on these time scales is limited to the frequency of data collection which was 30 minutes prior to November 2011 and 5 minutes after November 2011. The amount of precipitation per storm was compared to the groundwater level rise that occurred during the storm. The fraction of the groundwater level rise accounted for by the storm precipitation can be calculated by dividing the cumulative storm precipitation by the maximum groundwater level rise. Assuming that all precipitation reaches the groundwater during the time scale of the storm, all flow is vertical, and all groundwater is associated with fracture porosity, this parameter provides a crude estimate of the fracture porosity within the saturated zone. The seasonal response to rainfall was evaluated by identifying the initial, significant groundwater response which resulted in a seasonally elevated water table. This was distinguishable from small increases and recessions generated by modest Fall storms. The water table elevation in W2 and W13 recedes below the elevation of the bottom of the well, therefore pressure transducer data derived from these time periods was not included in hydrograph analyses. Groundwater from W1, W3, and W10 are also from summer recession hydrograph analyses because of daily pumping for groundwater sampling which complicated the quantitative interpretation of the groundwater recession.

Rock moisture measurement

Rock moisture was monitored in shallow and deep boreholes using a neutron probe (CPN 503DR Hydroprobe, Instrotek Inc. Serial No. 4340702152). Appendix B provides general discussion of neutron probe theory and sources of error as well as specific details pertaining to the calibration and interpretation of neutron probe data in this study. Downhole surveys were conducted in deep (4-30 m) groundwater monitoring wells (Figure 3.1). Groundwater monitoring wells used for neutron probe results reported here were drilled in 2007 (Wells 2, 5, 6 and 7) and 2010 (Wells 12, 13, 14, 15, and 16) and cased with continuously slotted PVC (see Appendix B) and sealed at the surface with cement

to prevent short circuiting of water down the hole. Monitoring wells were outfitted with submersible pressure transducers to monitor groundwater dynamics.

In the field, raw neutron counts, N [1](counts per 16 seconds), were measured throughout the unsaturated zone by lowering the probe down cased borehole at 0.3 m intervals. Neutron counts were converted to volumetric moisture content, θ (m³m⁻³) using a linear calibration between N and θ that depends on the borehole casing diameter and material (Appendix B). Changes in volumetric moisture content, $\Delta\theta$, are calculated as

$$\Delta\theta(z,t) = \theta(z,t) - \theta(z,t_0) \tag{3.1}$$

where z is the depth of measurement (m), t is the time of the survey and, in the analysis that follows, $\theta(t_0)$ is derived from a survey performed on October 25, 2015. This survey date was selected because it represented the driest survey for which data existed in all wells. Not all depths experience the driest conditions at the same time, and we explore this in the section addressing interseasonal storage, but we choose to define a changes in rock moisture using a single survey rather than the driest observation at each depth because we seek to understand the controls on the timing and spatial distribution of rock moisture storage, not just the full dynamical range. We therefore use individual survey dates as snapshots in time.

To quantify changes in the volume of water stored as soil and rock moisture, we define S (mm) as moisture storage relative to a reference date, here taken to be October 25, 2015. Moisture storage, S, is the integral of changes in moisture content over a depth interval:

$$S_{z1-z2} = \int_{z_1}^{z_2} \Delta\theta(z)\, dz \tag{3.2}$$

Soil moisture storage was computed by applying an observed moisture content change to a defined soil thickness over which the measurement applied. To compute rock moisture storage, S, from moisture content changes measured in boreholes via neutron moderation over time we assume that discrete measurements of change in moisture content, $\Delta\theta$, made at regular 0.3 m intervals reflect moisture content changes over the depth interval between the midpoints of successive measurements and therefore, $S(z)$ can be computed as

$$S(z,t) = [(z - 0.15) - (z + 0.15)] * \Delta\theta(z,t) * 1000\frac{mm}{m} \tag{3.3}$$

Discrepancies in survey-to-survey probe placement are expected to influence readings, and were therefore minimized in the field by using the same graduated cable for all surveys presented here. Further, analysis of S over depth intervals greater than the measurement interval helps to overcome errors introduced by potential survey-to-survey inconsistency in the location of the probe in the borehole. To analyze changes in moisture storage over

---

[1]Note that standard penetration resistance (Section: Drilling) is referred to as an "N-value" while neutron counts are denoted by the letter "N."

depth intervals greater than the measurement interval of 0.3 m, $S_{Z_1-Z_2}$ was calculated by summing $S(z)$ throughout the interval.

$$S_{z_1-z_2}(t) = \sum_{z_1}^{z_2} S(z,t) \tag{3.4}$$

The rate of change of rock moisture storage within a specified depth interval is calculated as the change in rock moisture observed between two discrete measurements divided the elapsed time between those measurements:

$$\frac{\Delta S_{z_1-z_2}}{\Delta t} = \frac{S_{Z_1-Z_2}(t_a) - S_{Z_1-Z_2}(t_b)}{t_a - t_b} \tag{3.5}$$

As a means of analyzing changes in rock moisture with depth, we define a parameter ΣS which is the amount of rock moisture stored at or above a particular depth. ΣS is calculated as the cumulative sum of S with depth:

$$\Sigma S(z,t) = \sum_{z_0}^{z} S(z,t) \tag{3.6}$$

To evaluate changes in storage throughout the profile, we also define the term unit storage capacity (mm/m) as the amount of storage observed within a particular measurement location at a particular time. Storage capacity is simply the change in moisture content, $\Delta\theta$ multipled by 1000 to achieve the units of mm/m.

Note that though the magnitude of θ and S in measured in rock depend strongly on the probe-specific, casing-specific, and material-specific calibration of the instrument, the spatial and temporal patterns explored here are largely independent of this calibration. Our analyses and conclusions generally rely on θ and S as a means of understanding patterns of water availability in time and space. However, comparisons between various components of the water balance and rock moisture are made by using a probe-specific and casing-specific calibration for an idealized material (see Appendix B). An idealized material is used because presently it is not feasible to develop a material specific calibration relationship at each measurement point.

Though methods for estimating uncertainty of neutron probe measurement exists for intensively characterized soils and granular material of established heterogeneity (e.g. Haverkamp et al., 1984, Vachaud et al., 1983), further research is needed in both calibration and quantification of uncertainty with neutron probe measurements in heterogeneous rock environments. This topic is explored in Appendix B, and here, we offer two measures of uncertainty. The first, instrument precision, is the smallest and easiest to quantify (Table B.5 in Appendix B). The mean standard deviation of all repeat measurements was 45 counts/16 s, which leads to an uncertainty of 2-3 mm/m. The maximum standard deviation of repeat measurements observed was 160 counts/16 s which leads to an uncertainty in S of 7-11 mm/m. The largest contribution to uncertainty in the calculation of $\Delta\theta$ and thus S is the slope of the calibration equation, α, used to calculate θ from N.

Since the calibration between N and θ is expected to be linear at moisture contents lower than approximately 0.4 (Schwanki et al. 1995, as well as our own experimental work in crushed rock shown in Appendix B), any uncertainty in α, the slope of the calibration equation, is easily translated into uncertainty in $\Delta\theta$ and S. Differences in material properties throughout the profile are expected to influence the relationship between N and θ (and thus ΔN and $\Delta\theta$), therefore, we expect α to vary throughout the profile. Presently, we lack methods for establishing an uncertainty estimate for S based on uncertainties in α itself or its variability throughout the profile. When compared to neutron probe data, data from gravimetric sampling and continuous TDR measurements in the upper 0.7-1.4 m reveal that α may be 1.4-1.9 times higher than the α for sand (Appendix B). Therefore, it is possible that the sand-based calibration we use here leads to an underestimate of rock moisture storage, particularly in the near surface. In summary, we use a single α throughout the profile that was established from a barrel calibration experiment on an idealized material (Appendix B) and the reported uncertainty is only the uncertainty associated with instrument precision.

3.5 Tables

Characteristics	Well Number											
	1	**2**	**3**	**5**	**6**	**7**	**10**	**12**	**13**	**14**	**15**	**16**
Elevation of Wellhead Above M.S.L. (m)	400	420	421.3	449	451.62	454	455	401.8	420	445	468	455
Total Depth of Well (m)	9.50	12.20	14.40	25.30	19.90	19.80	27.40	7.21	18.44	32.92	33.22	34.29
Casing Diameter (in)	2	2	2	2	2	2	2	2	2	3	3	3
Year Drilled	2007	2007	2007	2007	2007	2007	2007	2010	2010	2010	2010	2010

Table 3.1: Borehole elevation, depth, and casing diameter for wells drilled at Rivendell field site.

3.6 Figures
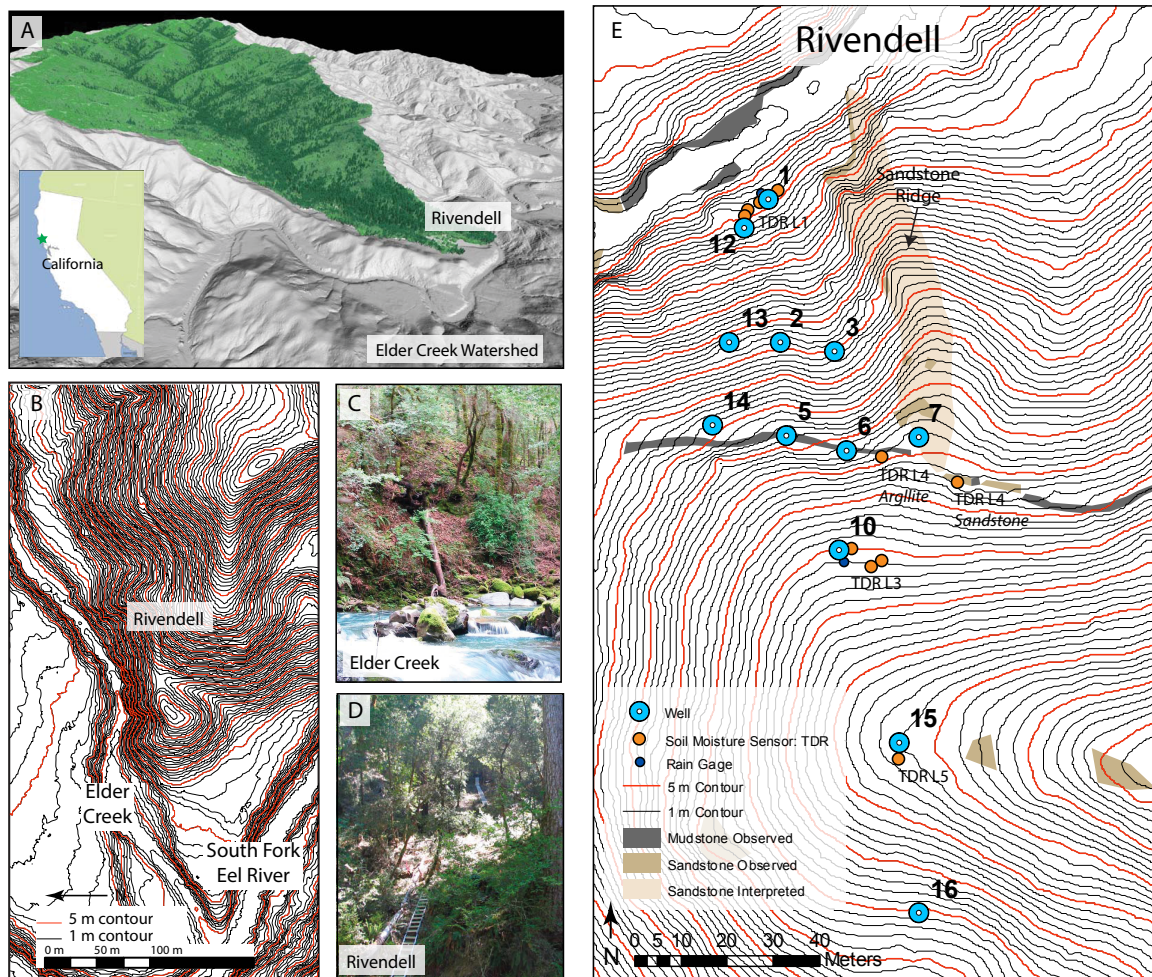
Figure 3.1: (A) Laser altimetry map of Elder Creek watershed derived from data collected by the National Centre for Airborne Laser Mapping. Vegetation within the watershed is coloured by canopy height (light green is brush and hardwoods, dark green is the taller conifers). Elsewhere, vegetation is filtered to reveal bare earth topography. Inset shows location of Elder Creek watershed within Northern California. (B) Location of Rivendell relative to Elder Creek and the South Fork Eel River. (C) Image of Elder Creek and (D) Rivendell Field Site. (E) Map of Rivendell field site (latitude 39 4304400N, longitude 123 3803900W) showing contours (1 and 5 m intervals) derived from airborne laser swath mapping data collected by the National Center for Airborne Laser Mapping (2009) and the location of wells, soil moisture (TDR), and precipitation gauges. A sandstone ridge that borders the Eastern side of the site is shown in light tan. Mapped lithology in exposures (along the channel and a road cut that bisects the site) reflects the dominance of nearly vertically bedded argillite with some competent sandstone interveds that can outcrop.

Bibliography

[1] S.P. Anderson, W.E. Dietrich, and G.H. Brimhall. Weathering profiles, mass-balance analysis, and rates of solute loss: Linkages between weathering and erosion in a small, steep catchment. *Geological Society of America Bulletin*, 114(9):1143, 2002.

[2] Suzanne Prestrud Anderson, William E Dietrich, David R Montgomery, et al. Subsurface flow paths in a steep, unchanneled catchment. *Water Resources Research*, 33(12):2637–2653, 1997.

[3] Yuko Asano, Taro Uchida, and Nobuhito Ohte. Residence times and flow paths of water in steep unchannelled catchments, Tanakami, Japan. *Journal of Hydrology*, 261(1):173–192, 2002.

[4] E.W. Banks, C.T. Simmons, A.J. Love, et al. Fractured bedrock and saprolite hydrogeologic controls on groundwater/surface-water interaction: a conceptual model (Australia). *Hydrogeology Journal*, 17(8):1969–1989, 2009.

[5] M Blumstock, D Tetzlaff, IA Malcolm, G Nuetzmann, and C Soulsby. Baseflow dynamics: Multi-tracer surveys to assess variable groundwater contributions to montane streams under low flows. *Journal of Hydrology*, 527:1021–1033, 2015.

[6] Michael Bonell. Progress in the understanding of runoff generation dynamics in forests. *Journal of Hydrology*, 150(2-4):217–275, 1993.

[7] Susan L Brantley, Molly E Holleran, Lixin Jin, and Ekaterina Bazilevskaya. Probing deep weathering in the Shale Hills Critical Zone Observatory, Pennsylvania (USA): the hypothesis of nested chemical reaction fronts in the subsurface. *Earth Surface Processes and Landforms*, 38(11):1280–1298, 2013.

[8] J. Büdel. Double surfaces of leveling in the humid tropics. *Zeitschrift für Geomorphologie*, 1:223–225, 1957.

[9] J St Clair, S Moon, WS Holbrook, et al. Geophysical imaging reveals topographic stress control of bedrock weathering. *Science*, 350(6260):534–538, 2015.

[10] B.A. Ebel, K. Loague, D.R. Montgomery, and W.E. Dietrich. Physics-based continuous simulation of long-term near-surface hydrologic response for the Coos Bay experimental catchment. *Water Resources Research*, 44(7):W07417, 2008.

[11] National Science Foundation. National Science Foundation, Program solicitation 12-575. 2012.

[12] Marty D Frisbee, Fred M Phillips, Andrew R Campbell, Fengjing Liu, and Steve A Sanchez. Streamflow generation in a large, alpine watershed in the southern Rocky Mountains of Colorado: Is streamflow generation simply the aggregation of hillslope runoff responses? *Water Resources Research*, 47(6), 2011.

[13] V Cody Hale, Jeffrey J McDonnell, Michael K Stewart, et al. Effect of bedrock permeability on stream base flow mean transit time scaling relationships: 2. Process study of storage and release. *Water Resources Research*, 2016.

[14] Atul H Haria and Paul Shand. Evidence for deep sub-surface flow routing in forested upland Wales: implications for contaminant transport and stream flow generation. *Hydrology and Earth System Sciences Discussions*, 8(3):334–344, 2004.

[15] Shin'ya Katsura, Ken'ichirou Kosugi, Tasuku Mizutani, Suemi Okunaka, and Takahisa Mizuyama. Effects of bedrock groundwater on spatial and temporal variations in soil mantle groundwater in a steep granitic headwater catchment. *Water Resources Research*, 44(9):n/a–n/a, September 2008.

[16] M Katsuyama, M Tani, and S Nishimoto. Connection between streamwater mean residence time and bedrock groundwater recharge/discharge dynamics in weathered granite catchments. *Hydrological Processes*, 24(16):2287–2299, 2010.

[17] K Kosugi, M Fujimoto, S Katsura, and H Kato. Localized bedrock aquifer distribution explains discharge from a headwater catchment. *Water Resources . . .*, 2011.

[18] Ken'ichirou Kosugi, Shin'ya Katsura, Masanori Katsuyama, and Takahisa Mizuyama. Water flow processes in weathered granitic bedrock and their effects on runoff generation in a small headwater catchment. *Water Resources Research*, 42(2):n/a–n/a, February 2006.

[19] Cédric Legout, Jérome Molenat, Luc Aquilina, et al. Solute transfer in the unsaturated zone-groundwater continuum of a headwater catchment. *Journal of Hydrology*, 332(3):427–441, 2007.

[20] Andrew H Manning and Jonathan Saul Caine. Groundwater noble gas, age, and temperature signatures in an Alpine watershed: Valuable tools in conceptual model development. *Water resources research*, 43(4), 2007.

[21] Jean-Christophe Maréchal, Murari RR Varma, Jean Riotte, et al. Indirect and direct recharges in a tropical forested watershed: Mule Hole, India. *Journal of Hydrology*, 364(3):272–284, 2009.

[22] MJ Pavich. Regolith residence time and the concept of surface age of the Piedmont "peneplain". *Geomorphology*, 2(1):181–196, 1989.

[23] Shengwen Qi, Zhong Qi Yue, Faquan Wu, and Zhonghua Chang. Deep weathering of a group of thick argillaceous limestone rocks near Three Gorges Reservoir, Central China. *International Journal of Rock Mechanics and Mining Sciences*, 46(5):929–939, 2009.

[24] Laura K Rademacher, Jordan F Clark, David W Clow, and G Bryant Hudson. Old groundwater influence on stream hydrochemistry and catchment response times in a small Sierra Nevada catchment: Sagehen Creek, California. *Water resources research*, 41(2), 2005.

[25] Craig Rasmussen, Peter A Troch, Jon Chorover, et al. An open system framework for integrating critical zone structure and function. *Biogeochemistry*, 102(1-3):15–29, 2011.

[26] Daniella M Rempe and William E Dietrich. A bottom-up control on fresh-bedrock topography under landscapes. *Proceedings of the National Academy of Sciences*, 111(18):6576–6581, 2014.

[27] B.P. Ruxton and L. Berry. Weathering of granite and associated erosional features in Hong Kong. *Geological Society of America Bulletin*, 68(10):1263–1292, 1957.

[28] C Soulsby, D Tetzlaff, N Van den Bedem, et al. Inferring groundwater influences on surface water in montane catchments from hydrochemical surveys of springs and streamwaters. *Journal of Hydrology*, 333(2):199–213, 2007.

[29] Peter Troch, Emiel Van Loon, and Arno Hilberts. Analytical solutions to a hillslope-storage kinematic wave equation for subsurface flow. *Advances in Water Resources*, 25(6):637–649, 2002.

[30] Peter A Troch, Claudio Paniconi, and E Emiel van Loon. Hillslope-storage Boussinesq model for subsurface flow and variable source areas along complex hillslopes: 1. Formulation and characteristic response. *Water Resources Research*, 39(11), 2003.

[31] CJ Wilson and WE Dietrich. The contribution of bedrock groundwater flow to storm runoff and high pore pressure development in hollows. *IAHS-AISH publication*, (165):49–59, 1987.

Chapter 4

Critical zone characterization

4.1   Introduction

The structure and hydrologic dynamics of hillslope interiors are largely inferred via the composition of streamflow or isolated observations within wells, trenches, or roadcuts. In the few studies that do drill into the critical zone, wells are often too shallow to characterize the full extent of the critical zone (e.g. Ebel et al., 2008) or are sited in valley bottoms or ridge tops but do not permit for a hillslope critical zone structure to be established (e.g. Padilla et al., 2015, Hale and McDonnell, 2016). In this chapter, I introduce the first attempt to fully characterize the structure of a deep critical zone across a hillslope unit, from channel to divide. I describe the Eel River Critical Zone observatory Rivendell field site and the results of drilling and groundwater monitoring that reveal the general pattern of weathering and hydrologic dynamics of the critical zone.

4.2   Results

Critical zone vertical profiles: Summary overview

Figure 4.1 summarizes the vertical variation in critical zone characteristics at each of 12 wells. Figures 4.2-4.5 show each row at a larger scale. The wells are arranged in Figure 4.1 parallel to their relative elevations so that one can see the gross patterns of critical zone properties and dynamics in a single figure. Each well is represented by two adjacent profiles. In the first profile the vertical variation in material properties obtained from drilling are portrayed. The second summarizes the entirety of the hydrologic dynamics in each well hole. The material properties shown in the first profile of the pair are (see legend): 1) the material type- soil, saprolite, weathered bedrock, and fresh bedrock. Gaps in the profile record where no samples were collected via standard penetration testing. Fresh bedrock is typically represented by a thin line because we were only able to penetrate several centimeters into fresh bedrock. Wells 5, 6 and 7 were drilled on the road bed, consequently the soil and much of the saprolite were absent. These drill holes are located relative to the reconstructed original surface (by projecting the adjacent ground surface in the road cut across the road). 2) Mineral coatings and precipitates - red-colored oxide coatings on fracture surfaces (likely iron-oxide), blue or black-colored oxide coatings on fracture surfaces (likely Mn oxides), white precipitate (includes calcite and laumontite), 3) sandstone blocks associated with thin sandstone interbeds, and 4) tree roots. Also shown in the first profile is the vertical variation in penetration resistance. Figure 4.6 shows the data for all the wells plotted as three groups (based on relative proximity) as the observed blow counts per penetration distance. In Figure 4.1 the data have been normalized relative to the maximum resistance (lowest blow counts) such that the range is from 0 to 1.0. The second profile of the pair for each well in Figure 4.1 show four key hydrologic features: 1) the portion of the hole that remains saturated all year long, 2) the seasonally saturated zone, 3) the relative time spent by the groundwater table at each

level (horizontal scale not shown but ranges from zero to 1.0), and 4) the neutron probe counts recorded by repeat profile surveys with the neutron probe. The wider the range of counts at a given depth below the surface, the large the range of rock moisture change.

Weathering profiles

The material profiles (Figure 4.1) can be grouped into three zones: soil, weathered bedrock (consisting of saproilte and weathered fractured-bedrock) and fresh bedrock (Table 4.1). Soil thickness measurements across the site do not exceed 75 cm and generally lie between 30 cm and 50 cm. The entire hillslope is soil mantled with the exception of isolated outcrops of fractured and moderately weathered sandstone interbeds (Figure 3.1). These stony soils are dilated by biogenic disturbance, contain abundant macroporosity, and despite being derived from an argillite, show no signs of seasonal cracking.. Soils are loam, clay loam, or silty clay. The saprolite properties are highly variable, as it lies between a completely disaggregated, dilated state of the soil and the strongly structured state of the weathered fractured-bedrock. It can be sufficiently disaggregated that it takes on a granular, soil-like appearance despite retaining corestones, remnants of bedding structure, and in some locations weakly systematic fracture patterns. Abundant fine-grained debris may separate relict blocks ranging in sizes from millimeters to centimeters, and roots, root castes, and burrows are locally common in the shallow saprolite. The deeper saprolite typically retains more visibly the bedrock structure and is overall much less disrupted. The saprolite is sufficiently broken that it can be excavated with a shovel. Nearly the entire mass is oxidized. The transition from saprolite to weathered fractured-bedrock is gradational with distinctly more clay-sized weathering products occupying fractures within the saprolite. The weathered fractured-bedrock consists of hard matrix blocks bounded by fractures of varying frequency and orientations. Generally the open fracture density decreases with depth. Fractures were observed at a variety of scales. Here the weathering is largely restricted to fracture surfaces and the matrix blocks appear generally unweathered. In many instances, however, the blocks could be broken by hand, revealing fractures whose surfaces were coated with oxides, and between the fractures granular material infills or precipitates were common. These small, barely visible fractures (before breaking the matrix blocks open) do not appear to be associated with bedding planes and instead may collectively form rectilinear blocks or conchoidal chips. In general, the narrow, usually disrupted (due to augering) drill samples prevent mapping bedding planes. Such bedding (which was roughly vertical) in the weathered bedrock, was visible in the road cut. The transition from weathered to fresh bedrock, Z_b, (see Chapter 2) was marked by a lack of oxidation along fracture surfaces, a decrease in fracturing observed during drilling, a change in mechanical strength revealed via an increase in penetration resistance, and analysis of the color, friability, and general condition of material recovered during drilling. In some wells (e.g. W6 and W10), this transition was abrupt and all metrics used to identify this boundary were coincident (Figure 4.1). In other wells, weak evidence of weathering (e.g. oxidation along a fracture plane) was observed

below within otherwise unweathered rock. Penetration resistance data collected during drilling show significant increases in penetration resistance with depth and relatively distinct values of penetration resistance for each of the broad weathering categories proposed (Figure 4.6). For example, on average, 9 blows per foot were required to penetrate soil, while saprolite, weathered fractured-bedrock, and fresh rock required 30, 130, and 1400 respectively (Figure 4.6). Generally each of these three penetration resistance values are similar amongst wells grouped together in Figure 4.6 and show a similar form: linear increase with depth, then nearly constant values, and then a systematic but less rapid increase in the deepest penetration. The penetration resistance at which the values turn constant corresponds to the blow count transition from saprolite to weathered fractured-bedrock. The depth to this transition varies from about 3 m near the foot of the slope to 8 m upper part of the hillslope. The depth where the penetration resistance once again increases with increasing depth varies from 6 m in the lower part of the slope to 11 m at the upper part of the hillslope. The smoothed resistance data shown in Figure 1.3 show that the resistance change with depth display localized increases and decreases, presumably corresponding to variations in fracture density. Oxidation along fracture surfaces and the presence of precipitates within fractures was generally restricted to soil, saprolite, and weathered fractured- bedrock, though precipitates and iron oxide staining associated with discrete fractures in the fresh bedrock was observed in some wells (e.g. W15 and W14). Roots were most dense in the first 2.5 m, but some roots were found as deep as 16 m below the surface. Figure 4.7 shows a longitudinal profile of the critical zone with penetration resistance color-coded in each borehole. Figure 4.8 shows profiles of color quantified in core samples via digital photography and image processing which reflect the degree of weathering. An increase in "redness" is associated with a greater degree of iron staining which is a strong indicator of near surface alteration due to weathering. These two figures illustrate that the depth and intensity of weathering within the saprolite and fractured weathered bedrock intensifies upslope. During drilling, drill samples recovered from Wells 10, 15, and 16 showed distinctly greater degree of oxidation and fracturing above the fresh bedrock, while wells located downslope showed generally lower fracture density and frequency of weathering along fracture surfaces.

Hydrologic response profiles

Gross hydrologic response, as portrayed in Figure 4.1, varies with material properties variation with depth, and with topographic location. Similar to the classification proposed by Legout et al., 2007, we identify three distinct hydrology zones: chronically unsaturated zone (CUZ), seasonally saturated zone (SSZ), and chronically saturated zone (CSZ). These zones are shown in a profile of the site drawn along Wells 1, 3, 6, 10 and 15, which lie along a common topographic fall line (Figure 4.7). The depth to the transition to the seasonally saturated zone (top of light blue zone in Figure 4.1) varies respectively from 2.5 m at well 1, to 3 m, 6 m , 11 m and 19 m at Well 15. This indicates a significant increase in the chronically unsaturated (vadose zone) upslope (Figure 4.7). The depth

to the chronically saturated zone (top of the darker blue zone, Figure 4.1) also increases upslope: 5 m, 10 m, 13 m, 19 m and 26 m, respectively. The difference in elevation of these two transitions defines the maximum thickness of the seasonally saturated zone, and surprisingly it remains nearly constant upslope from well 3 (2.5m at Well 1, to 7 m, 7 m, 8m, and 7m). These two transitions (to seasonally saturated and transition to chronically saturated) roughly correspond to the transition in blow counts at about 100 blows/ft (seasonally saturated) to values that approach 1000 blows/ft (chronically saturated). Over 4 years of groundwater monitoring show that there is little variation of the minimum groundwater table position and that this chronically saturated level crudely corresponds to transition to fresh bedrock, which implies that groundwater perches on the fresh bedrock seasonally and nearly completely drains every years. In both 2007 and 2010, wells were drilled at the conclusion of the dry season in an effort to capture the full range of groundwater fluctuations that might occur within the hillslope. Drilling ceased when the water table had been penetrated or the drilling became too slow to proceed. In two wells (W13 and W2) groundwater monitoring subsequent to drilling revealed that the wells did not penetrate the deepest extent of the seasonal groundwater table because the wells drain completely.

Also shown in the hydrologic profile are raw neutron probe data that reveal the rock moisture dynamics of the critical zone (see Chapter 2). Three features are visible in these profiles. First, the vertical variation in moisture content is very consistent in successive years of measurements (these data represent 3 years of measurements in throughout wet and dry seasons). The spread of data at a particular depth reflects the dynamic range of rock moisture (i.e. the seasonal addition and depletion of water in the weathered bedrock), and this dynamic range generally declines with depth. Finally, data within the seasonally saturated zone (light blue in Figure 4.1) does not display a wide range of moisture content variation. The rock moisture dynamics are described in further detail in the chapter that follows. The general groundwater and unsaturated zone observations indicate that the hillslope interior experiences one of three hydrologic states, (unsaturated, seasonally saturated, or saturated) and the moisture dynamics are greatest where extensive weathering is observed.

4.3   Summary of results

We established the critical zone structure across a 4000 m2 hillslope, from channel to hillslope divide, through drilling and groundwater monitoring within 12 deep wells. Drilling and characterization revealed a 4-25 m thick zone of variably weathered, fractured bedrock that thickens upslope and a seasonally perched water table forms at its base. Standard penetration testing and core characterization reveal four distinct layers, soil, saprolite, fractured rock, and unweathered bedrock, and a general pattern of decreasing porosity and increasing mechanical strength with depth. The seasonally saturated zone occurs within fractured bedrock, which shows evidence of weathering primarily along

fracture surfaces. Below the seasonally saturated zone which drains to approximately the same elevation annually, rock remains saturated year round. Above the seasonally saturated zone, soil and weathered bedrock remain unsaturated year round but exhibit large changes in moisture content.

4.4 Tables

Depth Range (m)	Classification		Photo Example	Description	Depth Range Observed in Borehole (m)*											
					1	2	3	5	6	7	10	12	13	14	15	16
0.0 - 1.8	Soil	Soil		Granular, organic rich loam to silty clay, abundant rock chips, macropores, and roots	0.0 - 0.75	0.0 - 0.5	0.0 - 0.75	+	+	+	0.0 - 0.5	0.0 - 0.15	0.0 - 0.5	+	0.0 - 0.15	0.0 - 1.8
0.15 - 4.25	Weathered Rock	Saprolite		Pervasively fractured and weathered mudstone with bedding structure intact, discoloration along most fracture surfaces, matrix may disintegrate when immersed in water, fractures contain granular clay infill	0.75 - 1.0	0.5 - 5.0	0.74 - 4.25	1.0 - 1.5	+	0.7 - 4.2	--	0.15 - 0.5	0.5 - 1.75	0.5 - 2.0	0.5 - 3.75	1.8 - 3.0
0.5 - 23		Fractured, Weathered Mudstone		Some discoloration along discontinuity surfaces, matrix remains largely unweathered, granular fracture infill is rare	1.0 - 2.75	7.0 - 9.5	5.5 - 9.2	2.5 - 11.75	1.3 - 12.0	5.0 - 17.5	4.5 - 10.75	0.5 - 7.5	1.75 - 15.5	2.0 - 20.0	3.75 - 23.0	3.0 - 14.5
Greater Than 3.7 - 32	Fresh Rock	Unweathered Mudstone		No visible signs of weathering, joint faces lack staining with few exceptions, matrix is not easily broken by hand	4.0 - 6.0	--	10.75 - 14.5	13.0 - 23.25	13.5 - 18.0	--	21.0 - 24.0	--	--	21.5 - 33.0	23.0 - 34.0	31.0 - 31.5
Depth of Interface Between Fresh and Weathered Bedrock, Zb					6	15	14.5	14.5	16	16	18.3	3.7	10.7	21.3	19.8	32
*Observations are not continuous and are limited to intervals in which samples were retrieved and classified + Upper 0.7-1 m removed for road construction prior to drilling																

Table 4.1: **Summary of drilling characterization:** Depth ranges and descriptions of material recovered during drilling.

4.5 Figures
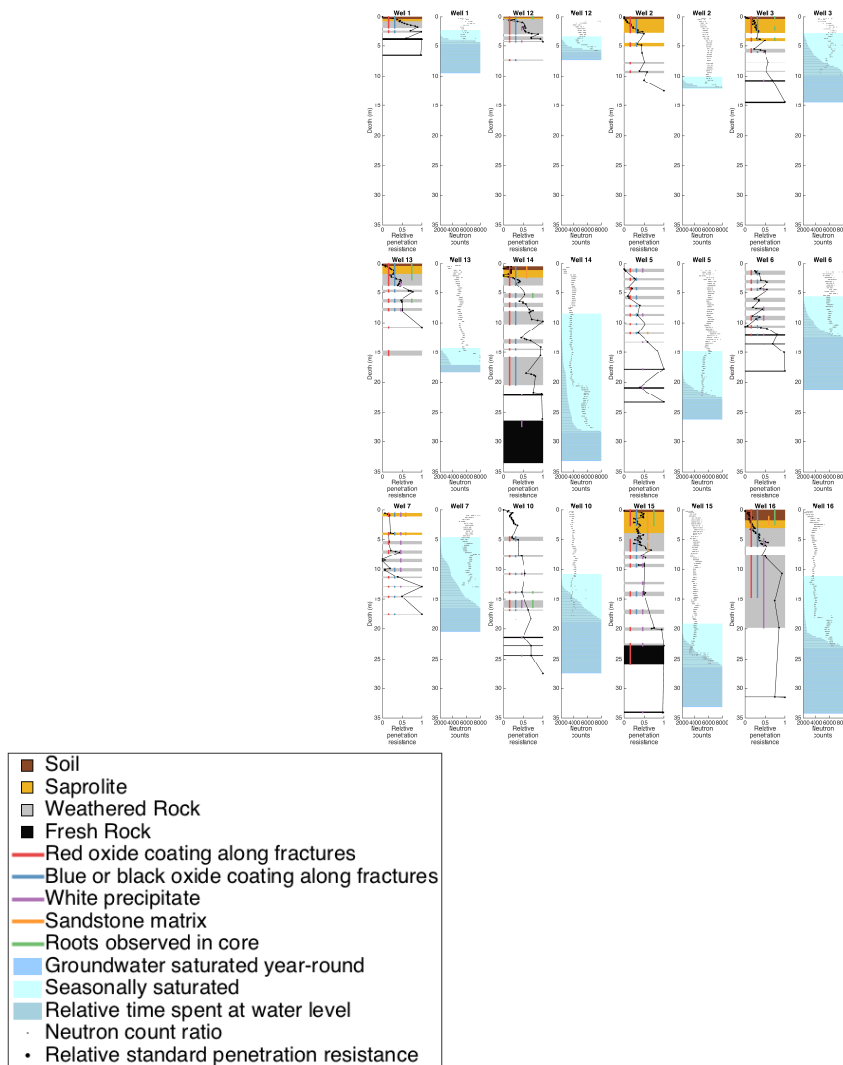
Figure 4.1: **Drilling and groundwater data in all wells:** Rivendell borehole profiles derived from drilling (left) and groundwater and vadose zone monitoring (right). Since drilling was accomplished via a combination of split spoon sampling (as part of the standard penetration resistance testing) and augering, drilling characterization data in the drilling profiles are restricted to depth intervals for which samples were retrieved for analyis and sample depth was well constrained. Relative penetration resistance is the $log_{10}(\frac{N(z)-N_{min}}{N_{max}-N_{min}})$ for each individual well for convenience of display. Groundwater monitoring data from water years 2012-2015 showed three distinct zones: the unsaturated zone (UZ), the seasonally saturated zone (SSZ), and the chronically saturated zone (CSZ). The SSZ is displayed as the maximum extent of groundwater fluctuation observed over the entire period of observation and the bottom boundary of the CSZ is the bottom of the well. Blue bars represent the fraction of time a particular depth remains saturated. Neutron count ratio for all data collected between 2009 and 2015 are shown in gray and are discussed further in Chapter 4.
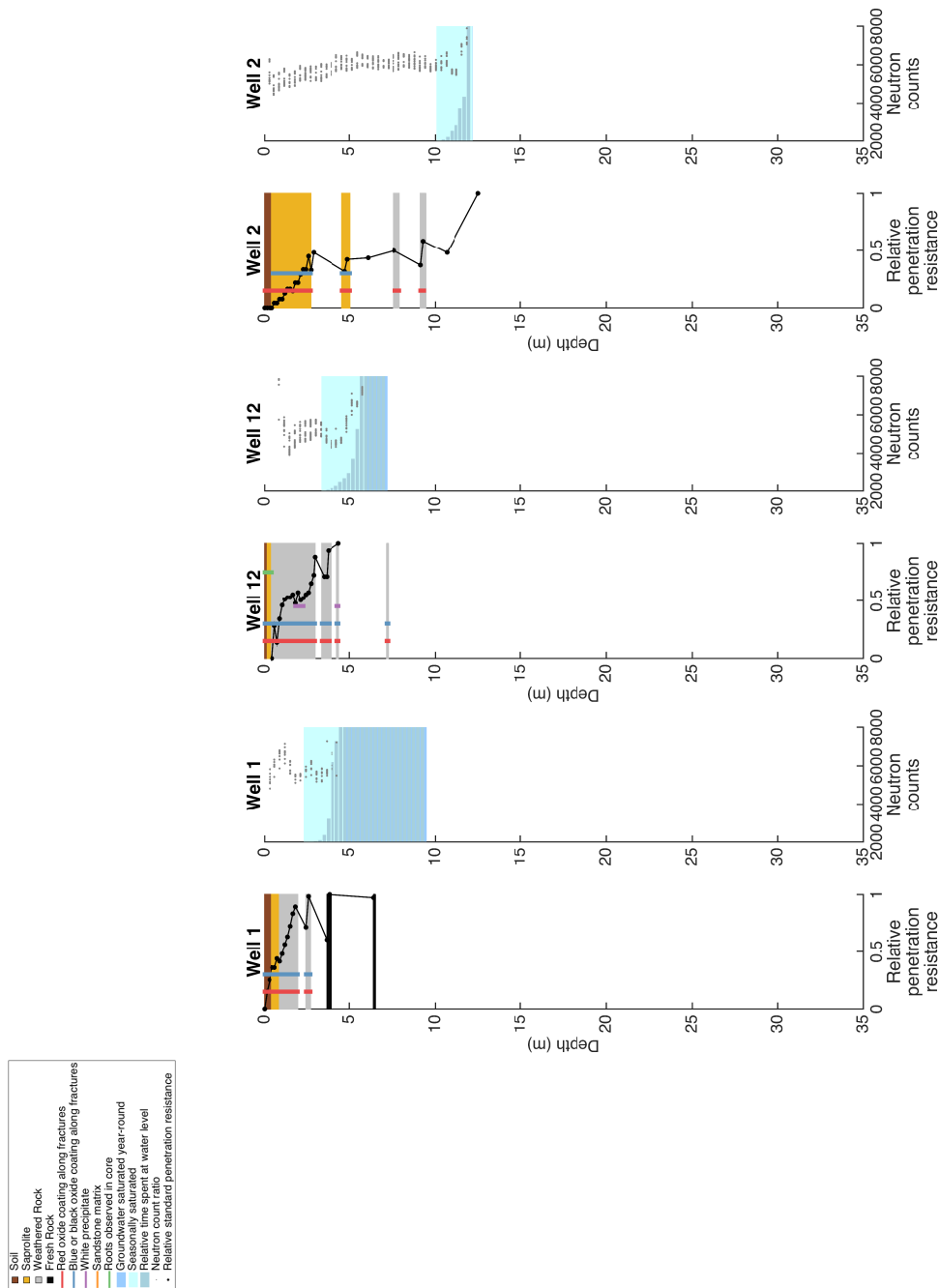
Figure 4.2: **Drilling and groundwater data Wells 1, 12, and 2:** Rivendell borehole profiles derived from drilling (left) and groundwater and vadose zone monitoring (right). Wells 12 and 1 are located at the base of the slope and Well 2 is located approximately mid-slope (Figure 3.1). Further description of datasets shown is provided in Figure 4.1.
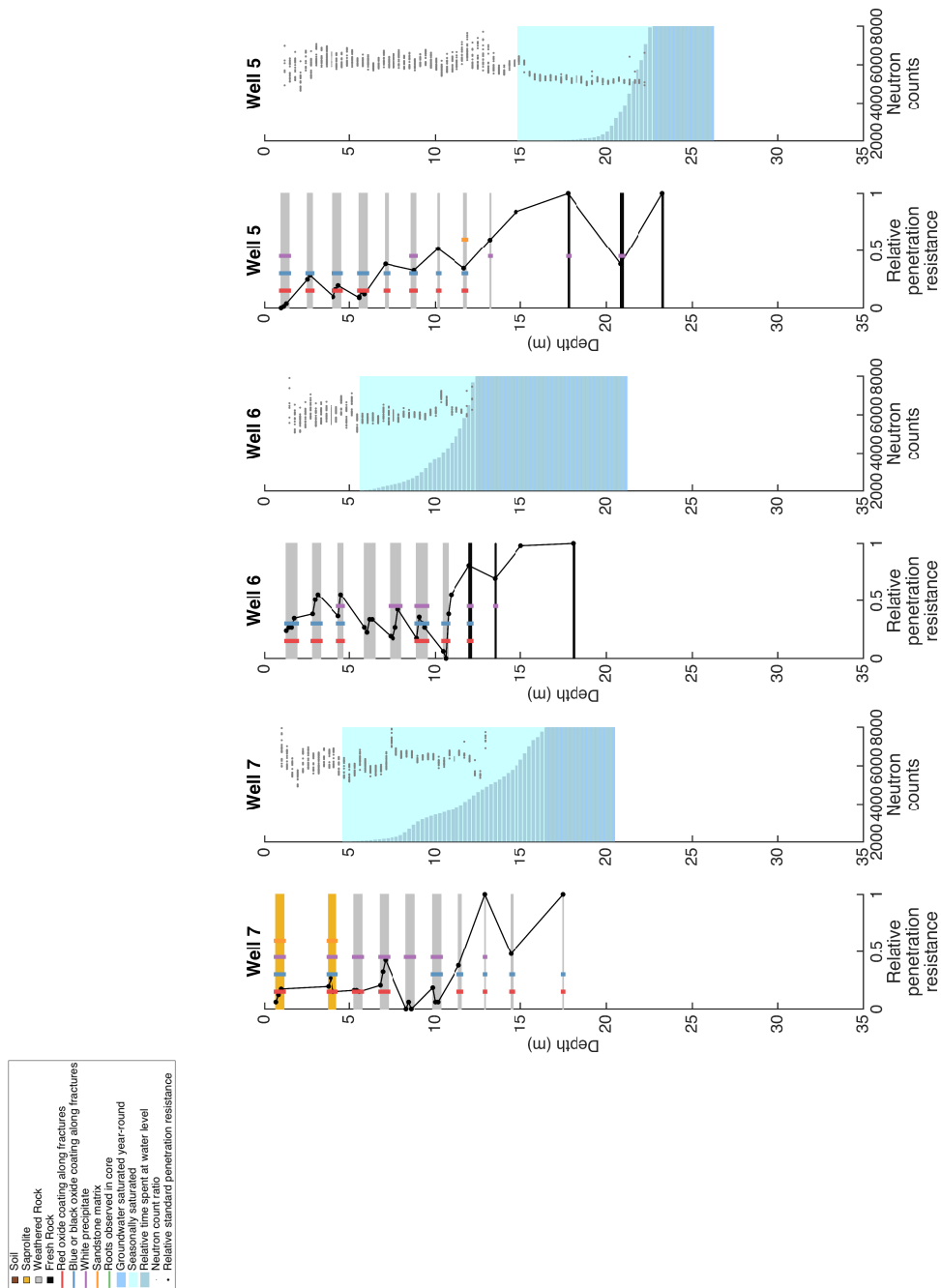
Figure 4.3: **Drilling and groundwater data in Wells 7, 6, and 5:** Rivendell borehole profiles derived from drilling (left) and groundwater and vadose zone monitoring (right). Wells located approximately along a road approximately mid-slope (Figure 3.1). Further description of datasets shown is provided in Figure 4.1.
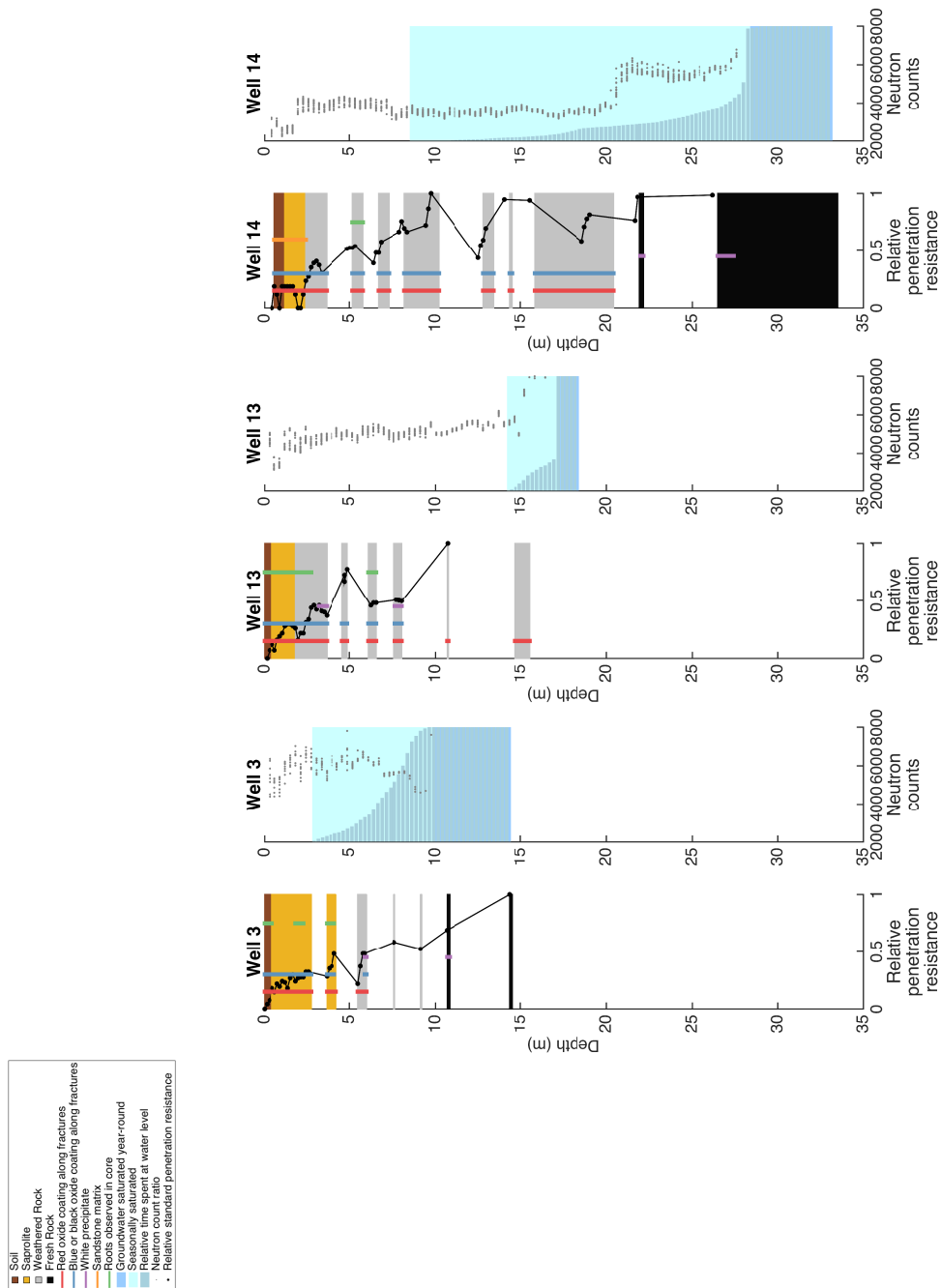
Figure 4.4: **Drilling and groundwater data in Wells 3, 13, and 14:** Rivendell borehole profiles derived from drilling (left) and groundwater and vadose zone monitoring (right). Wells located approximately mid-slope (Figure 3.1). Further description of datasets shown is provided in Figure 4.1.
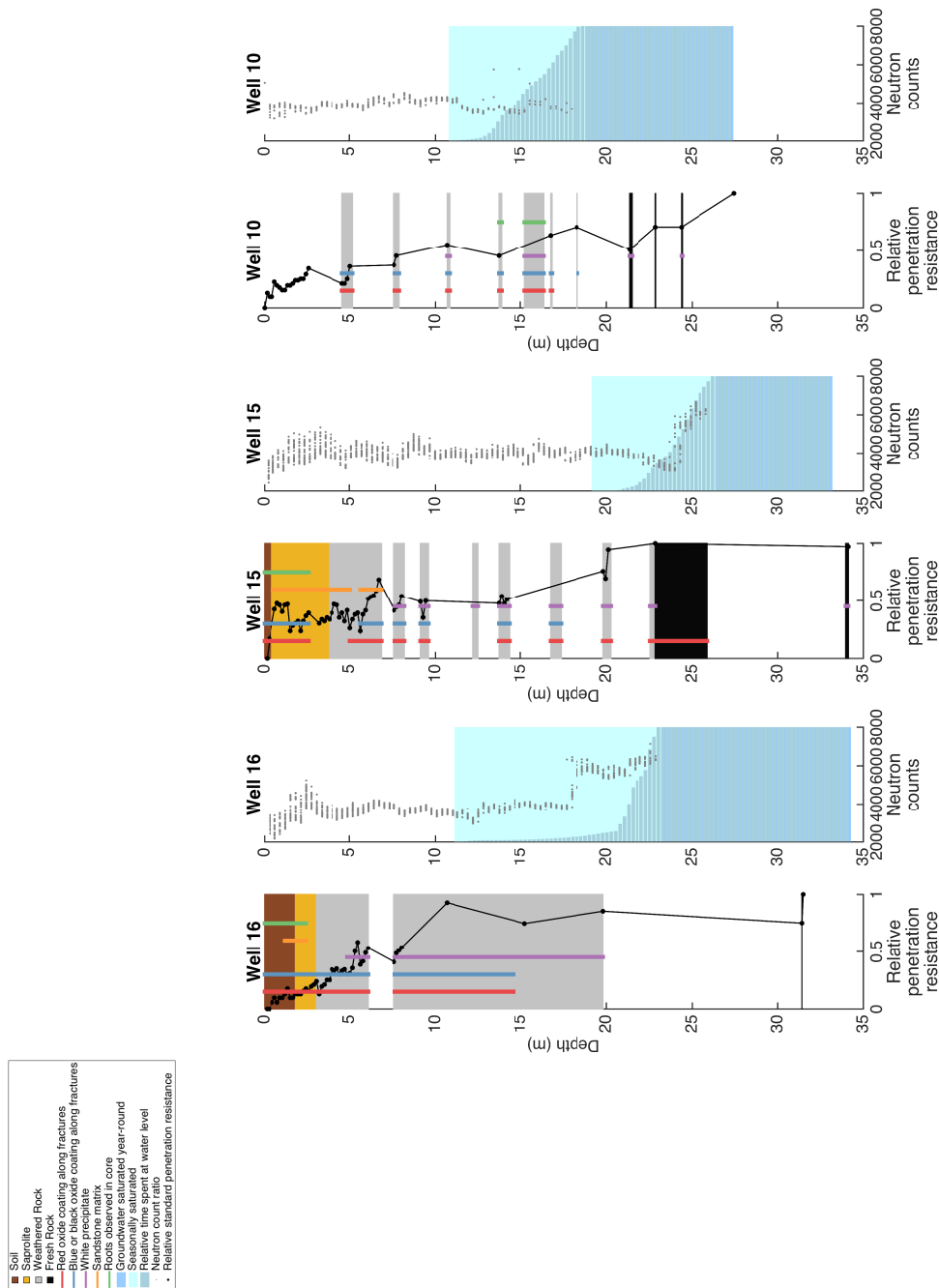
Figure 4.5: **Drilling and groundwater data in Wells 10, 15, and 16:** Rivendell borehole profiles derived from drilling (left) and groundwater and vadose zone monitoring (right). Wells located near the hillslope divide (Figure 3.1). Further description of datasets shown is provided in Figure 4.1.
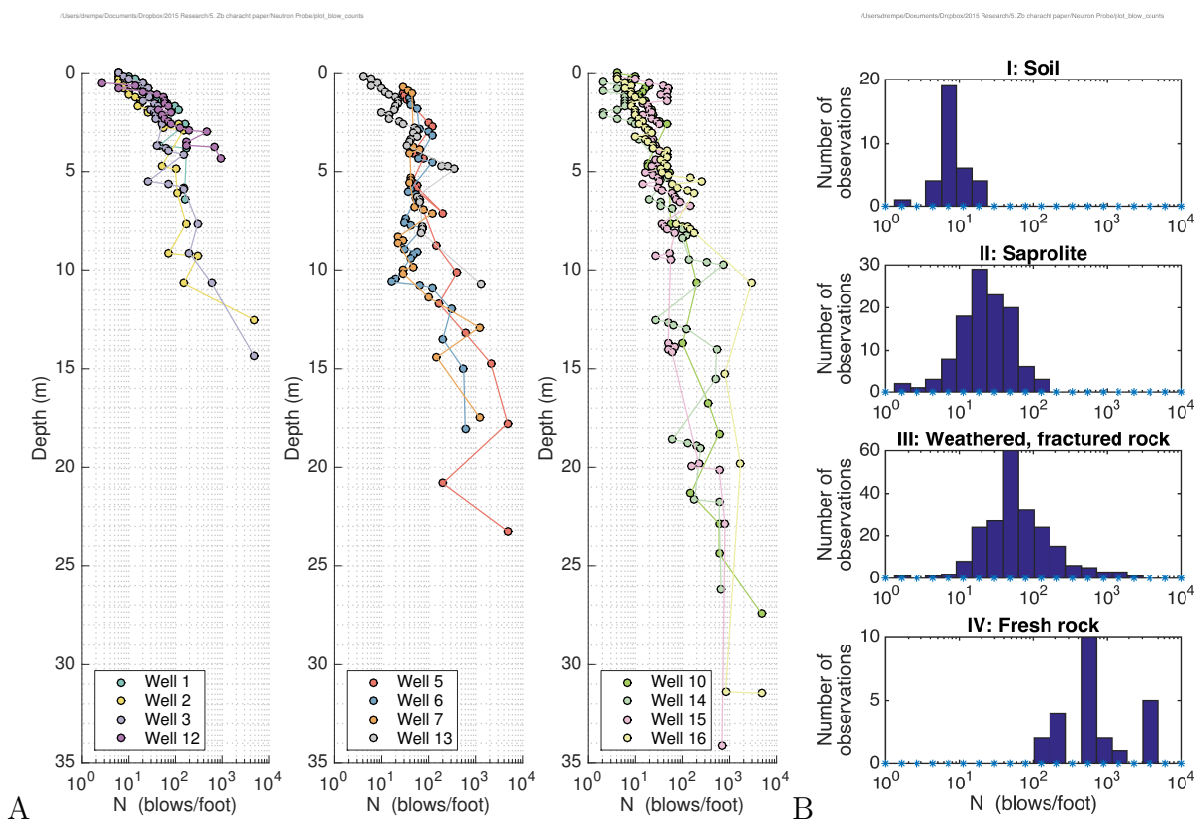
Figure 4.6: **Standard penetration resistance:** Standard penetration resistance, or N-value, is shown with depth in each well. Groups of wells are shown in increasing distance from Elder Creek towards the right (A). The four primary materials identified across the site (soil, saprolite, weathered rock and fresh rock) show distinct differences in penetration resistance (B).
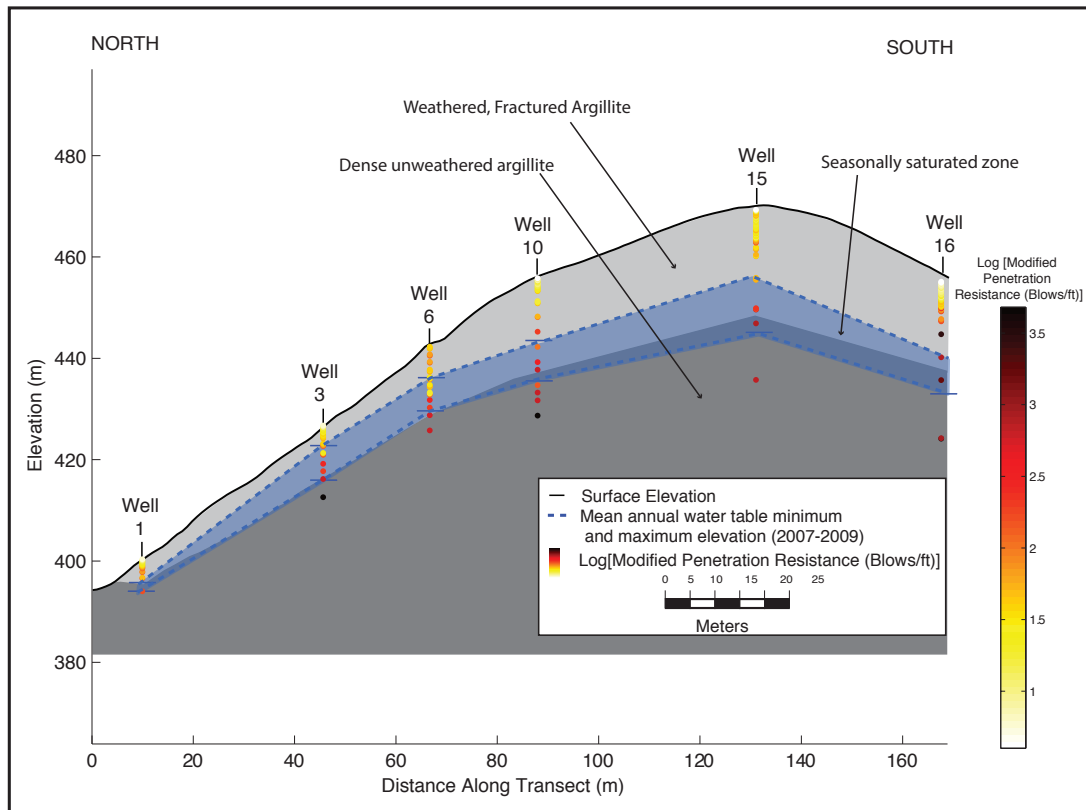
Figure 4.7: **Hillslope cross section showing hydrologic and weathering characterization:** Cross section through Wells 1, 3, 6, 10, 15, and 16 illustrating the structure of the critical zone established through drilling and groundwater monitoring. Standard penetration resistance, reflecting the relative mechanical strength, is shown as colored (in log scale) circles. Weathered and unweathered rock are shown in light and dark gray respectively and the seasonally saturated zone is shown as a light blue overlay. Material above the seasonally saturated zone is chronically unsaturated, while material below the seasonally saturated zone is chronically saturated.
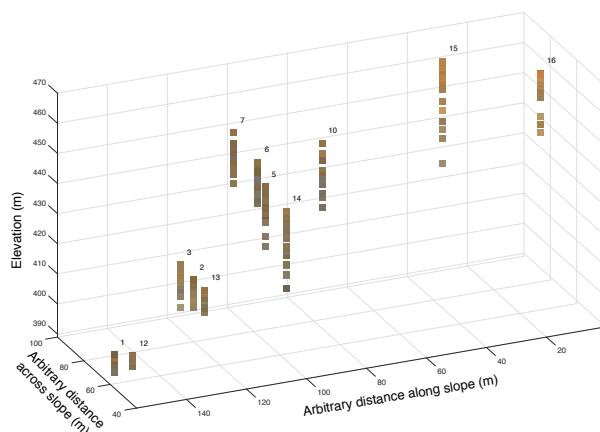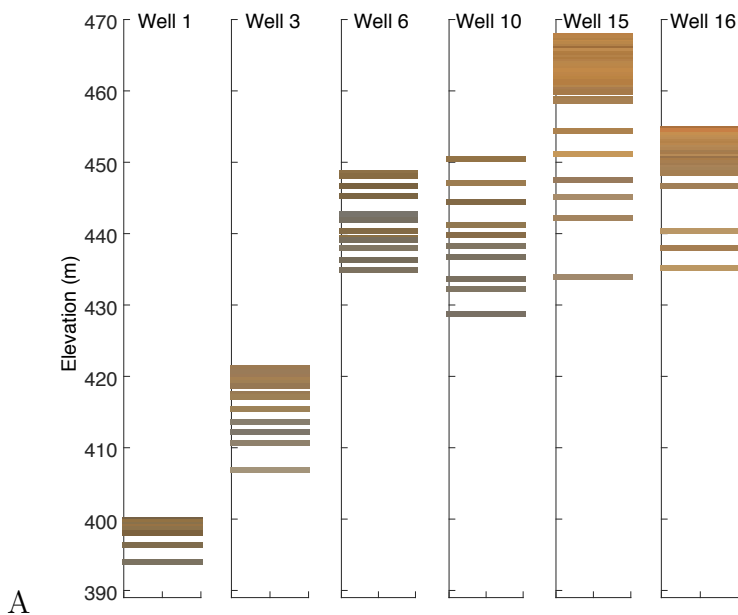
Figure 4.8: **Color of core retrieved in Rivendell wells:** Color of core samples in Wells 1, 3, 6, 10, 15, 16 (the same as those shown in the cross section in Figure 4.7) shown in order of slope position (A). Color data from all wells are plotted in three dimensions to illustrate an increase in redness upslope that reflects the increasing degree of weathering observed upslope. The parent rock is a dark grey and transitions to brown and red tones with increasing amount of iron oxide staining. Note that no core was retrieved in the upper 3 m in Well 10.

Bibliography

[1] S.P. Anderson, W.E. Dietrich, and G.H. Brimhall. Weathering profiles, mass-balance analysis, and rates of solute loss: Linkages between weathering and erosion in a small, steep catchment. *Geological Society of America Bulletin*, 114(9):1143, 2002.

[2] Suzanne Prestrud Anderson, William E Dietrich, David R Montgomery, et al. Subsurface flow paths in a steep, unchanneled catchment. *Water Resources Research*, 33(12):2637–2653, 1997.

[3] Yuko Asano, Taro Uchida, and Nobuhito Ohte. Residence times and flow paths of water in steep unchannelled catchments, Tanakami, Japan. *Journal of Hydrology*, 261(1):173–192, 2002.

[4] E.W. Banks, C.T. Simmons, A.J. Love, et al. Fractured bedrock and saprolite hydrogeologic controls on groundwater/surface-water interaction: a conceptual model (Australia). *Hydrogeology Journal*, 17(8):1969–1989, 2009.

[5] M Blumstock, D Tetzlaff, IA Malcolm, G Nuetzmann, and C Soulsby. Baseflow dynamics: Multi-tracer surveys to assess variable groundwater contributions to montane streams under low flows. *Journal of Hydrology*, 527:1021–1033, 2015.

[6] Michael Bonell. Progress in the understanding of runoff generation dynamics in forests. *Journal of Hydrology*, 150(2-4):217–275, 1993.

[7] Susan L Brantley, Molly E Holleran, Lixin Jin, and Ekaterina Bazilevskaya. Probing deep weathering in the Shale Hills Critical Zone Observatory, Pennsylvania (USA): the hypothesis of nested chemical reaction fronts in the subsurface. *Earth Surface Processes and Landforms*, 38(11):1280–1298, 2013.

[8] J. Büdel. Double surfaces of leveling in the humid tropics. *Zeitschrift für Geomorphologie*, 1:223–225, 1957.

[9] J St Clair, S Moon, WS Holbrook, et al. Geophysical imaging reveals topographic stress control of bedrock weathering. *Science*, 350(6260):534–538, 2015.

[10] B.A. Ebel, K. Loague, D.R. Montgomery, and W.E. Dietrich. Physics-based continuous simulation of long-term near-surface hydrologic response for the Coos Bay experimental catchment. *Water Resources Research*, 44(7):W07417, 2008.

[11] National Science Foundation. National Science Foundation, Program solicitation 12-575. 2012.

[12] Marty D Frisbee, Fred M Phillips, Andrew R Campbell, Fengjing Liu, and Steve A Sanchez. Streamflow generation in a large, alpine watershed in the southern Rocky Mountains of Colorado: Is streamflow generation simply the aggregation of hillslope runoff responses? *Water Resources Research*, 47(6), 2011.

[13] V Cody Hale, Jeffrey J McDonnell, Michael K Stewart, et al. Effect of bedrock permeability on stream base flow mean transit time scaling relationships: 2. Process study of storage and release. *Water Resources Research*, 2016.

[14] Atul H Haria and Paul Shand. Evidence for deep sub-surface flow routing in forested upland Wales: implications for contaminant transport and stream flow generation. *Hydrology and Earth System Sciences Discussions*, 8(3):334–344, 2004.

[15] Shin'ya Katsura, Ken'ichirou Kosugi, Tasuku Mizutani, Suemi Okunaka, and Takahisa Mizuyama. Effects of bedrock groundwater on spatial and temporal variations in soil mantle groundwater in a steep granitic headwater catchment. *Water Resources Research*, 44(9):n/a–n/a, September 2008.

[16] M Katsuyama, M Tani, and S Nishimoto. Connection between streamwater mean residence time and bedrock groundwater recharge/discharge dynamics in weathered granite catchments. *Hydrological Processes*, 24(16):2287–2299, 2010.

[17] K Kosugi, M Fujimoto, S Katsura, and H Kato. Localized bedrock aquifer distribution explains discharge from a headwater catchment. *Water Resources . . .*, 2011.

[18] Ken'ichirou Kosugi, Shin'ya Katsura, Masanori Katsuyama, and Takahisa Mizuyama. Water flow processes in weathered granitic bedrock and their effects on runoff generation in a small headwater catchment. *Water Resources Research*, 42(2):n/a–n/a, February 2006.

[19] Cédric Legout, Jérome Molenat, Luc Aquilina, et al. Solute transfer in the unsaturated zone-groundwater continuum of a headwater catchment. *Journal of Hydrology*, 332(3):427–441, 2007.

[20] Andrew H Manning and Jonathan Saul Caine. Groundwater noble gas, age, and temperature signatures in an Alpine watershed: Valuable tools in conceptual model development. *Water resources research*, 43(4), 2007.

[21] Jean-Christophe Maréchal, Murari RR Varma, Jean Riotte, et al. Indirect and direct recharges in a tropical forested watershed: Mule Hole, India. *Journal of Hydrology*, 364(3):272–284, 2009.

[22] MJ Pavich. Regolith residence time and the concept of surface age of the Piedmont "peneplain". *Geomorphology*, 2(1):181–196, 1989.

[23] Shengwen Qi, Zhong Qi Yue, Faquan Wu, and Zhonghua Chang. Deep weathering of a group of thick argillaceous limestone rocks near Three Gorges Reservoir, Central China. *International Journal of Rock Mechanics and Mining Sciences*, 46(5):929–939, 2009.

[24] Laura K Rademacher, Jordan F Clark, David W Clow, and G Bryant Hudson. Old groundwater influence on stream hydrochemistry and catchment response times in a small Sierra Nevada catchment: Sagehen Creek, California. *Water resources research*, 41(2), 2005.

[25] Craig Rasmussen, Peter A Troch, Jon Chorover, et al. An open system framework for integrating critical zone structure and function. *Biogeochemistry*, 102(1-3):15–29, 2011.

[26] Daniella M Rempe and William E Dietrich. A bottom-up control on fresh-bedrock topography under landscapes. *Proceedings of the National Academy of Sciences*, 111(18):6576–6581, 2014.

[27] B.P. Ruxton and L. Berry. Weathering of granite and associated erosional features in Hong Kong. *Geological Society of America Bulletin*, 68(10):1263–1292, 1957.

[28] C Soulsby, D Tetzlaff, N Van den Bedem, et al. Inferring groundwater influences on surface water in montane catchments from hydrochemical surveys of springs and streamwaters. *Journal of Hydrology*, 333(2):199–213, 2007.

[29] Peter Troch, Emiel Van Loon, and Arno Hilberts. Analytical solutions to a hillslope-storage kinematic wave equation for subsurface flow. *Advances in Water Resources*, 25(6):637–649, 2002.

[30] Peter A Troch, Claudio Paniconi, and E Emiel van Loon. Hillslope-storage Boussinesq model for subsurface flow and variable source areas along complex hillslopes: 1. Formulation and characteristic response. *Water Resources Research*, 39(11), 2003.

[31] CJ Wilson and WE Dietrich. The contribution of bedrock groundwater flow to storm runoff and high pore pressure development in hollows. *IAHS-AISH publication*, (165):49–59, 1987.

Chapter 5

Rock moisture

5.1 Introduction

Until recently, the subsurface hydrologic processes that dictate the availability of water to vegetation and the transformation of rainfall to runoff were thought to be restricted to a shallow porous mantle of soil (see review by Bonnell, 1993). There is now a growing recognition that, particularly in hilly and mountainous topography developed into bedrock, significant flow occurs through the rock beyond the soil (e.g. Wilson and Dietrich, 1987, Soulsby et al., 2007, Haria and Shand, 2004) and water stored in rock is accessible to vegetation (Zwiniecki and Newton, 1996, Graham et al., 2010, Schwinning, 2010). Additionally, hydrologic dynamics within weathered bedrock have been recognized as influencing biogeochemical cycling (e.g. Buss et al., 2010; Berryman et al., 2015), regional climate (e.g., Condon et al., 2013, Kleidon and Keimann, 1999, Lee et al., 2005), groundwater recharge (e.g. Marechal et al., 2006), and patterns of weathering (e.g. Violette et al., 2010, Brantley and Lebedeva, 2013). However, due to the inaccessibility of the weathered bedrock zone underlying landscapes, the role of weathered bedrock on dictating hydrologic dynamics is largely inferred through the composition and timing of streamflow (e.g. Ofterdinger et al., 2008). Where weathered bedrock is investigated through drilling (e.g. Gabrielli et al., 2012), trenching (e.g. Tromp von Meerveld et al., 2007), or tunneling (e.g. Shimojima et al., 2000), the hydraulic behavior of the weathered bedrock is usually inferred through monitoring of the overlying soil or underlying groundwater, or through interpretation of fluxes that transit the weathered bedrock. Very few studies have directly investigated the unsaturated, fractured bedrock region between the soil and groundwater (e.g. Haria et al., 2003, Ireson et al., 2006, Price, 1980, Jardine et al., 1999, Jardine 2009, Salve et al., 2012). Recently, at the Rivendell field site, Salve et al. (2012) identified that a significant fraction of incoming precipitation is stored in weathered seasonally, and proposed the term "rock moisture" to describe the exchangeable water hosted by weathered, fractured bedrock.

Here, I propose that the previously recognized but poorly described rock moisture reservoir is a distinct and important part of the hydrologic cycle. In an effort to advance understanding of rock moisture and its relative global significance, I performed an intensive multi-year investigation into the temporal and spatial dynamics of rock moisture across a hillslope, where, through long term monitoring of rock moisture, I establish the spatial structure of rock moisture and demonstrate its significance to ecological processes. Our study relies on the site and methods described in Chapter 3, chiefly the continuous monitoring of precipitation and groundwater, the monitoring of soil, shallow saprolite and weathered bedrock using time domain reflectometry and, importantly, periodic surveys of rock moisture in deep wells via neutron probe. I build upon prior work at the site, described in Chapters 3 and 4, to present, for the first time, the direct study of rock moisture dynamics across an entire hillslope.

5.2   Results

In the Mediterranean climate of our site, distinctly wet and dry seasons permit us to track the addition and depletion of rock moisture in a seasonal cycle. Figure 5.1 shows the seasonal pattern of rainfall, solar radiation, soil moisture, groundwater level, and streamflow across the site. Here I report the rock moisture dynamics by following moisture changes throughout the the year.

Conclusion of dry season

The end of the dry season is marked by small storms that occur in August and September. Before these storms arrive, seasonal minima in streamflow, soil moisture, and rock moisture occur while groundwater levels show evidence of continued recession into the wet season (Figure 5.1). Flow in Elder Creek is on the order of 0.1 mm/d. Profiles of rock moisture conditions at the conclusion of the dry season are shown in Figure 5.2 in 5 deep wells measured over the two-year period of 2014-2015 (well numbers labeled at the top of the plot, map of wells is shown in Figure 3.1). The heavy black line represents the reference dry survey (Oct 25 2015) and the colored lines represent end of dry season values from September 2014 and 2015, showing the similarity in the two years. (Note that shallow wetting occurred in September 2014, shown in purple, in response to 46 mm rainfall.) The light grey lines track measurements from all other surveys during the nearly three-year monitoring period to illustrate the variability in rock moisture observed. Also shown, in light blue bars, is a relative measure of the time a particular depth remains saturated (i.e. below the water table).

Comparison of all rock moisture measurements made throughout the entire monitoring period (shown in gray in Figure 5.2) to an October 25 2015 measurement (shown in black) reveals that rock moisture, at all other times of year that were surveyed, almost always exceeds the rock moisture measured in October of 2015. We therefore use this survey as a reference dry survey which we compare to other surveys. Some individual measurement locations show rock moisture conditions lower than the reference dry survey (e.g. 12 m depth in Well 5) where local conditions may promote further depletion of rock moisture beyond the end of the dry season and thus, some limited interannual storage of rock moisture.

Similarly, we used the October 25, 2015 TDR (continuous time domain reflectometry sensors, see Chapter 3) to document moisture change in the soil and shallow saprolite and weathered bedrock. Figures 5.3 and 5.4 show the time series of the change in soil moisture content, $\Delta\theta$, relative to a dry reference soil moisture content for continuous measurements made in soil (Figure 5.3) and shallow saprolite and weathered bedrock (Figure 5.4) via time domain reflectometry. The location of the TDR sensors is shown in shown in Figure 3.1 and the sensor installation is noted in Table 5.1. The moisture content of both soil and saprolite reaches a consistent seasonal low at the end of the summer that is within 1% of the reference dry value.

Initial wetting

At the start of the wet season, continuous soil moisture monitoring across the site reveals that storms as small as 13 mm generate a moisture content increase at depths beyond the soil at the start of the wet season (Salve et al., 2012). In the Fall of 2014, progressive wetting was monitored via continuous soil moisture sensors (to 0.35 m depth in soil, 0.7-1.4 m depth in saprolite), neutron probe surveys in wells (0.3-26 m) and continuous groundwater records. The results are shown in Figure 5.5.

Figure 5.5A shows the cumulative seasonal precipitation[1], and Figure 5.5B and 5.5 show the record of shallow soil and saprolite moisture during the same period. Solid colored vertical lines in Figure 5.5A, 5.5B, 5.5C, and 5.5E represent the timing of rock moisture surveys in Wells 6, 7, 15, 16, which are shown in Figure 5.5D. Shown in gray in Figure 5.5D are rock moisture surveys conducted at other times of year. Groundwater levels for wells 6, 7, 15, 16 are shown in Figure 5.5E.

In response to 48 mm of precipitation on September 24, 2014, a small and transient moisture increase was detected by sensors located in saprolite (Figure 5.5C) and some but not all soil moisture sensors (Figure 5.5B). (In this context, transient is meant to refer to a rapid increase and decrease that takes place at the timescale of a precipitation event, in contrast to a sustained increase.) No changes in deeper (>1 m) rock moisture [2] (shown in orange in Figure 5.5D) were observed in response to the first 48 mm of the season and no groundwater changes were observed (including wells not shown in Figure 5.5E) .

In response to an additional 114 mm of rainfall in October (cumulative seasonal precipitation 212 mm, shown in light orange in Figure 5.5), soil moisture rose by 2-10%, saprolite moisture rose by 10-15%, and Well 5, 6, 7, and 16 showed increases in moisture content in the upper 1.5-5 m (Figure 5.5). The interpreted depth of the wetting front is denoted by a horizontal dashed line. Isolated moisture content increases occur beyond the wetting front depth indicating non-sequential wetting and the presence of preferential flowpaths(e.g. 6 m in Well 7).

After 18 days of no rain following the 114 mm event, moisture content in soil declined or was sustained (Figure 5.5B) while rock moisture was either sustained or increased in wells. In Well 7, the wetting front progressed by approximately 0.6 m between surveys (from 3.2 to 3.8 m) providing an estimate of wetting front propagation of 4x10^{-7} m/s. No groundwater response in Wells 15 and 16 was observed (Figure 5.5E), while a small, transient groundwater response was observed in Wells 6 and 7 (a rise of 0.22 m and 0.16 m respectively), and Wells 1, 12, 3, and 14 (not shown in Figure 5.5E) rose and fell as well.

Following the addition of 210 mm rainfall (cumulative seasonal precipitation of 468 mm, shown in dark green in Figure 5.5), moisture content in soil and saprolite rose to a higher, sustained level, a wetting front progressed at depth (only Wells 15 and 16

---

[1]The calculation of cumultive seasonal precipitation begins, here, in August to accommodate September storms that arrive before the official start of the "water year" on Oct 1.

[2]Note that only W15 was surveyed at this time.

were surveyed at this time), and groundwater levels rose and were temporarily sustained in Wells 6 and 7. Transient groundwater responses were observed in Wells 15 and 16 approximately 12 days after the response in Wells 6 and 7.

Figure 5.6 shows the change in moisture content, $\Delta\theta$, in successive surveys for the initial wet season in water years 2014 and 2016 in Wells 6, 7, 15 and 16 [3](water year 2015 is shown in Figure 5.5). In all years of observation, a wetting front advances during the early part of the wet season. Once the moisture content rises to an apparent limiting value, this moisture content remains elevated as wetting advances downward.

Figure 5.7 shows the relationship between the depth of the wetting front, noted in Wells 6, 7, 15 and 16 in three successive years (2014-2016, Figure 5.6), and the cumulative seasonal precipitation at the time of the survey. In different wells, the relationship between wetting front depth and seasonal cumulative precipitation is similar. The slope of the line in Figure 5.7 is nearly the same for 3 of the 4 wells.

Wet season

Rock moisture profiles collected during the wet season of 2014 and 2016 are shown in Figure 5.8A. We compare surveys throughout 2016 (shown in green, blue, and purple) to a February 25, 2014 survey (red) where the wetting front had not fully advanced in Wells 5, 15, and 16[4]. Data derived from all other surveys conducted over the period of observation are shown in gray for reference. Arrows denote the full thickness of the seasonally saturated zone.

In wells where the wetting front had fully advanced by February 21 2014, the seasonal maximum rock moisture response (i.e. the change in rock moisture, $\Delta\theta$) in 2014 and 2016 was nearly identical at all depths (Figure 5.8A). In both years, $\Delta\theta$ was at the highest end of the dynamic range. The cumulative seasonal precipitation at the time of the survey is noted for each year. Within the Spring of 2016, additional rainfall did not alter the maximal $\Delta\theta$ condition as rainfall passed through the unsaturated zone to the water table. Continuous measurements of soil moisture (Figure 5.3) and saprolite (Figure 5.3) show that, during the wet season, larger fluctuations of moisture content are observed in soil relative to that in saprolite monitored at 1 and 1.4 m depth.

Between December 29, 2015 (cumulative precipitation 865 mm) and March 16, 2016 (cumulative precipitation 2102 mm), groundwater levels fluctuated through the entire thickness of the seasonally saturated zone (bounded by dotted lines in Figure 5.8A). During the wet season, no detectable change in moisture content is observed at depths that are transiently saturated (Figure 5.8A).

Total rock moisture storage, S, (see Chapter 3 for caclulation method) in the upper 10 m is shown in Figure 5.8B. (The colors of the bars correspond to the profiles in Figure 5.8A.) Rock moisture storage in the upper 10 m shows no significant relationship with

---

[3]These wells were the most frequently surveyed.

[4]Few wet season surveys (preceding the full advance of the wetting front) were successfully collected prior to 2016.

seasonal cumulative precipitation and the maximum condition is repeatable in different years.

Vertical structure of θ and $\Delta\theta_{max}$

Because rock moisture content, θ, is bound by a seasonal minimum and maximum moisture content (at nearly all surveyed depths), we can define a $\Delta\theta_{max}$ and S_{max} using the reference dry survey (October 25, 2015) and a survey conducted in March 16, 2016 (cumulative precipitation 2102 mm, shown in purple in Figure 5.8A). In Figure 5.9 the minimum and maximum $\Delta\theta$ are shown in red and blue respectively, and the results of successive surveys collected at different times throughout the year are shown in gray. Blue bars denote, as in previous plots, the fraction of time a particular depth is saturated.

In each well, $\Delta\theta$ generally follows the same vertical pattern with diminishing changes over time with depth. Several distinctive zones are observed and Figure 5.10 illustrates these zones in Wells 13, 14, 15, and 16 in terms of θ.

The shallowest zone (shown in dark green in Figure 5.10), which lies mostly in saprolite, exhibits low average θ but high $\Delta\theta$. (Note that soils are shallower than the shallowest measurement depth and are therefore not captured by these data.) The abrupt transition around 1.5-2 m depth, reflects an increase in bulk density with depth. The concentration of solid neutron absorbing material (i.e. not water) increases as bulk density of the material increases. We do not observe this transition in Wells 7, 6, and 5 because the upper part of the profile was removed for the construction of a road (Figure 5.9). Moisture content changes ($\Delta\theta$) in the shallowest zone tend to be lower than $\Delta\theta$ observed at depths immediately below the transition (denoted by a dashed line separating dark and light green in Figure 5.10).

Between 1.5 m and 7-12 m, a zone of high $\Delta\theta$ (shown in light green in Figure 5.10) is observed in all wells across the slope. This is reflected by the largest $\Delta\theta$ (i.e. highest deviation between wettest and driest measurements) in Figure 5.9. Figure 5.9 also shows that in all wells except for Well 5, $\Delta\theta$ decreases gradually with depth. In Well 5, a sandstone interbed was encountered between 11-13 m which will be discussed in more detail in the following section. The decreasing changes in moisture content with depth are illustrated in Figure 5.10 by a transition from green to yellow, which highlights where the variability between successive measurements (i.e. the differences between the stacked gray lines) diminishes. At depths highlighted in yellow in Figure 5.10, minimal variability in θ (i.e. low $\Delta\theta$) in successive measurements is observed.

The blue square in Figure 5.10 denotes the seasonally saturated zone. Light blue horizontal bars at the base of Figures 5.10 and 5.9 represent the relative amount of time a particular depth spends below the water table. Note the upper light blue line that delineates the highest elevation of the seasonally saturated zone. In most wells the groundwater only momentarily reaches these high levels. The seasonally saturated zone occurs within the zone where the smallest changes in θ occur. Thus, the water table rise is not accompanied by sustained changes in water content. This suggests that very limited,

but very conductive porosity translates storm precipitation into large groundwater level changes. In Wells 2 and 12, significant $\Delta\theta$ are observed nearly throughout the profile, but notably, within the seasonally saturated zone show minimal changes in ϑ. In Wells 6 and 7, located midslope, significant changes in θ occur in the upper part of the seasonally saturated zone, i.e. the water table very briefly (on the order of day(s) per year) intersects the zone where significant rock moisture is stored seasonally (Figure 5.9).

An abrupt and significant increase in θ (shown in orange in Figure 5.10) occurs at the base of the seasonally saturated zone. This abrupt increase in θ with depth is observed in all surveys and, we hypothesize, reflects a transition in material properties (and accompanying change in moisture content) rather than an abrupt change in moisture content alone. Across this boundary, the neutron response increases by 3000 counts/16 seconds, corresponding to a moisture content change of greater than 20%, which is unlikely to occur abruptly within the fine grained argillite underlying our site (see Appendix B). We infer that a different calibration is needed for this material (see Appendix B for discussion of calibration) and that such a calibration would also lead to much smaller magnitude $\Delta\theta$ than what is shown in Figure 5.10. Therefore, though changes in θ are observed within the orange zone in Figure 5.10, a more appropriate material specific calibration would diminish these changes. At present, lacking an appropriate calibration and acknowledging that the calibration equation we use leads to significant overestimates of $\Delta\theta$, we exclude measurements made within this zone from estimates of changes in rock moisture storage.

Lithologic heterogeneity

Within each of the zones identified in Figure 5.10, θ shifts modestly throughout the profile and these shifts are repeatable in all surveys. These perturbations reflect material property changes likely associated with variability of the parent rock material. Such variation is expected for an interbedded sedimentary environment and was detected during drilling.

For example, as mentioned above, in Well 5 a region of high changes in θ occurs between 11-13 m. Here, a sandstone interbed showing intense oxidative staining was detected during drilling. This interbed was not detected by standard penetration tests. Similarly, an intensely weathered sandstone interbed is located at a discrete and abrupt change in θ at 7.5 m in Well 7. Standard penetration tests is this case did show a lower mechanical strength than surrounding material (see 7.5 m depth in Well 7 in Figure 4.5 within Chapter 4).

A small increase in θ and $\Delta\theta$ in Well 6 is detected at 7 m. Here, instead of a sandstone interbed, we observed in our drill core a discrete layer of less weathered, but highly fractured argillite located between oxidatively weathered and fractured argillite. However, standard penetration test results in Well 6 do not show any significant correspondence with these discrete sources of heterogeneity in θ and $\Delta\theta$ (see Figure 4.5 in Chapter 4 where raw neutron counts are plotted next to standard penetration testing results).

These examples of fine-scale heterogeneity suggest that material properties, including

the degree of weathering, may influence the storage of rock moisture. However, information about the material properties alone (e.g. fracturing, presence of weathering products, and mechanical strength defined by standard penetration tests) may not predict zones of enhanced or reduced seasonal moisture storage as is reflected by the pattern of θ in Well 7 described above. We hypothesize that the small spatial scale (<1 m) differences in θ observed throughout the profiles (and which persist within the range of moisture content observed (Figure 5.9)), is likely due to lithologic heterogeneity that weathering processes have not homogenized.

Comparison of soil and rock moisture storage

Table 5.1 shows the seasonal changes in soil moisture and shallow rock moisture observed via continuous TDR sensors. The average seasonal change in soil moisture, which reflects the seasonal difference in moisture content excluding storm-driven peaks, is 0.1 and ranges from 0.03-0.17 (Table 5.1). The average seasonal change in shallow saprolite and rock moisture between 0.7 - 1.4 m depth is 0.13, and ranges from 0.1-0.15 (Table 5.1).

The seasonal change in θ (i.e. $\Delta\theta_{max}$) in soil and saprolite (Table 5.1) is plotted in Figure 5.11 with depth (gray squares), and compared to results of rock moisture surveys in wells (colored circles). The inset focuses on the upper 5 m. Seasonal moisture content changes diminish with depth, and the largest changes in moisture content occur in the soil and shallow saprolite. Seasonal moisture content changes in soil and shallow saprolite is similar and higher than $\Delta\theta_{max}$ at deeper depths (Figure 5.11). Beyond 5 m, $\Delta\theta_{max}$ tends to be less than 0.04 (40 mm/m).

Assuming a soil thickness of 30 cm, which is typical for our site, the seasonal soil storage, S_{max}, (defined as the change in moisture content multiplied by the layer thickness) is 30 mm. Because soils may be up to 75 cm thick in some locations, and the maximum seasonal change we observe is 0.17, the seasonal storage of moisture in soil may be up to 128 mm in some locations. Figure 5.12A plots the seasonal rock moisture storage, S_{max}, measured in various depth intervals for each well. Note that depth intervals are not uniform. Gray shading represents the soil S_{max} of approximately 30-128 mm.

Figure 5.12A shows that greater than 50 mm of rock moisture storage is observed in the upper 0.3-2 m, and in some instances up to 120 mm is stored in the upper 2 m. Therefore, though the seasonal change in moisture content (i.e. unit storage capacity) is significantly larger in soil than rock, the amount of storage observed in the upper 0.3-2 m of rock is comparable to that observed in the thin soils.

Moisture content changes at depths greater than 2 m are small (0.01-0.08) (Figure 5.11), but the amount of rock moisture is large because of the large thickness of of the rock moisture storage zone. Between 2-5 m depth, rock moisture storage ranges between 60-210 mm and the average rock moisture storage across all wells is 113 mm in this depth interval.

Beyond 5 m, the volume of rock moisture storage depends on the upper extent of the

seasonally saturated zone at the time of the survey used to estimate $\Delta\theta_{max}$[5]. In wells that are chronically unsaturated between 5-10 m, rock moisture storage exceeds 50 mm and can be as high as 177 mm. The highest rock moisture changes ($\Delta\theta_{max}$) in the upper 10 m and thus the largest rock moisture storage (S_{max}) are observed near the drainage divide in Wells 15 and 16 (Figure 5.12A).

An estimate of the seasonal rock moisture storage, S_{max}, in the chronically unsaturated zone is shown in Figure 5.12B. The thickness of the chronically unsaturated zone differs among wells (surveyed depth intervals are shown in the legend of Figure 5.12B). The chronically unsaturated zone holds between 96-617 mm across the site (Table 5.2), with the largest volume of rock moisture held at the drainage divide (Well 15).

With the exception of Well 12, located at the base of the hillslope (where the water table approaches 3.5 m below the surface) and Well 6 (where the water table was high at the time of the survey used to calculate $\Delta\theta_{max}$ and some of the weathered bedrock zone is missing due to road construction), rock moisture in the chronically unsaturated zone exceeds the seasonal moisture in soil (shaded gray in Figure 5.12B).

To compare rock moisture storage in the chronically unsaturated zone and the unsaturated portion of the seasonally saturated zone (which differs in thickness throughout the year) we compare the unit storage capacity of these two zones among all wet season surveys. The unit storage capacity is simply the moisture content change ($\Delta\theta$) expressed in terms of mm/m of water, and the median represents the median value throughout the depth interval of interest in a single survey. Figure 5.13 shows that, with the exception of Wells 6 and 7, the unit storage capacity in the unsaturated zone (orange) is consistently higher than the storage capacity in the seasonally saturated zone (blue) (Figure 5.13).

Seasonal groundwater response and rock moisture

In Figure 5.14 cumulative precipitation and runoff are plotted for each year starting on October 1. The difference between the two lines is water loss to interception, evaporation, and transpiration. Monitoring of successive years of cumulative precipitation and well dynamics (Figure 5.14A) reveals that, seasonally, there is some cumulative amount of rain that occurs during the Fall before the wells rise significantly and become responsive to individual storm events. This initial seasonal groundwater response (shown as colored circles on Figure 5.14A), though variable across the hillslope, generally coincides with a seasonal increase in discharge in Elder Creek (shown in terms of cumulative seasonal runoff in white in Figure 5.14A). The abrupt flattening of the cumulative precipitation through each year shows the shut-off of rainfall and the rapid decline in discharge such that very little of the total runoff occurs during the summer.

Figure 5.14B summarizes and expands these data to a longer monitoring period. For each well the mean and standard deviation cumulative seasonal precipitation at the time

---

[5]In Wells 6 and 7, approximately 2 m of the highly dynamic rock moisture zone was saturated at the time of the survey used to calculate S_{max} and therefore S_{max} we report is likely significantly less than the actual S_{max}.

of the seasonal groundwater rise is shown by a solid bar and dashed lines, respectively. The least amount of cumulative precipitation needed to generate a response occurs at the base of the hillslope, but this value may be influenced by the rising Elder Creek water level, which responds to early wet season storms. Midslope (Wells 14 through 7) share similar values of 260 to 310 mm cumulative rainfall. Further upslope the cumulative precipitation increased from 420 (Well 10) to 620 mm at the divide (Well 15). There is relatively modest variation in these values at individual wells in success years. This upslope increase in cumulative precipitation to the onset of significant groundwater rise corresponds to the upslope increase in thickness or intensity of weathering (and thus amount of porosity for unsaturated moisture storage) of the critical zone and indicates that the lower part of the hillslope will contribute to storm runoff through elevated groundwater level earlier in the wet season while the upper part of the hillslope is still primarily accumulating rainfall as rock moisture storage at this time. Since the dominant runoff pathway observed is rapid groundwater flow through the fractured, weathered bedrock to the channel, the controls on the response of the groundwater system controls the timing of runoff in Elder Creek, both in dictating peak flows and wet season runoff, and in dictating the amount of baseflow over the long dry season.

The amount of precipitation needed to generate the seasonal groundwater response (mean for each well ranges from 260-620 mm) is greater than the storage capacity of the soil (30-128 mm) except for, in some years, the well located at the base of the hillslope (Well 12). Thus, the seasonal runoff response is likely not dependent on satisfying a seasonal soil moisture deficit alone, and as the profiles show, the wetting front by these threshold precipitation amounts has advanced well into the weathered bedrock.

Figure 5.15 shows the wet season rock moisture storage, S, in the upper 10 m as a function of cumulative seasonal precipitation at the time of the survey.[6] Data collected in different years are represented by different colors and the seasonal cumulative precipitation for each year is labeled along the x-axis (Figure 5.15). Vertical bars represent the timing of the seasonal groundwater rise observed in that well.

Rock moisture monitoring observations throughout the early wet season (see Section "Initial wetting") indicate that prior to the seasonal response of the groundwater table, a wetting front propagates up to approximately 10 m depth. In Figure 5.15, we show that in all years of observation, the addition of precipitation leads to an increase in rock moisture storage early in the wet season. In most wells, the relationship between rock moisture storage and seasonal cumulative precipitation is similar in successive years (each year is represented by a different color). The dashed line marks the 1:1 relationship. We observe that, in a few instances, rock moisture storage very early in the wet season is equal to or exceeds measured precipitation. The water balance requires that maximum rock moisture storage not exceed precipitation less soil moisture storage and interception. Hence, rock moisture storage cannot equal or exceed rainfall. Minor errors may arise from

---

[6]Wells 13 and 2 are excluded from this analysis because groundwater recedes below the bottom of the well and Well 12 is excluded because of the strong dependence of its response on stage in Elder Creek.

1) the underrepresentation of rainfall by the rain gauge (located in the meadow across from the site, see Chapter 3), or 2) the overestimation of rock moisture storage by the neutron probe (via the calibration of neutron counts and moisture content). Nonetheless, the nearly linear relationship between precipitation and rock moisture storage early in the wet season indicates that much of the early wet season rainfall is stored in the unsaturated zone. After groundwater levels rise (marked by vertical lines in Figure 5.15), rock moisture storage plateaus and is insensitive to the addition of precipitation.

Figure 5.16A plots the seasonal cumulative precipitation at the time of groundwater response (error bars represent one standard deviation from the mean) against the consistent value of rock moisture storage in the upper 10 m that is observed after the groundwater response occurs (S_{max}). Figure 5.16B plots the water table depth at the time of the seasonal groundwater response against the cumulative seasonal precipitation at the time of the seasonal response. This shows that the differences in timing of the groundwater response across the hillslope is better explained by the volume of rock moisture storage that must be filled before the response occurs than the travel distance to the water table.

Depletion of rock moisture during the dry season

The dry season, which is marked by 13-23 weeks of no significant rain in the summer months, typically occurs between April and October. To evaluate the structure and timing of rock moisture depletion over the dry season, I performed periodic surveys throughout the summer in three different years (2014-2016). In those years, seasonal cumulative precipitation during the wet season ranged from 1078-2170, and the final wet season storms occurred in April and ranged from 112-246 mm (Table 5.3). Rock moisture surveys were conducted approximately 7, 11-12, and 15-17 weeks after the final storm of the Spring (Table 5.3).

The results of these periodic rock moisture surveys are shown in Figures 5.17 and 5.18. In both figures, data shown in gray reflect the maximum rock moisture condition and data collected at different times during the dry season are overlain in different colors to illustrate progressive drying throughout the summer. Each color represents a different elapsed time into the dry season and different hues of the same color reflect data collected in different years. Figure 5.17 shows profiles in terms of changes in moisture content, $\Delta\theta$, in the upper 15 m and Figure 5.18 shows these same data in terms of the depth cumulative rock moisture storage, ΣS, throughout the profile.

Surveys conducted 7 weeks following the final storm of the wet season (shown in blue in Figure 5.17) tend to deviate from the seasonal maximum (gray) only in the upper 2-5 m, reflecting the initiation of drying in the upper part of the profile. Subsequent surveys (shown in green and orange) demonstrate continued rock moisture depletion in the upper parts of the profile, and the initiation of depletion in progressively deeper layers as the wet season progresses.

Figure 5.18 shows the depth cumulative rock moisture storage, ΣS (i.e. the volume of

rock moisture stored at or above a particular depth). The value of ΣS at the deepest data point is equivalent to the total volume of rock moisture storage within the whole profile. The flattening of these curves in deeper parts of the profile indicates that the majority of the rock moisture storage resides in the upper parts of the profile. Some wells (e.g. Wells 5 and 13) show nearly vertical ΣS with depth beyond 10 or 15 m, while other wells (e.g. Wells 14, 15, 16), show small changes in rock moisture at depths greater than 15 m (Figure 5.18). These small changes at depth reflect rock moisture which may, eventually, if out of reach of vegetation, recharge the groundwater table.

Twelve weeks following the final Spring storm, rock moisture is elevated relative to the end of the dry season (shown in green in Figures 5.17 and 5.18). The volume of rock moisture storage measured within different depth intervals at each well are shown in Table 5.4. Table 5.4 also shows the seasonal maximum rock moisture storage (in bold) and the percentage of seasonally dynamic rock moisture remaining at different times during the dry season. In the upper 5 m, 12 weeks into the summer, rock moisture storage in all wells (up to 95 mm) is greater than double soil moisture storage (9-15 mm) (Table 5.4). Between 5 and 10 m depth, in excess of 40 mm of rock moisture storage (37-52% of the seasonal maximum) is observed 12 weeks into the summer across the site. Hence, more water is held as rock moisture than as soil moisture during most of the dry season.

Table 5.4 also shows the percentage of the seasonal maximum rock moisture storage that remains in each depth interval at different times during the summer. Surveys in different years are shown, including a significant drought year in 2014 (less than half the mean annual precipitation). No significant or systematic difference between different years of observation is observed, thus the pattern of rock moisture depletion is relatively consistent from year to year, including following years of different total seasonal precipitation.

5.3   Discussion

Conceptual model for a seasonal rock moisture cycle

Figure 5.19 presents a conceptual illustration of a seasonal rock moisture cycle. Because we monitor changes in moisture content and cannot distinguish between rock moisture stored in fractures or the rock matrix, we illustrate changes in rock moisture in Figure 5.19 as blue shading. Blue lines denote fractures, and where they are below the water table (denoted by the dashed black line), they are saturated.

At the conclusion of the dry season (Figure 5.19A), rock moisture added during the wet season is depleted to approximately the same level year after year. In a few locations, water added in one year may not be lost by the next. The first small (often < 20 mm) storms of the season (Figure 5.19B) increase soil moisture and can transport water preferentially beyond the soil. Groundwater level (marked by the black dashed line) continues to recede despite the addition of rainfall, and some wells show a short-lived response to rainfall (note lower position of the dashed line in 1.20B relative to 1.20A). This period of continued

groundwater drainage may extend up to three months (usually September to November) into the onset of periodic wet season rain.

After the arrival of the first major storms of the wet season (Figure 5.19C), but before a seasonal wetting front propagates through the entirety of the seasonally dynamic rock moisture zone, precipitation is stored as soil and rock moisture. Wetting progresses downward through the weathered bedrock zone. Early storms, in some instances, lead to a short-lived rise of the water table, and downslope wells may rise and fall with discharge in Elder Creek, but groundwater in upslope wells is generally unresponsive to these early wet season storms and continues to slowly recede despite the addition of rainfall.

After 210 mm (at the base of the hillslope) to 620 mm (at the ridge top) of cumulative precipitation has fallen (Figure 5.19D), the wetting front reaches the depth beyond which rock moisture is seasonally invariant (7-12 m). Further rainfall leads to delivery to and rapid rise of the groundwater table. Upslope wells, which store a larger volume of rock moisture annually, respond later than downslope wells.

This seasonal delay of groundwater and runoff to wet season precipitation is observed via streamflow (Sayama et al., 2010) and groundwater (Hale and McDonnell, 2016) time-series in other seasonally dry sites where runoff occurs through fractured bedrock. However, to our knowledge, the rock moisture observations at Rivendell are the first attempt to directly measure the temporal and spatial patterns of deep unsaturated zone storage that lead to such a delay. At our site, the volume of rock moisture storage is a better predictor of the seasonal delay in groundwater response than the distance to the water table at the time of response and because the cumulative precipitation at the time of the groundwater response is proportional to rock moisture storage, the volume of rock moisture available for transpiration may be deduced from this seasonal delay.

After the seasonal groundwater response occurs, soil moisture rises and falls in response to storms while rock moisture maintains a relatively constant elevated level and groundwater responds to incoming precipitation relatively rapidly. The depth of the seasonally dynamic rock moisture zone extends to the seasonally saturated zone at the lower end of the hillslope, while upslope, significant seasonal changes in rock moisture are disconnected from the saturated zone by several meters of fractured rock within which the water table rapidly rises and falls without generating detectable changes in rock moisture.

As the dry season progresses (Figure 5.19E), soil moisture decreases rapidly, while rock moisture decreases more slowly and dries from the top down. Annual rock moisture storage decline greatly exceeds summer runoff in Elder Creek (17-58 mm, Table 1.5), which is fed by receding groundwater within the hillslope. Given the continual recession of the water table and the slow rate of depletion of rock moisture, we conclude that the majority of seasonal rock moisture storage is lost to transpiration rather than downward drainage.

Controls on the vertical structure of rock moisture dynamics: material properties and transpiration demand

Rock moisture dynamics in the upper and lower regions of the weathered bedrock zone exhibit distinctly different behavior: the shallow region which remains unsaturated year round, shows large changes in rock moisture (i.e. high $\Delta\theta$), while the depths that host a seasonally fluctuating water table show small changes in rock moisture (i.e. low $\Delta\theta$). Importantly, both regions rapidly transmit the signal of rainfall to the saturated zone during the wet season. Below the seasonally fluctuating water table is a zone which remains chronically saturated.

Figure 5.20A illustrates a simplified one-dimensional conceptual framework for this three-layer hydrologic system. The total amount of pore space is illustrated as a thick black line and shading denotes the proportion of that pore space occupied by air and water. Shallow depths, above the boundary between high and low $\Delta\theta$ (for convenience, we refer to this boundary as the $\Delta\theta$ *boundary*) are chronically unsaturated. Here, large changes in rock moisture (shown in light blue) are observed, and some residual water is stored that is not seasonally exchanged (shown in dark blue). The remainder of the pore space is air filled (denoted by dotted diagonal lines). At greater depth, below the $\Delta\theta$ boundary, the proportion of water that is residual water (i.e. not exchanged) increases. At these greater depths, the total rock moisture (shown in light blue in Figure 5.20) is less, despite periodic saturation that drives storm runoff (shown in hatched gray). The deepest zone is chronically saturated (Figure 5.20A) within largely impermeable bedrock. We propose that the same approximate volume of residual water as the seasonally saturated zone is stored here, and some very small volume of groundwater within fractures may contribute to streamflow (shown as hatched gray).

Above the $\Delta\theta$ boundary, 1) Oshun et al., (2015) find high variability in the stable isotope composition of pore fluid extracted from rock samples obtained during drilling 2) samples of rock matrix saturated in a laboratory show high variability in gravimetric moisture (see Appendix B), 3) low standard penetration resistance is measured (interpreted as mechanical weakness, see Figure 4.6 in Chapter 4) and 4) slow seasonal wetting and drying occurs. Below the $\Delta\theta$ boundary, there is 1) limited to no variability in pore fluid stable isotope composition (Oshun et al., 2015), 2) limited to no variability in saturated matrix gravimetric moisture content, 3) high standard penetration resistance, 4) limited evidence of weathering beyond fracture surfaces, and 5) rapid saturation and desaturation (i.e. groundwater fluctuations) in response to small additions of water.

Taken together, these observations indicate that above the $\Delta\theta$ boundary, the pervasively fractured, weathered bedrock stores rock moisture in a variety of reservoirs that exchange with incoming precipitation at seasonal and shorter time scales, while, below the $\Delta\theta$ boundary, matrix blocks remain permanently saturated with residual water and rock moisture and groundwater are isolated to fractures. The hypothesized rock moisture reservoirs that lead to these local hydraulic properties are illustrated in Figure 5.20 B and C.

Above the $\Delta\theta$ boundary (Figure 5.20B), rock moisture (shown in light blue) may be held within interconnected pores of the weathered matrix (e.g. Zwieniecki and Newton, 1996), within weathering rinds or oxide coatings (e.g. Tokunaga and Wan 2001), and clays and secondary weathering products that either form in place or are transported and stored within fractures (e.g. McKay et al. 2005). All of these shallow rock moisture storage reservoirs are observed. Figure 5.21A shows an exposure of 3.5 m deep weathered, pervasively fractured argillite during the wet season where we observed films of water along fracture surfaces and moist clays (light brown colored granular material in the photograph) between fractures. Figure 5.21B shows a closer view of a fracture surface with clay weathering products and oxide coatings.

Both above and below the $\Delta\theta$ boundary, rock moisture may occur as a film along fracture surfaces (e.g. Rutter et al., 2006), within fracture roughness features (e.g. Price et al., 1980), or as a capillary bridge between fractures (e.g. Dragila and Weisbrod, 2004). Figure 5.20B, which illustrates the rock moisture conditions below the $\Delta\theta$ boundary, shows these fracture related rock moisture reservoirs. Residual water held in the matrix is colored dark blue while rock moisture held in fractures is colored light blue to emphasize that, in this zone, rock moisture changes, as well as seasonal saturation, occur almost entirely within fractures.

The material property changes with depth influence the amount of rock moisture storage that may develop, but material properties alone may not explain the pattern of rock moisture decline over the dry season (and thus the seasonal dynamic). The decline can occur by only two processes, transpiration by deeply rooted trees or gravitational drainage. A simple water budget calculation strongly suggests that this decline is dominantly due to transpiration (see section above). There is also strong evidence that trees at Rivendell use rock moisture. Oshun (2016) concluded from extensive stable isotope measurements that Douglas fir primarily use rock moisture and neighboring hardwoods primarily use soil moisture. The isotope measurements were supported with a tracer test during the summer of 2014 in which heavy dD was injected in the saprolite (~1.5 m deep) at the base of Douglas Fir and various hardwood trees. The tracer was found in the Douglas fir but not the hardwoods. Furthermore, during drilling, roots were observed to 16 m (Figure 4.1) and mycorrhizal fungi were observed along fracture surfaces to depths of at least 5 m.

Depth of rooting is important because the observed rock moisture depletion at Rivendell occurs to depths in excess of 10 m. Data on maximal rooting depth in mature Douglas fir are limited (Stone and Kalisz, 1991, Canadell et al, 1996). However, in similar rock types in Oregon, Douglas fir are observed within rock (e.g. Wang et al., 1995, Roering et al., 2003) to depths of at least 2 m (Zwiniecki and Newton,1994). Rooting depth alone may not dictate the full depth extent of water extraction, because, for example, Allen (1991) observe fungal hyphae at distances greater than 2 m from the roots of young Douglas fir in Western Oregon. These observations suggest that, despite a lack of data on the maximal rooting depth at our site, water may be directly extracted by roots or their symbiotes to 10 m depth and the $\Delta\theta$ boundary may represent the maximum depth of

seasonal extraction of rock moisture by vegetation.

The association of material properties, rock moisture dynamics, and exploitation by trees suggests the possibility that tree water use may, in fact, promote weathering that in turn increases the rock moisture storage capacity. The $\Delta\theta$ boundary may mark the signature of trees on critical zone evolution. The greater rock moisture storage and stronger weathering observed upslope may reflect the imprint of rhizosphere weathering processes on rock that has experienced a longer residence time on its transit through the critical zone. Trees rooted in rock promote weathering via a variety of biochemical and biomechanical processes including, for example, microfracturing mineral grains (Schwartzman and Volk, 1989) and producing organic and inorganic acids, which dissolve minerals (Yatsu, 1988). These weathering processes increase the moisture storage capacity of the rhizosphere by generating and connecting pore space and precipitating water retentive secondary minerals (Kelly et al., 1998). Thus, the vertical structure of $\Delta\theta$ may reflect the penetration depth of vegetation-relateds biotic weathering. This suggests a coevolution of critical zone structure, topography, and vegetation. The role of vegetation on driving landscape evolution (e.g. Pawlik, 2013) and weathering and critical zone evolution (e.g. Brantley et al., 2011) has long been recognized, but due to challenges associated with directly measuring processes in the deep rhizosphere, particularly, in bedrock, many questions remain about the controls on the depth extent of rooting and weathering, and how the complex interactions between roots, fungi, bacteria, archea, water and minerals dictate the fluxes of solutes, water, and gases in the critical zone.

This vertical structure of $\Delta\theta$ has significant implications on hydrogeochemical processes beyond the rhizosphere, which may control the timing and chemical composition of groundwater and streamflow. The enhanced porosity and large $\Delta\theta$ that may be associated with a deep rhizosphere: 1) leads to a delay of the seasonal response of runoff to rainfall and a dominance of downslope sources of water to runoff in the early part of the wet season, 2) imposes a vertical hydraulic conductivity gradient which limits the upper extent of the seasonally saturated zone and thus the route storm runoff takes to the stream, and 3) through interconnected porosity, promotes exchange and mixing of water in the diversity of rock moisture reservoirs that exist in the near surface. Below the rhizosphere, no mechanism exists to significantly reduce the moisture content of the rock matrix (in contrast to, for example, the direct extraction of water by mycorrhizal fungi (Taylor et al., 2009). At this greater depth, the chronic saturation of matrix blocks and storm-driven fracture flow influences geochemical evolution of water in several way: 1) weathering reactions and solute exchange within the rock matrix are mostly limited to slow, diffusional processes (Brantley and White, 2009), 2) the rapid flow through fractures does not permit sufficient time for exchange with the matrix which leads to little expected geochemical evolution of water within the seasonally saturated zone, and 3) the rapid fluctuation of the water table (i.e. rapid saturation and desaturation of fractures) permits the introduction of reactive fluids to the boundary between weathered and unweathered bedrock at the base of the seasonally saturated zone.

Continual saturation of matrix blocks within the seasonally saturated zone also sug-

gests, that a continuous water phase may be present between the rooting zone and the chronically saturated zone despite the pervasive fractured, thick unsaturated zone that separates the two. In their studies of rock moisture dynamics in fractured chalks in the U.K., Haria et al., (2003) and Price (1980), both propose that tension saturation in the rock matrix tens of meters above the water table represented a capillary fringe within the rock matrix, and that this capillary fringe may extend closer to the surface than a separate capillary fringe that occurs within tension saturated fractures and microfractures directly above the saturated zone. The $\Delta\theta$ boundary may represent the upper limit of matrix tension saturation due to the increase in porosity generated by rhizosphere weathering processes. It is possible that the tension saturation of the rock matrix hydraulically links moisture dynamics above the $\Delta\theta$ boundary to the saturated zone, transmitting the signal of vegetative water extraction to the saturated zone. Unraveling the hydraulic continuity between the rhizosphere and water table will be key to understanding how the atmosphere, via roots, exerts a control on groundwater and streamflow dynamics.

Figure 5.22 presents a conceptual model of the rock moisture structure across the hillslope and the influence of the structure of rock moisture on ecohydrologic processes. Three panels (A, B, and C) separate the hillslope into the three coupled components which influence the observed structure of rock moisture: vegetation (A), fractures (B), and matrix blocks (C). The topmost panel (D) reflects our observations of high rock moisture changes in the chronically unsaturated zone and low rock moisture changes in the seasonally saturated zone. Beyond the lower extent of the saturated zone, rock remains chronically saturated and restricts seasonal hydrologic dynamics to the weathered bedrock zone. Across the hillslope, tree roots may extend to nearly the same depth and promote a near surface layer of both fracture (B) and matrix (C) alteration which promotes rock moisture storage. At upslope positions, the interface between the seasonally saturated and chronically saturated zone is separated from this seasonally dynamic rock moisture storage zone by meters of fractured, but otherwise largely unaltered bedrock, that transmits storm runoff. This observed vertical structure reflects the dual ecohydrologic function of rock moisture: the seasonal storage of moisture in the near surface for seasonally water stressed vegetation and the transport of rainfall to the saturated zone which feeds the channel network during the wet and dry season.

Global significance of rock moisture to vegetation

In uplands forests, soils are commonly thin, and often do not provide enough storage capacity to meet the evapotranspiration demand of vegetation (Graham et al., 2010). For decades, weathered, fractured bedrock, which is commonly encountered within 1 m of the surface (sensu Wald et al., 2012), has been proposed as a source of seasonal water storage for vegetation in seasonally dry climates (e.g. Wahrhaftig, 1965, Arkley, 1981), and only recently has been quantified (see Schwinning, 2010). Several studies of moisture use by vegetation rooted in bedrock point to a diverse number of conditions (rock types, climates, topography) where the availability of what we define here as rock moisture

may dictate species composition (Zwiniecki and Newton, 1996), response of vegetation to drought (Kukowski et al., 2013), and the return of rock moisture to the atmosphere via transpiration (Schwinning, 2013).

The availability of rock moisture has been demonstrated in rock types which exhibit a wide range of weathering and water holding properties, including granites which weather to soil like grus (e.g. Graham et al., 1997), metasedimentary rocks whose rough fractures host retentive clays (e.g. Zwiniecki and Newton, 1996), and limestone which generates cavernous voids that can accumulate soil like material (e.g. Querejeta et al. 2007). In the karst Yucatan peninsula of Mexico, rock moisture has been identified as a critical resource to vegetation (Querejeta et al., 2007), and the matrix of the limestone bedrock appears to remain unweathered while discrete dissolution features accumulate soil and clays which hold moisture for dense root networks which are restricted to these dissolution features (Estrada Medina et al., 2010). In granites, the dissolution of individual mineral grains within the rock matrix promotes interconnected porosity and water retention within the rock itself. This rock moisture within the matrix is accessible to roots or their symbiotes directly (Hubbert et al., 2001). In weathered sedimentary rocks, rock moisture is held in a variety of reservoirs, each with its own water retention properties, including fracture surfaces, weathering products, and potentially at shallow depths, within rock matrix that has been significantly weathered, as observed in the upper 4 m by Zwieniecki and Newton (1996). Rock moisture use by plants may not be restricted to specific rock types, but an understanding of how rock moisture is held and accessed as a result of specific weathering processes (which may have a lithologic or mineralogical dependence) may allow for the prediction of where and when rock moisture is available and how vegetation interacts with it. Fractures alone may not ensure rock moisture storage, a diversity of pore sizes and the generation of clays may be needed.

At our site, precipitation exceeds potential evapotranspiration on an annual basis, however, the concentration of precipitation during the wet seasons leads to seasonal water stress. Schwinning, 2010 documents six studies in diverse tree species within mediterranean and sub-humid climates where 11-100% of the water use by trees is derived from rock and suggests water held in the underlying bedrock may be particularly important in seasonally dry and semi-arid climates. Beyond water stressed regions, the extraction of nutrients by roots and fungi may lead to a dependence on rock moisture in humid regions as well (Graham et al., 2010) and thus, rock moisture may be important to vegetation in a variety of climates and not only those that are water-stressed.

Studies of groundwater recharge in arid and semi-arid climates indicate that precipitation very rarely penetrates the rhizosphere and almost all of incoming precipitation is accommodated within the shallow part of the profile (see review by Seyfried et al., 2005). At our site, though preferential flow may drive rapid downward transport of water out of reach of direct evaporative loss (even during the driest conditions) a seasonal rock moisture storage capacity must be filled and exceeded before significant downward drainage and recharge of groundwater occurs and thus almost all of the initial wet season precipitation is held within the rhizosphere. This early season response may represent the

behavior of semi-arid or arid climate systems.

Wang and Narasimhan (1985), hypothesized that in arid areas in particular, the high capillary pressures observed within the rock matrix (e.g. Nativ et al., 1995) prevents rapid downward migration of water via preferential flow pathways due to imbibition of water by the rock matrix. This is in constrast to more humid areas where lack of matrix imbibition allows for rapid and deep transport. Our observations, which point to the chronic saturation of rock matrix at some depth supports this hypothesis. Hence, the saturation of the rock matrix may represent a fundamental difference that influences the behavior and function of rock moisture, and its use by vegetation, in different climates. Additionally, the rapid drainage of the rhizosphere prevents saturation which can limit rooting depth among non-hydromorphic species (Richardson and Vepraskas 2000, White 2007). Therefore, the significance of rock moisture to ecosystems may depend on the properties of the rock which balance transport and storage, and these properties may manifest differently in different climates.

5.4 Summary of results

Despite annual variation in total rainfall and the the timing and intensity of storms within the wet season, the amount of rock moisture that is seasonally added and subsequently depleted in the weathered bedrock at any particular location is nearly identical in successive years. This puts a distinct, annually repeated bound on dry season rock moisture availability. The volume of seasonally exchanged rock moisture in the near surface varies from 85 mm near the base of the slope to 615 mm at the ridge, corresponding to stronger weathering of the near surface (upper 5-12 m) upslope. The average annual rock moisture storage across the entire hillslope is 284 mm. Soil moisture storage is 30 mm on average. In a drought year (2014), where the site received 1078 mm of rainfall (nearly half of the annual average), this average rock moisture storage constituted 26% of the annual rainfall.

Seasonally, the initial storms are almost entirely accommodated by storage in soil and rock moisture as a wetting front progresses up to 12 m within the weathered, fractured rock. Rainfall in excess of the annually repeated rock moisture storage capacity is rapidly transformed to runoff throughout the wet season, likely traveling through fractures. Nearly all of the rock moisture is held in the upper 5-12 m of weathered bedrock, below which no significant changes in rock moisture are detected despite transient storm-driven saturation at those depths. The vertical structure of rock moisture is not altered with the addition of rainfall throughout the wet season and is consistent in different years. Over the long dry season, the up to 128 mm stored in the thin soils is rapidly depleted, while the dynamic rock moisture zone is slowly depleted, retaining up to 100 mm 15 weeks into the dry season. The timing and spatial pattern of rock moisture depletion over the dry season is the same in wet and dry years where rainfall varied by 2.5 times.

5.5   Tables

Material	Depth (m)	Material Description	Method	Θ			ΔΘ		Comments	Source
				Minimum	Maximum	Wet Season Mean	Maximum	Seasonal		
Soil	0.05	Soil	TDR	0.04	0.22	0.12	0.18	0.08	15 cm TDR in Backfilled Trench	Rivendell TDR L3T2
	0.1	Soil	TDR	0.07	0.40	0.24	0.33	0.17	15 cm TDR	Rivendell TDR L3T2
	0.15	Soil	TDR	0.06	0.26	0.17	0.20	0.10	15 cm TDR	Rivendell TDR L3T2
	0.2	Soil	TDR	0.11	0.37	0.23	0.26	0.13	15 cm TDR	Rivendell TDR L3T2
	0.3	Soil	TDR	0.10	0.35	0.21	0.26	0.12	15 cm TDR	Rivendell TDR L3T2
	0.5	Soil	TDR	0.07	0.35	0.18	0.28	0.12	15 cm TDR	Rivendell TDR L3T2
	0.33	Soil	TDR	0.07	0.28	0.15	0.22	0.08	30 cm TDR in Backfilled Augered Hole	Rivendell TDR L3S1
	0.27	Soil	TDR	0.08	0.30	0.19	0.22	0.11	30 cm TDR in Backfilled Augered Hole	Rivendell TDR L3S2
	0.3	Soil	TDR	0.09	0.28	0.19	0.19	0.09	30 cm TDR in Backfilled Augered Hole	Rivendell TDR L3S3
	0.15	Soil	TDR	0.09	0.34	0.18	0.25	0.09	15 cm TDR in Backfilled Trench	Rivendell TDR L5
	0.35	Soil	TDR	0.19	0.44	0.32	0.25	0.13	15 cm TDR in Backfilled Trench	Rivendell TDR L5
	0.7	Soil	TDR	0.26	0.46	0.37	0.20	0.11	15 cm TDR in Backfilled Trench	Rivendell TDR L5
	0.29	Soil	TDR	0.02	0.38	0.13	0.35	0.11	30 cm TDR in Backfilled Augered Hole	Rivendell TDR L1S1
	0.15	Soil	TDR	0.07	0.51	0.14	0.44	0.06	30 cm TDR in Backfilled Augered Hole	Rivendell TDR L1S2
	0.25	Soil	TDR	0.02	0.18	0.05	0.16	0.03	30 cm TDR in Backfilled Augered Hole	Rivendell TDR L1S3
	0.25	Soil	TDR	0.09	0.51	0.14	0.42	0.05	30 cm TDR in Backfilled Augered Hole	Rivendell TDR L1S4
Saprolite	0.7	Argillite Fracture Infill	TDR	0.19	0.39	0.34	0.20	0.15	30 cm TDR Pressed Between Fractures	Salve and Rempe, 2012
	0.7	Weathered Argillite Matrix	TDR	0.20	0.37	0.33	0.17	0.13	30 cm TDR Drilled into Rock Matrix	Salve and Rempe, 2012
	0.7	Sandstone Fracture Infill	TDR	0.11	0.26	0.21	0.15	0.10	30 cm TDR Pressed Between Fractures	Salve and Rempe, 2012
	0.7	Weathered Sandstone Matrix	TDR	0.18	0.33	0.30	0.15	0.12	30 cm TDR Drilled into Rock Matrix	Salve and Rempe, 2012
	1	Interbedded Sandstone and Mudstone Saprolite	Gravimetric Sampling	0.24	0.46	--	0.22	--	Manually Collected, May Not Capture Full Range of Moisture Contents	Oshun dissertation
	1	Interbedded Sandstone and Mudstone Saprolite	TDR	0.28	0.47	0.39	0.20	0.11	30 cm TDR in Backfilled Trench	Rivendell TDR L5
	1.38	Interbedded Sandstone and Mudstone Saprolite	TDR	0.20	0.43	0.34	0.24	0.14	30 cm TDR in Backfilled Trench	Rivendell TDR L5

Table 5.1: **Seasonal and maximum moisture content changes in soil and saprolite:** Continuous moisture content observations in soil and saprolite.

Well	Unsaturated Zone				Seasonally Saturated Zone			
	Depth Interval (m)	S (mm)			Depth Interval (m)	S (mm)		
		Mean	Standard Deviation	Maximum (S max)		Mean	Standard Deviation	Maximum (S max)
12	1.2 - 3.5	52	36	96	4 - 7	27	11	49
2	0.3 - 9.5	178	106	291	10 - 12	23	11	41
13	0.3 - 14	107	57	194	14 - 15	1	1	3
7	1 - 4.5	96	53	177	5 - 20	73	33	121
6	1.8 - 4.5	69	37	124	5 - 20	66	35	116
5	1.5 - 14	191	143	445	14 - 25	21	13	47
14	0.4 - 8	148	83	237	8 - 20	79	39	129
15	0.2 - 18	295	190	617	18 - 23	14	13	52
16	0.3 - 7	164	105	372	7 - 17	46	33	105
All Wells		144		284		39		74

Table 5.2: **Rock moisture storage in the saturated and seasonally saturated zone:** Comparison of rock moisture storage observed in all wet season surveys (between October and May) in the unsaturated zone, seasonally saturated zone, and the lower part of the seasonally saturated zone that exhibits an abrupt transition to high neutron counts.

Well 12 : 1.2 to 3.5 m
Well 2 : 0.3 to 9.5 m
Well 13 : 0.3 to 14 m
Well 7 : 1 to 4.5 m
Well 6 : 1.8 to 4.5 m
Well 5 : 1.5 to 14 m
4 to 8 m
2 to 18 m
3 to 7 m

Year	Cumulative Seasonal Precipitation (mm)	Precipitation in Final 35 Days of Wet Season (mm)	Date of Final Wet Season Storm	Date of Neutron Probe Survey	Days Since Final Wet Season Storm	Precipitation Since Final Large Storm (mm)
2014	1078	246	4/29/14	6/17/14	49	14
				7/23/14	85	16
				8/12/14	105	16
2015	1374	112	4/9/15	6/2/15	54	19
				6/27/15	79	19
				8/6/15	119	19
2016	2170	172	4/22/16	6/12/16	51	28

Table 5.3: **Summer rock moisture survey timing and precipitation data:** To track the drying of rock moisture, neutron probe surveys were conducted at different intervals throughout the summer over several years. In all The timing and amount of summer precipitation received is shown

Depth Interval	Date		Rock Moisture Storage, S (mm)									Mean S (mm), % of Seasonal	Median S (mm), % of Seasonal	Standard Deviation
			Well 12	Well 2	Well 13	Well 7	Well 6	Well 5	Well 14	Well 15	Well 16			
0.3 - 2 m	**Seasonal Maximum**	**16-Mar-16**	**33**	**58**	**58**	**52**	**15**	**32**	**61**	**106**	**130**	**61**	**58**	**36**
	7 Weeks into Summer	17-Jun-14	12	20	19	--	--	--	18	--	61	26 , 43	19 , 33	20
		2-Jun-15	15	34	27	14	25	11	15	69	70	31 , 51	25 , 43	23
		12-Jun-16	12	33	22	11	6	14	32	66	78	30 , 50	22 , 38	25
	12 Weeks into Summer	23-Jul-14	3	6	12	14	2	7	6	20	38	12 , 20	7 , 12	11
		27-Jun-15	8	15	14	9	11	--	-1	50	48	19 , 32	13 , 22	19
	15-17 Weeks into Summer	12-Aug-14	--	--	7	16	2	-8	1	19	22	8 , 14	7 , 12	11
		6-Aug-15	10	1	6	7	1	4	0	22	23	8 , 14	6 , 10	9
2 - 5 m	**Seasonal Maximum**	**16-Mar-16**	**61**	**95**	**56**	**119**	**110**	**123**	**89**	**216**	**147**	**113**	**110**	**48**
	7 Weeks into Summer	17-Jun-14	27	29	31	--	--	--	57	--	84	46 , 40	31 , 28	25
		2-Jun-15	40	79	24	67	125	52	62	145	89	76 , 67	67 , 61	39
		12-Jun-16	71	67	28	71	73	40	48	168	108	75 , 66	71 , 65	42
	12 Weeks into Summer	23-Jul-14	15	8	19	24	25	25	20	95	36	30 , 26	24 , 22	26
		27-Jun-15	28	21	17	40	66	--	23	112	66	47 , 41	34 , 31	33
	15-17 Weeks into Summer	12-Aug-14	--	--	13	15	20	15	11	55	28	22 , 20	15 , 14	15
		6-Aug-15	8	5	8	14	13	15	0	44	21	14 , 13	13 , 12	13
5 - 10 m	**Seasonal Maximum**	**16-Mar-16**	**--**	**122**	**77**	**12+**	**20+**	**124**	**142**	**177**	**43**	**114**	**123**	**48**
	7 Weeks into Summer	17-Jun-14	11	66	71	--	--	--	74	--	75	59 , 52	71 , 58	27
		2-Jun-15	30	117	68	80	80	71	77	140	53	80 , 70	77 , 63	32
		12-Jun-16	8	105	58	74	66	67	80	145	22	69 , 61	67 , 54	41
	12 Weeks into Summer	23-Jul-14	13	24	50	63	39	10	47	90	45	42 , 37	45 , 37	25
		27-Jun-15	13	44	51	67	76	--	61	106	58	60 , 52	60 , 48	27
	15-17 Weeks into Summer	12-Aug-14	--	--	35	42	22	7	34	63	34	34 , 30	34 , 28	17
		6-Aug-15	11	11	35	39	29	17	20	47	31	27 , 23	29 , 24	13
10 - 15 m	**Seasonal Maximum**	**16-Mar-16**	**--**	**--**	**-1**	**+**	**+**	**175**	**72**	**77**	**40**	**73**	**72**	**65**
	7 Weeks into Summer	17-Jun-14	--	27	3	--	--	--	54	--	50	34 , 46	39 , 53	24
		2-Jun-15	--	36	6	23	3	68	47	25	40	31 , 43	31 , 42	22
		12-Jun-16	--	18	-13	7	2	111	35	22	23	26 , 35	20 , 28	38
	12 Weeks into Summer	23-Jul-14	--	21	4	16	4	2	31	42	19	17 , 24	18 , 24	14
		27-Jun-15	--	18	-4	14	4	--	39	30	25	18 , 25	18 , 25	15
	15-17 Weeks into Summer	12-Aug-14	--	--	9	16	0	-9	28	37	23	15 , 20	16 , 22	16
		6-Aug-15	--	7	0	14	8	12	23	21	18	13 , 18	13 , 18	8
15 - 30 m	**Seasonal Maximum**	**16-Mar-16**	**--**	**--**	**--**	**--**	**--**	**7**	**--**	**22**	**89**	**39**	**22**	**44**
	7 Weeks into Summer	17-Jun-14	--	--	-3	--	--	--	63	--	7	22 , 57	7 , 32	36
		2-Jun-15	--	--	0	--	--	22	42	32	-18	16 , 40	22 , 100	24
		12-Jun-16	--	--	0	--	--	-10	64	3	9	13 , 34	3 , 14	29
	12 Weeks into Summer	23-Jul-14	--	--	-3	--	--	25	6	-6	-12	2 , 5	-3 , -14	14
		27-Jun-15	--	--	--	--	--	--	-17	36	-20	0 , -1	-17 , -76	31
	15-17 Weeks into Summer	12-Aug-14	--	--	-1	--	--	15	-13	-35	-19	-11 , -27	-13 , -57	19
		6-Aug-15	--	--	-4	--	--	9	-41	31	-30	-7 , -18	-4 , -18	29

+ The water table was high at the time of the survey used to define the seasonal maximum rock moisture storage. We therefore lack estimates for the seasonal maximum storage in the lower portion of the dynamic rock moisture zone in Well 6 and 7.

Entries of "--" reflect that no data were collected for one of three reasons: 1) a survey was not conducted, 2) the measurement depth exceeds the well depth, or 3) the measurement depth was saturated at the time of the survey.

Table 5.4: **Seasonal maximum and dry season rock moisture storage**: Seasonal maximum rock moisture (bold) in different depth intervals compared to rock moisture storage measured throughout the dry season (at 7, 12, and 15-17 weeks after the final wet season storm). The mean, median and, standard deviation for all wells across the site are shown on the right.

Water Year	Total Annual Precipitation (mm)	Total Annual Runoff (mm)	Total Annual Inercepion (20% of Precipitation) (mm)	Total Annual Evapotranspiration (mm)	Total Summer Runoff (mm)
2009	1492	782	298	412	52
2010	1905	1332	381	192	38
2011	2092	1465	418	208	17
2012	1557	918	311	328	14
2013	1447	862	289	295	58
2014	1027	472	205	350	27
2015	1359	769	272	318	31

Table 5.5: **Annual Elder Creek water budget**: Precipitation (measured at the Angelo Reserve HQ weather station), runoff (measured at the Elder Creek stream gauge), interception (estimated as 20% of measured precipitation), evapotranspiration (calculated as precipitation less runoff and interception), and measured summer runoff. Water year begins in October of the preceding year and ends in the water year listed.

5.6 Figures
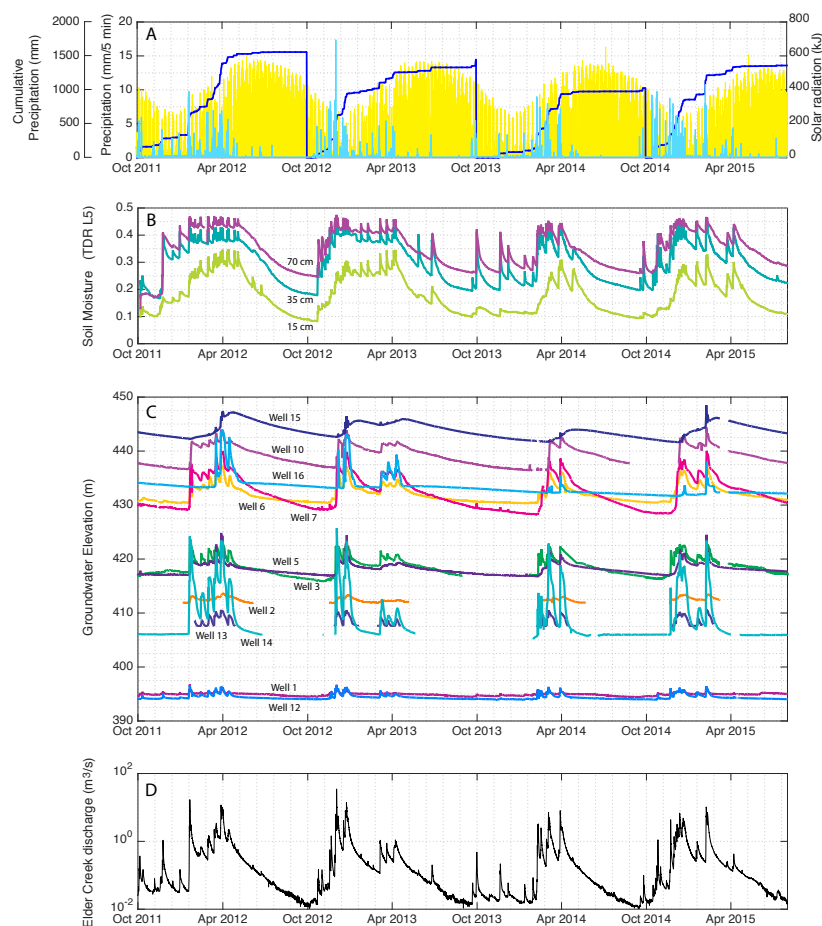
Figure 5.1: **Seasonal pattern of precipitation, solar radiation, soil moisture, groundwater, and streamflow at Rivendell 2011-2015:**(A) Solar radiation (yellow), precipitation (light blue) and cumulative seasonal precipitation (dark blue) measured at Angelo HQ weather station (http://sensor.berkeley.edu) (B) Soil moisture measured via TDR sensors at the ridge top near Well 15 at 15, 35, and 70 cm depth. (C) Elevation of groundwater table in wells across the site. Wells are individually labeled. Periods of inexplicable noise or disturbance of the water table due to sampling or pumping were removed from the record and not shown. The water table at Well 2 (orange) and Well 13 (dark purple) falls below the bottom of the well, therefore, records of water level only exist when the groundwater elevation exceeds the elevation of the bottom of the well. The relatively constant low water table position in Wells 14 (teal) and 16 (light blue) is greater than 5 m from the bottom of the well. (D) Elder Creek discharge (USGS Station 11475560).
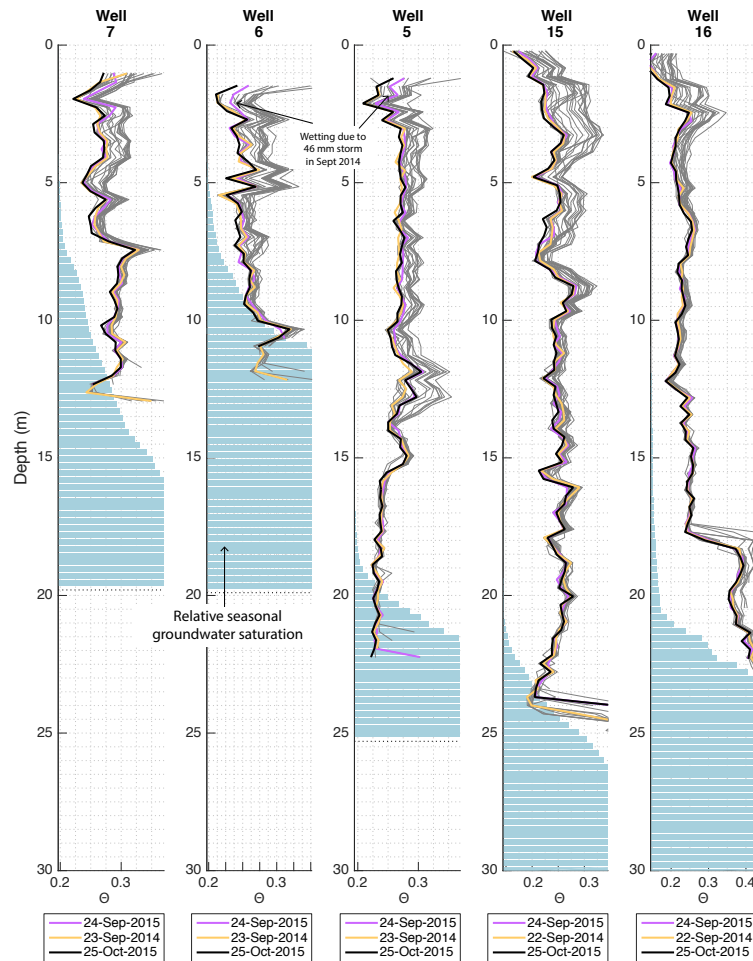
Figure 5.2: **End of dry season rock moisture profiles:** Rock moisture content, θ, measured in Wells 7, 6, 5, 15, and 16 at the end of the dry season in September 2014 (yellow), September 2015 (purple), and October 2015 (black). The survey conducted on October 25, 2015 is used as a reference dry survey to which all other surveys are compared.Gray lines represent all rock moisture profiles over the 3 years of observation. Blue bars are a relative measure of the fraction of time that a particular depth remains below the water table. Dashed lines represent the bottom of the well. Note that 46 mm fell in September 2014 leading to the wetting of the upper part of the profile in some wells.
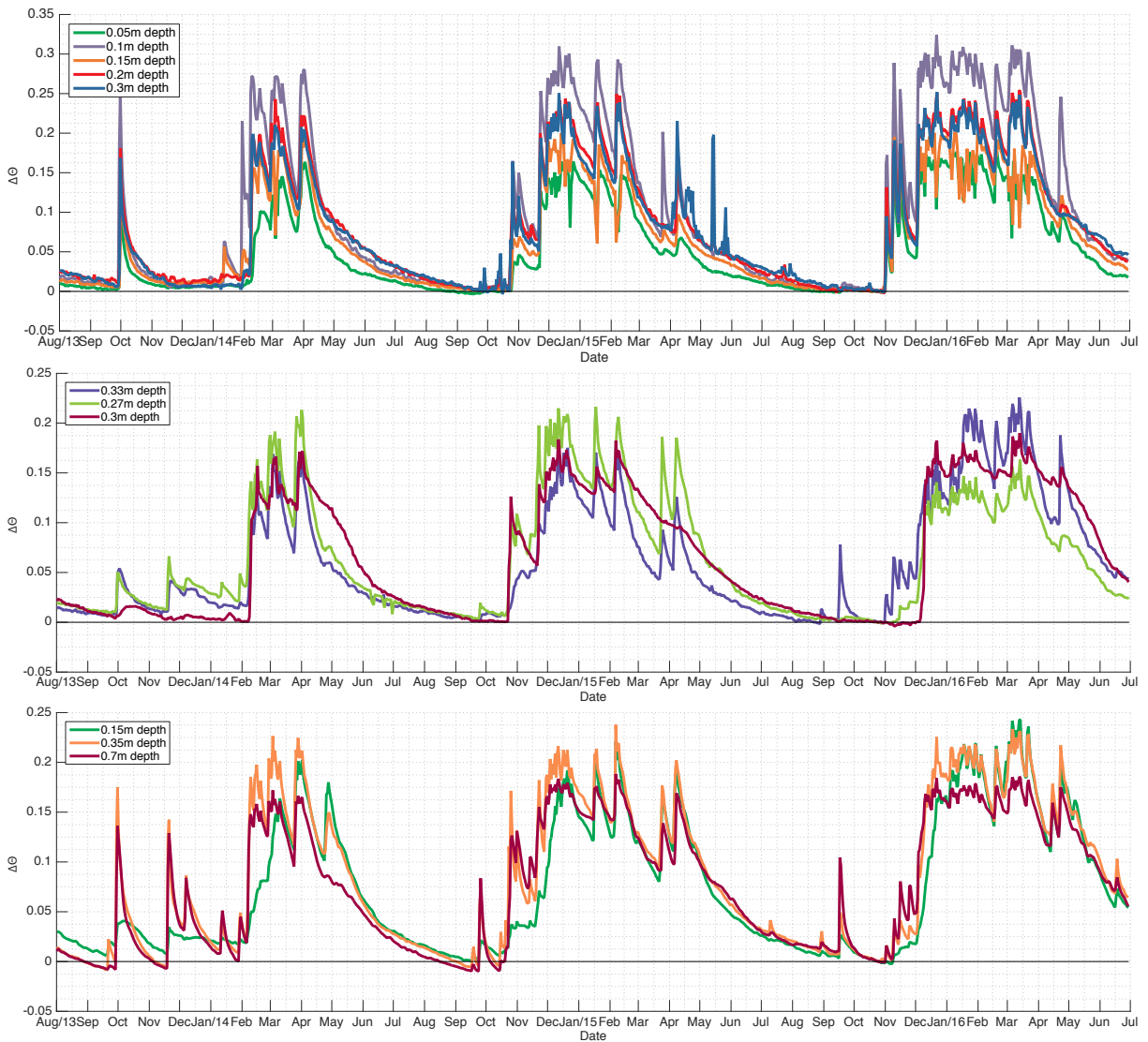
Figure 5.3: **Change in soil moisture:** Change in soil moisture content relative to reference dry date of Oct 25 2015 (i.e. $\Delta\theta = \theta(t) - \theta_{10/25/2015}$) measured by three different TDR configurations. A) T-series TDR inserted sub-horizontally into small trench within soil and then backfilled. B) S-Series TDR: Installed vertically in augered holes in soil and backfilled with native soil. C) L5 TDR: TDR inserted into the wall of a 1.5 m deep trench at the ridge top (Oshun, 2015).
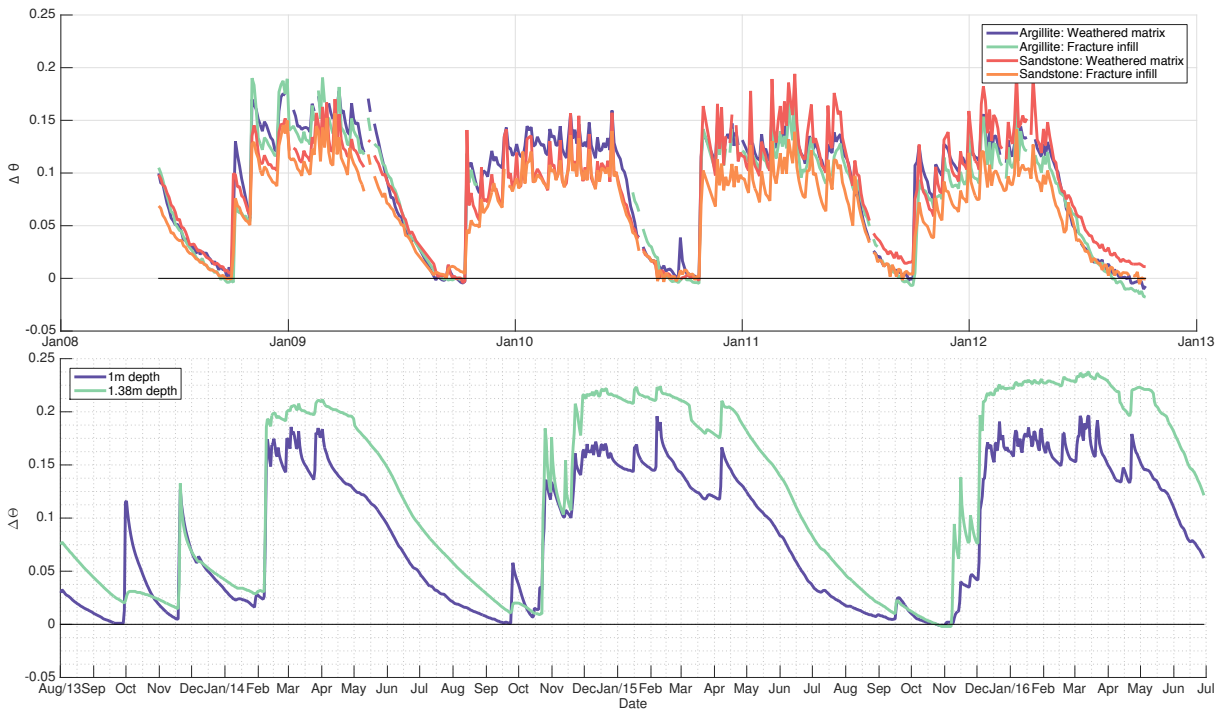
Figure 5.4: **Change in moisture content of shallow saprolite and weathered bedrock:** Changes in rock moisture content, $\Delta\theta$ measured via continuous monitoring of TDR installed in weathered, fractured rock and saprolite. In the top panel (L4 TDR), data are derived from different installation techniques described in Salve and Rempe, 2013 in the two types of rock we observe across the site, sandstone and argillite. The "weathered matrix" TDR were installed by drilling holes for the TDR prongs into the matrix of weathered bedrock in a trench face which was then backfilled. The "fracture infill" probes were pressed into the space between fractures. Missing data in the argillite fracture infill dataset are the result of power outages in 2009-2010. Degradation of the quality of L4 TDR data prevented the calculation of $\Delta\theta$ from the reference dry day, and instead, the minimum moisture content was used as a reference dry measurement. In the bottom panel, L5 TDR data are shown. TDR were pressed into a strongly saprolitized deep trench located at the ridge top. In the L5 TDR, Oct 25 2015 was used as the the reference moisture content from which $\Delta\theta$ was calculated.
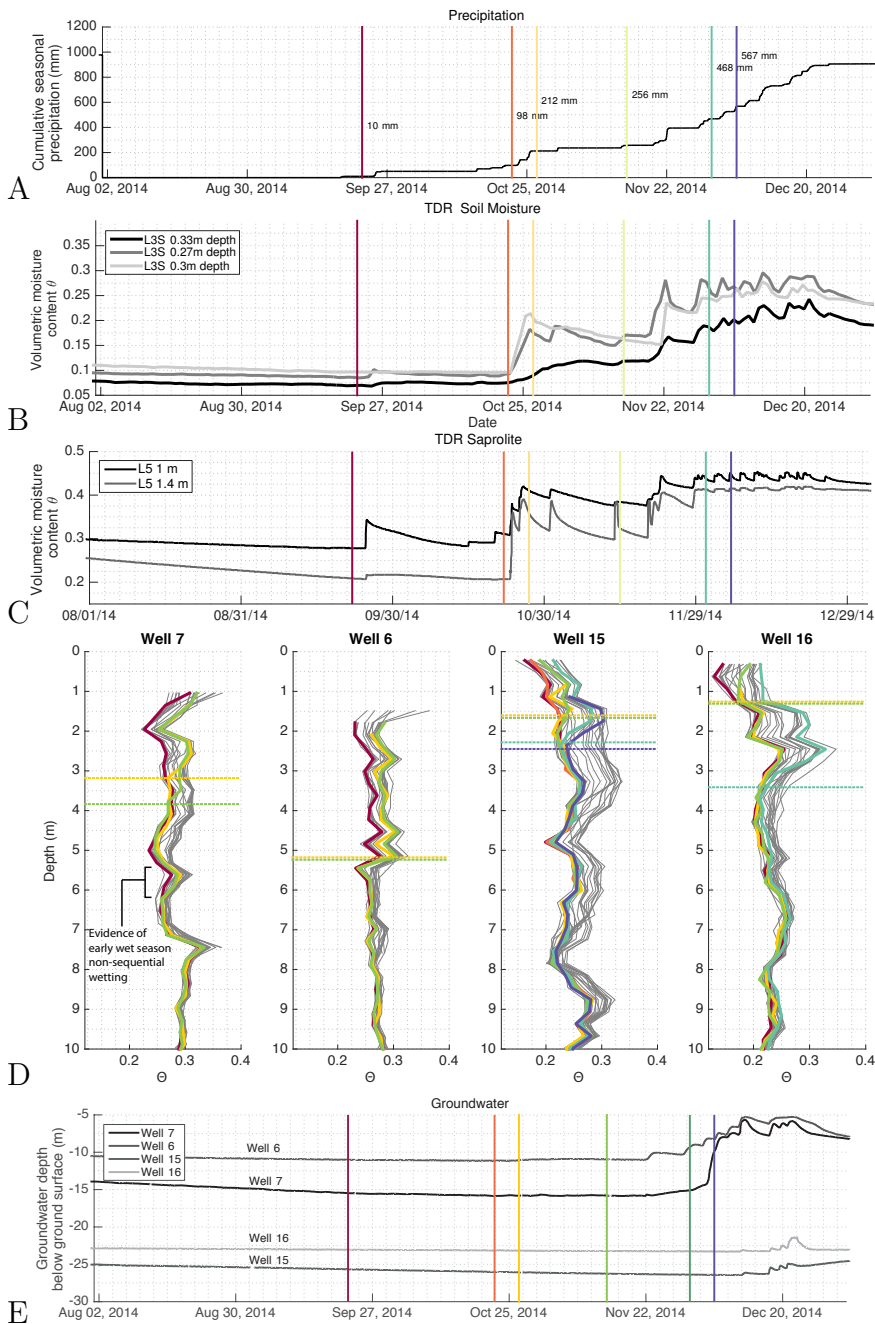
Figure 5.5: **Initial wet season response of soil, rock moisture and groundwater to precipitation:** The initial wet season response of the hydrologic system to small rain events in the Fall of 2014. Precipitation (A), soil moisture (B), shallow saprolite moisture (C), rock moisture (D), and groundwater level (E) are shown. Colored vertical lines in A, B, C, and E correspond to rock moisture survey dates shown in D. Gray lines in D represent all rock moisture survey data collected, solid vertical lines are data collected during the initial wet season in 2014, and dashed lines represent the approximate depth of the wetting front interpreted from the rock moisture survey. Note that cumulative seasonal precipitation (A) is calculated starting Aug 1.
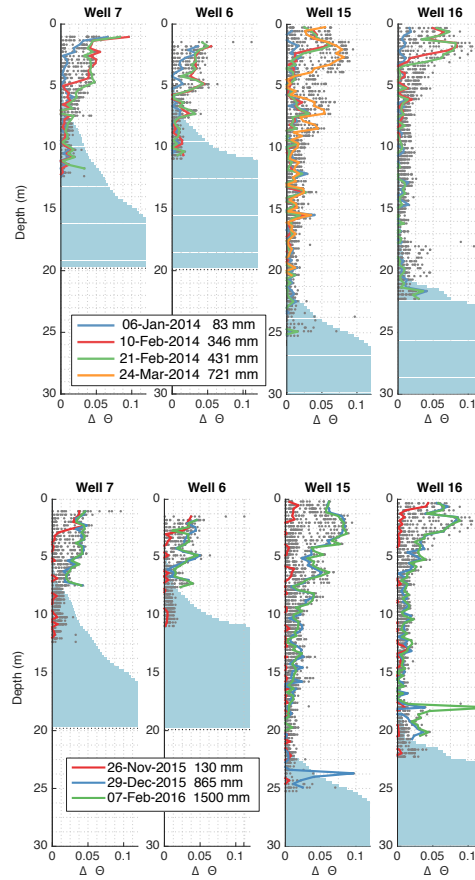
Figure 5.6: **Rock moisture seasonal wetting:** Changes in rock moisture, $\Delta\theta$, in the initial months of the 2014 and 2016 wet season. All data collected are shown in gray Note that not all wells were surveyed during every survey date. Profiles show the propagation of wetting fronts as well as evidence non-sequential wetting. As the wet season progresses, subsequent surveys show little to no change in moisture content.
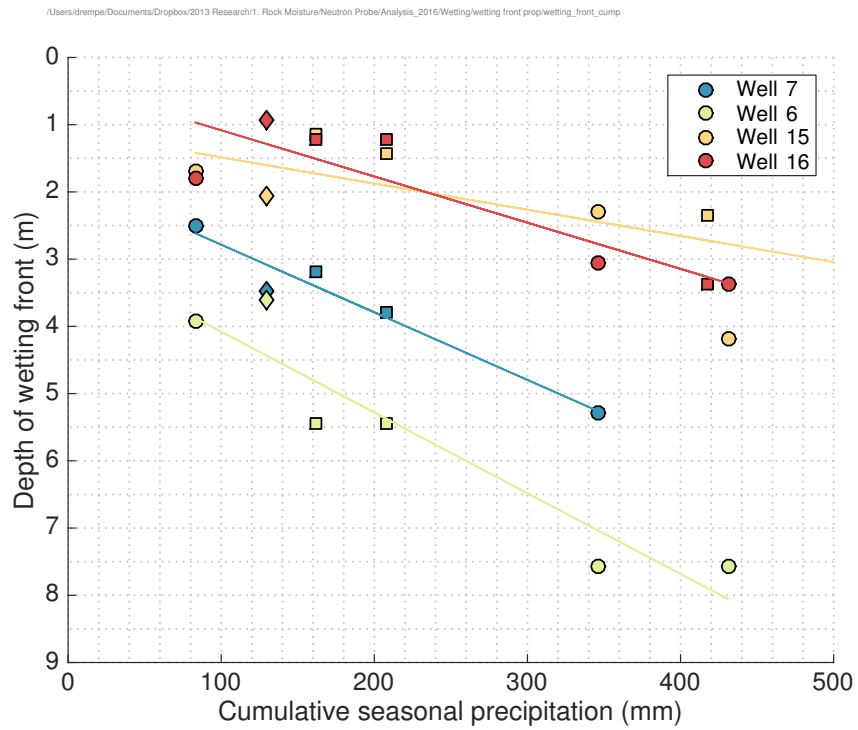
Figure 5.7: **Early wet season wetting front propagation in Wells 6, 7, 16 and 15:** Early wet season wetting front depth within weathered, fractured rock in Wells 6, 7, 15, and 16. Circles, squares, and diamonds are for WY 2014, 2015, and 2016 respectively. Corresponding profiles of $\Delta\theta$ are shown in Figure 5.6.
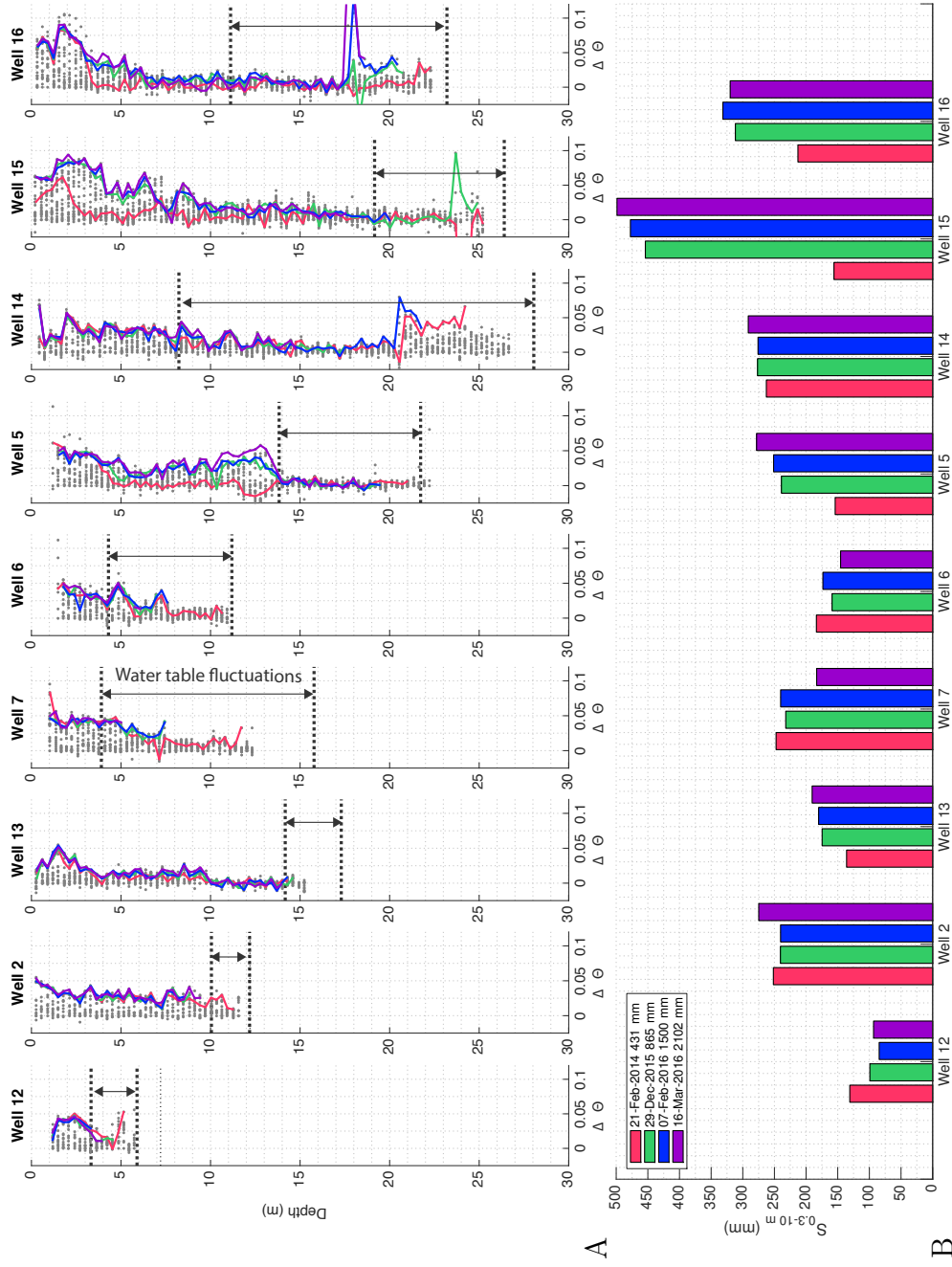
Figure 5.8: **Profiles of repeatable maximum wet season rock moisture**: Rock moisture $\Delta\theta$ (A) and storage in the upper 10 m (B) during the wet season. Addition of precipitation does not significantly influence the amount or pattern of water stored as rock moisture during the wet season. Arrows represent the seasonally saturated zone where the water table fluctuated between December 29, 2015 and March 16, 2016. Each survey extended to the depth of the water table at the time of the survey. This depth was different among surveys. A wetting front in Wells 5 and 15 had not fully advanced at the time of the Feb 21 2014 survey, leading to significantly lower storage at that time.
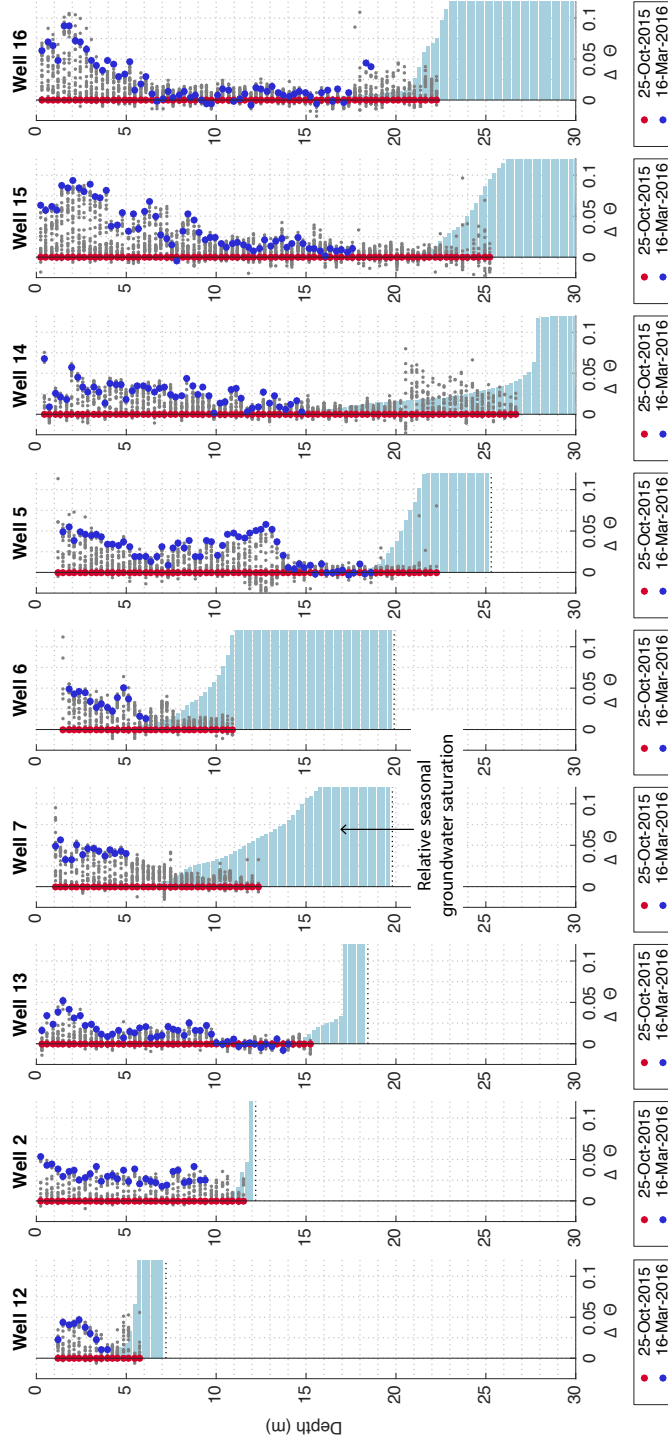
Figure 5.9: **Profiles of seasonal change in rock moisture, $\Delta\theta$:** Change in rock moisture between March 16, 2016 (cumulative seasonal precipitation 2102 mm) and October 25, 2016 reflects roughly the entire range of $\Delta\theta$ observed over multiple years of monitoring. All data collected and analyzed are shown in gray to demonstrate that not all measurement locations show a maximal value at this measurement date. The bottom of each well is denoted with a dashed line and the light blue bars indicate the relative amount of time that a particular depth interval remains saturated (i.e. below the water table).
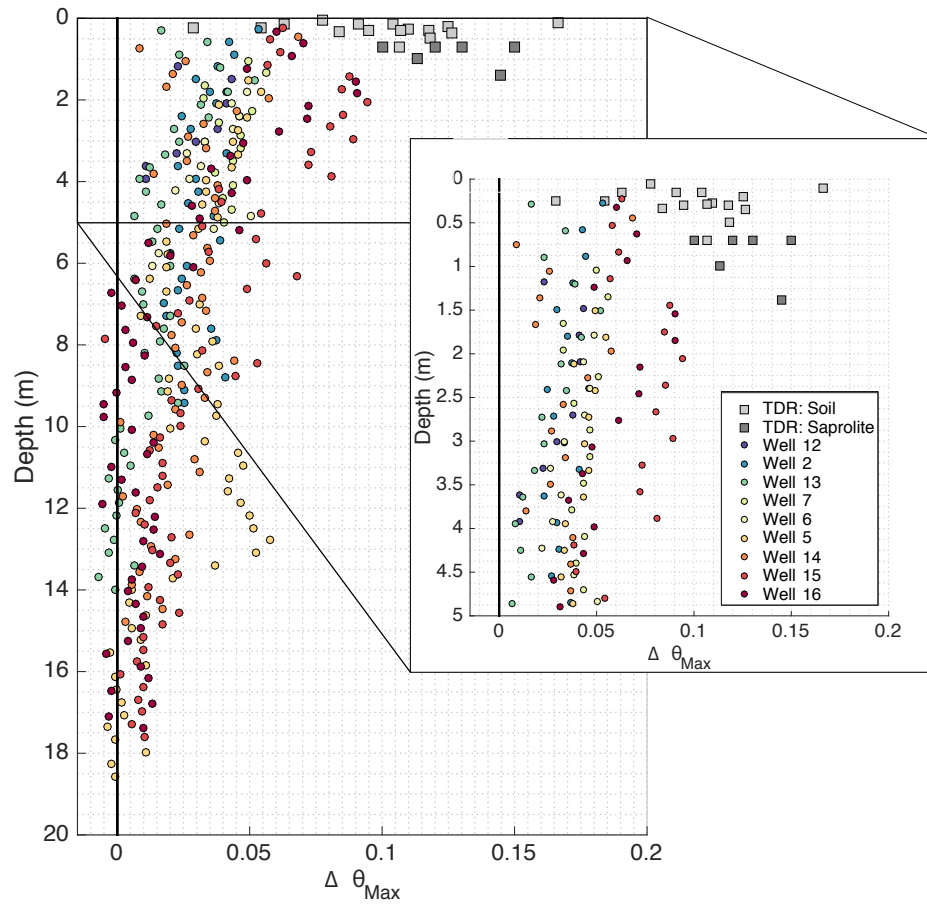
Figure 5.11: **Seasonal change in soil moisture and rock moisture, $\Delta\theta_{max}$:** Seasonal moisture content change, $\Delta\theta_{max}$, with depth. Moisture content changes in wells are derived from neutron probe surveys conducted in October 2015 and March 2016. Seasonal changes in moisture content in TDR installed in soil and saprolite (Table 5.1) were computed as the difference between the mean wet season moisture content and the minimum observed moisture content. Inset shows the same data, highlighting 0-5 m depth interval.
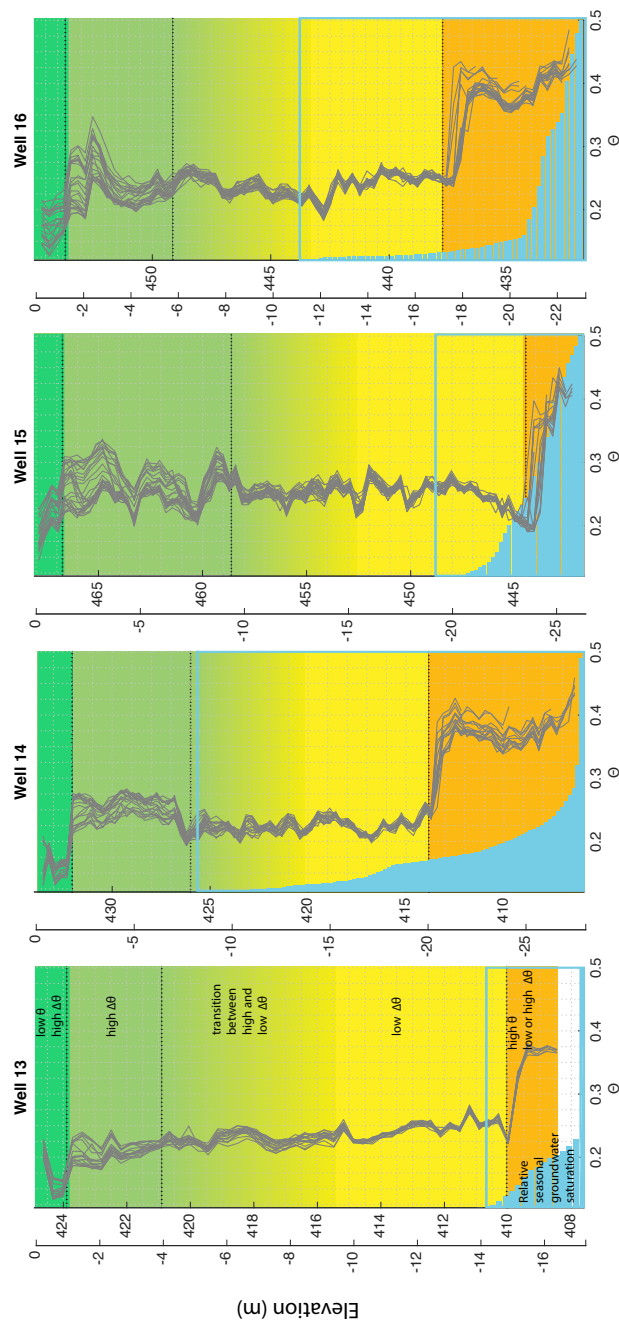
Figure 5.10: **Vertical structure of θ in deep wells:** Deep wells show several discrete layers exhibiting similar changes in θ in successive surveys. All survey data collected are shown in gray and interpreted layers are colored with dashed lines denoting rough boundaries between layers. The seasonally saturated zone is denoted by a blue box and the relative amount of time a particular depth experiences seasonal saturation is shown as light blue horizontal bars. Changes in θ diminish with depth. A shallow zone of low θ (dark green) is associated with low bulk density near surface saprolite, and a deep zone of high θ (orange) is associated with dense bedrock.
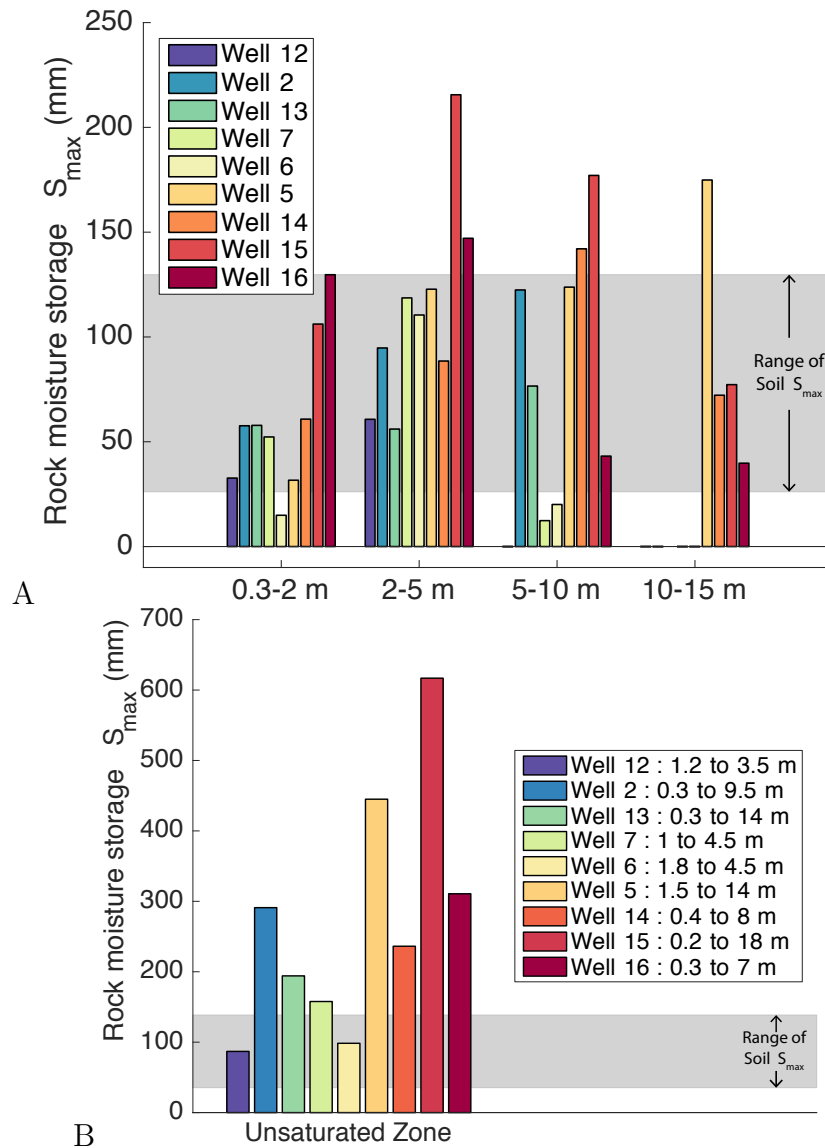
Figure 5.12: **Seasonal rock moisture storage, S_{max}:** Seasonal rock moisture storage, S_{max}, in different depth intervals (A) and throughout the chronically unsaturated zone (B). Note that total well depths and the thickness of the unsaturated zone at the time of the March 16, 2016 survey are different for each well (see Table 5.2). The water table was high at the time the data were collected in Wells 6 and 7, therefore, S_{max} does not account for a significant fraction of rock moisture storage in those wells.
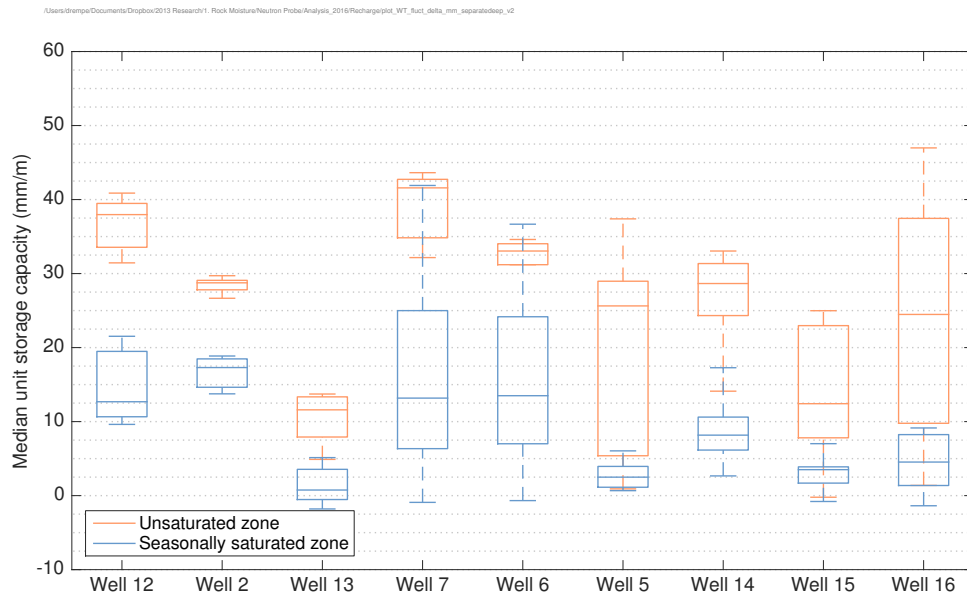
Figure 5.13: **Rock moisture unit storage capacity in the unsaturated and seasonally saturated zone:** The median rock storage unit storage capacity (change in moisture content, here expressed in units of mm/m) in the unsaturated zone (orange) and seasonally saturated zone (blue) shows higher storage capacity in the unsaturated zone. The median was computed from all wet season surveys where cumulative seasonal precipitation exceeded 500 mm. Note that the thickness of the unsaturated and saturated zone differs among wells and the thickness of the unsaturated portion of the seasonally saturated zone differs among surveys. Depth intervals for each well are shown in Table 5.2.
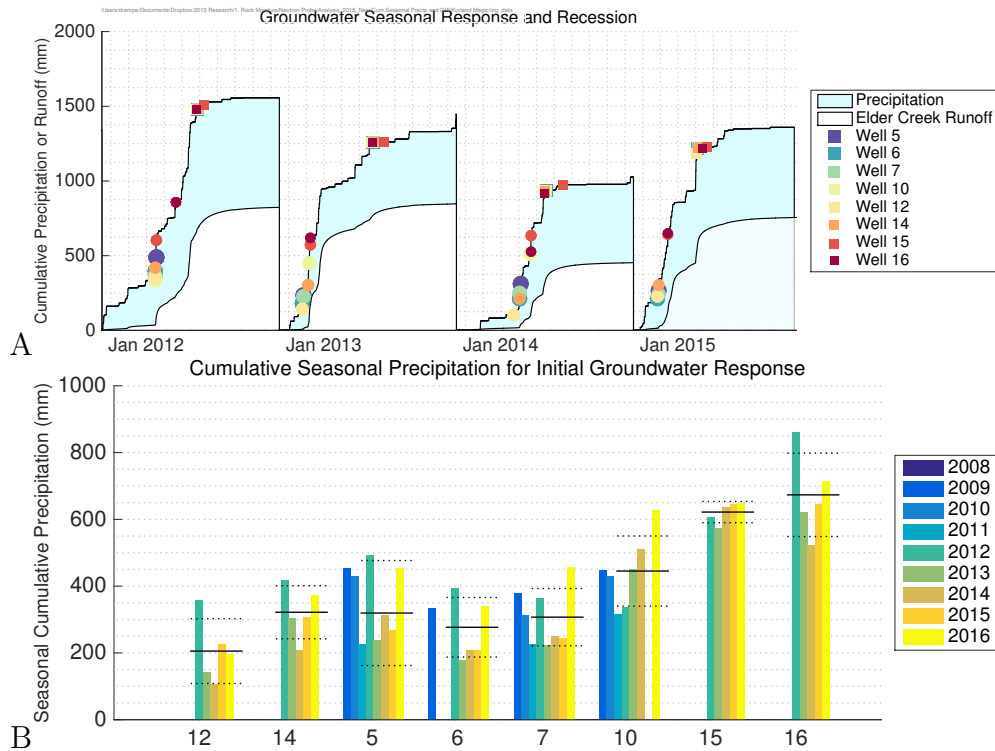
Figure 5.14: **Timing of seasonal groundwater response:** (A) The timing of the seasonal groundwater rise (circles) and recession (squares) plotted on the record of cumulative seasonal precipitation (shaded blue) and cumulative seasonal runoff (white) for water years 2011-2014. (B) The cumulative seasonal precipitation at which the initial seasonal groundwater rise occurs is relativvely consistent year to year. Solid bars reflect the mean for each well and dashed lines represent one standard deviation from the mean. Wells 1 and 3 are excluded from this analysis because of well pumping for groundwater sampling and Wells 13 and 2 are excluded because the groundwater level falls beyond the depth of the well.

96
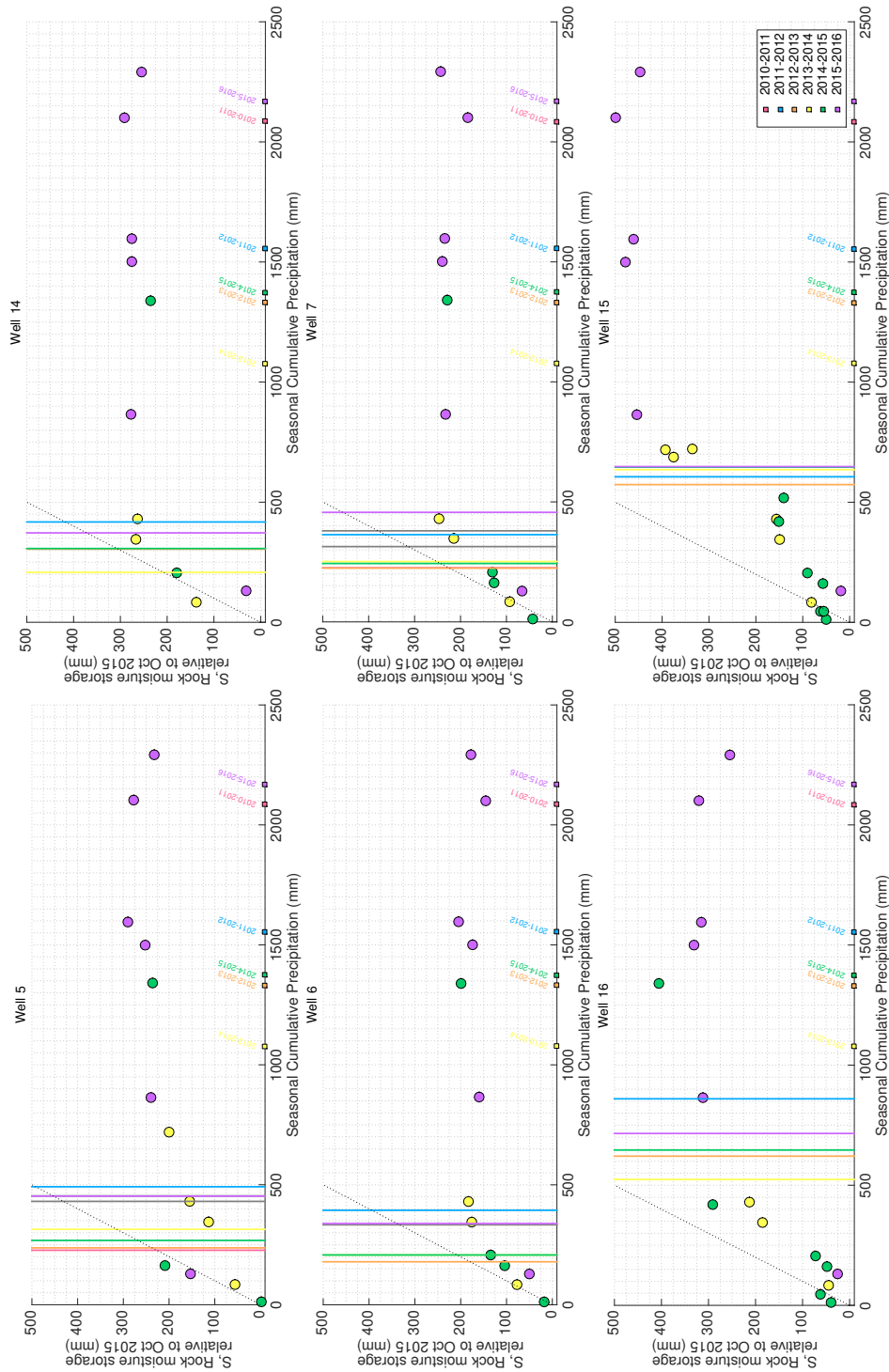
Figure 5.15: **Rock moisture storage throughout the wet season:** Rock moisture storage, S, in the upper 10 m (colored circles) is plotted against seasonal cumulative precipitation at the time of the survey. Vertical lines reflect the timing of the initial response of the groundwater table. Squares aligned along the x-axis represent the total cumulative seasonal precipitation in a given year. Color of circles, squares, and lines represents the year of data collection (shown in legend). The dashed line is the 1:1 line.
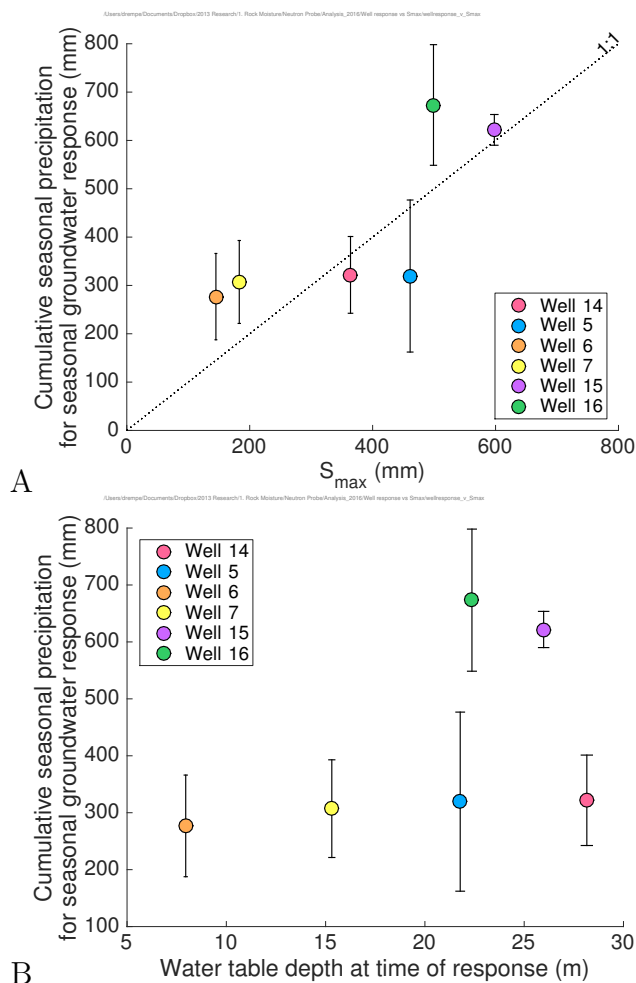
Figure 5.16: **Relationship between seasonal groundwater response seasonal change in rock moisture,** S_{max}**:** The amount of precipitation observed at the time of the seasonal groundwater response at a particular well is proportional to the volume of rock moisture storage (S_{max}) observed in that well (A) but does not correspond with the depth to groundwater table at the time of the seasonal response (B). The mean cumulative seasonal precipitation for response over 5 years of observation (shown as a solid horizontal bar in Figure 5.14) is plotted and the error bars represent one standard deviation (shown as a dashed horizontal bars in Figure 5.14) . The mean depth of the groundwater table at the time of response over all years of observation is shown in (B) and varies at most by 1.5 m (at Well 16). S_{max} accounts for the entire profile. Well 12 is excluded because the groundwater response is strongly tied to streamflow. Wells 2 and 13 are excluded because the water level falls beyond the depth of the well.
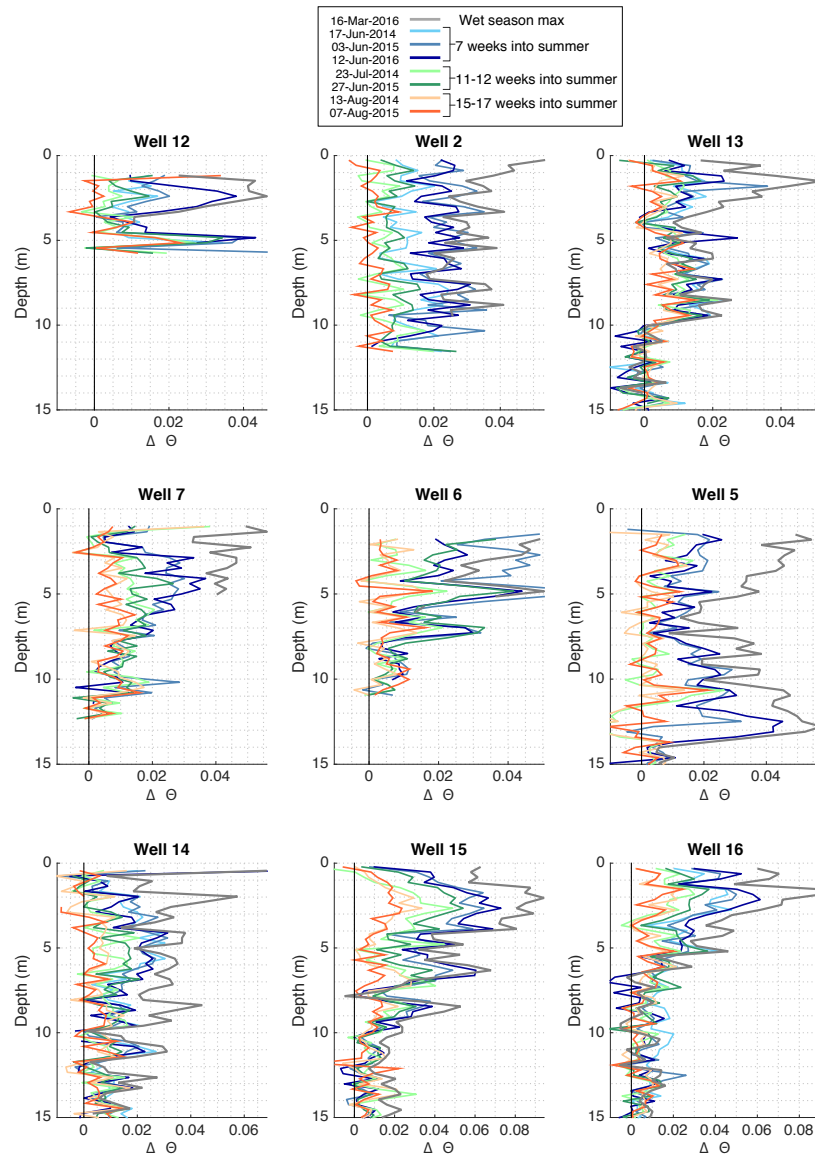
Figure 5.17: **Dry season rock moisture depletion:** The change in moisture content, $\Delta\theta$, in the top 15 m is shown for surveys conducted in the summers of 2014, 2015, and 2016 (see Table 5.3). Different hues of the same color represent measurements from different years taken approximately the same time after the final wet season storm. Grey represents the wettest measurement (March 2016). Blue, green, and orange reprsent 7, 12, and 15 weeks into the summer respectively.Despite large differences in the seasonal cumulative precipitation each year (Table 5.5), the pattern of rock moisture depletion throughout the summer is relatively consistent year to year.
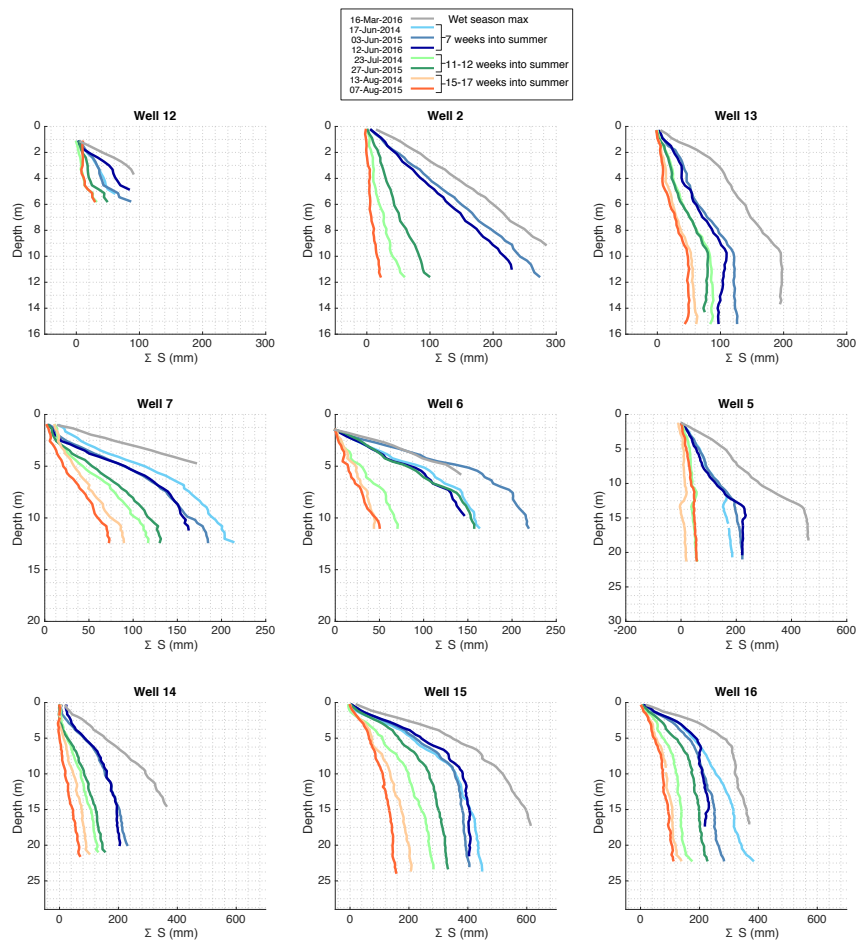
Figure 5.18: Dry season rock moisture storage: The depth-cumulative rock moisture storage, ΣS, is shown for surveys conducted in the summers of 2014, 2015, and 2016. Different years are represented by different hues of the same color and color represents similar elapsed time from the start of summer. Grey represents the wettest measurement. Blue, green, and orange reprsent 7, 12, and 15 weeks into the summer respectively. ΣS is defined as the amount of water stored as rock moisture relative to Oct 2015 at or above a particular depth. Note that the upper part of the profile in Wells 12, 5, 6, 7, and 14 was not monitored, therefore these depths are not accounted for in the calculation of cumulative storage throughout the profile.
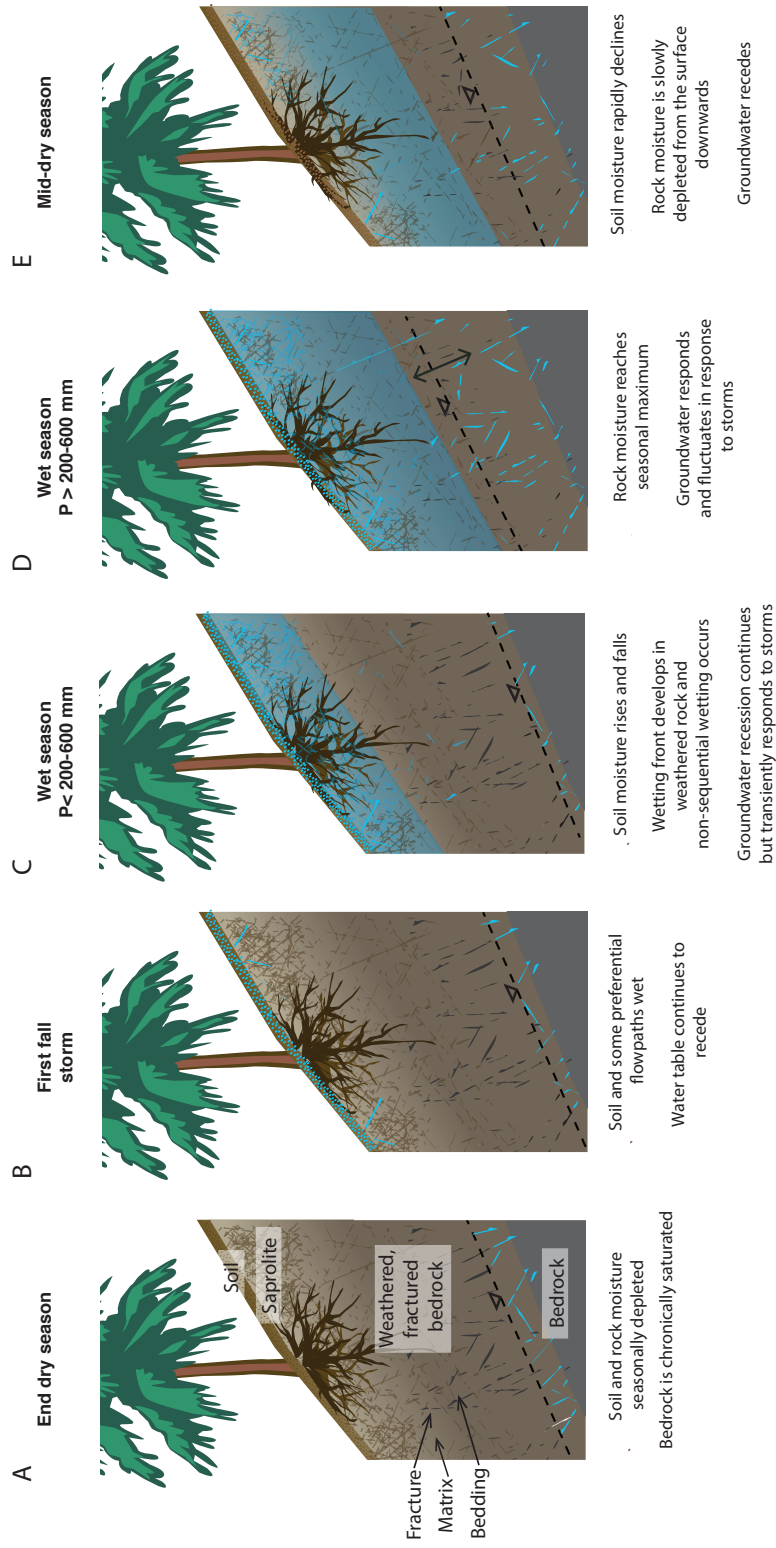
Figure 5.19: **Conceptual model for a seasonal rock moisture cycle:** The addition and depletion of soil moisture, rock moisture, and groundwater is shown throughout the year.
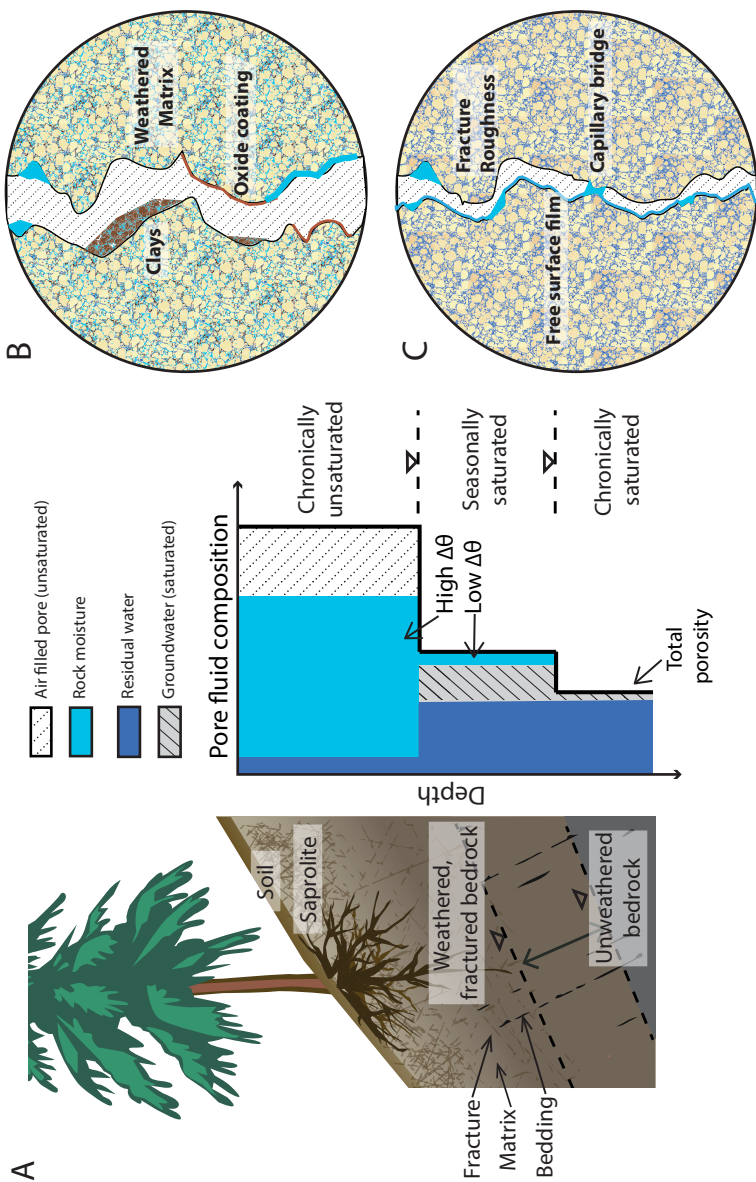
Figure 5.20: **Conceptual model of rock moisture storage mechanisms:** (A) One dimensional hillslope weathering profile and corresponding profile of rock moisture. Solid black line represents the total porosity and colors (described in legend) represent the composition of the pore fluid. Rock moisture changes (light blue) are greatest in the chronically unsaturated zone. In the seasonally saturated zone, less rock moisture is exchanged and larger proportion of the porosity is comprised of water that is not exchanged seasonally. The lowest porosity occurs within the chronically saturated zone and very little water is exchanged. Hypothesized rock moisture storage reservoirs are shown in A and B. (B) In the "high $\Delta\theta$" zone, rock moisture is held in the interconnected pores of weathered matrix blocks, clay weathering products within fractures, and along fractures including within oxide coatings. (C) In the "low $\Delta\theta$" zone, matrix blocks are chronically saturated and fractures are seasonally saturated. When fractures are unsaturated, rock moisture is held within roughness features along fractures, as a capillary bridge between fractures, and as a free surface film.
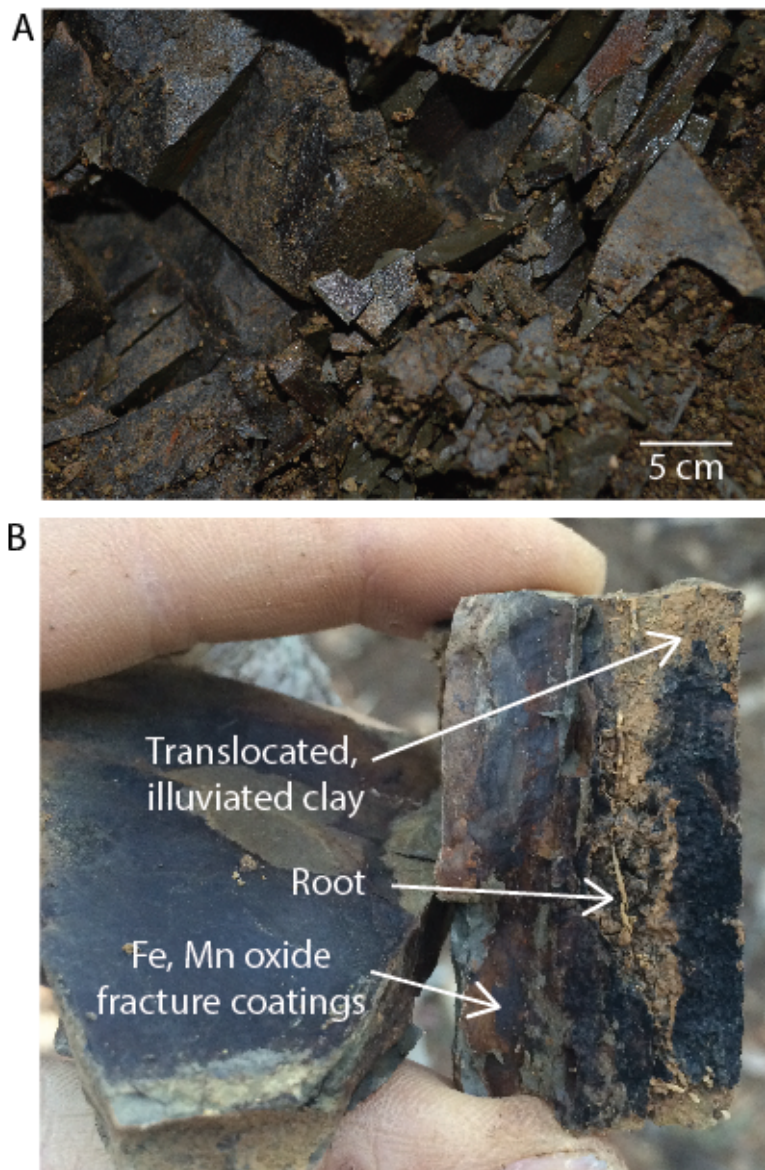
Figure 5.21: (A) Photograph of 3.5 m pervasively fractured trench face where, upon excavation, rock moisture storage was observed along fractures and within granular material occupying fractures. The saturation state of the rock matrix was not evaluated. (B) Components of the rock moisture storage observed to occur within and along fractures.
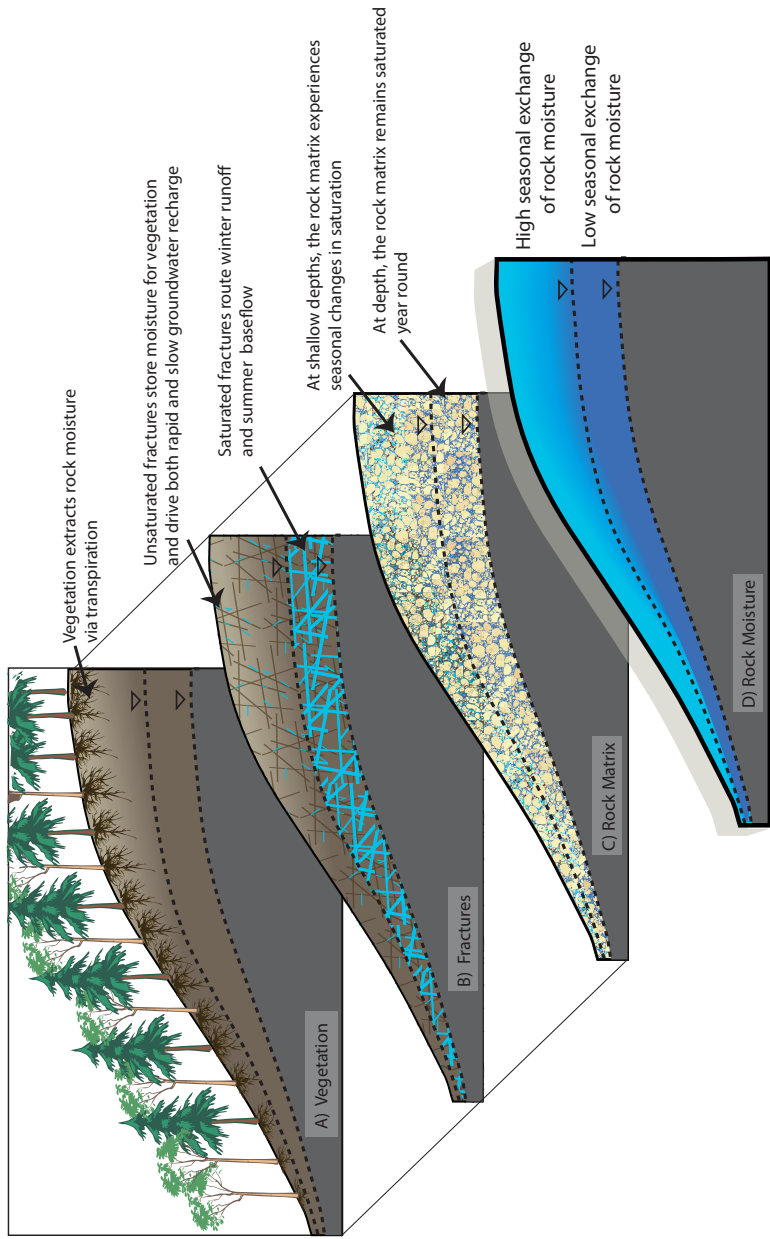
Figure 5.22: **Conceptual model for the structure of rock moisture across a hillslope:** The interplay between vegetation and weathering lead to a structure of rock moisture storage across the hillslope that influences critical zone processes. Rock moisture dynamics are greatest in the near surface where roots extract moisture (A), unsaturated fractures generate rapid and slow recharge (B), and the rock matrix is weathered(C). At depth, rock moisture changes are minimal because water is primarily routed through few but conductive fractures that generate rapid runoff during the wet season and baseflow during the dry summers (B).

Bibliography

[1] S.P. Anderson, W.E. Dietrich, and G.H. Brimhall. Weathering profiles, mass-balance analysis, and rates of solute loss: Linkages between weathering and erosion in a small, steep catchment. *Geological Society of America Bulletin*, 114(9):1143, 2002.

[2] Suzanne Prestrud Anderson, William E Dietrich, David R Montgomery, et al. Subsurface flow paths in a steep, unchanneled catchment. *Water Resources Research*, 33(12):2637–2653, 1997.

[3] Yuko Asano, Taro Uchida, and Nobuhito Ohte. Residence times and flow paths of water in steep unchannelled catchments, Tanakami, Japan. *Journal of Hydrology*, 261(1):173–192, 2002.

[4] E.W. Banks, C.T. Simmons, A.J. Love, et al. Fractured bedrock and saprolite hydrogeologic controls on groundwater/surface-water interaction: a conceptual model (Australia). *Hydrogeology Journal*, 17(8):1969–1989, 2009.

[5] M Blumstock, D Tetzlaff, IA Malcolm, G Nuetzmann, and C Soulsby. Baseflow dynamics: Multi-tracer surveys to assess variable groundwater contributions to montane streams under low flows. *Journal of Hydrology*, 527:1021–1033, 2015.

[6] Michael Bonell. Progress in the understanding of runoff generation dynamics in forests. *Journal of Hydrology*, 150(2-4):217–275, 1993.

[7] Susan L Brantley, Molly E Holleran, Lixin Jin, and Ekaterina Bazilevskaya. Probing deep weathering in the Shale Hills Critical Zone Observatory, Pennsylvania (USA): the hypothesis of nested chemical reaction fronts in the subsurface. *Earth Surface Processes and Landforms*, 38(11):1280–1298, 2013.

[8] J. Büdel. Double surfaces of leveling in the humid tropics. *Zeitschrift für Geomorphologie*, 1:223–225, 1957.

[9] J St Clair, S Moon, WS Holbrook, et al. Geophysical imaging reveals topographic stress control of bedrock weathering. *Science*, 350(6260):534–538, 2015.

[10] B.A. Ebel, K. Loague, D.R. Montgomery, and W.E. Dietrich. Physics-based continuous simulation of long-term near-surface hydrologic response for the Coos Bay experimental catchment. *Water Resources Research*, 44(7):W07417, 2008.

[11] National Science Foundation. National Science Foundation, Program solicitation 12-575. 2012.

[12] Marty D Frisbee, Fred M Phillips, Andrew R Campbell, Fengjing Liu, and Steve A Sanchez. Streamflow generation in a large, alpine watershed in the southern Rocky Mountains of Colorado: Is streamflow generation simply the aggregation of hillslope runoff responses? *Water Resources Research*, 47(6), 2011.

[13] V Cody Hale, Jeffrey J McDonnell, Michael K Stewart, et al. Effect of bedrock permeability on stream base flow mean transit time scaling relationships: 2. Process study of storage and release. *Water Resources Research*, 2016.

[14] Atul H Haria and Paul Shand. Evidence for deep sub-surface flow routing in forested upland Wales: implications for contaminant transport and stream flow generation. *Hydrology and Earth System Sciences Discussions*, 8(3):334–344, 2004.

[15] Shin'ya Katsura, Ken'ichirou Kosugi, Tasuku Mizutani, Suemi Okunaka, and Takahisa Mizuyama. Effects of bedrock groundwater on spatial and temporal variations in soil mantle groundwater in a steep granitic headwater catchment. *Water Resources Research*, 44(9):n/a–n/a, September 2008.

[16] M Katsuyama, M Tani, and S Nishimoto. Connection between streamwater mean residence time and bedrock groundwater recharge/discharge dynamics in weathered granite catchments. *Hydrological Processes*, 24(16):2287–2299, 2010.

[17] K Kosugi, M Fujimoto, S Katsura, and H Kato. Localized bedrock aquifer distribution explains discharge from a headwater catchment. *Water Resources . . .*, 2011.

[18] Ken'ichirou Kosugi, Shin'ya Katsura, Masanori Katsuyama, and Takahisa Mizuyama. Water flow processes in weathered granitic bedrock and their effects on runoff generation in a small headwater catchment. *Water Resources Research*, 42(2):n/a–n/a, February 2006.

[19] Cédric Legout, Jérome Molenat, Luc Aquilina, et al. Solute transfer in the unsaturated zone-groundwater continuum of a headwater catchment. *Journal of Hydrology*, 332(3):427–441, 2007.

[20] Andrew H Manning and Jonathan Saul Caine. Groundwater noble gas, age, and temperature signatures in an Alpine watershed: Valuable tools in conceptual model development. *Water resources research*, 43(4), 2007.

[21] Jean-Christophe Maréchal, Murari RR Varma, Jean Riotte, et al. Indirect and direct recharges in a tropical forested watershed: Mule Hole, India. *Journal of Hydrology*, 364(3):272–284, 2009.

[22] MJ Pavich. Regolith residence time and the concept of surface age of the Piedmont "peneplain". *Geomorphology*, 2(1):181–196, 1989.

[23] Shengwen Qi, Zhong Qi Yue, Faquan Wu, and Zhonghua Chang. Deep weathering of a group of thick argillaceous limestone rocks near Three Gorges Reservoir, Central China. *International Journal of Rock Mechanics and Mining Sciences*, 46(5):929–939, 2009.

[24] Laura K Rademacher, Jordan F Clark, David W Clow, and G Bryant Hudson. Old groundwater influence on stream hydrochemistry and catchment response times in a small Sierra Nevada catchment: Sagehen Creek, California. *Water resources research*, 41(2), 2005.

[25] Craig Rasmussen, Peter A Troch, Jon Chorover, et al. An open system framework for integrating critical zone structure and function. *Biogeochemistry*, 102(1-3):15–29, 2011.

[26] Daniella M Rempe and William E Dietrich. A bottom-up control on fresh-bedrock topography under landscapes. *Proceedings of the National Academy of Sciences*, 111(18):6576–6581, 2014.

[27] B.P. Ruxton and L. Berry. Weathering of granite and associated erosional features in Hong Kong. *Geological Society of America Bulletin*, 68(10):1263–1292, 1957.

[28] C Soulsby, D Tetzlaff, N Van den Bedem, et al. Inferring groundwater influences on surface water in montane catchments from hydrochemical surveys of springs and streamwaters. *Journal of Hydrology*, 333(2):199–213, 2007.

[29] Peter Troch, Emiel Van Loon, and Arno Hilberts. Analytical solutions to a hillslope-storage kinematic wave equation for subsurface flow. *Advances in Water Resources*, 25(6):637–649, 2002.

[30] Peter A Troch, Claudio Paniconi, and E Emiel van Loon. Hillslope-storage Boussinesq model for subsurface flow and variable source areas along complex hillslopes: 1. Formulation and characteristic response. *Water Resources Research*, 39(11), 2003.

[31] CJ Wilson and WE Dietrich. The contribution of bedrock groundwater flow to storm runoff and high pore pressure development in hollows. *IAHS-AISH publication*, (165):49–59, 1987.

Chapter 6

Runoff generation

6.1 Introduction

In this chapter, we focus on the response of the groundwater system to rainfall and its variability across an upslope thickening weathering profile. In previous chapters we identified that the hydrologic dynamics within the Rivendell hillslope are controlled by the development of a thick (up to 25 m) weathering front into fractured bedrock. An increasing number of hydrologic investigations in uplands landscapes are reporting a large fraction of runoff originating from fractured bedrock (e.g. Onda, 2001, 2006, Banks et al., 2009), however, there is no established framework for identifying what attributes of a particular landscape (i.e. lithology, tectonic history, climate) can be used to predict how water may be partitioned between shallow and deep or rapid and slow flowpaths. Further, there are few observations of temporal dynamics of fractured bedrock runoff generation to contribute to an understanding of how the structure of the critical zone influences the timing of runoff. Observations are needed to constrain models that are used to predict a variety of processes that depend on how runoff is routed including stream temperature for aquatic ecosystems, reactive transport of solutes used to quantify rates of weathering, and the influence of landuse changes such as shifts in vegetation or retention dams on streamflow. Here, we seek to connect observations of critical zone structure to the hydrologic response observed in a steep, deeply weathered hillslope in an effort to identify the salient behaviors that may be generalizable to this and other landscapes where runoff through fractured bedrock occurs. We also seek to link our observations at Rivendell to those made in other steep hillslopes of similar lithology to understand what factors (e.g. climate, mineralogy) lead to different runoff mechanisms for similar rock types.

Groundwater monitoring at the Rivendell field site over 9 years shows that a seasonally perched water table forms within fractured rock above a boundary between weathered and unweathered rock. As shown in Chapter 5, incoming rainfall first drives up rock moisture. Once a storage capacity is reached additional incoming rain passes along fractures that transmit water to groundwater table perched on Zb, the fresh bedrock boundary. This groundwater build up then drives runoff. During the long dry summer, the groundwater system slowly drains. Here, I describe the wet season response of the groundwater system and the groundwater recession in detail and examine all of these observations (the seasonal response, the rapid response to storms, and the slow recession) in the context of the critical zone structure, i.e. across the hillslope from channel boundary condition to groundwater divide.

6.2 Results

Wet season groundwater response to rainfall

The timing and magnitude of the groundwater response to individual storms is highly variable in space and time. Here I examine up to 50 individual storm-response signals

over a 5-year period (2008-2012) at each well. Table 6.1 summarizes the observations and Figures 6.1-6.7 show the spatial and temporal pattern of groundwater response. Wells 1 and 12 are included in this analysis, although their response is likely driven by water level dynamics of nearby Elder Creek. The mean lag to peak (lag between the centroid of the storm precipitation and the peak groundwater response) falls between 22 and 31 hours for 7 of the 10 upslope wells. The three midslope wells drilled into the dirt road bed had distinctly longer lag times (39 to 70 hours) (Figure 6.1). The upslope most wells, Wells 15 and 16 displayed the least variance in lag, but also had the least number of distinctive storm signals to analyze. Surprisingly, the lag to peak does not increase with increasing critical zone thickness (and depth to the water table) (Figure 6.2).

Figure 6.2 shows the lag to peak as a function of the depth to the water table at each well. Surprisingly, the lag to peak does not increase with increasing critical zone thickness (and depth to the water table). The only well that shows a clear trend of lag with depth to the water table is Well 5, in which the lag increases with depth. Well 10 appears to have a relatively short lag at greatest depth, then a much greater lag at a shallower depth which then shortens with still greater rise to the surface. For the wells with a large number of storms analyzed, the variance in lag to peak approaches an order of magnitude at a given depth. Given that travel distance should influence the lag from rainfall to groundwater response, it is also surprising that there is no vertical pattern to the lag to peak values in nearly all the wells (Figure 6.3A).

The velocity of the peak response (Figure 6.4) varies by over an order of magnitude at a given depth. A weak trend towards faster mean velocities with greater depths is consistent with the lack of depth dependency in the lag to peak time. Figure 6.5 shows that at Wells 7 and 10 the lag to peak systematically increased by more than an order of magnitude as the wet season progressed. Five years are shown, and in each year the start of the wet season has a much shorter lag time than then the eventual end point. None of the other wells show this pattern. As indicated in Figure 6.2, this change is not a function of depth below the surface. Instead, for the same water table level, later in the season the lag to peak is greater than at the start of the wet season. Similarly, the time to initial response, defined as the time between initiation of precipitation and initation of well response, does not show a relationship with critical zone structure (i.e. depth of the water table or slope position) (Figure 6.3B). However, the time to initial response is generally shorter than the lag to peak.

The time to the initial response of the groundwater (measured as the time between the initiation of rainfall within a given storm and the initial groundwater rise) is plotted in Figure 6.6. This time to initial response also does not show a relationship with critical zone structure (i.e. depth of the water table or slope position) (Figure 6.3B). The time to intial response is generally shorter than the lag to peak.

The velocity of the initial response (measured as the distance to the water table divided by the time of initial response) is reported in Table 6.1 and plotted in Figure 6.4. The fastest initial response velocities occur within Wells 3, 6, 7 and 10, which lie along the subtle valley on the site, but there is no obvious pattern with critical zone structure i.e.

velocity is not proportional to depth of the water table. Figure 6.6 suggests that at three wells (3, 6, and 10) there may be a slight tendency for the timing of the initial response to decline with shallow depths to the water table, otherwise, similar to the lag to peak, there is no apparent velocity variation with depth below the surface for an individual well and for a given depth the variation in velocity between individual storms can exceed an order of magnitude (Figure 6.4). A comparison of the velocity of initial response and velocity of peak response (Figure 6.7) shows that in all wells, the velocity of the initial response is faster than the velocity of the peak response. In seven of the upslope wells the mean velocity of initial response is between 40 and 72 cm/hr (1.1 x 10^{-4} m/s to 2 x 10^{-4} m/s) for the other three the values are 126, 147 and 154 cm/hr.

The rapid response of the water table to storms, as indicated by the velocity of initial response, suggests that relatively small amount of recharge leads to a large water level response, and by implication, relatively small amount of porosity to fill to cause saturation. The total storm precipitation divided by the groundwater level rise that occurred during that storm provides a crude estimate of the fracture porosity, assuming that all precipitation reaches the groundwater during the time scale of the storm, all flow is vertical, and all saturation changes occur in unsaturated fractures. Though these assumptions are likely not valid (e.g. the steep hydraulic gradient drives lateral groundwater flow) this metric nonetheless indicates that there is variability in the amount of water needed to raise the water table by a given amount among and within wells. At Rivendell, on average, about 50 mm precipitation leads to a 1 m rise in water level (0.05 m/mm shown in Figure 6.8).There is no apparent pattern in the volume of water needed to raise the water table across the hillslope and all wells show that most storms generate a change in saturation of less than 10% (m of rain per m of groundwater rise) (Figure 6.8). Hence, these data suggest that in the seasonally saturated zone where groundwater levels are dynamic, there is about 5% porosity that is filled by storm recharge and then drained. In some wells that experience exceptional groundwater level increases of several meters per storm (e.g. Well 14), the precipitation needed to drive increases in the water table approaches 1% (Table 6.1).

Dry season recession of groundwater

Figures 6.9 and 6.10 show the temporal dynamics of the wells during the dry season recession. In Figure 6.9 the water level recession since the end of the final storm of the wet season is tied to the absolute elevation datum. Multiple years are shown. Figure 6.10A plots the drop in water level at each well that occurs in the final 60 days of the dry season (i.e. the 60 days before the first fall storms). These two plots demonstrate that over 4 years of groundwater monitoring there is relatively modest variation in successive years at individual wells in the seasonal groundwater table recession during the dry season. This occurs despite differences in seasonal cumulative precipitation and the timing of the final precipitation of the season. In Wells 1, 12, 15 and 16 (the wells at the base and at or near the ridge), water levels did progressively drop with each drier year. As

Figure 6.9 indicates, the well water level recession slopes are similar in successive years, hence the water table height at the start of the dry season and timing of the onset of the dry season should influence the water level differences in successive years. There is, nonetheless, significant variability in the pattern and timing of the groundwater recession over the early part of the dry season among wells that mostly likely reflects local critical zone properties or hydraulic conductivity structure. For example, W14 and W16, drain in the initial 2 weeks of the summer, while W15, W7 and W5 drain steadily throughout the dry season (Figure 6.10A). Despite differences in early dry season groundwater recession, groundwater levels drop between 0 and 1.7 m over the final 60 days of the summer and this observation is fairly consistent year to year within each well.

The gradual recession of the well water levels records the hillslope groundwater drainage that sustains summer baseflow in Elder Creek. Between 2009 and 2015, runoff in Elder Creek over the summer ranged from 14-58 mm (1-7% of the total runoff, 0.1 to 0.4 mm/d) (Table 5.5). This runoff linearly increased with the magnitude of the final 30 days of precipitation ($R^2 = 0.45$), but showed no correlation with annual precipitation. Total late summer runoff (last 60 days of summer prior to the first storm of the following wet season) varied from 5 to 17 mm. Only 5 to 6 mm of runoff occurred during this period in 2012-2014. In wells upslope from the toe of the slope (i.e. excluding Wells 1 and 12), groundwater levels continue to recede for a few months after the initiation of the wet season rains. Even in 2014, following a dry year (less than half mean annual precipitation) and long summer (140 days), Elder Creek remained flowing, supporting salmon populations as the groundwater slowly drained from the hillslope, and continued to recede even after the arrival of small fall storms.

Figure 6.10B shows an estimate of groundwater contribution to baseflow. The volume of baseflow was calculated, at each well, by multiplying the change in groundwater level observed in the last 60 days of summer by an estimate of porosity. We choose a porosity of 5%, as described above. Using the water table drop and a porosity of 5%, we arrive at groundwater estimates of baseflow from less than 5 mm to over 60 mm (6.10B) that are consistent in each well in different years. Elder Creek runoff over the final 60 days of the dry season (5-6 mm) is less than an estimate of the groundwater contribution to baseflow, which ranges from 5 to 50 mm among wells.

The groundwater response across the hillslope

Figure 6.11 places these vertical dynamics observed in individual wells in a longitudinal context. Here Elder Creek discharge is plotted as a function of well water level at locations along the hillslope from near the channel to the ridge. The very strong correlation at Well 1 is likely driven by the hydraulic connection between the creek and the well, i.e. the Elder Creek is immediately adjacent to Well 1 and influences water level there. Well 3 shows that at low flow Elder Creek discharge may rise and fall by over an order of magnitude independently of Well 3 water level. As Elder Creek discharge rises, however, the high level in Well 3 corresponds to high Elder Creek discharge. Some points lie below the

cluster of data suggesting that occasionally Elder Creek discharge declines more rapidly that does the water level in the well. At Well 10 the dissociation between Elder Creek discharge and water level in the well is even greater. At relatively low water levels the Elder Creek discharge can reach its full range of discharge variation. The well level and discharge are unrelated in time. The correlation improves at highest water level but less so than at Well 3. In contrast, at the divide, i.e. Well 15, there is no relationship between Elder Creek stream flow and well water level. These data imply that generally the smaller rainfall-runoff events are driven by the rapid groundwater dynamics of the lower portion of the hillslope. The effective contributing area for a given storm then must spread upslope through the winter. Despite the response time to storms in the groundwater being similar across the hillslope (Figure 6.3), the number of storm events that generate a corresponding well response declines upslope, hence the spreading dissociation of groundwater and runoff data in Figure 6.11

The seasonal disassociation of upslope groundwater from dynamics at the base of the slope is illustrated by Figure 6.12A which compares streamflow (shown as Elder Creek stage), the groundwater response at the base of the hillslope (Wells 12 and 1), and groundwater at the drainage divide (Well 15). The stage in Elder Creek can rise and fall over the course of several storms before the groundwater level at the ridge rises (Figure 6.12B). At the conclusion of the wet season, discharge and groundwater levels at the base of the slope recede while Well 15 continues to rise in the initial part of the dry season (Figure 6.12C). Figures 6.13 and 6.14 show the groundwater response and cumulative seasonal precipitation in all wells across the slope except for Well 3 which had inexplicable electronic noise during significant parts of the monitoring period, and Wells 2 and 13 which are dry for much of the year. The groundwater response at Well 15 generally shows a more diffuse response to the arrival of the wet season than wells located across the hillslope. Groundwater levels in Wells 15 and 16 are more strongly influenced by the magnitude of seasonal precipitation than downslope wells. Well 15 continues to recede after the arrival of rain as other wells respond seasonally (Figure 6.14). These plots further support the interpretation that storm runoff in Elder Creek may be driven by groundwater dynamics in the downslope portion of the hillslope, especially during the early part of the wet season.

The 12 wells allow us to construct, crudely, contour maps of the groundwater surface under the hillslope. To do this we select specific days through the season, use natural neighbor interpolation (Matlab, R2015) to contour groundwater elevations. Although there are only three wells in the upper part of the hillslope, a relatively simple topographic surface is revealed by this procedure. Figure 6.15 shows a colorized 5 m interval contour map of the groundwater table near the end of the dry season (Sept 26, 2011) and after winter rains when water levels are high (March 30, 2012). In both cases, from Well 10 down to the base of the hillslope the contours define a smoothly varying surface. This surface however is not oriented the same direction as the surface topography. Instead the mean trend of the surface is oriented about 35 degrees relative to the mean trend of the surface topography. This orientation difference matches the shorter travel distance

to Elder Creek for some wells and for others the distance along this path is about the same as following the surface topography. The wet season surface topography is steeper in the lower ½ of the slope (due to significant groundwater rise relative to the base of the hillslope) and suggests a pattern of flow convergence close to the side of the mapped field. These maps also imply a different flow path and relative contributing area associated with each well. Specifically the upslope contributing area that would drain past wells 1 and 12 is relatively limited and originates on the sandstone ridge. If groundwater does follow the gradient of the water table, water at Well 6 would flow towards Well 5 and then Well 13. This is a very different path if we relied only on the ground surface topography. That topography would suggest water at Well 6 would drain towards to Well 3 and 1. Well 10 flow path according to the groundwater topography is even more divergent from the ground surface topographic maximum fall path.

The series of profiles presented in Figure 4.1 put the groundwater response in the context of the chronically unsaturated zone, the seasonally saturated zone and the chronically saturated zone shown. It is the dynamics of the seasonal saturated zone that sets the lower and upper bound of the other two zones. Figure 4.1 defines the range of the seasonally saturated zone (the light blue) and shows the relative percent of time the water table spends at the various heights within the seasonally saturated zone (darker blue horizontal bars on the light blue background). Note that in most of the wells the darker blue tone bars approach the vertical boundary well below the top of the light blue box, implying that there are just a few short lived events that shoot up to the shallow heights indicated by the upper level of the blue box. The shapes of the groundwater hydrographs shown in Figure 6.13 and 6.14 show this characteristic of the seasonally saturated zone: rain events are marked by sharp rises, but rapid decline once rainfall diminishes. The slope of the water table recession after storms is steepest when the water table is elevated. In some wells (e.g. Well 5, Well 6, and Well 12), the recession of the water table progressively slows in time, while other wells show abrupt and consistent changes in the slope of the recession in time. Regions within the seasonally saturated zone where the water table recession slows may be associated with hydraulic conductivity barriers or sources of lateral flow.

6.3   Discussion

Though many hillslope runoff studies have inferred that flow through fractured bedrock occurs at the event (e.g.. Wilson and Dietrich, 1987, Mulholland, 1993 Montgomery et al. 1997) and seasonal (e.g. Stewart et al., 2007) timescale, few have documented its occurrence directly (e.g. Banks et al., 2009, Haria and Shand, 2006) or identified the role that the development and structure of a weathering front plays on the hillslope scale hydrologic response (e.g. Anderson et al., 1995, Montgomery et al., 2002), particularly in a water-limited seasonally dry environment. Here I present, for the first time, documentation of a critical zone structure across a hillslope that directly influences the magnitude

and timing of runoff through weathered bedrock.

The hydrologic response of shales and the development of the critical zone

Runoff through fractured bedrock is not unique to shales and is common in a variety of rock types including granites (e.g. Legout et al., 2007, Kosugi et al. 2008, Katsuyama et al. 2011, Uchida and Asano, 2010), volcanic rocks (e.g. Iwagami et al., 2010, Hale and McDonnell, 2016) and metamorphic rocks (Marechal et al., 2009). Shale (here used as a general term for clay rich rock, which include the argillites that dominate our study site) comprises approximately 25-34% of the terrestrial surface (Amiotte-Suchet et al., 2003, Durr and Meybeck, 2005) and surprisingly, can be highly conductive in the near surface despite its extremely low hydraulic conductivity at depth. At our site, soils and weathered rock are sufficiently conductive to accommodate the observed rainfall intensities, which are generally below 4.5 mm/hr ($1e^{-6}$ m/s), without generating overland flow or shallow subsurface stormflow through soils or saprolite. All runoff beyond rock moisture storage capacity enters the weathered fractured bedrock, where it perches above nearly impermeable bedrock and travels downslope, likely through a fracture network.

At other sites where runoff processes in shales have been investigated, a variety of runoff pathways have been identified and, though explicit weathering processes are not always directly investigated, runoff pathways are often linked to patterns of weathering. Near surface weathering, particularly in shales, can act to both reduce or enhance hydraulic conductivity and the controls on this remain unclear. For example, in a shale hillslope in Texas, thick cracking soils were observed to promote rapid seasonal recharge to a seasonal water table in fractured, conductive shale bedrock early in the wet season when cracks were open, and once cracks closed due to the wetting of the soil matrix, water was routed as overland flow (Allen et al., 2005). Additionally, occlusion of fractures by either translocated clay or clay weathering products formed in situ may reduce conductivity and promote lateral subsurface stormflow within saprolite (e.g. McKay et al., 2005). This is proposed to be a common condition in the extensively weathered piedmont of the Eastern U.S. (e.g. Tromp-van Meerveld et al., 2007). In a temperate shale hillslope in Australia, much of the runoff occurs through fractured bedrock but overland flow is frequently observed during intense rainfall events (Leaney et al., 1993, Banks et al., 2009). In first order catchments in shales across Japan, investigators have shown through hydrometric and geochemical means (e.g. Onda et al., 2001,), as well as direct drilling (e.g. Padilla et al., 2015), that, similar to our site, infiltrating rainfall transits soils and saprolite (and sometimes surface volcanic deposits) to generate storm runoff through the fractured shale bedrock. In central Pennsylvania, 15 m of fractured shale, despite underlying till in some places, drives most runoff (Gburek and Urban, 1990, Risser et al., 2009). In New Zealand, dating of streamflow and groundwater in a steep shale landscape suggested that over 87% of discharge originated from bedrock groundwater (the rest attributed to overland flow),

and travel through a thick, fractured unsaturated zone was inferred to delay the arrival of water by several years while also rapidly transmitting pressure signals that drive storm runoff.

This shows that a variety of hydrologic responses are observed in shales, at least within humid or seasonally dry landscapes, despite exhibiting roughly similar rock types. We also note, that owing to their depositional environment, shales, are often interbedded with coarser grained material of distinctly different hydraulic conductivity and this strong contrast leads to runoff patterns and topography unique to interbedded sedimentary rocks (e.g. Urban and Pasquarell,1992, Frisbee et al., 2016) that complicates our ability to quantify the role of rock type on runoff.

The diversity of hydrologic processes in hillslopes underlain by shale points to specific attributes of the shale that drives critical zone evolution. In the absence of clays or cracking soils, accumulation of groundwater occurs at the base of the weathering profile and promotes rapid runoff through fractures (e.g. Padilla et al., 2015, Molenat et al., 2011 Onda et al., 2005), while clay precipitation shallower in the profile tends to promote water storage or transient shallow subsurface stormflow (e.g. Travelletti et al., 2011, Banks et al., 2011). The location of weathering fronts (that can act as hydraulic conductivity interfaces) has be tied to the transport of fluids (O_2, CO_2, and H_2SO_4) and parent rock mineralogy (e.g. Brantley and Lebedeva, 2011, Brantley et al., in press). Sulfide minerals are prevalent in clay rich rocks and when exposed to oxygen generate acids that dissolve primary minerals leading to an expected relationship between oxygen transport and weathering front depth. Wetzel and Einsele (1991) showed that the pattern and rate of porosity formation in various shales may be predicted by initial porosity and organic matter content linking the eventual weathered state of the rock to the original composition. Parent mineralogy in shales can also be linked directly to the size distribution of clay weathering products and their ability to occlude both fractures and weathered matrix pores (Cumbie and McKay, 1998). Therefore the mineralogical properties that control conductivity as rock weathers may be measurable, in the parent material, which may permit us to predict runoff processes from parent mineralogy. Additionally, geotechnical and mining investigations, that tend to perturb the environment, have revealed how rapidly pyrite oxidation and sulfuric acid generation can alter hydraulic and mechanical properties of shale (sensu Hawkins 2014). Therefore, at the time scale of landscape evolution, initiation of porosity at the base of the weathering front might be considered instantaneous and governed by fluid transport entirely and thus easier to model.

Together, these observations suggest that a unifying theory for landscape evolution, weathering, and water storage in clay rich rocks may be developed that may even allow us to tease out the role of vegetation, climate, and tectonics. Additionally, recent studies of other lithologies including a diverse set of crystalline rocks have identified common porosity initiating reactions and controls on those reactions (e.g. biotite oxidation (Buss et al., 2006), carbonate dissolution (White et al., 2005; Williams et al., 2007) and plagioclase feldspar dissolution (Brantley and White, 2009; Behrens et al., 2015). These observations along with evidence that the propagation of reaction fronts in the subsurface is strongly

tied to fluid flow within the hillslope, suggest that theoretical frameworks for critical zone evolution may be extended across different rock types and that the study of both runoff (and water storage) and weathering processes together are needed to advance our understanding of how landscapes route water.

The intensive investigation of runoff processes in Coos Bay, Oregon, a steep hillslope underlain predominantly by sandstone, offers a unique opportunity to compare critical zone development and hydrologic processes (Anderson et al., 1995, Montgomery et al., 2002). Table 6.2 summarizes properties of each. Both Rivendell and Coos Bay are undoing active uplift and erosion, with lower erosion rates measured at Coos Bay (0.1mm/yr) compared to Rivendell 0.2 to 0.4 mm/yr) (Table 6.2). Both sites receive nearly the same mean annual rainfall. The Coos Bay hillslope, however, is steeper and shorter in length. At both sites the depth to fresh bedrock increases towards the divide, but the depth to Zb (the fresh bedrock boundary) at Coos Bay is only 9 m at the divide with most of the chemical weathering occurring within the first meter. The organic-rich soil that mantles the weathered bedrock at Coos Bay has a density less that 1.0 gm/cm3, is laced with root holes and large animal burrows, and has exceptionally high saturated hydraulic conductivity. Nonetheless, tracer tests demonstrate that rainfall passed through the soil as plug flow (not as preferential flow along the macroporosity) (Anderson et al., 1997). The underlying fractured bedrock is blocky, saprolite is thin to absent, and the fractures are highly conductive, but shallow. Rainfall passes through the soil as unsaturated flow, drains into the fractures, but downslope flow in the fractures locally exceeds the fracture storage and forces flow back to the soil. This exfiltrated water flows downslope a short distance and re-infiltrates into the fractured bedrock. Local exfiltration eventually caused the site to fail as a landslide in a major rainstorm (Montgomery et al., 2002). Montgomery et al. (1997) and Anderson et al found, through monitoring of the piezometric response to natural and artificial rainfall and geochemical tracing, that nearly all runoff is through the fractured bedrock. Torres et al (1998) showed that as the system became wet (experimental sprinkling was sustained long enough to generate steady state conditions), the water potential in the soil, groundwater, and streamflow became "delicately linked" such that a spike of rainfall caused a response in the groundwater and runoff much faster than would occur by fluid advection. They proposed this occurred via a pressure wave. No measurement of rock moisture was attempted at Coos Bay, but given the shallow, and relatively minor weathering of the rock, seasonal rock moisture storage may be much less. The weathered sandstone blocks, however, may contain more rock moisture than the argillite matrix blocks of Rivendell.

In a similar setting to Coos Bay, but a different field site (Needle Branch), Hale and McDonnell (2016), found similarly shallow fractured bedrock but observed active response of deep (30-35 m) fractured bedrock to rainfall during the wet season. Similar to Rivendell, they find that wells undergo some seasonal cycle of activation where they are unresponsive to storms early in the season, but eventually respond rapidly to rainfall. One of their wells located at a drainage divide, shows a more subdued and seasonal time scale response to rainfall (similar to Well 15 at Rivendell) as compared with other wells,

which fluctuate repeatedly in response to storms within the same dynamic range. They also find, similar to Rivendell, that water levels in wells drilled into fractured bedrock at the base of the hillslope mimic patterns of discharge in the stream. However, Hale and McDonnell (2016) find much smaller water table fluctuations (< 2 m) relative to those observed at Rivendell (which can exceed 10 m). Further, stable isotope and dating of groundwater and streamflow at Needle Branch lends support to the observations at Coos Bay, which show that much of the runoff originates from the near surface fractured layer. Despite geomorphic similarities between the Oregon Coast Range sites (Coos Bay and Needle Branch) and Rivendell within the Northern California Coast Range (Table 6.2), differences in critical zone structure (thickness and material properties) cause important differences in hydrologic (and thereby geochemical) processes.

Perched bedrock groundwater flow and surface topography in hilly and mountainous landscapes

Recent studies have explored the influence of heterogeneity in saturated conductivity associated with fractured weathered bedrock and concluded that bedrock groundwater flow direction can be predicted from surface-topography in mountainous landscapes (e.g. Welch et al., 2012). However, several field observations have proposed that topography may not be a sufficient predictor of groundwater behavior within a hillslope (e.g. Devito et al., 2005, Haught and van Meerveld, 2011, Penna et al., 2014, Western et al., 1999) and have suggested that soil thickness (Buttle et al., 2004), the topgoraphy of the soil-bedrock boundary (Freer et al., 2002; Tromp-van Meerveld and McDonnell, 2006), and structural features such as faulting (e.g. White and Burbey, 2007, Hutchinson and Moore, 2000) control hillslope groundwater flowpaths to a greater degree than surface topography. At Rivendell, the topography of the fresh bedrock surface, Zb, leads to groundwater flow that is generally downslope towards the channel, but oriented along the three dimensional Zb surface which diverges from topography. Interbasin flow (i.e. in this case, the discharge of hillslope groundwater in a channel other than the adjoining channel at the base of the hillslope) is not likely to be significant because groundwater accumulates seasonally within the hillslope and recedes to the nearly impermeable fresh bedrock surface which lines the channel. The connection between surface topography and the topography of the Zb surface is thus needed to predict groundwater flow paths.

Where hydraulic conductivity is documented in fractured bedrock, it is shown to decrease with depth (e.g., Davis and Turk, 1964, Snow, 1973, Tiedeman et al., 1998, Stober and Bucher, 2006, Jiang et al., 2009, Boutt et al., 2010). There is significant uncertainty, however, about how to represent this decrease in numerical models used to predict runoff in steep catchments (e.g. Welch and Allen, 2014). Scale dependent saturated conductivity measurements influence the prediction of unsaturated fluxes and water table fluctuations (Evans et al., 2001) that drive runoff in steep uplands. For example, Montgomery et al., (2002) found at Coos Bay that the near-surface fractured bedrock saturated conductivity,

through which all runoff occurred, displayed no depth dependence and varied by over five orders of magnitude. They associated this variance with variable intersection of conductive fractures with individual bore holes. In fractured media, it is not apparent that quantification of fracture attributes such as fracture density and aperture width yield information about saturated (e.g. Doughty and Karasaki, 2002) or unsaturated (e.g. Dahan et al., 2000) fluxes because, for example, only a fraction of fractures tend to actively conduct water (e.g. Liu et al., 1998). We suspect that, at our site, due to heterogeneity at a variety of scales and the dominance of fractures (potentially associated with bedding planes) in routing runoff, the explicit field quantification or characterization of conductivity may be a less useful metric for predicting runoff than an understanding of the vertical and lateral structure of the hillslope and the interplay between saturated and unsaturated dynamics. As our data show, hydrometric observations may yield insights into how to best parameterize flow in such complex systems.

One of the distinctive features of the site is, once rock moisture reaches its storage capacity, the rapid transformation of rainfall to runoff through a thick (up to 25 m) unsaturated zone. Salve et al., 2012, first proposed that runoff at Rivendell occurs primarily via fracture flow. This was based on documenting the first rains of each of three years that caused groundwater response well before the wetting front had advanced into the weathered bedrock. They also noted that the lower part of unsaturated weathered bedrock showed no moisture content change, even as storm runoff must have passed through this zone. In our study, analysis of the groundwater dynamics led to the surprising outcome that generally the response time is not strongly depth dependent. Lag to peak and lag to initial response show, in some wells, a tendency for increasing lag time with depth, but the variance at a given depth can approach an order of magnitude. The lag to peak and initial response velocities tend to be within an order of magnitude of 10^{-4} m/s, a value matching theoretical values proposed for fracture flow (Tokunaga and Wan, 2001). The lack of a simple linear increase in lag times with depth may point to antecedent moisture effects, variable fracture filling with rainfall intensity, and pressure wave contributions. The slower response for the lag to peak compared to the lag to initial response may record the delayed response caused by the necessity for the groundwater to rise up with filling pore space, as compared to simply responding.

Groundwater rises and falls in response to a storm in the seasonally saturated is not accompanied by significant rock moisture content changes in rock. The minimal rock moisture change associated with large magnitude water level fluctuations (up to11 m at Well 14) suggest that small changes in water content are needed to both saturate the fractured rock within the seasonally saturated zone and transport water to the saturated zone. Laboratory analysis of matrix blocks shows that the rock matrix at depth is likely chronically saturated, promoting the routing of infiltrating water in to fractures. Lysimeter extracted water and groundwater are distinctly isotopically heavier than the bulk water cryogenically extracted from the same location, suggesting exchange processes that might occur between matrix held water and fracture flow water do not control mobile water composition.

Vrettas and Fung (2015) developed a two parameter model to simulate runoff conditions at Rivendell that can be implemented at the spatial scale of global and regional climate models. Without explicitly modeling flow through fractures, Vrettas and Fung simulated the groundwater dynamics for 6 years of groundwater monitoring data from Well 1-Well 10, using Richard's equation and a novel stochastic representation of hydraulic conductivity that permitted rapid transport as unsaturated flow. Their parameterization perturbs a structure of declining conductivity with depth (tied to observed critical zone structure, rather than an arbitrary e-folding depth applied across the hillslope) and this perturbation of the conductivity structure, in effect, simulates preferential flow paths without explicitly accounting for their distribution or controls on transport within them. Their analysis shows that they could not produce the observed groundwater response using a standard dependence of hydraulic conductivity on saturation (using a Van Genuchten water retention parameterization), which is futher support that runoff occurs via preferential pathways (fractures). They also demonstrate that >80% saturation is needed to generate flow using standard water retention characteristics, which may describe the conditions we observe within the seasonally saturated zone. Using this stochastic representation of hydraulic conductivity, Vrettas and Fung (2015) use the observed precipitation and water table fluctuations to parameterize their model and derive an estimate of lateral flow that is transported downslope and becomes runoff. They also estimate a time series of unsaturated storage (i.e. sustained changes in saturation) that show that much of the incoming precipitation is stored within fractured rock, rather than soil, consistent with our observations. Their model, thus provides a means of predicting the contribution of hillslope groundwater to runoff, and the amount of water that may be seasonally stored, through a fracture dominated system without expressly accounting for fractures and their water retention properties. Future work is aimed at identifying the role of vegetation, through evapotranspiration, in influencing the temporal pattern of groundwater response and runoff. This approach permits the generalization of our observations to the scale of global climate models and the incorporation of fractured bedrock groundwater into global water cycle dynamics.

6.4   Summary of results

This chapter reports the groundwater dynamics at the Rivendell study site. The groundwater response to rainfall is quantified through analysis of storm hydrographs and and linked to the structure of the upslope thickening critical zone. In a previous chapter, I established that a gradient in the extent of weathering led to differences in the threshold seasonal precipitation needed to generate a seasonal groundwater response across the hillslope. Here, I show that leads to the lower portion of the hillslope contributing to storm runoff well before the upper part. Along the lower portion of the hillslope, the water table is highly responsive to storms and fluctuates seasonally within the same depth intervals. Upslope, the water table is responsive to many (but not all) individual storms

and the seasonal water table rise is proportional to the seasonal cumulative precipitation.

Surprisingly, we found that at all wells across the slope, the timing of the groundwater response to storms (once the rock moisture has reached typical storage capacity) does not show any significant relationship with slope position or dependence depth to the water table. The rapid initial response of groundwater to individual rainfall events during the wet season lies between 10^{-5} and 10^{-3} m/s, generally exceeds the lag to peak, and signifies that rapid transport, likely via a network of fractures, drives the groundwater response. Large (up to 11 m) rises in groundwater level are observed in response to individual storms, leading to an average 50 mm of rainfall per 1 m rise, suggesting that a very small volume of water is needed to transition the weathered bedrock from an unsaturated to saturated state.

During the dry season, the gradual recession of the water table in all wells follows the same pattern ever year, showing greater sensitivity to the magnitude of the final storm of the preceding season than the total seasonal precipitation. Evidence of progressive lowering of the seasonal low position of the water table is observed in wells at the base of the slope (1 and 12) and near the groundwater divide (15 and 16). The rapid response of the water table routes most precipitation as runoff during the wet season, while slow drainage of the seasonally perched water table over the dry season maintains baseflow in the channel network.

6.5 Tables

Well Number	Lag to Peak (hours)						Velocity of First Response (m/s)						Fracture Porosity Estimated from Cumulative Storm Precipitation and Water Level Rise		
	Mean	Median	Standard Deviation	Minimum	Maximum	Storms Analyzed	Mean	Median	Standard Deviation	Minimum	Maximum	Storms Analyzed	Mean	Standard Deviation	Storms Analyzed
1	14	12	8	5	36	50	1.6×10^{-4}	1.6×10^{-4}	2.0×10^{-4}	5.48×10^{-5}	1.2×10^{-3}	50	0.08	0.03	50
2	28	27	13	11	74	31	2.1×10^{-3}	2.1×10^{-3}	3.0×10^{-3}	3.5×10^{-5}	1.5×10^{-2}	49	0.11	0.11	30
3	25	22	14	2	59	40	1.1×10^{-3}	1.1×10^{-3}	3.0×10^{-3}	3.3×10^{-5}	1.5×10^{-2}	50	0.06	0.10	39
5	70	56	45	23	153	18	1.6×10^{-3}	1.6×10^{-3}	1.0×10^{-2}	8.8×10^{-5}	3.0×10^{-2}	25	0.03	0.02	17
6	49	36	33	2	125	30	1.4×10^{-3}	1.4×10^{-3}	6.0×10^{-3}	4.4×10^{-5}	3.0×10^{-2}	49	0.05	0.05	27
7	39	30	34	3	118	33	1.2×10^{-2}	1.2×10^{-2}	1.2×10^{-2}	4.9×10^{-5}	5.6×10^{-2}	44	0.06	0.06	28
10	31	21	31	3	107	35	1.4×10^{-4}	1.4×10^{-4}	5.0×10^{-4}	6.1×10^{-5}	2.6×10^{-3}	42	0.18	0.46	29
12	13	11	10	6	43	22	1.9×10^{-4}	1.9×10^{-4}	1.0×10^{-4}	6.2×10^{-5}	4.9×10^{-4}	26	0.06	0.03	22
13	22	17	12	11	43	10	3.4×10^{-4}	3.4×10^{-4}	1.0×10^{-4}	1.7×10^{-4}	4.2×10^{-4}	14	0.12	0.14	10
14	22	21	10	7	36	16	4.3×10^{-4}	4.3×10^{-4}	3.0×10^{-4}	2.0×10^{-4}	9.4×10^{-4}	16	0.01	0.01	16
15	23	19	10	16	44	12	4.1×10^{-4}	4.1×10^{-4}	1.0×10^{-3}	2.1×10^{-4}	5.0×10^{-4}	14	0.07	0.05	12
16	26	19	15	14	54	10	1.9×10^{-3}	1.9×10^{-3}	1.0×10^{-3}	1.2×10^{-3}	3.0×10^{-3}	10	0.10	0.12	10

Table 6.1: **Storm hydrograph analysis:** Storm hydrograph analysis results from 2009-2012 storms. Lag to peak is defined as the time from centroid of storm to peak well response. Velocity of initial response is defined as the distance to the water table at the start of storm divided by the time from initial precipitation to initial well response. Fracture porosity is estimated by dividing the water level rise by the cumulative storm precipitation.

Landscape attribute	Rivendell	Coos Bay
Mean annual precipitation	2000 mm	1900 mm
Annual runoff	1600-1800 mm	1300 mm
Vegetation	Mixed conifer and hardwood	Clear-cut conifer mixed with hardwoods
Lithology	Shale with sandstone interbeds	Fine-grained grewacke with shale interbeds
Structure of fresh bedrock	Vertical bedding, intensely sheared,fractures mostly closed	Anti-dip slope, close conjugate joints at depth
Hillslope gradient	30 degrees	43 degree for upper part 34 degree in including lower spring
Hillslope length	132 m	52 to 77 m
Channel incision/uplift rate	0.2 to 0.4 mm/yr	0.1 mm/yr
Residence time in weathered zone	~50,000-120,000 years, increasing upslope	~50,000 years
S_w (slope of fresh bedrock surface)	0.38	0.61
Soil	Loam, clay loam, or silty clay, up to 46% clay and organic matter content ranging from 4-9%	Bulk density of 0.8 gm/cc, Organic rich, silty sand, depth 0.5 to 1.4 (in hollow)

Table 6.2:   Comparison of climate, vegetation, lithology, and geomorphology in Coos Bay (Oregon) and Rivendell (California).

6.6 Figures
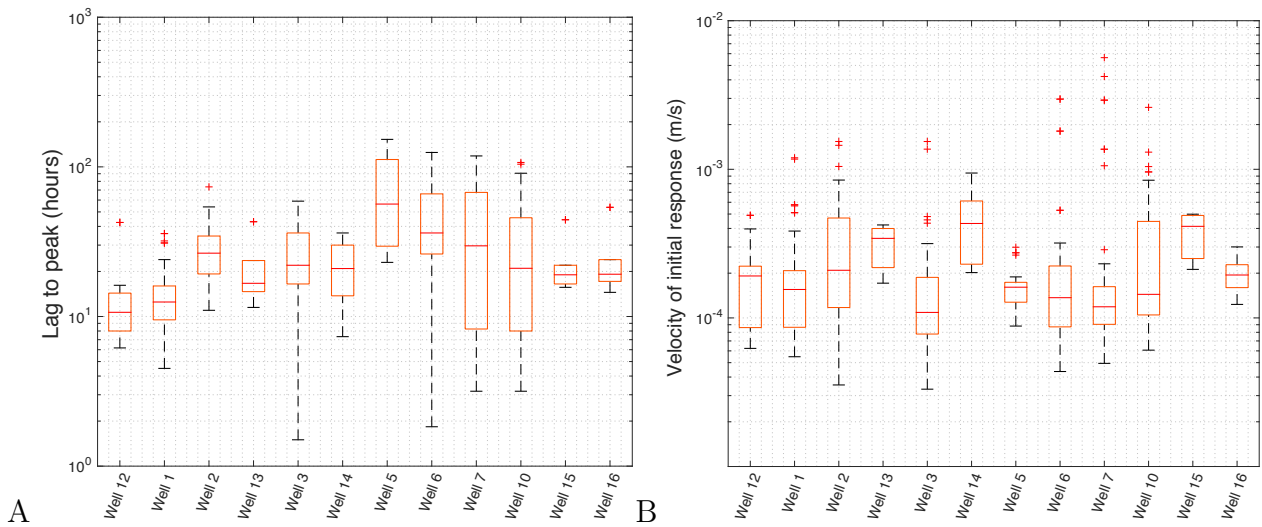
Figure 6.1: Lag to peak (A) and velocity of initial response (B) for storms between 2008-2012. Wells are positioned roughly in order of slope position (increasing wellhead elevation to the right). The box represents the interquartile range (25-75th percentile) with the median denoted by the line bisecting the box. Outliers are denoted by plus signs. Data are listed in Table 6.1.
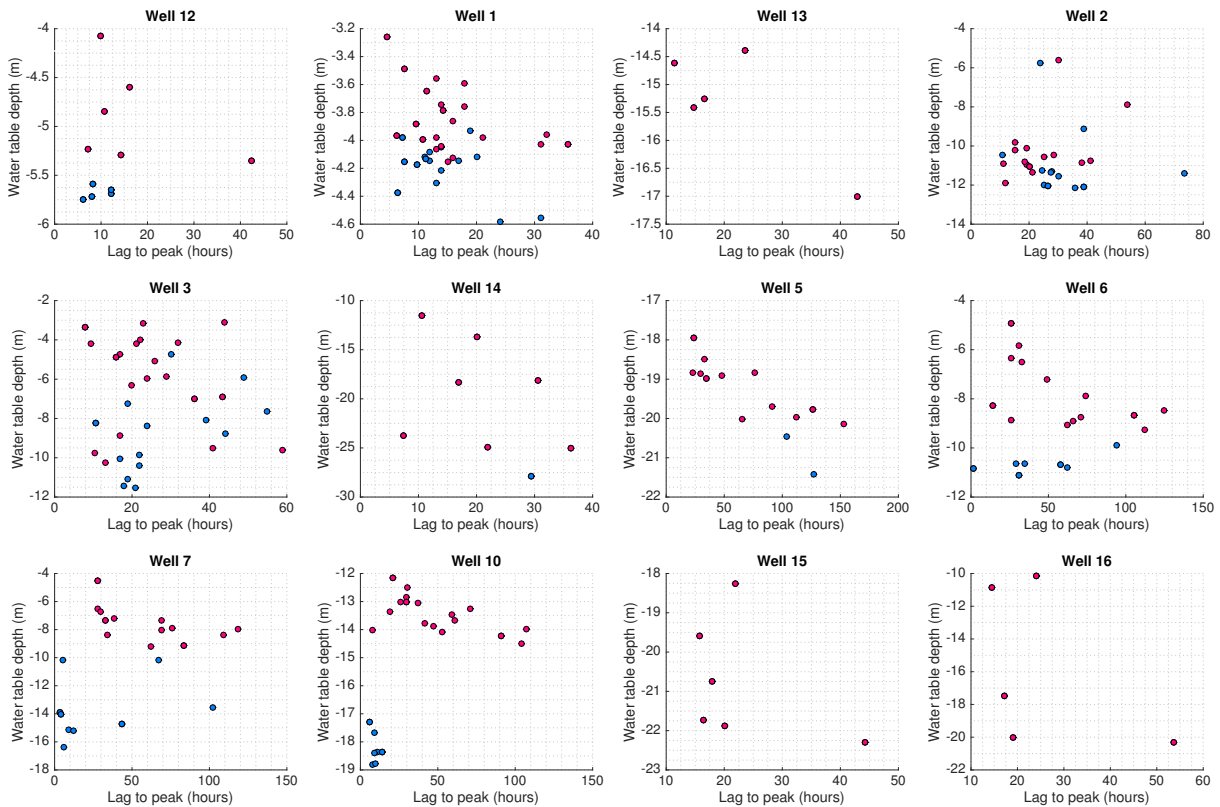
Figure 6.2: **Relationship between water table depth and lag to peak:** Lag to peak as a function of the water table depth observed at the time of initial response. Colors represent storms that occurred before (blue) and after (red) upslope wells (15 and 16) respond seasonally (typically at approximately 600 mm of seasonal cumulative precipitation).
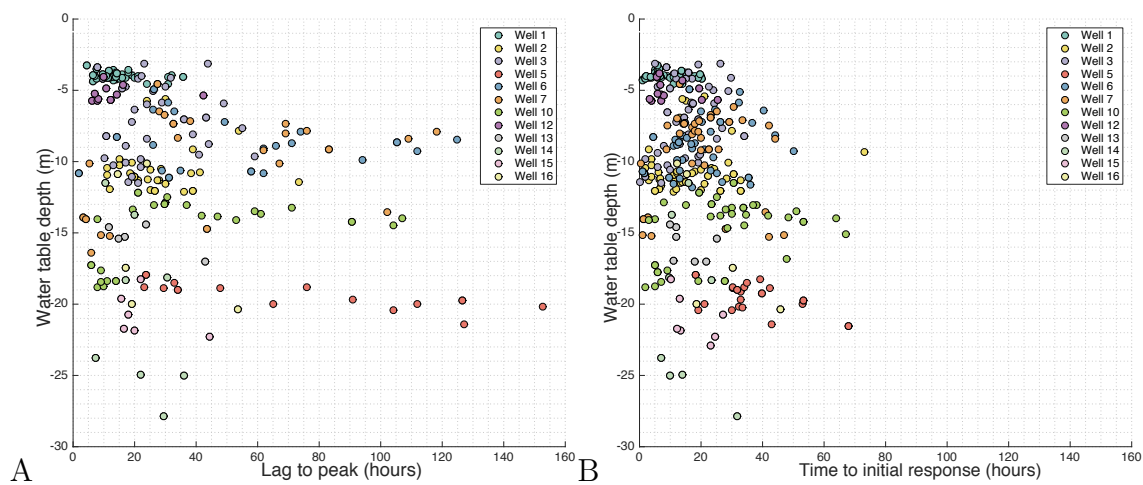
Figure 6.3: **Relationship between water table depth and timing of well response:** Timing of well response (lag to peak (A) and initial response (B)) is not strongly related to the distance to the water table (i.e. the depth of the water table).
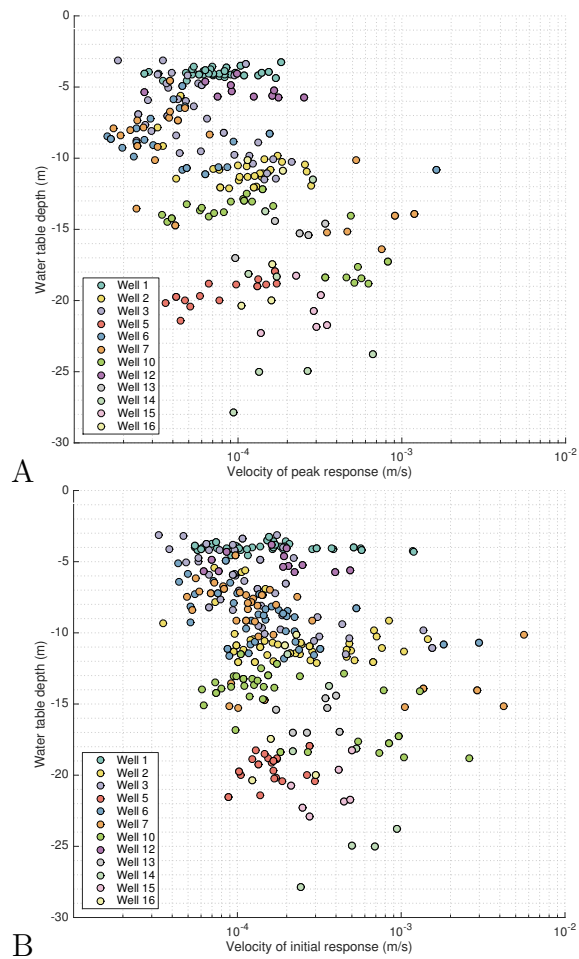
Figure 6.4: **Relationship between water table depth and velocity of well response:** The velocity of peak (A) and initial (B) response are not strongly related to the position of the water table.
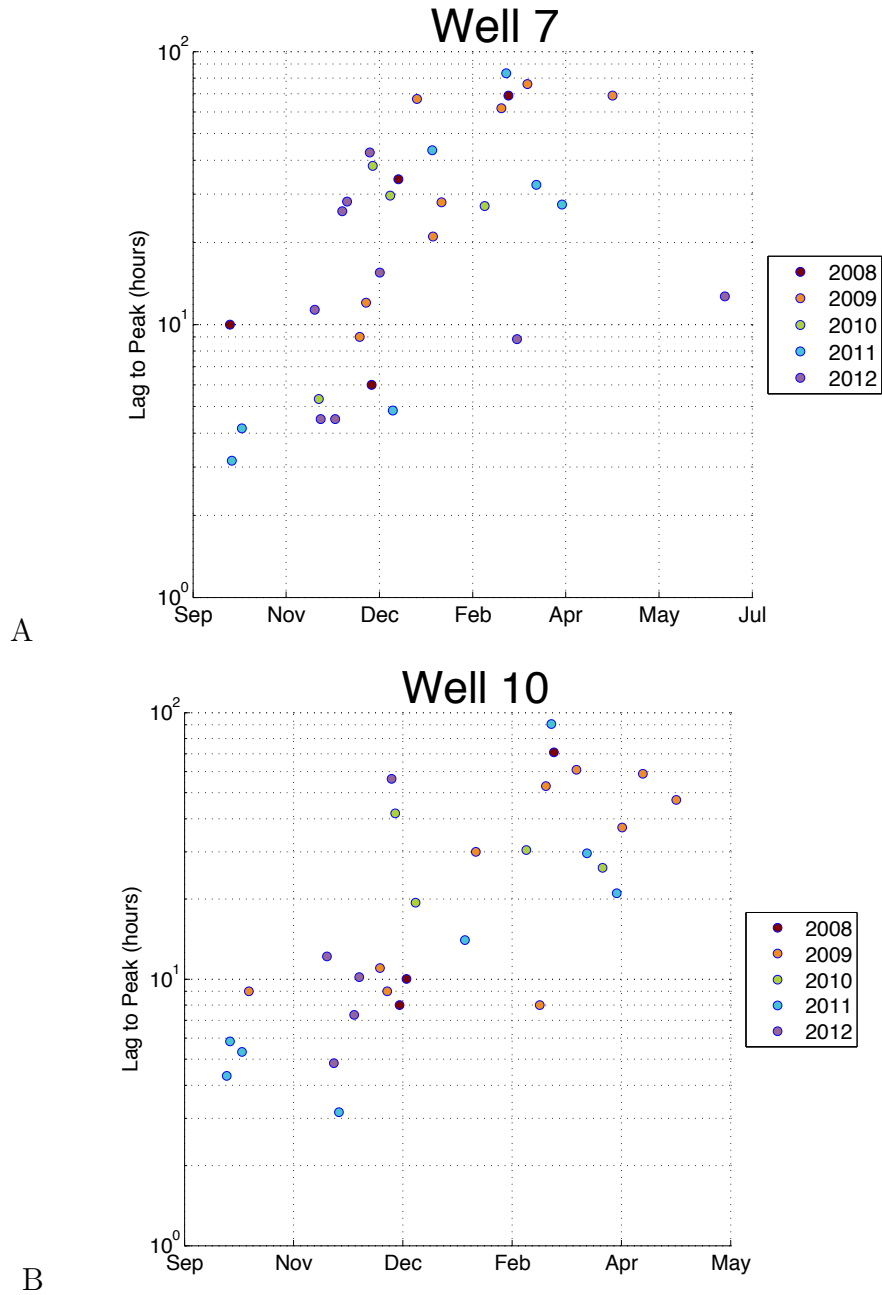
Figure 6.5: **Seasonal time series of lag to peak in Well 7 and Well 10:** In Well 7 and Well 10, the lag to peak increases throughout the wet season. In other wells, there is no apparent relationship between cumulative seasonal precipitation and the timing of the well response to storms.
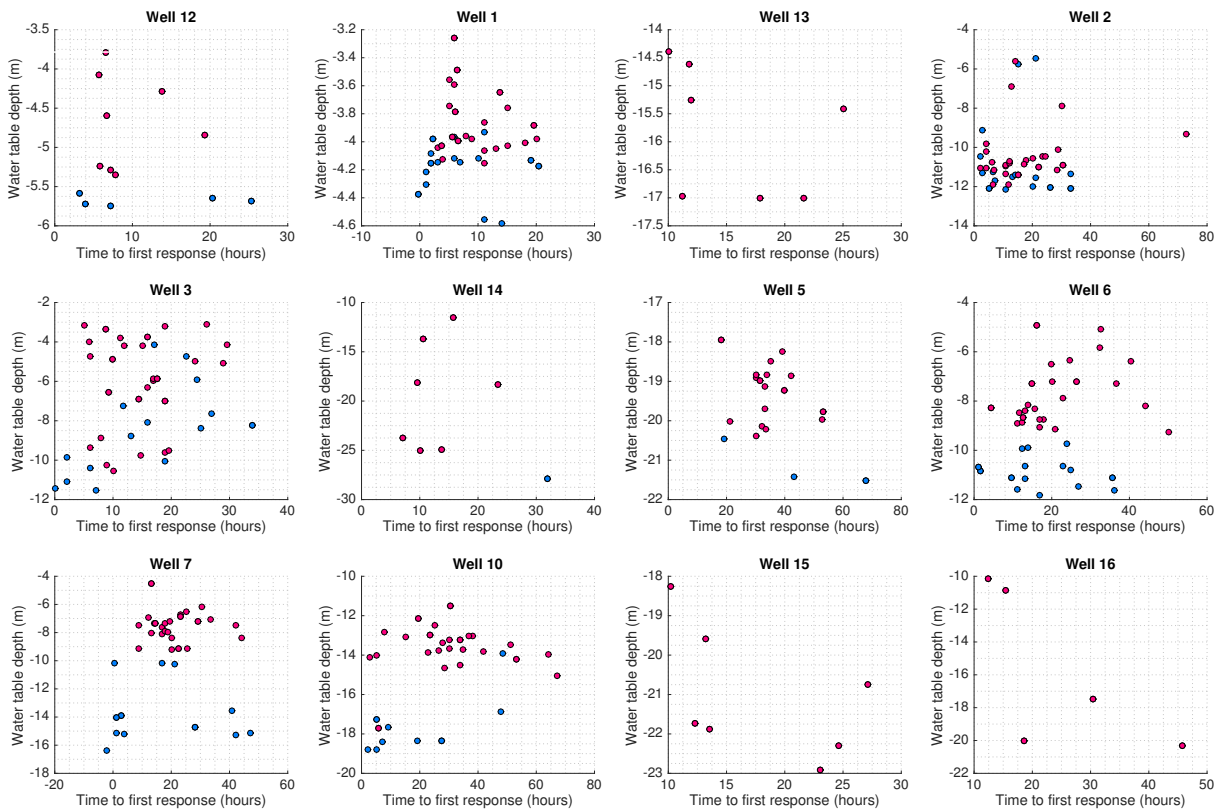
Figure 6.6: **Relationship between water table depth and time to initial response:** Time to initial response as a function of water table depth of the initial response. Colors represent storms that occurred before (blue) and after (red) upslope wells (15 and 16) respond seasonally (approximately 600 mm of seasonal cumulative precipitation).
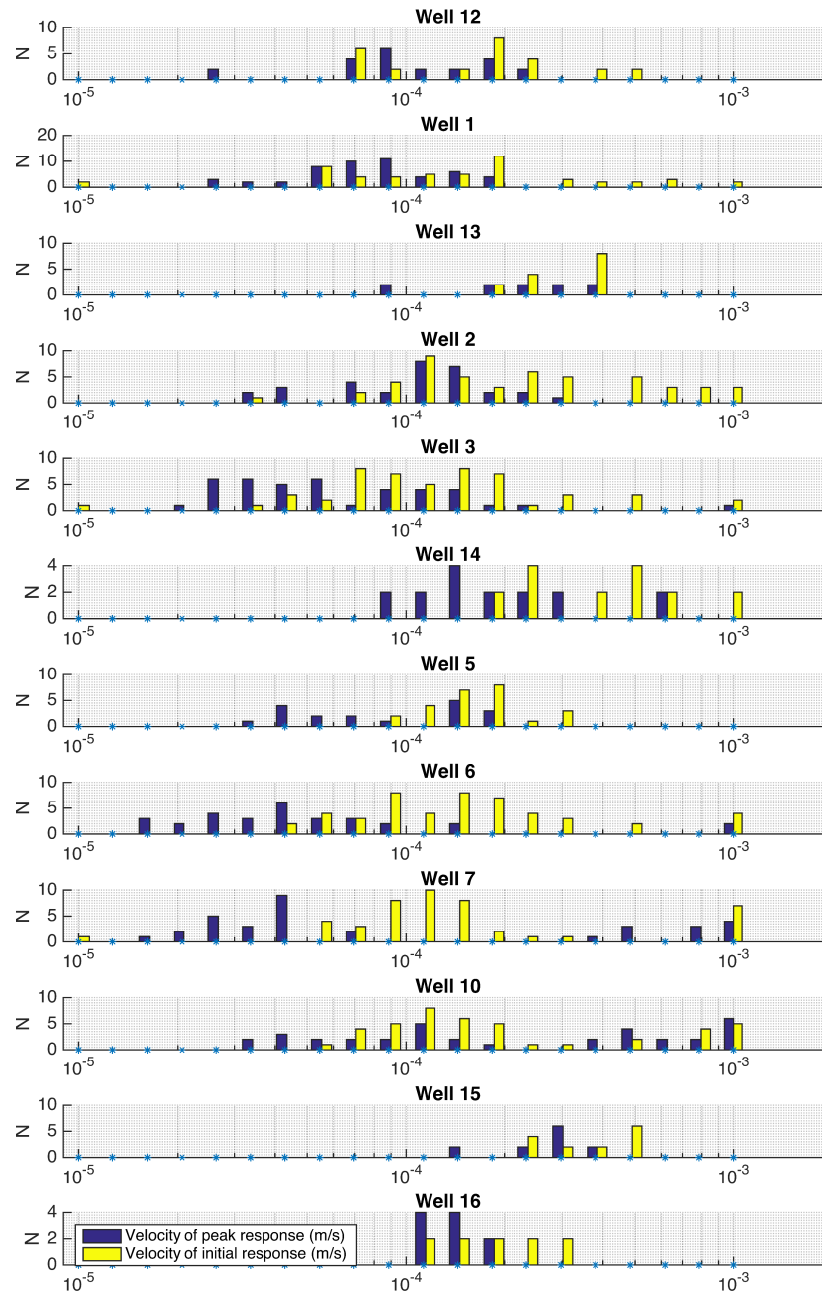
Figure 6.7: **Comparison of velocity of peak and initial response:** Velocity of peak (blue) and initial (yellow) response ranges from 10^{-5} to 10^{-3}, however, there is a tendency for the velocity of initial response to exceed the velocity of peak response. The velocity of initial response is defined as the distance to the water table at the time of the initial response divided by the time between first recorded precipitation and first recorded well response. The velocity of the peak response is defined as the distance to the water table peak divded by the time between the centroid of precipitation event and the peak of the well response.
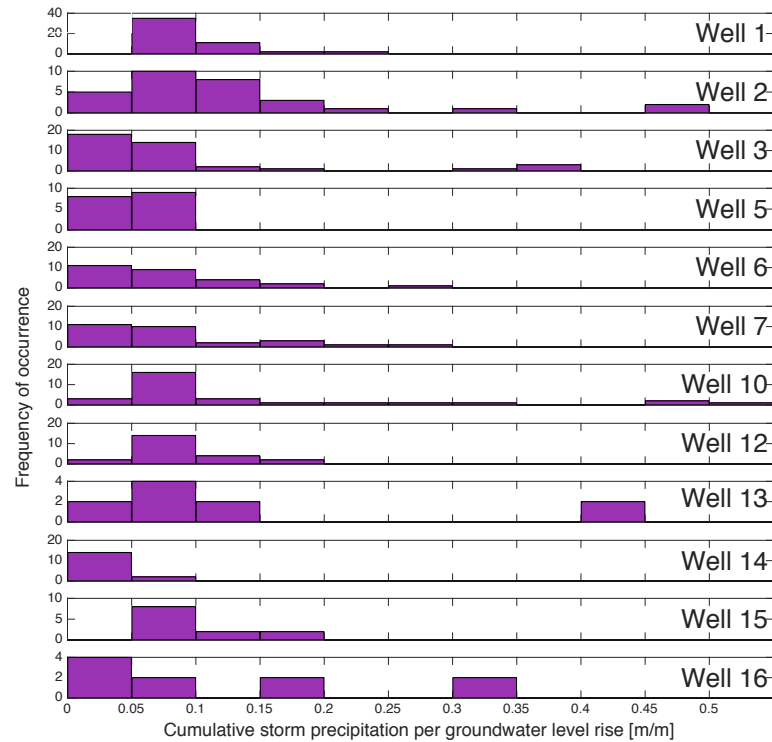
Figure 6.8: **Groundwater response to individual storms:** Fracture porosity was estimated by evaluating the groundwater level rise in response to individual storm events. For each storm, the total amount of storm precipitation was divided by the observed groundwater level rise that occurred during that storm. Histograms of fracture porosity (i.e. the cumulative storm precipitation per groundwater level rise) are shown for each well individually.
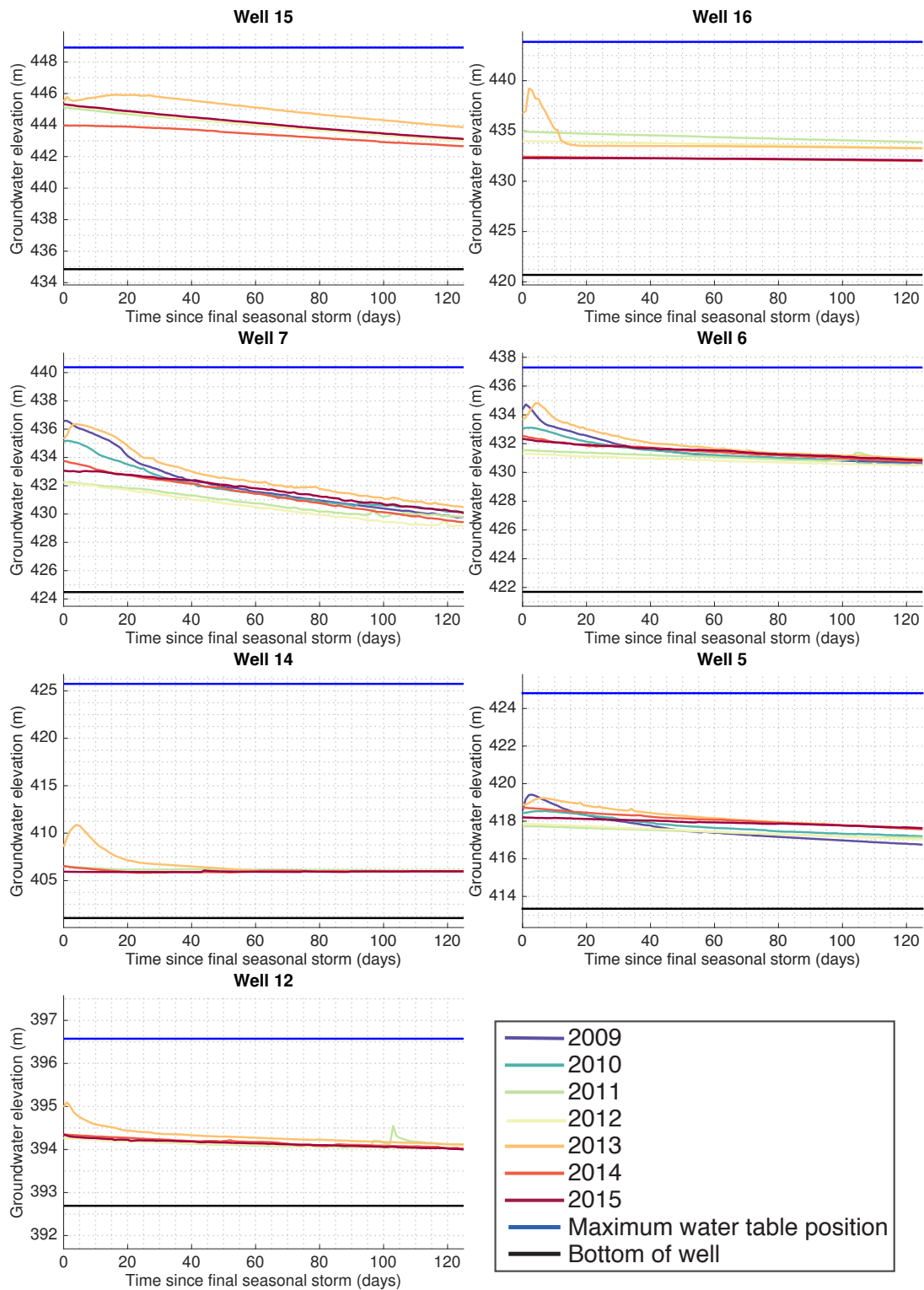
Figure 6.9: **Groundwater recession 2009-2015:** The recession of groundwater during the dry season is nearly the same in different years. The upper extent of the seasonally saturated zone is shown as a horizontal blue line and the bottom of the well is denoted by a horizontal black line. Note that groundwater levels are shown in terms of elevation and the range of elevations shown differs for each well.
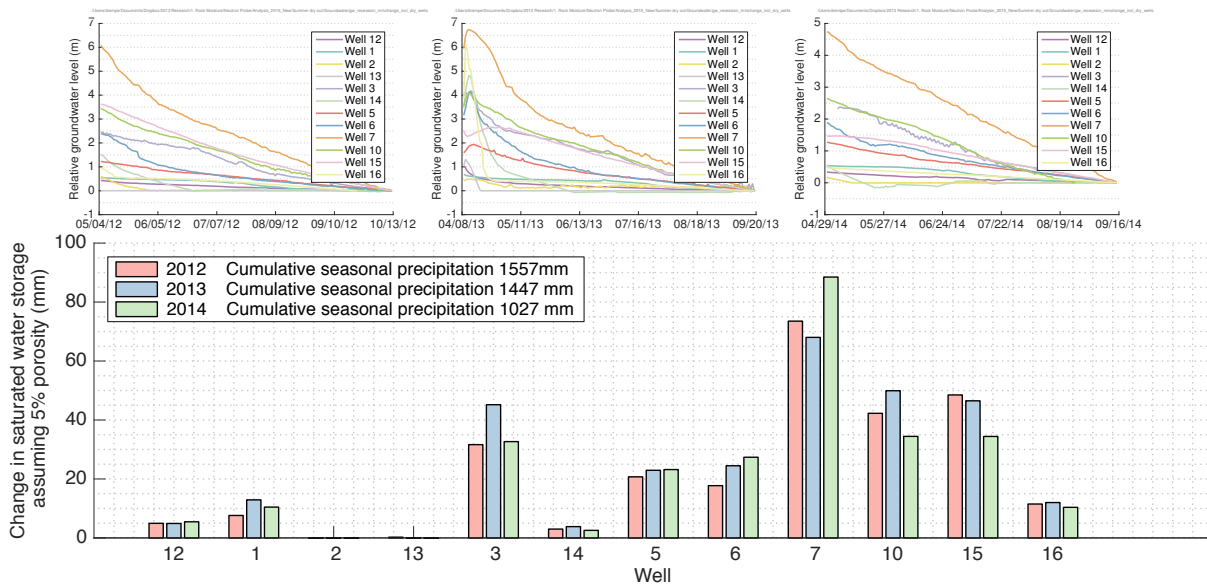
Figure 6.10: **Groundwater contribution to summer baseflow:** Groundwater recession (between the final and initial storms of the wet season) for three summers following years of variabile cumulative seasonal precipitation (Table 5.5). Groundwater level is shown relative to the end of dry season groundwater level (A-C). The amount of water stored in the saturated zone during last 60 days of the dry season in 2012-2014 is estimated assuming 5% porosity. Wells are roughly in order of increasing distance upslope. Water level in W13 and W2 drops below the elevation of the bottom of the well. Runoff in Elder Creek over the last 60 days of summer in 2012-2014 is between 5 and 6 mm.
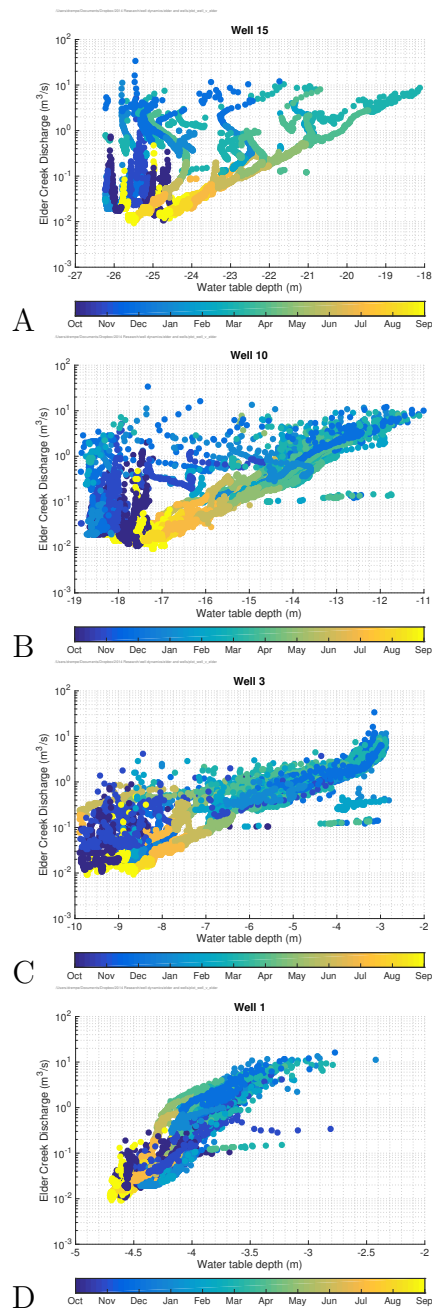
Figure 6.11: **Elder Creek discharge and groundwater level:** Elder Creek discharge is plotted against the water table depth. Wells 1 (located downslope), 3, 6, and 15 (located at the topographic divide) are arranged vertically in order of their relative location on the hillslope. Discharge in Elder Creek is strongly tied to changes in groundwater level in the lower portion of the slope, while upslope, there is an increasing lag and disconnection between storm-to-storm and seasonal changes in groundwater level with discharge.
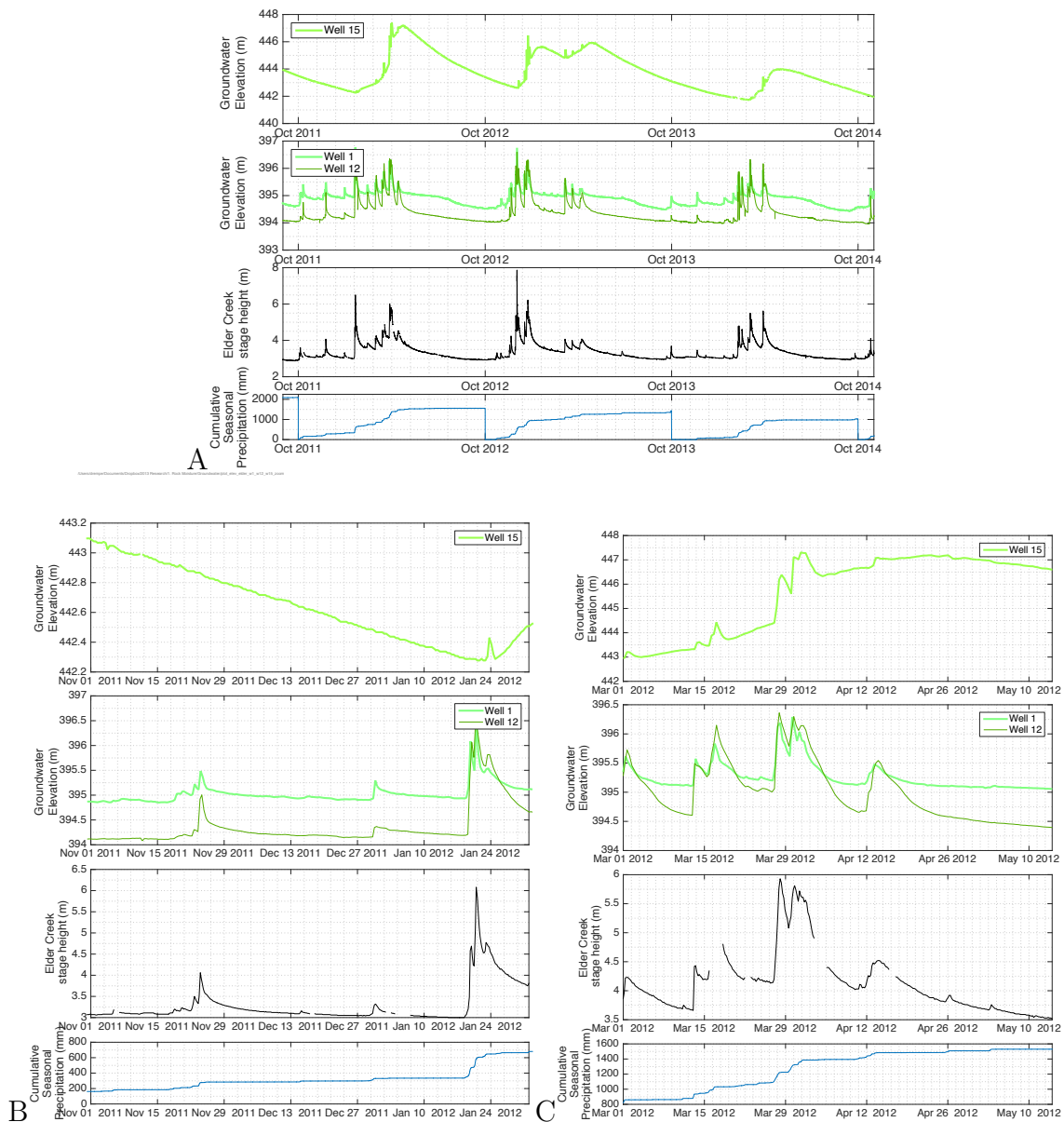
Figure 6.12: **Elder Creek Well 1 and Well 12 2011-2014:** In A, B, and C, the elevation of the water table in wells at the groundwater divide (Well 15, top panel) and near the channel (Wells 1 and 12, second panel) are compared to the stage height in Elder Creek (black line). The the cumulative seasonal precipitation is shown in blue in the bottom panel. Three years (2012-2015) are compared in A to illustrate the relatively diffuse response of the groundwater divide relative to downslope wells which show similar response to precipitation as Elder Creek. The early wet season (B) and the start of dry season (water year 2012) (C) are shown to illustrate that the groundwater divide is less responsive to individual storms than downslope wells.
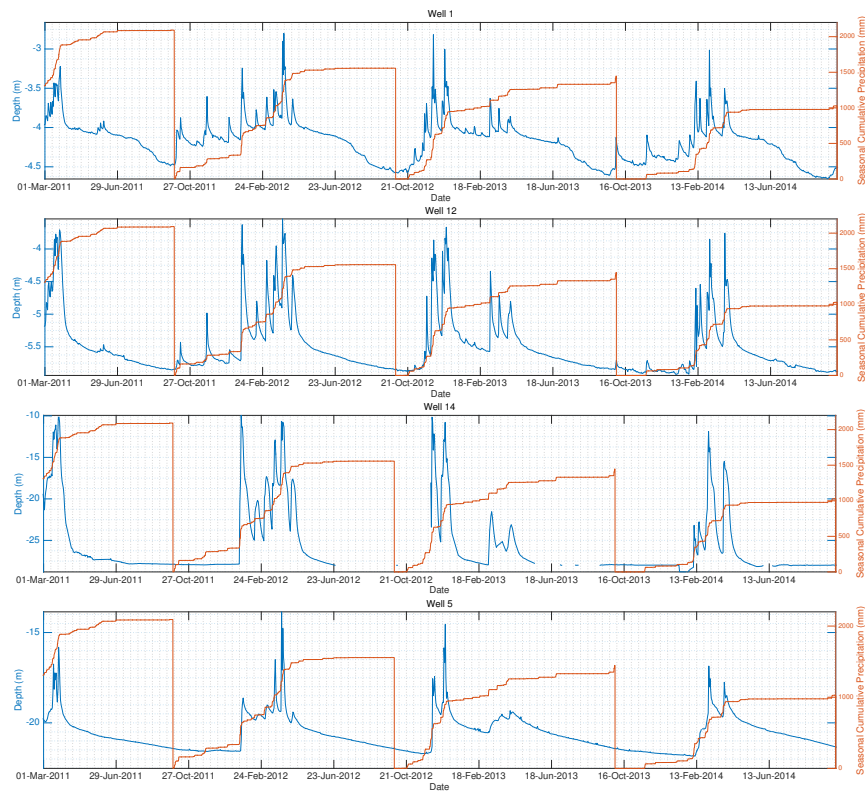
Figure 6.13: **Groundwater level and cumulative seasonal precipitation Wells 1, 12, 14, and 5:** Groundwater level (blue) in Wells 1, 12, 14, and 5 and cumulative seasonal precipitation (orange) for water years 2011-2014. Water years start Oct 1. Water levels fluctuations are tied to storms and occur within the same depth intevals in different years.
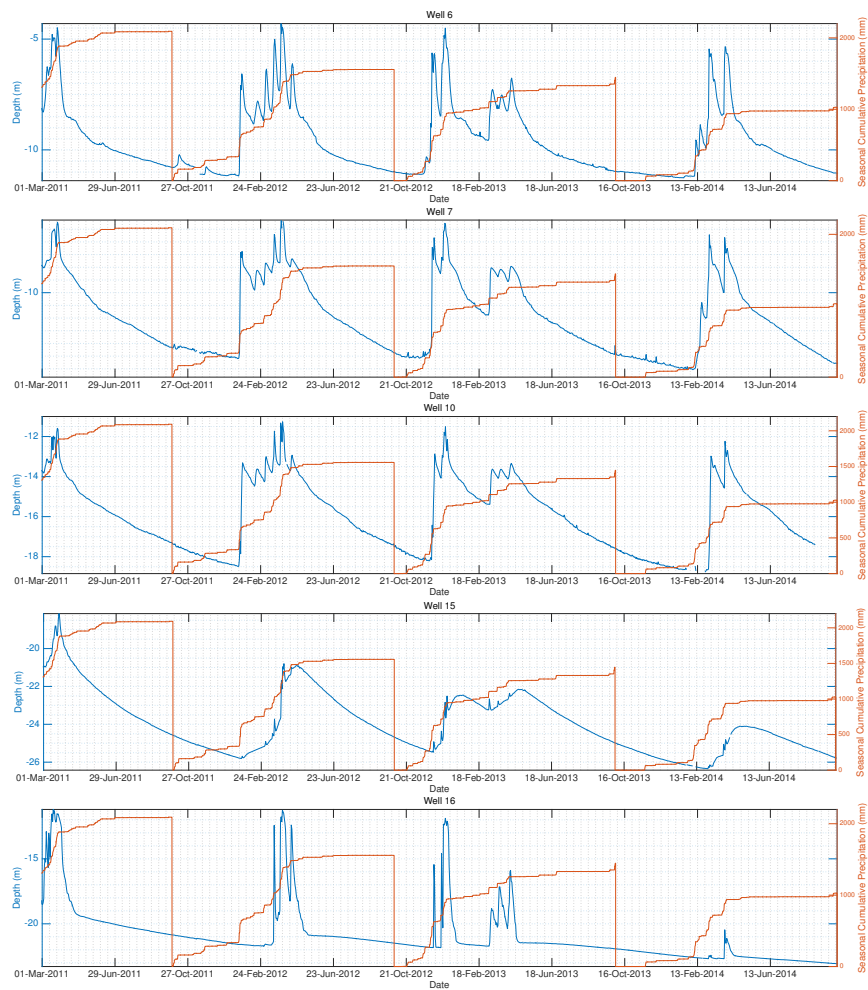
Figure 6.14: **Groundwater level and cumulative seasonal precipitation in Wells 6, 7, 10, 15, and 16:** Groundwater level (blue) in Wells 6, 7, 10, 15, and 16 and cumulative seasonal precipitation (orange) for water years 2011-2014. Water years start Oct 1. Wells 15 and 16 show progressive lowering of the seasonal low water table position in successive dry years.
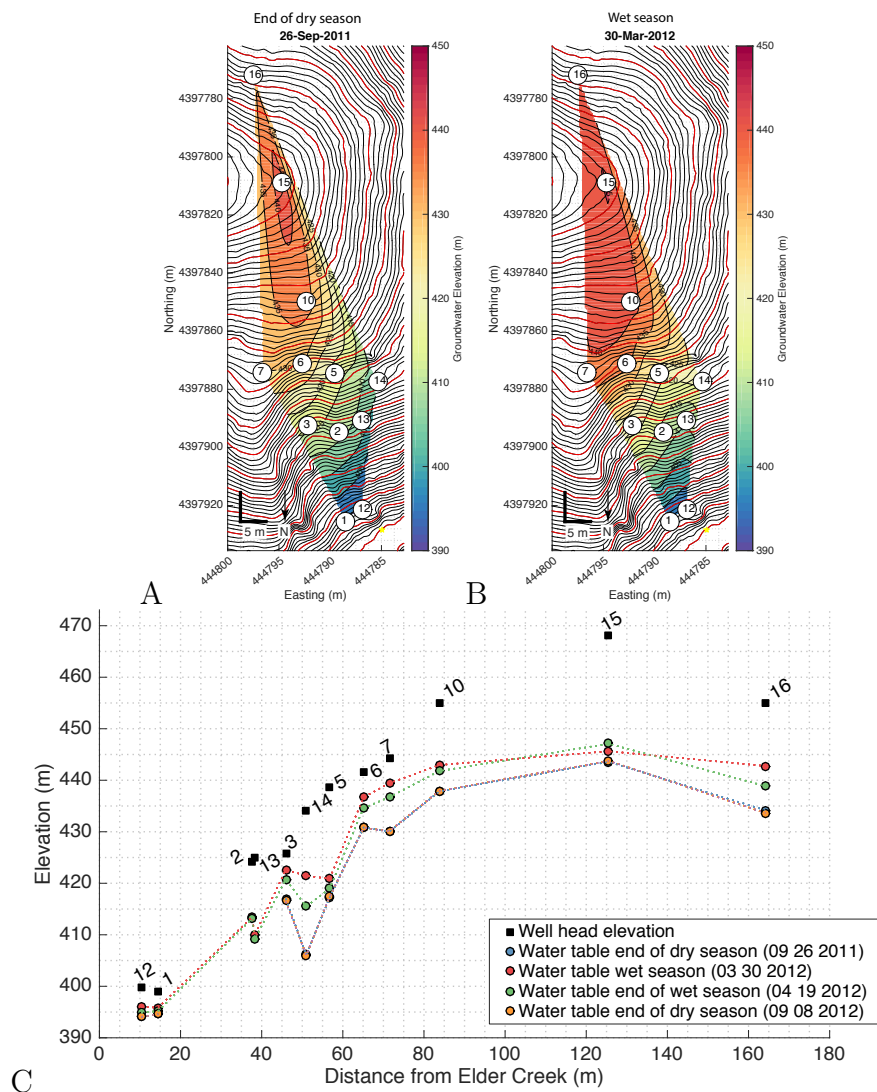
Figure 6.15: **Groundwater elevation across Rivendell**: Computed contours of groundwater elevation (colors) are shown over the ground surface topography (1 m contours in black, 5 m contours in red). The contoured groundwater surface is shown during the dry (A) and wet (B) season. (Note that Wells 1 and 3 are excluded from the contouring analysis during both the wet and dry season because of well pumping for groundwater sampling. Wells 13 and 2 are excluded from the dry season contour calculation because the groundwater level falls beyond the depth of the well.) (C) Groundwater elevation as a function of distance from Elder Creek throughout water year 2012 (including the dry (A) and wet (B) periods contoured above).

Bibliography

[1] S.P. Anderson, W.E. Dietrich, and G.H. Brimhall. Weathering profiles, mass-balance analysis, and rates of solute loss: Linkages between weathering and erosion in a small, steep catchment. *Geological Society of America Bulletin*, 114(9):1143, 2002.

[2] Suzanne Prestrud Anderson, William E Dietrich, David R Montgomery, et al. Subsurface flow paths in a steep, unchanneled catchment. *Water Resources Research*, 33(12):2637–2653, 1997.

[3] Yuko Asano, Taro Uchida, and Nobuhito Ohte. Residence times and flow paths of water in steep unchannelled catchments, Tanakami, Japan. *Journal of Hydrology*, 261(1):173–192, 2002.

[4] E.W. Banks, C.T. Simmons, A.J. Love, et al. Fractured bedrock and saprolite hydrogeologic controls on groundwater/surface-water interaction: a conceptual model (Australia). *Hydrogeology Journal*, 17(8):1969–1989, 2009.

[5] M Blumstock, D Tetzlaff, IA Malcolm, G Nuetzmann, and C Soulsby. Baseflow dynamics: Multi-tracer surveys to assess variable groundwater contributions to montane streams under low flows. *Journal of Hydrology*, 527:1021–1033, 2015.

[6] Michael Bonell. Progress in the understanding of runoff generation dynamics in forests. *Journal of Hydrology*, 150(2-4):217–275, 1993.

[7] Susan L Brantley, Molly E Holleran, Lixin Jin, and Ekaterina Bazilevskaya. Probing deep weathering in the Shale Hills Critical Zone Observatory, Pennsylvania (USA): the hypothesis of nested chemical reaction fronts in the subsurface. *Earth Surface Processes and Landforms*, 38(11):1280–1298, 2013.

[8] J. Büdel. Double surfaces of leveling in the humid tropics. *Zeitschrift für Geomorphologie*, 1:223–225, 1957.

[9] J St Clair, S Moon, WS Holbrook, et al. Geophysical imaging reveals topographic stress control of bedrock weathering. *Science*, 350(6260):534–538, 2015.

[10] B.A. Ebel, K. Loague, D.R. Montgomery, and W.E. Dietrich. Physics-based continuous simulation of long-term near-surface hydrologic response for the Coos Bay experimental catchment. *Water Resources Research*, 44(7):W07417, 2008.

[11] National Science Foundation. National Science Foundation, Program solicitation 12-575. 2012.

[12] Marty D Frisbee, Fred M Phillips, Andrew R Campbell, Fengjing Liu, and Steve A Sanchez. Streamflow generation in a large, alpine watershed in the southern Rocky Mountains of Colorado: Is streamflow generation simply the aggregation of hillslope runoff responses? *Water Resources Research*, 47(6), 2011.

[13] V Cody Hale, Jeffrey J McDonnell, Michael K Stewart, et al. Effect of bedrock permeability on stream base flow mean transit time scaling relationships: 2. Process study of storage and release. *Water Resources Research*, 2016.

[14] Atul H Haria and Paul Shand. Evidence for deep sub-surface flow routing in forested upland Wales: implications for contaminant transport and stream flow generation. *Hydrology and Earth System Sciences Discussions*, 8(3):334–344, 2004.

[15] Shin'ya Katsura, Ken'ichirou Kosugi, Tasuku Mizutani, Suemi Okunaka, and Takahisa Mizuyama. Effects of bedrock groundwater on spatial and temporal variations in soil mantle groundwater in a steep granitic headwater catchment. *Water Resources Research*, 44(9):n/a–n/a, September 2008.

[16] M Katsuyama, M Tani, and S Nishimoto. Connection between streamwater mean residence time and bedrock groundwater recharge/discharge dynamics in weathered granite catchments. *Hydrological Processes*, 24(16):2287–2299, 2010.

[17] K Kosugi, M Fujimoto, S Katsura, and H Kato. Localized bedrock aquifer distribution explains discharge from a headwater catchment. *Water Resources . . .*, 2011.

[18] Ken'ichirou Kosugi, Shin'ya Katsura, Masanori Katsuyama, and Takahisa Mizuyama. Water flow processes in weathered granitic bedrock and their effects on runoff generation in a small headwater catchment. *Water Resources Research*, 42(2):n/a–n/a, February 2006.

[19] Cédric Legout, Jérome Molenat, Luc Aquilina, et al. Solute transfer in the unsaturated zone-groundwater continuum of a headwater catchment. *Journal of Hydrology*, 332(3):427–441, 2007.

[20] Andrew H Manning and Jonathan Saul Caine. Groundwater noble gas, age, and temperature signatures in an Alpine watershed: Valuable tools in conceptual model development. *Water resources research*, 43(4), 2007.

[21] Jean-Christophe Maréchal, Murari RR Varma, Jean Riotte, et al. Indirect and direct recharges in a tropical forested watershed: Mule Hole, India. *Journal of Hydrology*, 364(3):272–284, 2009.

[22] MJ Pavich. Regolith residence time and the concept of surface age of the Piedmont "peneplain". *Geomorphology*, 2(1):181–196, 1989.

[23] Shengwen Qi, Zhong Qi Yue, Faquan Wu, and Zhonghua Chang. Deep weathering of a group of thick argillaceous limestone rocks near Three Gorges Reservoir, Central China. *International Journal of Rock Mechanics and Mining Sciences*, 46(5):929–939, 2009.

[24] Laura K Rademacher, Jordan F Clark, David W Clow, and G Bryant Hudson. Old groundwater influence on stream hydrochemistry and catchment response times in a small Sierra Nevada catchment: Sagehen Creek, California. *Water resources research*, 41(2), 2005.

[25] Craig Rasmussen, Peter A Troch, Jon Chorover, et al. An open system framework for integrating critical zone structure and function. *Biogeochemistry*, 102(1-3):15–29, 2011.

[26] Daniella M Rempe and William E Dietrich. A bottom-up control on fresh-bedrock topography under landscapes. *Proceedings of the National Academy of Sciences*, 111(18):6576–6581, 2014.

[27] B.P. Ruxton and L. Berry. Weathering of granite and associated erosional features in Hong Kong. *Geological Society of America Bulletin*, 68(10):1263–1292, 1957.

[28] C Soulsby, D Tetzlaff, N Van den Bedem, et al. Inferring groundwater influences on surface water in montane catchments from hydrochemical surveys of springs and streamwaters. *Journal of Hydrology*, 333(2):199–213, 2007.

[29] Peter Troch, Emiel Van Loon, and Arno Hilberts. Analytical solutions to a hillslope-storage kinematic wave equation for subsurface flow. *Advances in Water Resources*, 25(6):637–649, 2002.

[30] Peter A Troch, Claudio Paniconi, and E Emiel van Loon. Hillslope-storage Boussinesq model for subsurface flow and variable source areas along complex hillslopes: 1. Formulation and characteristic response. *Water Resources Research*, 39(11), 2003.

[31] CJ Wilson and WE Dietrich. The contribution of bedrock groundwater flow to storm runoff and high pore pressure development in hollows. *IAHS-AISH publication*, (165):49–59, 1987.

Chapter 7

Conclusion

At our soil mantled study site (Rivendell), channel incision into a dense, low permeability argillite has led to hillslope development in which a highly conductive fractured, weathered bedrock region has formed above fresh, essentially impermeable bedrock. In this uplifting environment, the deep fresh bedrock rises towards the eroding land surface and, once crossing into the critical zone, undergoes progressive decay as it approaches the ground surface. The fresh bedrock surface that defines the bottom boundary of the critical zone (referred to as Z_b) rises from the channel to the ridge, but less rapidly than does the topographic surface. This leads to an upslope thickening of the weathered bedrock zone across the hillslope.

Individual vertical profiles drilled through the critical zone consist of a basal dense fresh bedrock above which, progressively shallower in the profile, fracture density and porosity increase, ultimately leading to intense breakdown of the bedrock such that it takes on progressively more soil-like appearance while retaining a relict rock structure (i.e. it becomes a saprolite). The abrupt transition of saprolite to physically mobilized soil occurs in the upper 30-75 cm. This vertical sequence is the same along the hillslope, from the channel to the ridge, but progressively the weathered bedrock zone thickens from 4 m near the channel to 25 m at the divide. The weathered bedrock zone, particularly in the near surface, is increasingly weathered towards the divide, which is consistent with an estimated longer travel time with increasing critical zone thickness.

Into this structured subsurface, rainfall enters annually and establishes three distinct hydrologic zones: 1) a chronically unsaturated zone, 2) a seasonally saturated zone, and 3) a chronically saturated zone. We observe no overland flow or subsurface runoff within the soil. All runoff to streams passes through 4-18 m of unsaturated fractured, weathered bedrock before entering a seasonal groundwater system within bedrock fractures. The most challenging to measure and consequently, least understood, region is the unsaturated zone (i.e. the chronically unsaturated and seasonally saturated zone). Here, we directly monitor the entire unsaturated zone throughout wet and dry seasons, from the surface to the groundwater table, using repeat neutron probe surveys in deep wells. Together with continuous monitoring of soil and groundwater dynamics, direct monitoring of the unsaturated zone reveals the importance of rock moisture, the exchangeable water within the fractured bedrock, on regulating the hydrologic dynamics across the site.

Direct monitoring of rock moisture over 3 years (including a drought year of less than half mean annual precipitation) reveals that an annually invariant volume of rock moisture (~280mm), equal to about 30 to 60% of the annual precipitation, is seasonally added and depleted in the upper 5-12 m across the hillslope. Seasonally, the weathered bedrock soaks up the initial rains of the wet season leading to a delay in the response of groundwater and runoff to seasonal rainfall. The first small storms of the season can elevate shallow rock moisture and generate a small, short-lived groundwater response. However, it is not until subsequent rains advance a wetting front through the upper 10-12 m of fractured, weathered rock that the groundwater responds significantly, extending upwards the form the lowest position of the annually receding groundwater table (which typically coincides spatially with the fresh bedrock boundary).

The groundwater response to the onset of the wet season is most delayed upslope, where due to extensive weathering, the rock moisture storage is greatest (370-620 mm). Rock moisture storage decreases downslope from 120-270 mm mid-slope to 100 mm near the channel. The seasonal delay of the groundwater response at the ridge leads to the condition where runoff in response to early wet season storms is generated by groundwater only from the downslope portion of the hillslope.

Following the advance of a seasonal wetting front, rock moisture remains elevated for the remainder of the wet season and the addition of rainfall does not alter the structure or amount of rock moisture held in the hillslope. Seasonal rock moisture addition is concentrated in the near surface and diminishes with depth, showing little to no change within the seasonally saturated zone. Pulses of rain generate a rapid groundwater response which raises the water table to varying heights into the weathered, fractured bedrock zone across the hillslope. Surprisingly, the timing of the groundwater response to storms is not dependent on the distance to the water table or slope position. Groundwater levels, on average, rise 1 m for every 50 mm of storm rainfall, leading to an estimate of fracture porosity in the seasonally saturated zone of 5%. The rapid groundwater response and lack of moisture content changes in the seasonally saturated zone, we propose, is due to the dominance of fracture flow bounded by year-round saturation of low permeability matrix blocks.

Though individual storms can raise the water table by up to 11 m, only at one well do storms drive the water table up to the shallow saprolite layer. Downslope wells respond to nearly every wet season storm, while upslope wells respond to many, but not all, storms. The upper height at which storm-driven groundwater peaks occur is similar year to year in downslope wells and roughly corresponds to the zone where large changes in rock moisture occur. Here, a large increase in porosity and likely saturated conductivity (as indicated by a large reduction in penetration resistance) caps the rise in groundwater leading to repeatable thickness of the seasonally saturated zone. Upslope, the uppermost extent of the seasonally saturated zone shows sensitivity to the total seasonal precipitation, rising higher in wetter years and receding lower in drier years.

The highly responsive fractured bedrock groundwater system leads to over 95% of runoff occurring during the wet season. Following the last storm of the wet season, the recession of streamflow, groundwater, soil and rock moisture begins. The dry season rock moisture reservoir in the upper 10 m (280 mm average across the hillslope) is more than double the 30-128 mm of soil moisture, which is rapidly depleted early in the dry season. Rock moisture dries from the top downwards and, when no more than 15 mm soil moisture remains at the time of peak transpiration of broad leaf trees (approximately 12 weeks into the 18 week long dry season), over 100 mm of rock moisture remains. This rock moisture is slowly depleted in the final months of the dry season and a comparison of a drought year with a year of average precipitation, shows no differences in the temporal pattern of rock moisture depletion during the dry season. The drop in groundwater levels at the end of the dry season is consistent year to year. Runoff of only 5 mm per month sustains flow in Elder Creek during the dry season

In the seasonally dry environment, the varying material properties with depth and the corresponding hydrologic response zones lead to a division of dry season ecologic function within the hillslope; The rock moisture in the chronically unsaturated zone supports transpiration while the slowly draining groundwater in the seasonally saturated zone sustains baseflow and thus river ecosystems. The defining features of rock moisture are the dual property of rapid transmission and sustained storage of water and the insensitivity of rock moisture availability to annual variability in precipitation. Our observations constrain existing models for flow through unsaturated fractured bedrock and the processes that depend on this flow such as biogeochemical cycling of carbon and nutrients, and the geochemical evolution of water through the critical zone. In landscapes developed into bedrock, rock moisture is likely an important player in partitioning water between runoff and transpiration and further fieldwork is needed to identify the controls on critical zone structure and how critical zone structure informs the significance of rock moisture globally.

Appendix A

Development of a steady state analytical model for fresh bedrock topography

A.1 Steady state analytical model for ground surface topography

In the proposed model, the ground surface topographic profile resulting from linear, diffusive transport processes defines the upper boundary of the weathered bedrock zone. To arrive at the one-dimensional, steady-state topographic profile for a soil mantled hillslope, we begin with the one dimensional version of the conservation of mass equation where bulk density is assumed to be constant (Dietrich et al., 2003) :

$$\frac{\partial Z_s}{\partial t} = U - \frac{\partial q_s}{\partial x} \tag{A.1}$$

Z_s is the surface elevation [L], U is the rock uplift rate $[LT^{-1}]$, q_s is the sediment transport rate per unit contour length $[MT^{-1}L^{-1}]$, and x is the distance from the hillslope divide [L]. By assuming that sediment transport is proportional to the local hillslope gradient $(\frac{\partial Z_s}{\partial x})$, we adopt the common expression:

$$q_s = -D\rho_s \frac{\partial Z_s}{\partial x} \tag{A.2}$$

where ρ_s is the soil bulk density (ML^{-3}) and D is a constant of proportionality referred to as the soil diffusivity $(L2T^{-1})$.

At steady state $(\frac{\partial Z_s}{\partial t} = 0)$, the uplift rate (U), erosion rate and channel incision rate (C_o) are equal. The soil thickness is constant and the rate of conversion of bedrock to soil is equal to the rate at which soil is removed by erosion, which can be written as $\rho_r C_o$ where ρ_r is the bulk density of weathered bedrock at the base of the soil column. The mass conservation equation can then be written as:

$$\rho_r C_o = -D\rho_s \frac{\partial^2 Z_s}{\partial x^2} \tag{A.3}$$

The previous equation can be rewritten in terms of the topographic curvature $(\frac{\partial^2 Z_s}{\partial x^2})$

$$\frac{\partial^2 Z_s}{\partial x^2} = -\frac{\rho_r}{\rho_s}\frac{C_o}{D} \tag{A.4}$$

s

Assuming symmetry about the ridgetop $(\frac{\partial Z_s}{\partial x} = 0$ at $x = 0)$ and that the surface elevation, Z_s, is expressed relative to the base of the hillslope $(z = 0$ at $x = L)$, the one-dimensional hillslope surface topography is given by

$$Z_s(x) = \frac{P_r}{P_s}\frac{C_o}{2D}(L^2 - x^2) \tag{A.5}$$

A.2 Steady state analytical model for groundwater drainage in fresh bedrock

In the proposed model, the elevation of fresh bedrock, Z_b, is assumed to correspond to the steady state elevation of the groundwater profile that develops within fresh bedrock in response to channel incision. To arrive at an expression for the 1-dimensional groundwater surface, we perform a mass balance on a fixed homogeneous, isotropic, incompressible volume element with a free surface of incompressible fluid. The flux of fluid can be described by Darcy's Law

$$q_x = -K\frac{dZ_b}{dx}$$

where K is saturated hydraulic conductivity $[L/T]$ and q_x is darcy velocity (fluid velocity is the darcy velocity divided by the porosity,$\varnothing$). The phreatic surface, Z_b, is the elevation of the fluid surface above a datum such that $\frac{dZ_b}{dx}$ is the horizontal pressure gradient. The solution for a free groundwater surface is complicated by the fact that the thickness through which flow occurs changes as groundwater is drained. However, when vertical components of flow are small or negligible, the Dupuit assumptions significantly simplify the solution (Bear, 1972). The Dupuit assumptions require a gently sloping water table surface such that equipotential surface are vertical (i.e. horizontal flow) and the Darcy velocity at the free surface is a function of horizontal distance rather than distance along the free surface. The Dupuit assumptions lead to the one-dimensional form of the Boussinesq Equation which describes unsteady flow in a phreatic aquifer with recharge, R:

$$\frac{K}{2}\frac{\partial^2 Z_b{}^2}{\partial x^2} + R = \varnothing\frac{\partial Z_b}{\partial t} \tag{A.6}$$

In the proposed model, recharge occurs through the introduction of saturated fresh bedrock into the groundwater system at a rate equal to the uplift rate or channel incision rate, C_o. Since only the fraction of the bedrock equal to the porosity,$\varnothing$, is comprised of water, R is defined as $\varnothing C_o$. Assuming steady state($\frac{\partial Z_b}{\partial t} = 0$) and employing the definition of R, we arrive at:

$$\frac{K}{2}\frac{\partial^2 Z_b^2}{\partial x^2} + \varnothing C_o = 0 \tag{A.7}$$

To arrive at an equation for Z_b as a function of x, the following boundary conditions are applied: 1) the channel, located at $x = L$, serves as the bottom of the flow system (i.e. $Z_b = 0$ at $x = L$) and 2) symmetry about the ridge top, located at $x = 0$, such that the ridge is a groundwater flow divide or no-flux boundary (i.e.$\frac{\partial Z_b}{\partial x} = 0$ at $x = 0$). For these boundary conditions, we arrive at the following solution for the steady state elevation of a groundwater table along a one-dimensional hillslope:

$$Z_b(x) = \sqrt{\frac{\varnothing C_o}{K}(L^2 - x^2)} \tag{A.8}$$

This solution for Z_b is a highly simplified approximation, however, the Dupuit assumptions and the resulting Boussinesq equation lead to reasonable approximations for the complex, non-linear unconfined groundwater flow problem we address here (Bear, 2013, Kirkham, 1967). Further, we focus our analysis on the ridge top (Z_{b0}), where errors associated with the Dupuit assumptions are reduced because it has been shown that as the water table surface becomes less steep at distances farther from the outlet, solutions obtained following the Dupuit assumptions become more consistent with the exact solution for a phreatic surface (2).

The value of this simple groundwater model is that all parameters are measurable independently of the model itself. They are physical attributes of the system and empirical data on ranges of values exist. This allows us to explore ranges of conditions that would favor Z_b extending well above the elevation of an adjacent channel. We can then use these conditions as a guide for field investigations.

The definition of recharge (A.8) leads to a surprising relationship between hydraulic conductivity and porosity and the height of Z_b. Because these parameters represent the trade-off between the amount of water that needs to be drained (through $\varnothing$) and the ability of the rock to drain that water (through K) they have the opposite effect on the solution, as expressed by the ratio, $K/\varnothing$ in S9.

Here we assume that the bottom of the flow system is the elevation of the channel. This bottom boundary condition is a construct of the model framework set by the Dupuit assumptions, which impose vertically averaged flow. As illustrated in Figure A.1, there is a significant vertical component to groundwater flow near the channel and ridge top in flows expected under hillslopes. Within the model framework, if the boundary of our flow domain is lowered to an elevation below the channel, Z_b is predicted to decrease (i.e. the proportion of the hillslope that is composed of fresh bedrock decreases). Allowing the bottom of the flow system to vary, however, introduces a free variable and does not address upward flow to the channel because vertical flow is not treated in the model.

The proposed analytical model for Z_b assumes steady state conditions. For the very low hydraulic conductivities and drainage rates shown to lead to Z_b above the elevation of an adjacent, incising channel, the steady state approximation may be reasonable over geomorphically significant time scales. Nonetheless, temporal variations in channel incision rate and lateral shifting of the channel into the hillslope are expected to affect the Z_b profile.

Consistent with the very low drainage rate of the fresh bedrock, seasonally perched groundwater is assumed not to recharge the fresh bedrock from above. Though seasonal ponding above Z_b is common due to the hydraulic conductivity contrast between weathered and fresh bedrock (e.g. Salve et al., 2012), the enhanced drainage due to the hydraulic head increase that results from ponding is likely negligible and transient. Further, by assuming steady state, we impose that the drainage rate equal the channel

incision rate, which is typically less than 1 mm/ year. At such a slow pace, the meteoric waters that perch above Z_b only rarely need to completely drain (laterally) to expose the Z_b boundary to the weathering effects of oxidants and drying. If meteoric waters reach equilibrium with bedrock minerals in the weathered zone then the position of Z_b would be greater than what is predicted by our model because the water that drains within the fresh bedrock would be displaced by equilibrated water, thus preventing any further chemical evolution within the fresh bedrock.

Here we treat flow in bedrock as Darcian as compared to having a significant fracture flow component. We assume that below Z_b, conductive fractures are rare and that reactive meteoric waters that may enter such fractures have only a local (near wall) weathering effect and do not influence the hillslope scale Z_b boundary. In the case that the density of conductive fractures significantly affects flow within the fresh bedrock, the lowering of Z_b is expected due to enhanced drainage.

Finally, it is important to point out that as saturated fresh bedrock travels from depth towards the surface, the fluids within the pore space of the fresh bedrock are not stationary. At great depth they are displaced by regional head gradients and, upon entering the near-surface environment, fluids are progressively displaced towards the drainage channels (Figure A.1,) even as the bedrock itself travels towards the surface. For steady-state conditions in which uplift and erosion are matched, Z_b is fixed in place as the rate of fluid drainage at Z_b matches the rate of bedrock uplift.

A.3 Analytical model for ground surface topography due to non-linear soil transport

The analytical model describing the thickness of the weathered zone at the ridge top (Eq. 4) employs a model to describe surface topography that relates soil flux and slope linearly. Alternatively, a non-linear relationship between soil flux and slope (Roering et al., 1999), can be used to arrive at an analytical expression that describes the thickness of the weathered zone (or the ratio of bedrock relief to surface relief, Z_{b0}/Z_{s0}).

Following the non-linear model, the 1-D analytical expression for the steady state surface profile is given by:

$$z_s(x) = -\frac{S_c^2}{2\beta}[\sqrt{D^2 + (2\beta x/S_c)^2} - Dln(\frac{\sqrt{D^2 + (2\beta x/S_c)^2} + D}{2\beta/S_c})]$$

$$+ \frac{S_c{}^2}{2\beta}[\sqrt{D^2 + (2\beta L/S_c)^2} - Dln(\frac{\sqrt{D^2 + (2\beta L/S_c)^2} + D}{2\beta/S_c})] \quad (A.9)$$

where $\beta = (\rho_r/\rho_s)C_o$, S_c is the critical slope, and D is the soil diffusivity $[L^2/T]$ (Roering et al., 2001). The boundary conditions used to arrive at this solution are the same as those used to arrive at Eq. 1: There is no soil flux across the ridge top($x = 0$) and the channel elevation ($z = 0$) occurs at $x = L$ where L is the hillslope length. The thickness of the weathered zone as a function of distance along the hillslope, H(x), is given by the difference between the surface elevation (Eq. S11) and bedrock elevation (Eq. 3) as:

$$H(x) = -\frac{S_c^2}{2\beta}[\sqrt{D^2 + (2\beta x/S_c)^2} - Dln(\frac{\sqrt{D^2 + (2\beta x/S_c)^2} + D}{2\beta/S_c})]$$

$$+ \frac{S_c^2}{2\beta}[\sqrt{D^2 + (2\beta L/S_c)^2} - Dln(\frac{\sqrt{D^2 + (2\beta L/S_c)^2} + D}{2\beta/S_c})] - \sqrt{\frac{C_o\varnothing}{K}}(L^2 - x^2) \quad \text{(A.10)}$$

At the ridge top, the ratio of bedrock relief (Z_{b0}) to surface relief (Z_{s0}) is:

$$\frac{Z_{b0}}{Z_{s0}} = \frac{\sqrt{\frac{C_o\varnothing}{K}(L^2)}}{-\frac{S_c^2}{2\beta}[D - Dln(\frac{D}{(\beta/S_c)})] + \frac{S_c^2}{2\beta}[\sqrt{D^2 + (2\beta L/S_c)^2} - Dln(\frac{\sqrt{D^2+(2\beta L/S_c)^2}+D}{(2\beta/S_c)})]} \quad \text{(A.11)}$$

The residence time of weathered material that arrives at the soil-bedrock boundary at the ridge top (T_{r0}) is calculated as the weathered thickness at the ridge top (H_0) divided by the channel incision rate (C_o) and is given by:

$$T_{r0} = \frac{-\frac{S_c^2}{2\beta}[D - Dln(\frac{D}{(\beta/S_c)})] + \frac{S_c^2}{2\beta}[\sqrt{D^2 + (2\beta L/S_c)^2} - Dln(\frac{\sqrt{D^2+(2\beta L/S_c)^2}+D}{(2\beta/S_c)})] - \sqrt{\frac{C_o\varnothing}{K}(L^2)}}{C_o}$$

$$\text{(A.12)}$$

Effectively, Eq. S11, S12, S13 are the non-linear analogs of Eq. 1, 4, and 6.

A.4 Climate controls on Z_b

Precipitation and runoff do not appear in the proposed model, however climate may be influential in several ways. First, hillslope length, and thus wavelength of ridge and valley topography, are set by the relative intensity of advective (channel incision) to diffusive (hillslope soil flux) processes that in turn may depend on climate and lithology (Perron et al., 2009, Perron and Fagherazzi, 2004). Climate, then, may influence the Z_b profile relative to the surface by affecting the length of hillslopes (Eq. 5).

Second, channel incision rates depend on frequency and magnitude of bedrock scouring events (Sklar et al., 2004), and if this is climate dependent, as is often proposed (e.g.

Molnar, 2001), then a direct connection between C_o and the Z_b profile may exist. Climate also plays a role in the degree of alteration of weathered material above Z_b and subsequently the erosional processes that influence surface topography. To a first approximation, the more water that passes through the weathered zone, the greater the net mass loss before the weathered rock is incorporated into the mobile soil layer. Thus, the weathered bedrock density, ρ_r, is likely climate dependent, and the smaller the residual density between soil and weathered bedrock, the lower the hillslope relief and thus the greater proportion of the hillslope that is underlain by fresh bedrock (Eq. 1). If collapse occurs with extensive solute losses in the weathered bedrock, then strain corrected bulk density (e.g. Brimhall and Dietrich, 1987), would need to be included in the analysis. Additionally, the soil density, ρ_s, may tend to be lower in cooler, wetter environments where dilational disturbances from biota and build up of organic matter can reduce soil densities to below$1.0 g/cm^3$ (e.g., Perron et al., 2009). Higher hillslope gradients, Sh, tend to develop with lower ρ_s (according to Eq.5) leading to a smaller Z_b/Z_s. Finally, the soil diffusivity term, D, is likely climate dependent (e.g. Fernandes and Dietrich, 1997).

It is important to note that in the proposed model, the bottom-up control refers specifically to the elevation of Z_b as opposed to the depth to Z_b. Climate dependent, top-down processes may affect the evolution of the surface, Z_s, and thus the relative thickness of the weathered bedrock zone, Z_{b0}/Z_{s0}. We propose that, where applicable, the bottom-up control on Z_b sets a limit on the depth to which climate-dependent top-down processes may occur.

A.5   References

1. Dietrich, W. E., Bellugi, D. G., Sklar, L. S., Stock, J. D., Heimsath, A. M., & Roering, J. J. (2003). Geomorphic transport laws for predicting landscape form and dynamics. Prediction in geomorphology, 103-132.

2. Bear, J. (2013). Dynamics of fluids in porous media. DoverPublications. com

3. Kirkham, D. (1967). Explanation of paradoxes in Dupuit-Forchheimer Seepage Theory. Water Resources Research, 3(2), 609-622.

4. Salve, R., Rempe, D. M., & Dietrich, W. E. (2012). Rain, rock moisture dynamics, and the rapid response of perched groundwater in weathered, fractured argillite underlying a steep hillslope. Water Resources Research,48(11).

5. Roering, J. J., Kirchner, J. W., & Dietrich, W. E. (1999). Evidence for nonlinear, diffusive sediment transport on hillslopes and implications for landscape morphology. Water Resources Research, 35(3), 853-870.

6.   Roering, J. J., Kirchner, J. W., Sklar, L. S., & Dietrich, W. E. (2001). Hillslope evolution by nonlinear creep and landsliding: An experimental study. Geology,29(2), 143-146.

7.   Perron, J. T., Kirchner, J. W., & Dietrich, W. E. (2009). Formation of evenly spaced ridges and valleys. Nature, 460(7254), 502-505.

8.   Perron, J. T., & Fagherazzi, S. (2012). The legacy of initial conditions in landscape evolution. Earth Surface Processes and Landforms, 37(1), 52-63.

9.   Sklar, L. S., & Dietrich, W. E. (2004). A mechanistic model for river incision into bedrock by saltating bed load. Water Resources Research, 40(6).

10.   Molnar, P. (2001). Climate change, flooding in arid environments, and erosion rates. Geology, 29(12), 1071-1074.

11.   Brimhall, G. H., & Dietrich, W. E. (1987). Constitutive mass balance relations between chemical composition, volume, density, porosity, and strain in metasomatic hydrochemical systems: results on weathering and pedogenesis.Geochimica et Cosmochimica Acta, 51(3), 567-587.

12.   Fernandes N. F., Dietrich W. E. (1997) Hillslope evolution by diffusive processes: The timescale for equilibrium adjustments. Water Resources Research 33:1307–1318. 13. Montgomery, D. R., Dietrich, W. E., Torres, R., Anderson, S. P., Heffner, J. T., & Loague, K. (1997). Hydrologic response of a steep, unchanneled valley to natural and applied rainfall. Water Resources Research, 33(1), 91-109.

14.   Montgomery, D. R., Dietrich, W. E., & Heffner, J. T. (2002). Piezometric response in shallow bedrock at CB1: Implications for runoff generation and landsliding. Water Resources Research, 38(12), 10-1.

15.   Freeze, R. A., & Cherry, J. A. (1977). Groundwater. Prentice-Hall.

16.   Gleeson, T., Smith, L., Moosdorf, N., Hartmann, J., Dürr, H. H., Manning, A. H., L. PH van Beek & Jellinek, A. M. (2011). Mapping permeability over the surface of the Earth. Geophysical Research Letters, 38(2), L02401.

17.   Anderson S. P., Dietrich W. E., Brimhall G. H. (2002) Weathering profiles, mass-balance analysis, and rates of solute loss: Linkages between weathering and erosion in a small, steep catchment. Geological Society of America Bulletin 114:1143.

A.6   Tables

Channel Incision Rate	Rock Bulk Density	Soil Bulk Density	Hillslope Length	Soil Diffusivity	Critical Slope	Ratio of Surface to Bedrock Relief at the Ridgetop
C_o	ρ_r	ρ_s	L	D	S_c	Z_{b0} / Z_{s0}
0.1 mm/yr	2.65 g/cm^3	1.35 g/cm^3	76 m	0.005 m^2/yr	1.2	0.83

Table A.1: Model parameters used to generate Fig. 4A and 4B from the Coos Bay site in the Oregon Coast Range.

A.7 Figures
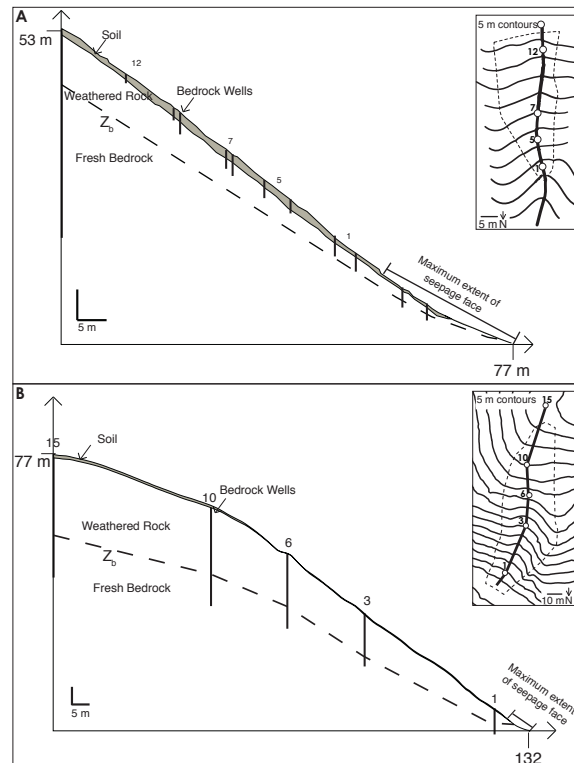
Figure A.1: Two study sites of actively eroding hillslopes where Z_b has been mapped through deep drilling:

A) CB1 catchment near Coos Bay within the Oregon Coast Range (13)

B) Rivendell field site located in the Angelo Coast Range Reserve (http://angelo.berkeley.edu) within the Northern California Coast Range (4). Not that the surface topography at both sites forms a subtle swale, most likely recording the effects of shallow landsliding (e.g. ref 14). Hence, the profiles are not for planar convex hillslopes.
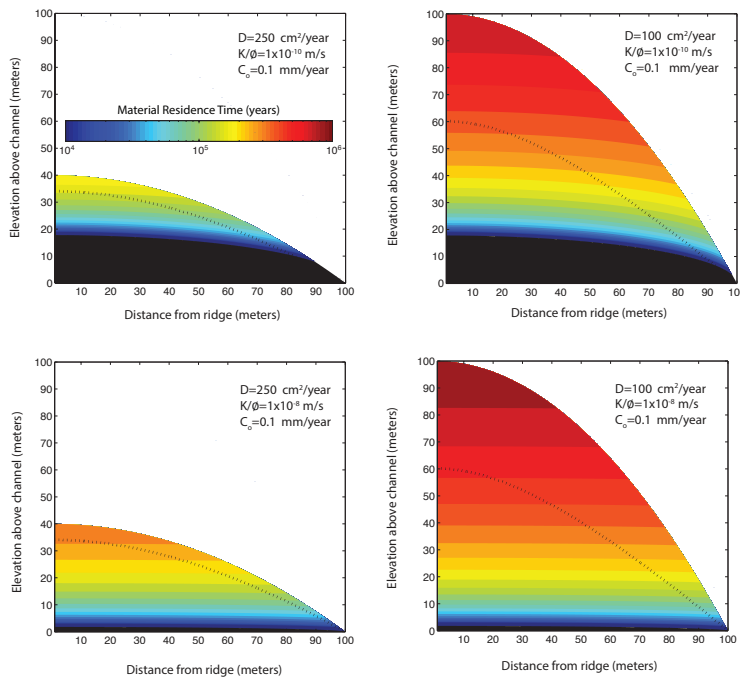
Figure A.2: The predicted surface (Z_s) and bedrock (Z_b) profiles and the calculated weathered bedrock residence time for four cases where C_o is held constant at 0.1 mm/yr and D (and thus S_h) and $K/\varnothing$ (and thus S_w) vary. The surface profile, $Z_s(x)$, was calculated using a linear relationship between soil flux and slope (Eq. 1). The residence time is calculated using the linear soil flux relationship. The dotted line represents $Z_s(x)$ calculated using a non-linear relationship between soil flux and slope (Eq. S1) and shown in Fig. 3C-F. The bedrock surface, Z_b, is defined by the color transition to black.
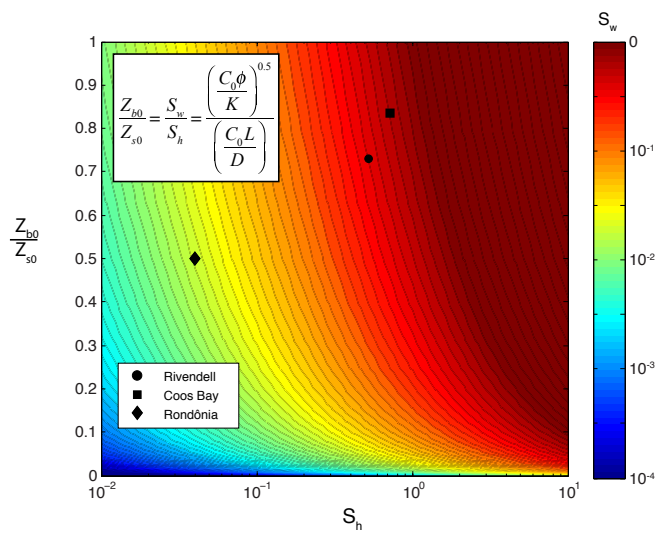
Figure A.3: The thickness of the weathered zone at the ridge top (expressed as the ratio of the ridgetop bedrock elevation, Z_{b0}, to the surface elevation, Z_{s0}) as a function of the mean hillslope gradient (S_h) and the mean groundwater table gradient (S_w), (contoured) for the linear soil flux case.
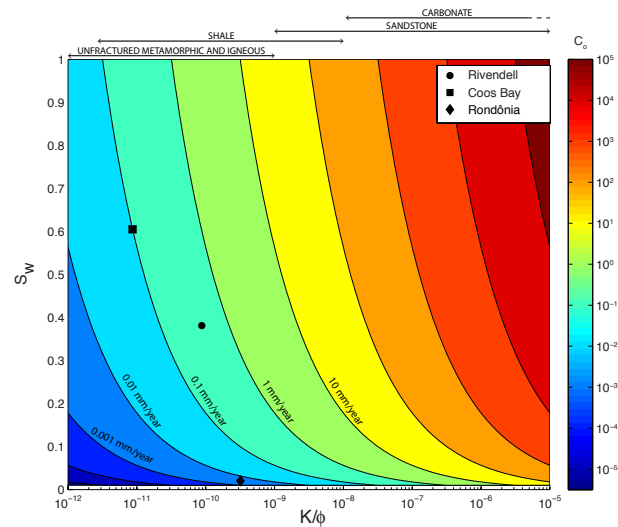
Figure A.4: The characteristic hydraulic gradient, S_w, is plotted as a function of bedrock $K/\varnothing$ and channel incision rate, C_o (contoured) for the linear soil flux case. Assuming a porosity, $\varnothing$, of 0.1, the range of $K/\varnothing$ associated with a particular rock type is denoted above the plot following lithology-permeability compilations reported by (15) and later supported by field data compiled by (16). For observed S_w and C_o, $K/\varnothing$ can be estimated. Alternatively, for observed C_o and known lithology, S_w can be estimated and for a known S_h, the ratio of the ridge top bedrock to surface relief (Z_{b0}/Z_{s0}) can be determined (Eq. 5).

Appendix B

Neutron probe and rock moisture measurement techniques

B.1   Introduction

To monitor the spatial and temporal dynamics of rock moisture in the field, a neutron probe was selected because it is portable, minimally invasive, and highly sensitive to changes in volumetric moisture content. For long term monitoring, neutron probes have proven stable and robust (e.g. Wierenga et al., 1987). A radioactive source (^{241}Am-Be) within the probe emits high energy ($>2x10^6$ MeV) neutrons, that upon collision with Hydrogen nuclei, are slowed. The approximately spherical cloud of slow, thermal neutrons (< 0.025 eV) are counted using a ^{3}He detector located within the probe and the raw neutron counts, N (counts per 16 seconds) are recorded. The radius of the sphere of influence is inversely related to the volumetric moisture content, θ, of the surrounding material (Olgaard, 1965; Kristensen, 1973) and can range from 0.16 m near saturation to 0.7 m in dry conditions (Gardner, 1986). N is generally linearly proportional to θ within the sphere of influence and a quantitative, stable relationship between N and θ can be established via a probe-specific and casing-specific calibration.

Field, theoretical and laboratory techniques can be used to establish this calibration relationship. The magnitude of θ relies on material specific calibration in the laboratory or field, and the challenges associated with material hetereogeneity and sampling of deep unsaturated material precludes the generation of a robust material or layer specific calibration at our study site at this time. Additionally, interfaces between material of varying bulk density has been shown to significantly influence the conversion of N to θ (Wilson, 1988, Yao et al., 2004) and the hetergeneous nature of fractured, bedded sedimentary rock leads to abundant interfaces between materials with different bulk densities. Theoretical calibration relationships, which are based on theoretical analysis of neutron diffusion, also require accurate knowledge of the distribution of material properties, specifically the solid phase elemental composition of the rock and soil. At present, it is not feasible to obtain these data within the heterogeneous weathered material that is the focus of this study, and therefore distinctions between changes in water content and changes in solid phase material properties can not be made within a theoretical, laboratory, or field calibration framework.

In this study, we seek to understand the controls on the spatial and temporal dynamics of water transport within weathered, fractured rock, and thus we focus on changes in θ over time rather than the absolute magnitude of θ. Neutron probe data have been shown to provide accurate measures of successive changes in θ at a specific location over time (e.g. Long and French, 1967). Quantitative interpretation of changes in moisture content have been made in well-characterized heteregeneous soil environments and considered within a water budget framework (e.g. Wierenga et al., 1987). The estimation of changes in θ relies on a calibration relationship between N and θ.

Given these challenges and the objective of the study, we use a variety of techniques to quanitatively evaluate the relationship between N measured in downhole surveys and the magnitude of moisture content changes that occur in the subsurface at our site. The objective of this document is to describe the results of efforts aimed at quantitatively

evaluating neutron probe measurements at the Rivendell field site. First, we describe the results of laboratory barrel calibration experiments where we establish a probe-specific and casing specific calibration relationship between N and θ for uniform materials. Second, we describe the results of co-located field (neutron probe) and laboratory (gravimetric) moisture content measurements that were taken when the monitoring boreholes were installed. We also quantify the proportion of bound or strucutral water and free water within saturated rock samples extracted from the neutron probe monitoring boreholes. Finally, we compare neutron probe monitoring results to continuous moisture content monitoring efforts at Rivendell.

The barrel experiments were used to derive a casing-specific and probe-specific calibration relationship between N and θ. The other datasets, in addition to the barrel experiments, were used to quantify uncertainty in the calibration relationship. Together, these methods provide constraints on changes in θ observed using successive neutron probe measurements and allow for the quantitative interpretation of changes in N in terms of θ.

To further minimize uncertainty in neutron probe derived moisture content measurements, several precautionary measures were taken in the field. Discrepancies in survey-to-survey probe placement are expected to influence readings (Wilson, 1988), and were minimized in the field by using the same graduated cable for the entire duration of the study. To avoid inter-probe differences, the analyses presented here are based on data derived solely from the same physical probe (CPN 503DR Hydroprobe, Instrotek Inc. Serial No. 4340702152). Other probes were used during the study (CPN rental and LBNL-owned) and the data derived from those probes was consistent in magnitude and pattern, however, the data are not shown here to limit uncertainty in the quantitative evaluation of water budget calculations. An inter-probe comparison can be derived (e.g. Ward et al., 2000) and used to compare datasets in future analyses.

B.2   Barrel Calibration

To develop a casing-specific and probe-specific relationship between volumetric moisture content, θ, and neutron counts, neutron probe measurements were made in 55 gallon drums filled with uniform material following laboratory calibration procedures described in Silvestri et al., 1999. A linear relationship between θ and N is commonly observed for moisture contents lower than approximately 40%. The drums were cased with the same casing used to line the boreholes at the Rivendell and Sagehorn field sites (see Table B.1) and neutron counts were measured in the drums at different volumetric moisture contents. The materials and their properties are listed in TableB.2. One motivation for performing a casing and probe-specific calibration, was to evaluate the role of material properties on relationship between changes in moisture content and changes in neutron counts (i.e. the slope of a linear calibration relationship) because this is the parameter on which our analysis relies. We therefore used two materials: sand and crushed rock. The weathered,

fractured fine-grained rock at the site is likely better represented by the crushed rock than the sand. Nonetheless, the two materials were used to evaluate the influence of material properties on the calibration.

Generally, neutron counts, N, are converted to a count ratio, C_R by dividing each measurement by a standard count, N_S to account for radioactive decay of the neutron source over time (i.e. $C_R = \frac{N}{N_S}$). The standard count is made within the probe shield atop the probe carrying case at the time of the survey. Over the course of the study, no long term changes in standard counts were detected that would reflect decay of the Am/Be source (Figure B.1). Repeat standard count measurements and duplicate measurements at downhole survey depths were taken regularly to track any changes in instrument precision in time and to evaluate any external influence on data quality (Figure B.2). Survey dates for which the standard count exceeded 2 standard deviations of the long term mean were excluded from this analysis and were associated with malfunctioning of the 3He detector which required maintenance. Kramer et al. (1995) report that random error in the standard measurement and monitoring measurements can compound and suggest that counts are used, rather than standard counts. Because no apparent temporal trend in standard count (Figure B.1A) or repeat measurement precision (Figure B.2B) was observed, and we seek to minimize uncertainty, we elected to regress develop a calibration relationship between N and θ, rather than C_R and θ.

Methods

Setup

The two types of casing present in the field (Table B.1) were used in the barrel calibration. Because they are continuously slotted (to serve as monitoring wells), aluminum tape (Nashua Brand 322) was applied to the exterior of the casing to prevent water from entering the borehole. The influence of the tape was evaluated by measuring counts in an air filled barrel with and without the tape. Count variation was approximately 4% on average, which exceeded the variability between repeat measurements for each treatment, and there was no clear relationship between counts measured with and without the foil. The effects of foil were therefore neglected on the calibration.

Volumetric water content measurement

Several methods for determining θ of the cabliration barrel contents were employed. First, volumetric moisture content of the calibration material were measured in the laboratory. Three 250 mL samples of each material were collected for gravimetric analysis. The initial moisture content was measured. One 250 mL sample of each material was saturated by adding a measured amount of water. The samples were weighed before and after saturation to determine the mass and volume of water added. This volume of water added was used the calculate the saturated water content. Second, A handheld portable TDR (Fieldscout, Spectrum Technologies, Inc.) was used on two different settings ("Standard"

and "Hi-Clay") on both materials at unsaturated (initial) and saturated (final) states. Lastly, a water balance over the barrel volume was calculated. The volume of water added to the barrel (volume of barrel less the volume of the casing) was used to calculate θ over the barrel. There was significant uncertainty in calculating the water budget over the barrel because of the tendency of water to pond and spill on the top of the barrel during water application. That measurement was used simply to verify general consistency with laboratory derived measurements. There was poor agreement among the TDR and gravimetric measurements which is likely due to the inaccuracy of the the calibration equations internally programmed in the TDR instrument (Spectrum Technologies, Inc.). Therefore, the laboratory derived gravimetric moisture content measurements were used to derive the calibration relationship betewen N and θ.

For saturated moisture content measurements, neutron probe surveys were made as the barrel was saturating (revealing clear wetting fronts, Figure B.4) and water was continually added until two conditions were met: ponding was observed on the top of the barrel and stable neutron counts were achieved in the middle of the barrel (Figure B.4). Due to experimental challenges, measurements in 2 inch casing were not made in unsaturated crushed rock. Instead, a value for unsaturated crushed rock in 2 inch casing was calculated using the relationship between the two casing sizes (Figure B.6) and the measurement made within the 3 inch casing (Table B.6).

Results

Separate linear calibration relationships were derived for the two materials (sand and crushed rock) and two casing diameters (2 inch and 3 inch). Data used for the calibration are shown in Table B.3 and the calibration equations are shown in Table B.4. Additionally, a calibration relationship between 2 inch and 3 inch PVC was derived (Figure B.6).

Calibration equation Due to uncertainties in material properties and the variability of material properties throughout the profile, the calibration equation used to derive θ from measurements of N in the field is the largest source of uncertainty in the calculation of $\Delta\theta$ and S. Here, we establish a calibration equation on an idealized material and compare the results of the calibration to field measurements to establish a framework for quantifying uncertainty in calculations of $\Delta\theta$ and S.

The change in moisture content resulting from a change in neutron counts is greater for neutron absorbing material. Therefore, the slope of a linear calibration bewteen neutron counts, N, and volumetric moisture content, θ, is greater for larger casing diameter and higher neutron absorbing material (crushed rock in this case). Separate calibration equations are established for different casing diameters (Table B.4).

Figure B.12 compares all field data to neutron probe measurements made in idealized materials at known moisture conditions. All field measurements exceed barrel calibration measurements made in unsaturated crushed rock and unsaturated sand demonstrating

that field conditions do not approach the low moisture contents measured in kiln dry sand (0.003) and dried crushed rock (0.1).

With the exception of some measurements made in the upper 2.5 m, almost all field measurements exceed the neutron counts measured for saturated crushed rock ($\theta = 0.26$). Therefore, almost all θ calculated from field measurements using the crushed rock calibration relationship would exceed the experimentally measured range (i.e. extrapolated) and all field rock moisture measurements would be interpreted as higher than saturated crushed rock. The crushed rock calibration relationship is therefore not representative of the neutron response at our field site. However, the establishment of a calibration relationship for crushed rock does provide some constraint on the influence of material properties on α for the same probe and casing material, and demonstrates that material properties in addition to moisture content influence the calibration relationship.

With the exception of measurements made near the water table in deep boreholes, all field measurements of N are less than that established for saturated sand ($\theta = 0.41$). Field measurements lie consistently between the neutron counts measured for saturated crushed rock and saturated sand. Moisture contents in the monitored boreholes in the field are therefore likely to be between approximately 0.26 and 0.41.

Neutron counts measured in a water-filled barrel were approximately 8000 and 12000 counts/16 second for the 2 inch and 3 inch casing respectively. This observation implies that measurements made in the field that approach 8000 or 12000 reflect a saturated borehole, rather than a saturated formation, and should be discarded. This results from the neutron probe approaching the water table as it is lowered in the borehole. At moisture contents greater than approximately 0.4, the relationship between N and θ is non-linear (Kramer et al., 1995). When compared to measurements made in sand and rock, our data in water-filled barrel confirm this non-linear behavior at high moisture content. This non-linearity may be important when interpreting the dynamics at depth in Wells 13, 14, 15, and 16, where we observe an abrupt and repeatable increase in N of approximately 2000 counts/16s and significant changes in N over time. These high count values may reflect moisture contents that lie within the zone described by a non-linear relationship between N and θ. If this is the case, then the changes in θ in this zone may be smaller than what would be predicted using a linear calibration relationship.

The crushed rock, which likely does not apply to the material at the site, has a higher calibration slope, α, relative to sand. Because of the linear calibration relationship, differences in the calibration slope are easily translated into differences in rock moisture storage. The crushed rock calibration slope, $\alpha_{crushedrock}$ is 1.37 times the slope for sand, α_{sand} (Figures B.4) leading to 1.37 times the amount of calculated rock moisture storage S. Comparison of the maximum change in moisture content, $\Delta\theta$ and depth-cumulative rock moisture storage, ΣS, in Well 15 (Figure B.13) shows that over the entire profile, the crushed rock calibration leads to a 200 mm difference in total amount of rock moisture storage in the unsaturated zone. The choice of calibration slope is therefore significant when using neutron probe data to calculate rock moisture storage, however, the complexity of the material precludes us from developing calibration relationships at each individual

measurement depth. Furhter, there is no established method for quantifying uncertainty in the slope of calibration equations. Therefore, our approach is to use a single calibration relationship and consider all data derived from that calibration relationship to be a "sand equivalent" measurement, i.e. the calculated moisture content change that would occur in a material with the same elemental composition as sand. It is important to note that this sand-equivalent calibration relationship is only expected to differ from what would be the true relationship due to differences in the concentration of neutron absorbing material (e.g. iron), not in pore structure or bulk density or any other material property. The concentration of neutron absorbers within solid material is the way in which bulk density influences the calibration. For the same solid material composition, a higher bulk density leads to a higher concentration of neutron absorbers and thus a higher slope of the calibration relationship (i.e. smaller change in counts needed to change moisture content).

Uncertainty in the slope of the sand calibration lies in the very small uncertainties in the parameters measured in the calibration (N and θ). Using the standard deviation of the measured parameters leads to an uncertainty in the slope of approximately 2.5% which leads to a 2.5% uncertainty in rock moisture storage, S. For Well 15 (Figure B.13) this would lead to an uncertainty of approximately15 mm over the entire profile, which is much less than the 2.2-3.2 mm/m uncertainty associated with instrument precision. Note that uncertainty in the barrel calibration arises mainly from the potential for air pockets to develop within the barrel (Kramer, 1995) during saturation which lead to spatial heterogeneity in moisture content and a discrepancy between laboratory and barrel conditions. This source of uncertainty is not accounted for in our calculations.

Radius of influence A higher concentration of neutron absorbing material leads to a smaller radius of influence, even at low moisture content. In soil and crushed rock filled barrels, a minor increase in neutron count was detected when 10 gallons of water were placed around the exterior of the barrel (Figure B.11). The radius of the barrel was approximately 28.6 cm, therefore, within very dry sand, the radius of influence may extend beyond 28.6 cm, however, at higher moisture contents, the radius of influence is expected to be confined to the immediate vicinity of the borehole ($<<$28 cm). within the borehole.

Influence of casing and casing diameter

The air gap between the probe and the subsurface environment as well as the casing material influences the relationship between $\theta$and N. Conditions closest to the probe are weighted most heavilty in readings, therefore the air gap and casing material are expected to strongly influence the neutron response. Less hydrogen is present in air than in soil and rock leading to a decrease in N with increases in casing diameter. Data from 3 inch and 2 inch barrel calibration experiments were compared to derive a relationship between 2 and 3 inch slotted PVC casing. The data appear linear but both linear and quadratic regression were performed. The quadratic fit was used to calculate a value for unsaturated crushed

rock with 2 inch casing because of difficulties encountered with this measurement during the experiment (Table B.4 and B.3). Future work will seek to make this measurement as well as measurements in other, diverse media. Generally, larger casing diameter leads to a reduction in the number of counts measured for a given moisture content. Even for 3 inch casing, however, jugs of water were detected in unsaturated (dry) sand approximately 28 cm away from the probe.

Differences in neutron response among the two casing diameters increased with increasing moisture content. In dry sand, N differed by <100 counts/16 seconds. Measurements made in water showed differences greater than 4000 counts/16 seconds. Calibration data show a tendency for the standard deviation to scale with the mean (i.e. the coefficient of variation remains consistent). However, repeat moisture content measurements in the field do not show a relationship between the standard deviation and mean of repeat measurements (Figure B.2). (Repeat measurements are performed routinely to evaluate instrument precision and detect any changes to precision.) A significant difference between measurements made in 2 inch and 3 inch boreholes is observed. Measurements range between 3500-5000 in 3 inch boreholes and 5500-7000 in 2 inch boreholes, which is consistent with barrel calibration observations which suggest that N in 2 inch boreholes is approximately 1.54 times that made in a 3 inch borehole. Standard deviations of repeat measurements in the field are in range of those measured in the barrel calibration experiments for unsaturated and saturated media, and in some instances, in both casing diameters, exceed the standard deviation of measurements made in a water filled barrel.

Measurements made in aluminum casing tend to closely resembles those taken in an unlined hole (Kramer et al., 1995). A minimum of a 15% reduction in N has been observed for PVC access tubes relative to aluminum casing (Marais, 1960). Manufacturer calibrations performed in aluminum casing and PVC show that schedule 40 causes a 50% reduction in N relative to aluminum (Table B.4).

At the time of drilling, neutron probe surveys were conducted in cased and uncased conditions in W15 and W16 during drilling and after drilling was complete (Figure B.8). In W15, drillers encountered a water table at approximately 26 m depth and this water was introduced to the upper portions of the borehole during the augering process. Neutron probe surveys conducted at the conclusion of the drilling therefore reflected elevated moisture contents associated with the drilling process. As expected, the introduction of schedule 40 PVC as casing served to shield neutrons and therefore decrease neutron counts or count ratio for a given measurement location. Neutron probe surveys were conducted in October of 2010 to allow near well-bore moisture content influence from drilling to subside. These Oct 10, 2010 np survey data were used for comparison with gravimetric moisture content measurements made at the time of drilling (Aug 18-20, 2010). The reduction in counts resulting from the installation of slotted PVC casing was significant. Uncased neutron counts were approximately 1.75 times those of cased conditions.

B.3   Laboratory gravimetric moisture content analysis

Methods

Thermogravimetric methods were used to evaluate the amount of free and structural water in the saprolite and rock. The amount of free water was determined by measuring the mass lost to heating at 105 C. The structural, or bound, water was determined by measuring the mass lost between 105 and 500 C. The amount of organic compounds present in the rock was characterized by measuring the mass lost to heating between 500 and 600 C.

Two types of samples were used to quantify free water 1) Bulk: the rock matrix including any particulates or soil like material that occupied fractures and 2) Rock matrix: chips of rock matrix which may have had fractures that were not observable. Both types of samples were collected during drilling but bulk samples were analyzed during drilling (August 2010). These samples were logged for lithologic characterization (primarily grain size), color, presence of weathering rinds, coatings, or precipitates, presence of roots, extent of fracturing, and friability. Samples of drill cuttings were immediately taken for gravimetic moisture content analysis. These samples consisted of the entire rock sample (bulk). The samples were bagged, placed in a cooler, and transported to a laboratory located within the Angelo Coast Range Reserve within hours of retrieval. To quantify the gravimetric moisture content at the time of samples, the samples were weighed before and after drying at 105 C for 24 hours or until mass was unchanged.

At a later time, different samples of just the rock matrix were taken from storage for measurement of saturated gravimetric moisture content. These samples of rock matrix were soaked in deionized water for 96 hours and dried by hand using Kim wipes until no moisture was observed on the Kim wipe. Some samples completely disintegrated during the soaking and wiping process and were not used for analysis (e.g. W7 30 ft, and W6 12 ft). The difference in mass between the soaked sample and the sample dried for 24 hours at 105 C was used to calculate the gravimetric moisture content. For both types of samples θ_{grav} was calculated as $\Theta_{grav} = \frac{m_{wet}-m_{dry}}{m_{dry}}$ where m_{wet} is the mass of the sample prior to oven drying, and m_{dry} is the mass of the sample after drying. The rock matrix samples were subjected to heating at higher temperatures to quantify the structural water and organic content. Importantly, the bulk samples were collected at the end of the dry season at the time of drilling and theoretically represent a minimum in dynamic moisture content. These samples were taken from Wells 14, 15, and 16.

Separate samples were used to quantify the total elemental composition of rock samples including loss on ignition. The loss on ignition, the percent mass lost to heating at 1000 C, is a measure of the organic content of the sample and was measured in these elemental analyses by ACME Analytical Laboratories, Ltd. (Vancouver, British Columbia, Canada). Upon heating, organic matter is oxidized to carbon dioxide and ash at temperatures

between apprxomiately 200 and 500ºC and carbon dioxide is released from carbonate minerals heated between approximately 700 and 900ºC. The detection limit for loss on ignition is approximately 0.1%. Detection limit for heating experiments is approximately 0.5%.

Bulk density was measured in samples that appeared to be minimally disturbed during standard penetration testing during drilling. Bulk density was measured by calculating the volume of the sample as the length within the sample barrel times the inner area of the barrel and weighing the dry sample after drying at 105 C for 24 hours.

Results

Gravimetric moisture content

The gravimetric moisture content of the rock matrix was measured in the laboratory (Figure B.14) and is consistently between 2 and 5% water by mass. Data from the upper 7 m indiciate that the bulk density of weathered material (bulk samples) ranges from 1-3 g/cm3. At other sites, the bulk density of mudstones or clay rich rocks may vary between 1.75 (saprolite) and 2.44 when weathered, but is typically 2.7 when unweathered (Dorch and Katsube, 1996). Given these bulk densities, the volumetric moisture content calculated from our gravimetric moisture content observations are approximately 5-14%. Analysis of the groundwater response to storms shows that, at depth, a very small fraction of the rock passes fluids in response to storms, while the remainder of the rock matrix may remain saturated (Chapter 6).

Gravimetric moisture content associated with free water, here defined as the water lost to heating at 105 C, was generally higher for bulk samples, particularly at depths shallower than 10 m (Figure B.15). At depth, matrix and bulk samples show similar water contents independent of depth and also a similar relationship between structural and free water (Figure B.15). Further, the water content of matrix samples that were soaked for 96 hours (approximating saturated conditions) were similar to those measured at the end of the dry summer suggesting that the rock matrix may remain saturated at depth. There appears to be a break in this relationship at approximately 10 m depth.A t shallow depths (<10 m), there is large variability in the amount of free water present in both matrix and bulk samples. This reflects the variability in porosity in the matrix. Median gravimetric moisture content of bulk samples at depths less than 10 m was 8.4% while shallow matrix samples were 6.2%. At depth, the median gravimetric moisture content for bulk and matrix samples were 5 and 4.1% respectively. The lower free water content of matrix samples likely reflects water retention within secondary weathering products in bulk samples.

The bulk samples were collected at the conclusion of the dry season and thus represent a seasonal low moisture content condition. The higher free water content of dry-season bulk samples relative to saturated matrix samples suggests that much of the free water resides within fractures, either along the fracture surface, or within clay minerals and

weathering products that occupy the fracture or pores within the matrix. Though our measurements do not indicate the potential at which the free water is held, the observation that the the free water within bulk samples exceeds that extracted from saturated matrix suggests that even at the conclusion of the dry season, there is water present in pores that are not associated exclusively with the rock matrix and thus might be more accessible to vegetation.

Loss on ignition (LOI), the fraction of mass lost due to heating at 1000 C, provides a measure of the carbon content of a rock as well as the amount of structural water present. Our data indicate that at shallow depths, the LOI and the structural and organic content (105-600 C) are in relatively good agreement while at depth, there is significant (discrepancy (of several percent) (Figure B.17). The difference between LOI (100-1000 C) and the independently measured structural and organic content (105-600 C), may be attributed to the carbonate mineral content because carbonates typically release carbon dioxide between 700 and 900 C. Carbonates are indeed detected in depth regions associated with large discrepancies between LOI and the structural and organic content (Figure B.17).

Neutron response to bound water

The neutron response does not distinguish between hydrogen in free or structural ("bound") water. This results in the potential for overestimation of the free water content when developing calibrations. A study attempting to correct for the influence of structural hydrogen in a clay soil found that bound water led to a parallel shift of the calibration slope (Babalola, 1971) (i.e. the slope of a linear calibration remained the same while the intercept changed). Gravimetric moisture content measurements of rock matrix samples reveal that there is significant variability in the amount of structural water throughout the profile (Figure B.15 and B.14) and there is no apparent relationship between free and structural water (Figure B.16). Among the samples analyzed, 45-80% of the water extracted from the saturated argillite matrix was free water and 20-55% of the water was structural water. The median value for the fraction of extracted water that was free water was 58%.Therefore, a significant amount of hydrogen detected by the neutron probe is associated with structural water. However, this structural water is only expected to influence the magnitude of $\theta$and not $\Delta\theta$ or Sat a particular location.

Gravimetric moisture content measurements of free water made using bulk samples extracted at the end of the summer range from 4-16% with a median value of 7.8% (Figure B.15). Significant variability is observed in the upper 10 m with decreasing variability at depth.

Comparison of neutron counts to gravimetric moisture content measured during drilling

Neutron counts measured during neutron probe surveys are proportional primarily to the abundance of hydrogen, which is present in free water as well as structural water.

In the previous section we demonstrated 1) free water may constitute around half of the total water present, 2) free water in bulk samples in some cases exceeded free water in saturated matrix samples, 3) there is no relationship between structural and free water and 4) there is significant depth-dependence to the relationship between structural and free water. Therefore, in addition to uncertainties in bulk density that influence the calculation of volumetric water content from gravimetric water content, we expect that, unlike neutron probe calibrations that are commonly developed in soils (e.g. Hu, 2009), the relationship between neutron counts and the amount of free water observed in bulk samples analyzed during drilling should not directly reveal a calibration relationship between volumetric water content and neutron counts. Nonetheless, these data provide insight into the relationship between neutron counts in a cased borehole and the amount of water present within bulk samples at the conclusion of the dry season. These data also provide constraints on the calibration relationship because of the fairly well constrained bulk density of weathered rock and soil (approximately 1.5-2.7 g/cm3) relative to moisture content and neutron counts.

Gravimetric moisture content measurements were compared to the nearest neutron probe measurement conducted shortly after drilling (Figure B.20). There is no clear relationship between gravimetric moisture content and neutron counts (Figure B.20), however there does seem to be a tendency for deep (>15 m) samples to have low $\theta_{gravimetric}$ and high N relative to shallower samples which span the entire range of $\theta_{gravimetric}$ and N.

Figure B.21 compares volumetric moisture content derived from neutron probe and gravimetric moisture content data. Neutron counts were converted to volumetric moisture content using the calibration relationship for sand in 3 inch casing (Table B.4) and gravimetric moisture content was converted to volumetric moisture content by multiplying by a range of bulk densities, ρ_{bulk}, from 1.4 - 2.7 g/cm3 typical of shale saprolite and matrix. The gravimetric data only account for free water while the neutron probe is sensitive to both bound and free water (and solid elemental composition), therefore, it is expected that the volumetric moisture content derived from gravimetric samples would be low relative to those measured by the neutron probe. Indeed, even for a large range of ρ_{bulk}, moisture contents derived from gravimetric samples tends to be lower than what is predicted by the neutron probe.

In argillite samples, the neutron probe derived volumetric moisture content measurement is generally higher than that derived from the gravimetric samples suggesting that structural water should be considered in the prediction of volumetric moisture content of free water in rock. The observation that many of the argillite samples lie between the 1:1 and 2:1 line on Figure B.21 is consistent with observations that structural water can comprise 20-55% of the water in the argillite (Figure B.16). Incorporation of structural water into the calculation of volumetric moisture content is necessary when a material specific, field calibration relationship between neutron counts and gravimetric sampling is sought. Here, we show that the magnitude of the moisture content measured by the neutron probe (and a calibration for sand) is reasonable when structural water is considered.

Note that use of the crushed rock calibration would lead to a larger difference between gravimetric and neutron probe derived volumetric moisture content measurements.

The shallowest samples in W14 and W15, which show much higher gravimetric derived moisture contents, are significantly coarser grained and are likely representative of sandstone interbeds. These samples show a distinctly different relationship between volumetric moisture content derived from neutron counts and gravimetric sampling likely because of the differences in bound water and possibly elemental composition. Further, data at the low range of ρ_{bulk} (which is more appropriate for these shallow weathered samples) show relatively good agreement between neutron probe and gravimetric data suggesting that the magnitude of moisture content detected by the neutron probe for sandstone saprolite samples may be distinguishable from the dominant argillite lithology and the neutron probe does a relatively good job of measuring moisture content for this material.

Little correspondence is observed when comparing neutron counts to gravimetric moisture content measurements (Figure B.20) demosntrating that individual measurement locations require different calibration intercepts, β. Because only one moisture content condition was measured at each depth, the data do not constrain variability in slope throughout the profile. However, gravimetric observations of the deepest samples in W14, W15, W16, suggest that a lower slope is needed to explain the neutron response. At these depths, the gravimetric moisture content measured at the time of drilling was very similar to that of soaked samples suggesting that very little change in moisture content occurs at these depths. Yet, despite small or no changes in moisture content over time, we observe relatively large changes in neutron counts (~1000 counts/16 s) in successive measurements. Therefore, at these depths, the changes in rock moisture predicted by the sand calibration equation may be higher than the actual changes.

The role of grain size

The matrix samples that were analyzed for free and structural water were classified by grain size as weathered and unweathered argillite, and sandstone to evaluate the role of weathering and lithology on the amount of structural water present, with the hypothesis that a larger proportion of structural water would be observed in the argillite samples. The organic content and structural water was fairly consistent among all types of samples and less structural water was present in sandstone samples. Additionally, the amount of free water in saturated samples tended to be highest in sandstone samples indicating potentially higher porosity in the weathered sandstone matrix. The lowest amount of free water was detected in the unweathered argillite matrix suggesting lower porosity in the unweathered argillite relative to weathered argillite and weathered sandstone matrix. In unweathered argillite matrix, there is approximately equal free and structural water suggesting that the total volumetric water content as detected by a neutron probe or time domain reflectometer would detect this strucutral water. However, by volume, only half of the total water, the free water, has the potential to be dynamic and change at a seasonal time scale.

B.4 Comparison of neutron probe monitoring results with continuous soil monitoring via TDR

Continuous TDR measurements in saprolite and fractured rock

Time domain reflectometry (TDR) sensors were used to monitor moisture content in shallow saprolite and fractured rock. Installation and calibration of the TDR instruments is described in Salve and Rempe, 2013, Salve et al., 2012, and Oshun, 2015. TableB.6 shows the changes in moisture content observed within the continuously monitored shallow saprolite and weathered rock. Water content rises seasonally and in response to storms. The maximum observed moisture content changes reflect the difference between the driest measurement and the maximum observed moisture content, which in all cases occurs directly in response to a precipitation event. These maximum moisture content changes ($\Delta\theta_{max}$) lie between 0.15 and 0.2. Using the wet season mean θ as a measure of the gross change in water content that occurs seasonally, the $\Delta\theta_{seasonal}$ for saprolite and weathered rock measurements lies between 0.1-0.15. These data suggest that depending on the timing of a neutron probe survey (i.e. if a survey occurs during a storm driven peak in moisture content) then neutron probe measurements within saprolite and fractured rock may only show a seasonal change of 10-15%. At shallow depths similar to locations of continuous TDR monitoring in saprolite, neutron count changes of apprxomiately 1500 counts/16 s are observed seasonally in 3 inch cased boreholes (Figure B.12). If these neutron count changes reflect 10-15% changes in θ then we may expect the calibration slope, α, to approach 7e-5 to 1.5e-4. Volumetric moisture content measurements made via gravimetric sampling at 1-1.4 m depths near the ridge top show a range of 24-46% ($\Delta\theta$=0.22) (J. Oshun personal communication) which leads to a calibration slope of 1.5e-4 (Table B.6). Seasonal moisture content changes measured in continuous TDR sensors suggest that changes in rock moisture, at least in the near surface saprolite, may be higher than what is calculated using the sand-equivalent calibration by up to 2 times.

Co-located TDR and neutron probe measurements

Moisture content data from TDR probes installed into a trench at 1 and 1.38 m near W15 were compared to neutron probe measurements at depths between 0.8 and 1.44 m in W15 in an attempt to derive a calibration relationship between volumetric moisture content and neutron counts. There are several reasons why comparison of TDR and neutron probe measurements are problematic, including the scale of measurement and the fidelity of the conversion of TDR data from dielectric to moisutre content. Nonetheless, a comparison between TDR and neutron probe measurements is performed here to evaluate how the neutron response and TDR response compare.

Volumetric moisture content measurements made via gravimetric methods near the trench at various moisture conditions have shown that the TDR calibration of dielectric to volumetric moisture content is consistently high (Oshun, 2015). Additionally, when

the TDR data are used to estimate the addition of soil moisture storage in response to storms, the data consistently show higher moisture changes than precipitation per event. It has therefore been established that TDR overestimate volumetric moisture content significantly and a material specific calibration between volumetric moisture content and dielectric is needed to use the L5 trench TDR quantitatively.

Figure B.19 compares TDR measurements made by two different probes (1 and 1.38 m depth) with neutron probe measurements made at several nearby depths. Though there is significant scatter, a linear fit to the data leads to slopes between 1e-4 and 2e-4 which is an order of magnitude higher than slopes measured in barrel calibration experiments. The maximum change in counts at 1-1.5 m depths in W15 are 3045-4872 and the maximum change in moisture content in the TDR at 1 and 1.38 m is 0.19-0.44. Using these maximum values to derive a linear relationship between N and θ leads to a slope of approximately 1.4e-4. Using the maximum range of moisture content measured via gravimetric sampling by Oshun (2015) and assuming that they correspond to the highest and lowest neutron probe measurements leads to a slightly lower slope of 1.1e-4. This high calibration slope implies that lower changes in counts are needed to generate changes in volumetric moisture content than what was observed in barrel experiments. Beyond issues with the TDR and their representativeness over the volume of observation for the neutron probe, there is a possibility that alteration to the near surface that occurred while drilling leads to an altered environment in the vicinity of the borehole at the depths used to derive this calibration. Cement grout was used to seal the top of the borehole, and though attempts were made to isolate the grout to the soil (<0.5 m), there is a possibility that grout traveled along the borehole wall and is detected by the neutron probe at depths beyond 0.5 m. The presence of grout would buffer the influence of saprolite moisture content changes on the neutron response, leading to a higher calibration slope than would be expected in the absence of grout. It is unknown at this time whether the low calibration slope can be attributed to this borehole construction artifact.

Assuming that well construction and TDR calibration issues are not at play, and that the L5 TDR- W15 neutron probe calibration slope represents the relationship between changes in N and changes in θ in a 3 inch slotted borehole in saprolite, then changes in storage estimated using the barrel calbiration slopes are significantly less than those that would be derived from the L5 TDR -W15 relationship. For example, the maximum change of counts observed between 0.8 and 1.44 m in W15 of 1849, leads to an estimate of 239 mm/m (i.e. 0.25 $\Delta\theta$) of rock moisture storage from the TDR calibration . For the same change in counts, the barrel calibration experiment predicts a change of 133 mm/m. Thus, assuming the TDR based calibration is correct, the barrel calibration may lead to underestimation of rock moisture storage, S, in the near surface in sandy saprolite by a factor of 1.94.

B.5 Summary: Quantitative interpretation of rock moisture measurements at Rivendell

A combination of barrel experiments, gravimetric sampling, and continuous monitoring were used to establish a quantitative framework for monitoring changes in rock moisture at the Rivendell field site. A casing-specific and probe-specific relationsip between neutron counts, N and volumetric moisture content, θ, was established in an idealized material (sand) in barrel experiments. Using this relationship, field neutron probe measurements were compared to continuous TDR monitoring and gravimetric moisture content measurements of material extracted at the time of drilling.

Within the uncertainty associated with the variability of bulk density and the presence of structural water, comparison of the field data with the gravimetric moisture content measurements support the use of the proposed calibration equation. However, gravimetric data from W14, 15, and 16 at the deepest sampled depth, show little difference in moisture content between saturated and drilled (end of dry season) conditions despite large observed differences in neutron counts over time. This suggests that at these depths, the proposed calibration equation overestimates rock moisture storage.

Continuous TDR measurements suggest that α, the slope of the calibration relationship between N and θ, may be 1.94 times higher than the proposed calibration relationship. Additionally, barrel experiments in crushed rock suggest that α may be 1.37 times higher than the relationship established in sand. There is significant uncertainty associated with both the TDR and the crushed rock barrel calibration experiment, however, the data indicate that the proposed calibration relationship may underestimate rock moisture storage significantly.

The two primary sources of uncertainty in calculations of θ, $\Delta\theta$, and S are instrument precision and uncertainty in the slope of the calibration relationship between N and θ. Given the dependence of the calibration on material properties and the fact that material property variability is not feasibly characterized at the spatial resolution detected by the neutron probe, further research is needed to adequately quantify the uncertainty associated with variability in the calibration equation within a heterogeneous profile. Further research is also required to evaluate uncertainty in the slope for a single complex material. In this study, the reported uncertainty is limited to the uncertainty associated with instrument precision (Table B.5) and all data and calculations are reported as a sand-equivalent moisture content. Deviations from the sand-equivalent moisture content are only expected to result from differences in the concentration of neutron absorbing material.

B.6 Well Profile Depth Corrections

Twelve wells were drilled across the Rivendell field site to monitor changes in rock moisture and groundwater levels. To account for differences in well construction and well

location, data are represented in "profile depth." For example, four monitored wells (Wells 14, 5, 6, 7) are located along a roadcut and therefore are missing native soil and saprolite that were removed at the time of the road construction. Reconstructions of the pre-road cut surface yield a profile depth that represents the depth in the weathering profile from the original ground surface (Figure B.22). While drilling Well 12, drillers removed approximately 1 m of material, therefore the first neutron probe measurement within Well 12 is located at 1.5 m from the original ground surface. Drilling of Wells 13, 14, 15, and 16 resulted in significant disturbance in the uppermost 0.5 m. To prevent short circuiting of water through this disturied interval, 4 inch PVC was placed around the well casing and concrete was poured at the surface to fill the disturbed space. Therefore, neutron probe measurements in the first 0.5-0.75 m are discarded in these wells depending on the depth extent of the 4 inch PVC and concrete.

B.7 Tables

Rivendell Well Number	Well Surface Elevation (m)	Total Well Depth (m)	Well Casing Diameter (in)	Well Casing Diameter at Surface (in)
1	400	9.50	2	2
2	420	12.20	2	2
3	421.3	14.40	2	2
5	449	25.30	2	2
6	451.62	19.90	2	2
7	454	19.80	2	2
10	455	27.40	2	2
12	401.8	7.21	2	2
13	420	18.44	2	4
14	445	32.92	3	4
15	468	33.22	3	4
16	455	34.29	3	4

Table B.1: Properties of borehole casing in wells installed in the Rivendell field site.

Sample Description		Dry Bulk Density (g/cm3)		Laboratory Volumetric Moisture Content (%)				TDR Volumetric Moisture Content (%)				Comments
				Dry Moisture Content		Saturated Moisture Content		Dry Moisture Content		Saturated Moisture Content		
		Mean	Standard Deviation	Mean	Standard Deviation	Mean	Standard Deviation	Standard Calibration	High Clay Calibration	Standard Calibration	High Clay Calibration	
Sand	Kiln Dried, 30 Mesh Silica Sand Cemex	1.60	0.018	0.003	0.000	0.413	0.005	0.0	1.1	26.9	52.5	Significant Time Required To Allow Air to Escape During Saturation Process
Crushed Rock	Blue Pathway Fines (Mechanically Crushed Fine Grained Rock) American Soil and Stone in Richmond, CA.	1.58	0.027	0.100	0.008	0.257	0.040	3.2	3.9	12.8	25.2	Settling and Compaction Occurs Upon Adding Water

Table B.2: Properties of material used in barrel calibration experiments.

Casing Diameter (in)	Condition	Material	Neutron Counts		Laboratory Volumetric Moisture Content	
			Mean	Standard Deviation	Mean	Standard Deviation
3	Wet	Crushed rock	2897	47	0.257	0.040
3	Dry	Crushed rock	1309	44	0.100	0.008
3	Wet	Sand	6160	50	0.413	0.005
3	Dry	Sand	458	22	0.003	<0.001
2	Wet	Crushed rock	3778	105	0.257	0.040
2	Dry	Crushed rock	1503*	--	0.100	0.008
2	Wet	Sand	8742	32	0.413	0.005
2	Dry	Sand	365	13	0.003	<0.001
2		Water	12115	128	1.000	--
3		Water	8045	122	1.000	--
*Unsaturated crushed rock was not measured during the calibration experiment, but was derived from the 3 inch data and a relationship between 3 inch and 2 inch casing (Figure #).						

Table B.3: Barrel calibration measurements.

Description	Casing Diameter (in)	Casing Type	Slope	Intercept
Barrel calibration, crushed rock	3	Slotted PVC	9.90×10^{-5}	-2.94×10^{-2}
Barrel calibration, sand	3	Slotted PVC	7.20×10^{-5}	-2.99×10^{-2}
Barrel calibration, crushed rock*	2	Slotted PVC	7.00×10^{-5}	-5.16×10^{-3}
Barrel calibration, sand	2	Slotted PVC	4.80×10^{-5}	-1.54×10^{-2}
Manufacturer	2	Aluminum	2.29×10^{-5}	-6.42×10^{-3}
Manufacturer	2	PVC Sch 40	3.88×10^{-5}	-8.67×10^{-2}
*Unsaturated crushed rock was not measured during the calibration experiment, but was derived from the 3 inch data and a relationship between 3 inch and 2 inch casing (Figure #).				

Table B.4: Parameters for linear calibration between neutron counts, N, and volumetric moisture content, θ.

	Standard Deviation of Repeat Neutron Probe Measurements		
	N (Counts per 16 s)	Θ (m^3/m^3) *	
		2 inch	3 inch
Max Observed	160	0.008	0.012
Mean Observed	45	0.002	0.003
*Theta was calculated assuming the calibration equation for sand			

Table B.5: Uncertainty associated with instrument precision is quantified by comparing repeat measurements. The maximum and mean standard deviation of repeat measurements is shown in units of counts and moisture content, where moisture content was derived from counts using the α_{sand}.

Saprolite Depth (m)	Material Description	Method	Min Θ	Max Θ	Wet Season Mean	Max ΔΘ	Seasonal ΔΘ	Comments	Source
0.7	Argillite Fracture Infill	TDR	0.19	0.39	0.34	0.2	0.15	Pressed Between Fractures	Salve and Rempe, 2012
0.7	Weathered Argillite Matrix	TDR	0.2	0.37	0.33	0.17	0.13	Drilled into Rock Matrix	Salve and Rempe, 2012
0.7	Sandstone Fracture Infill	TDR	0.11	0.26	0.21	0.15	0.10	Pressed Between Fractures	Salve and Rempe, 2012
0.7	Weathered Sandstone Matrix	TDR	0.18	0.33	0.3	0.15	0.12	Drilled into Rock Matrix	Salve and Rempe, 2012
1.0	Interbedded Sandstone and Mudstone Saprolite	Gravimetric Sampling	0.24	0.46	--	0.22	--	Manually Collected, May Not Capture Full Range of Moisture Contents	Oshun Dissertation
1.0	Interbedded Sandstone and Mudstone Saprolite	TDR	0.28	0.47	0.39	0.20	0.11	30 cm TDR in backfilled trench	Rivendell TDR L5
1.38	Interbedded Sandstone and Mudstone Saprolite	TDR	0.20	0.43	0.34	0.24	0.14	30 cm TDR in backfilled trench	Rivendell TDR L5

Table B.6: Seasonal and maximum moisture content changes observed in TDR sensors installed in fractured, weathered rock. The mean wet season θ is the mean θ over the 2014-2015 wet season.

Well	Profile depth at ground surface (m)	
5	1	
6	1.3	
7	0.7	
14	0.3	

Table B.7: Depth below reconstructed ground surface at Well 5, 6, 7, and 14 (i.e. the depth within the profile represented by the contemporary ground surface).

B.8 Figures
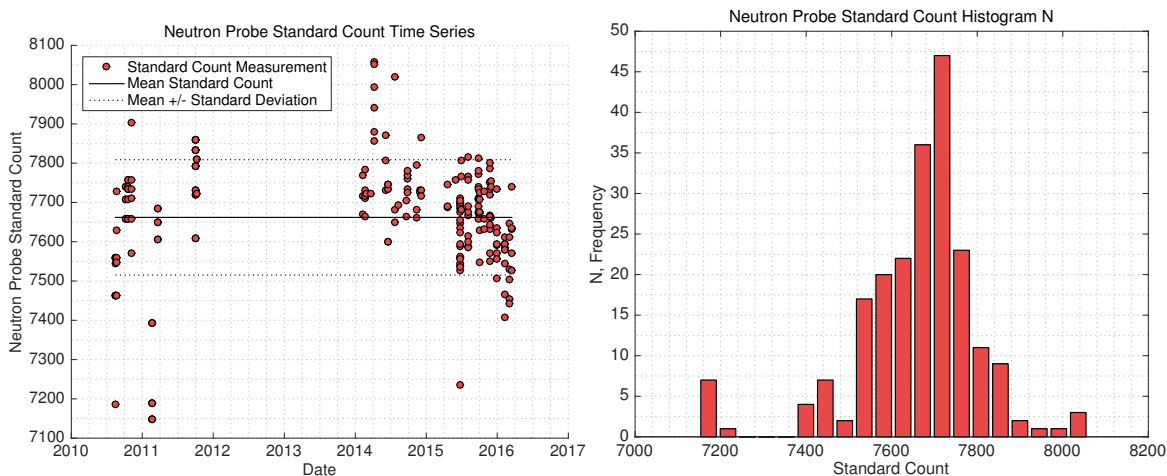
Figure B.1: Standard count measurements, which can be used to quantify the decrease in neutron flux of the radioactive source over time due to decay, does not show a systematic decrease over the period of observation. Relatively large variability in standard counts is observed.
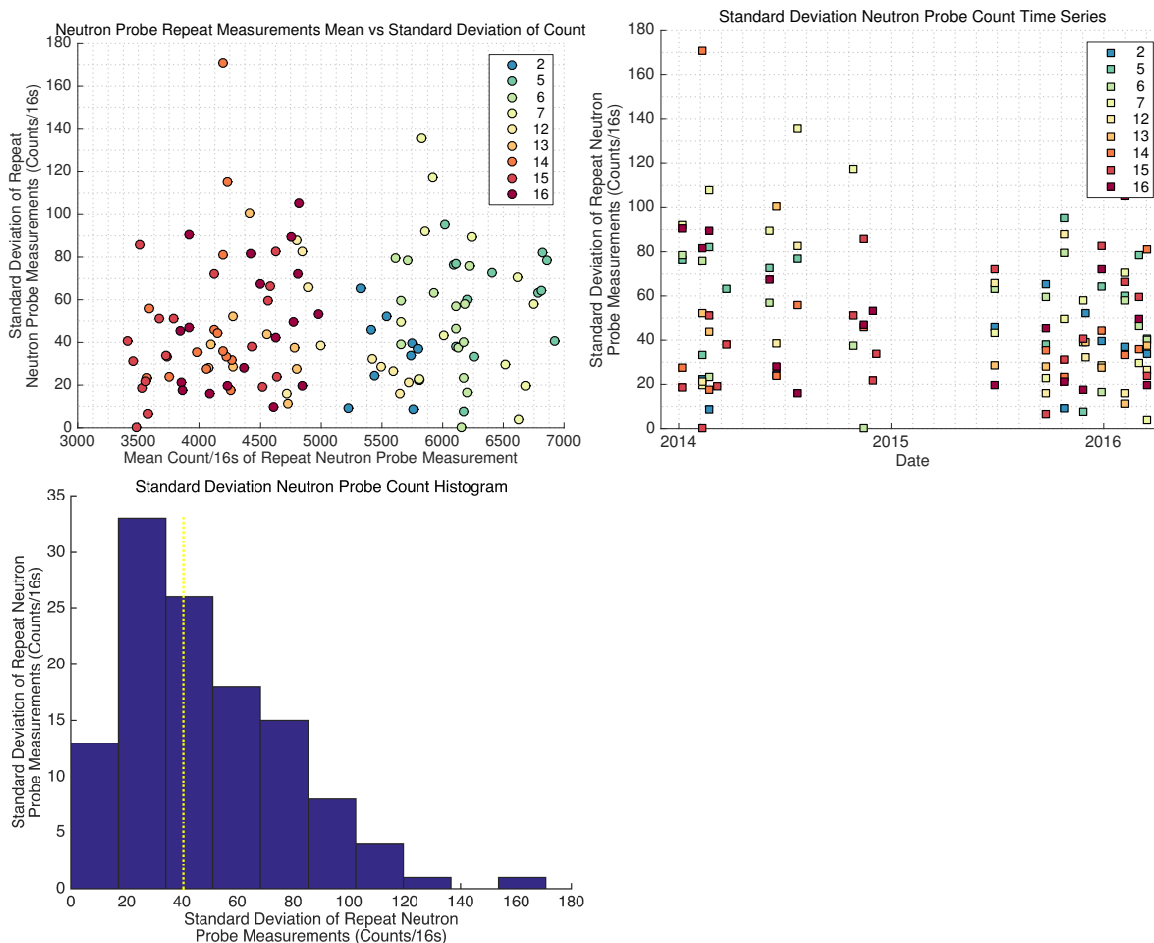
Figure B.2: Repeat measurements are taken regularly to evaluate the precision of the neutron probe. They are often but not always taken at 10 m depth in the same well. Standard deviation does not show any relationship with time or measurement location (Colors reflect Well Number). Precision does not scale with magnitude of measurement (i.e. no relationship is observed between the magnitude of the measurement and the standard deviation). The median of the standard deviation for all repeat measurements was used as a measure of uncertainty for neutron count measurements (yellow line).
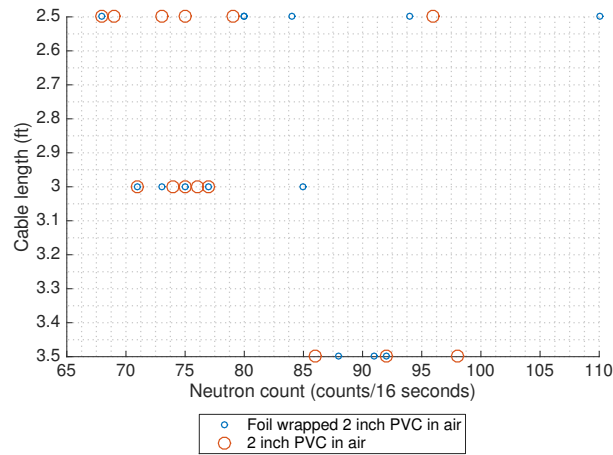
Figure B.3: Alumnium tape was used to wrap slotted PVC casing during barrel calibration. The influence of the foil tape was negligible.
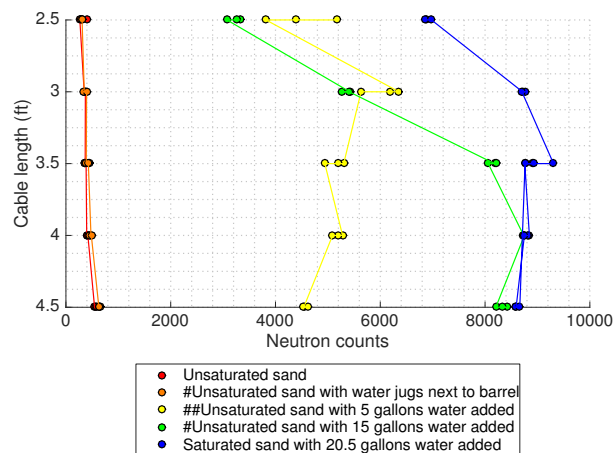
Figure B.4: Results of neutron surveys performed in 2 inch casing during wetting of barrel. Cable length represents the depth within the barrel. Edge effects of the barrel are observed at 2.5 ft cable length.
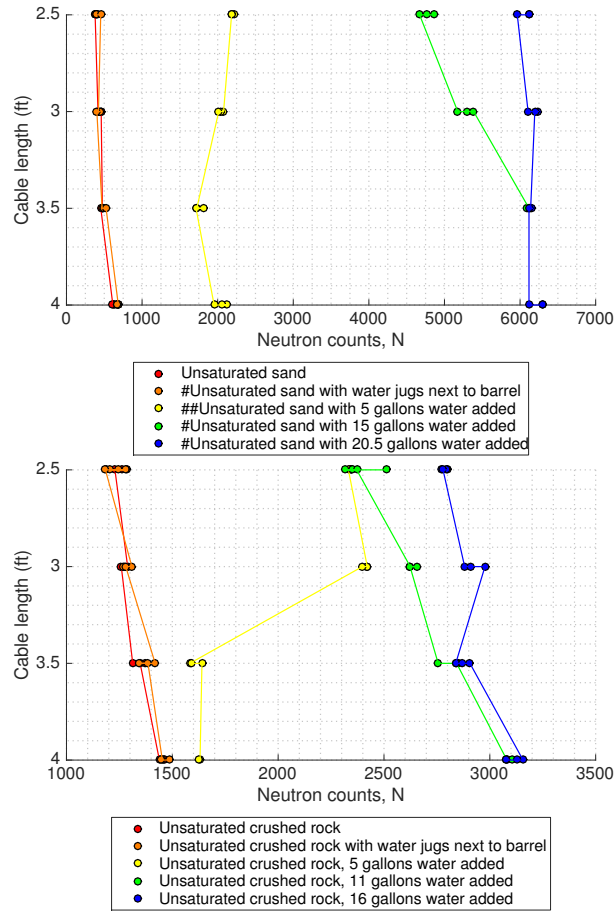
Figure B.5: Results of neutron surveys performed in 3 inch casing during wetting of barrel. Cable length represents the depth within the barrel. Edge effects of the barrel are observed at 2.5 ft and 4.5 cable length.
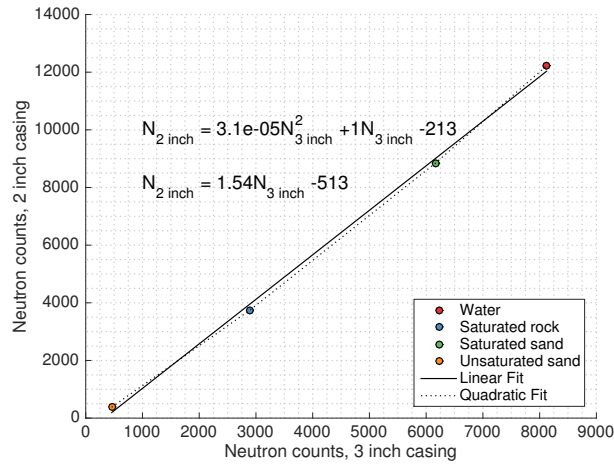
Figure B.6: Relationship between neutron counts measured in 3 inch casing and 2 inch casing in barrel calibration experiments.
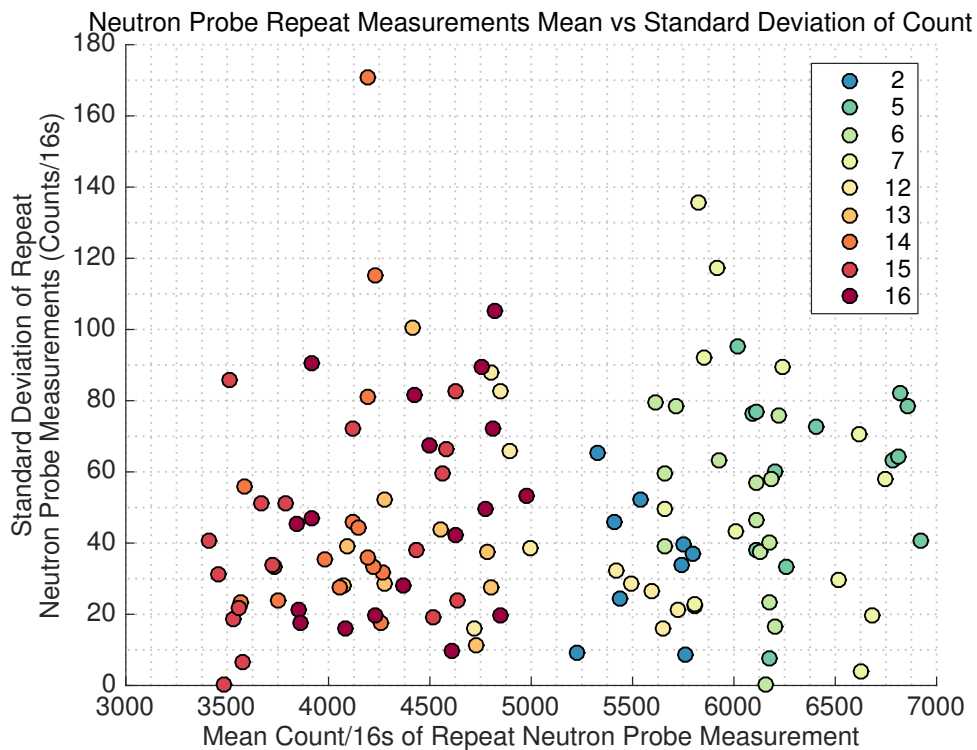
Figure B.7: In the field, repeat measurements are performed routinely to evaluate instrument precision. There appears to be no relationship between the mean and standard deviation of neutron counts, nor is there significant difference between the standard deviation measured in 2 inch (W2-7) and 3 inch (W12-16) wells.
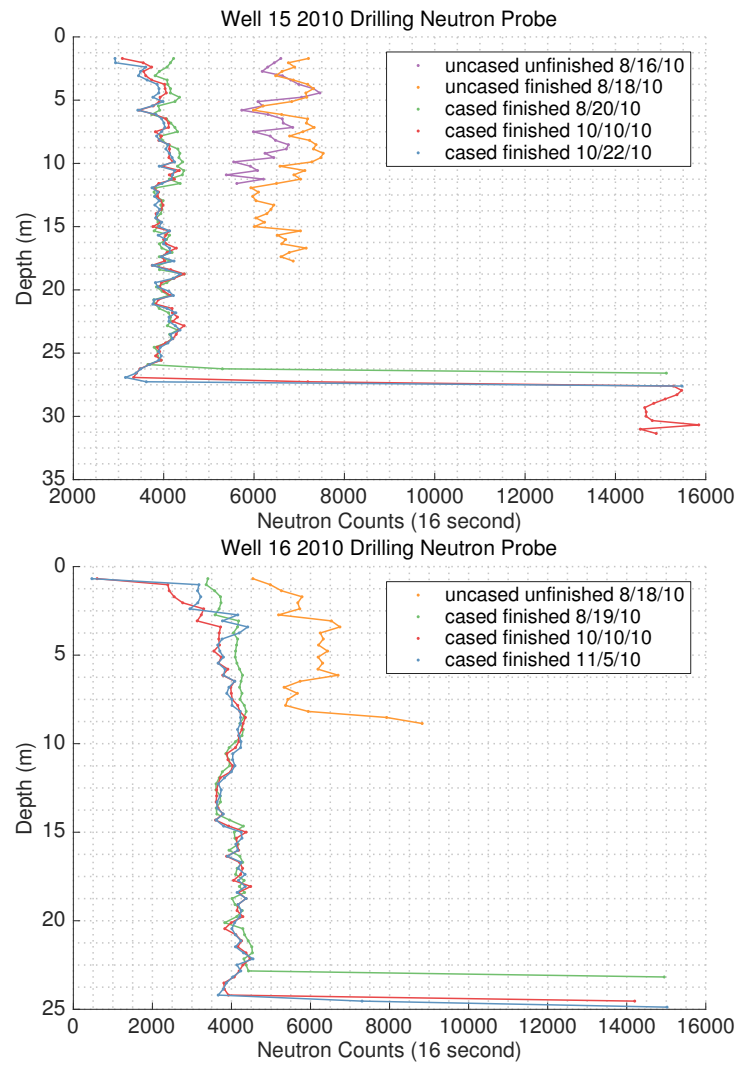
Figure B.8: In Wells 15 and 16, neutron probe surveys were conducted in cased and uncased conditions during drilling and after drilling was complete.
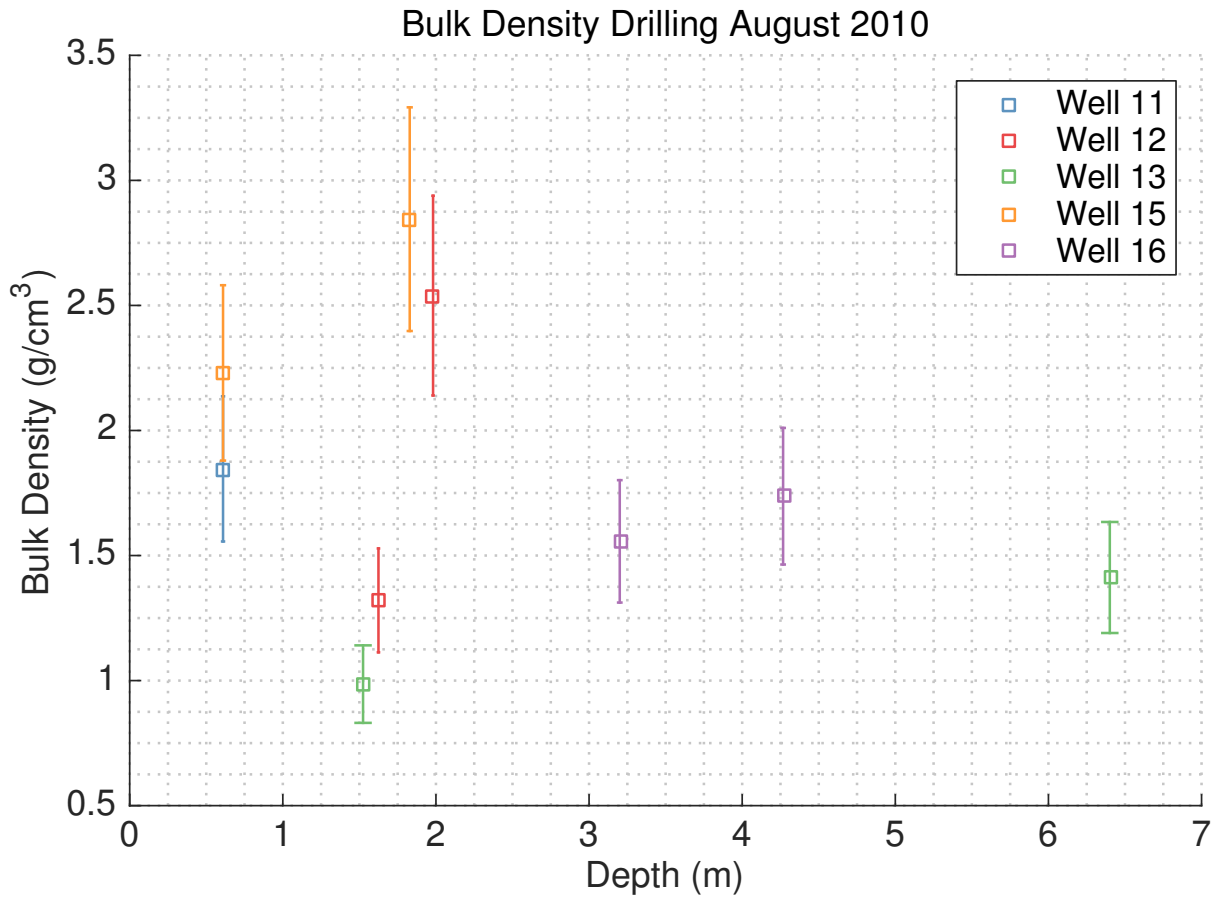
Figure B.9: Bulk density measurements made during drilling by measuring the volume of intact core retrieved via CPT.
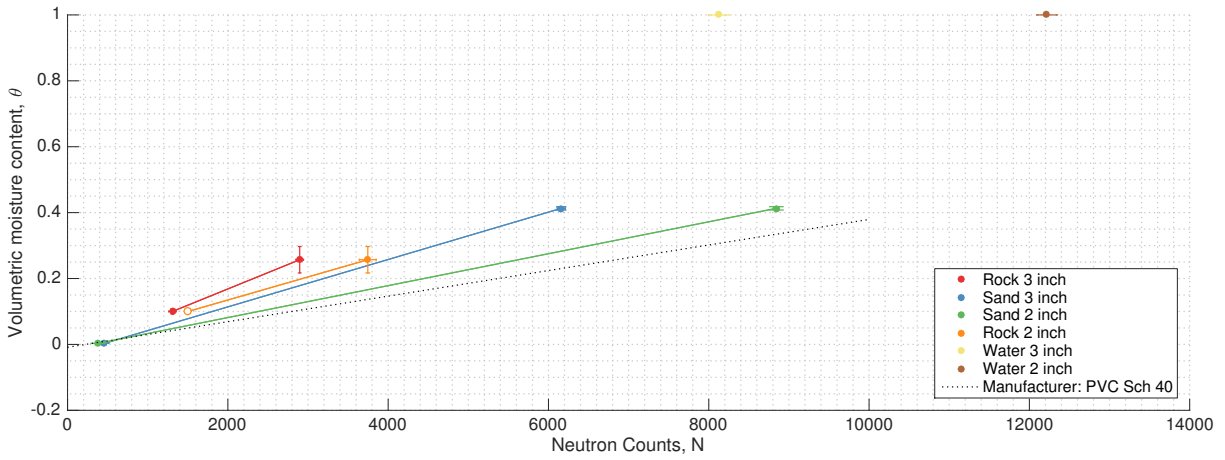
Figure B.10: Relationship between neutron counts and volumetric moisture content measured via barrel calibration. The slope and intercept of the linear regression are shown in Table B.4. Filled circles denote measured values, while the open circle denotes a calculated value derived from the relationship between 2 inch and 3 inch casing (Figure B.6). Error bars represent one standard deviation.
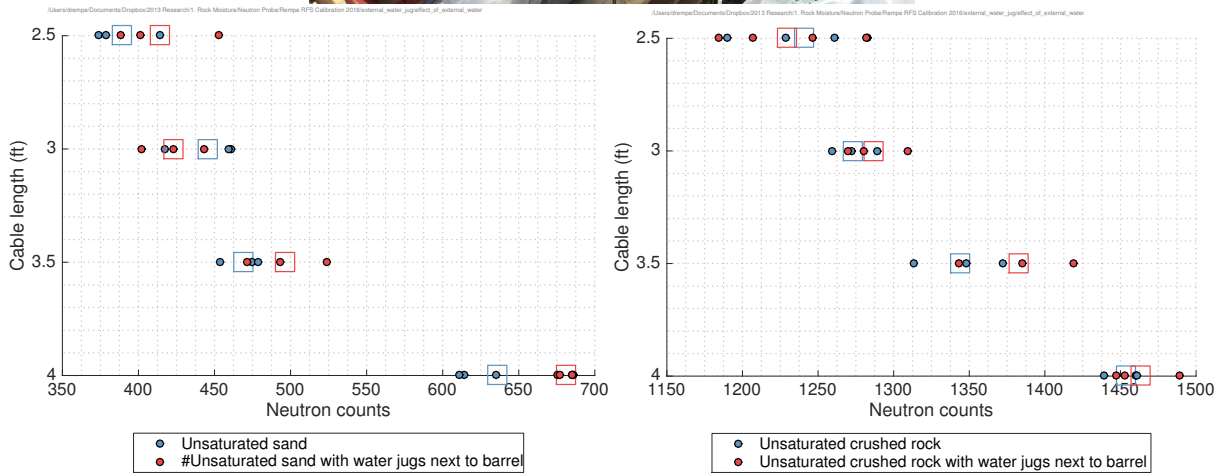
Figure B.11: Photos of barrel calibration setup for 3 inch casing (A) with water jugs placed on the exterior of the barrel to evaluate the radius of influence of the measurement on unsaturated sand (B) and crushed rock (C). Individual measurements within the barrel (represented by cable length) are shown and the average of those measurements is denoted by a square.
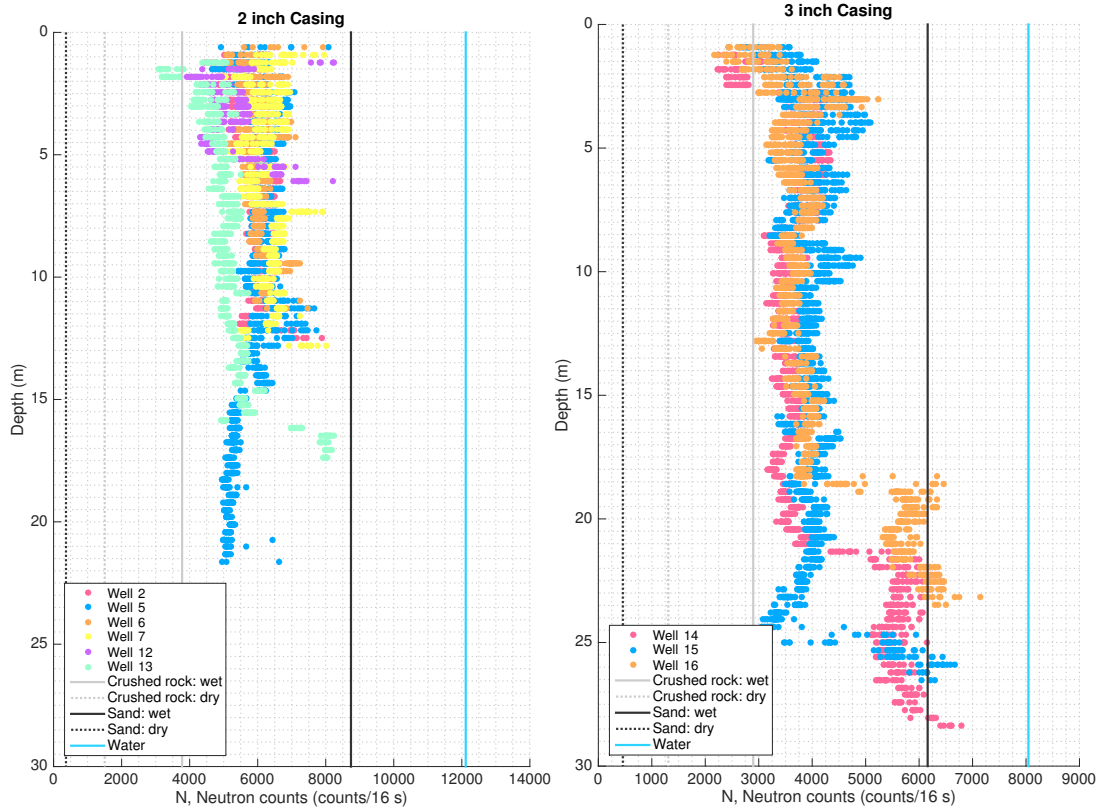
Figure B.12: Field data from 2 inch (A) and 3 inch (B) slotted PVC cased boreholes from the Rivendell field site compared with neutron counts measured in barrel calibration experiments.
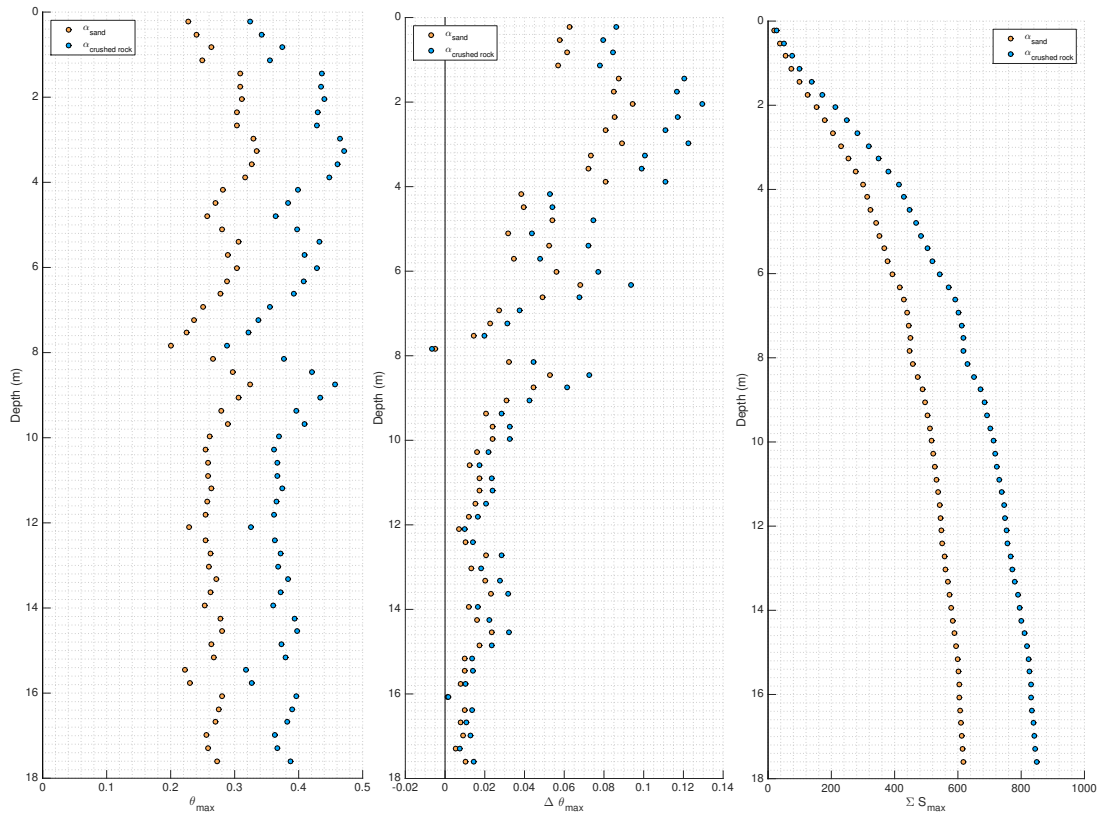
Figure B.13: The influence of calibration slope, α, on the caluclation of θ, $\Delta\theta$. and ΣS, for the wettest measurement (March 16, 2016).
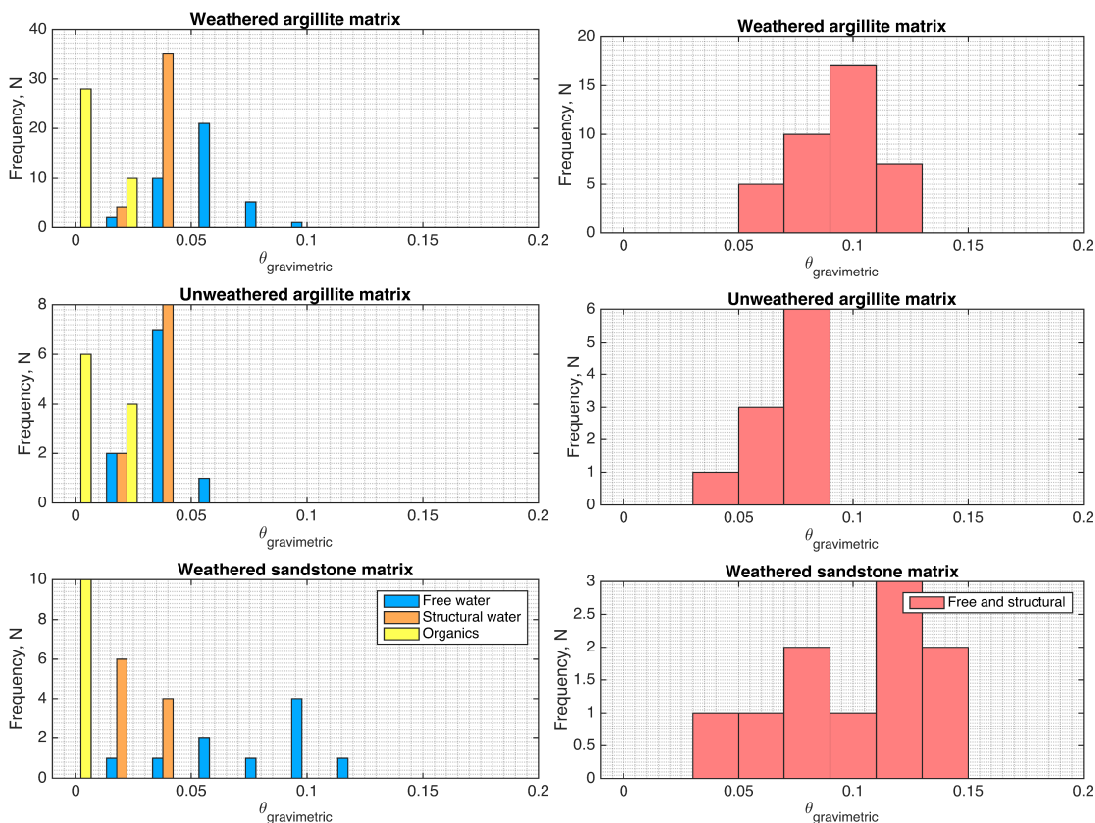
Figure B.14: Results of thermogravimetric experiments quantifying the fraction of mass associated with free and structural (bound) water, and organics. Samples were classified as weathered and unweathered argillite, and sandstone. The organic content and amount of structural water was fairly consistent among all types of samples, while the amount of free water in saturated samples tended to be highest in sandstone samples indicating higher porosity in the weathered sandstone. The lowest amount of free water was detected in the unweathered argillite matrix suggesting lower porosity in the unweathered argillite relative to weathered argillite matrix. In unweathered argillite matrix, there is approximately equal free and structural water suggesting that the total volumetric water content as detected by a neutron probe or time domain reflectometer would detect this structural water. However, by volume, only half of the total water, the free water, has the potential to be dynamic and change at a seasonal time scale.
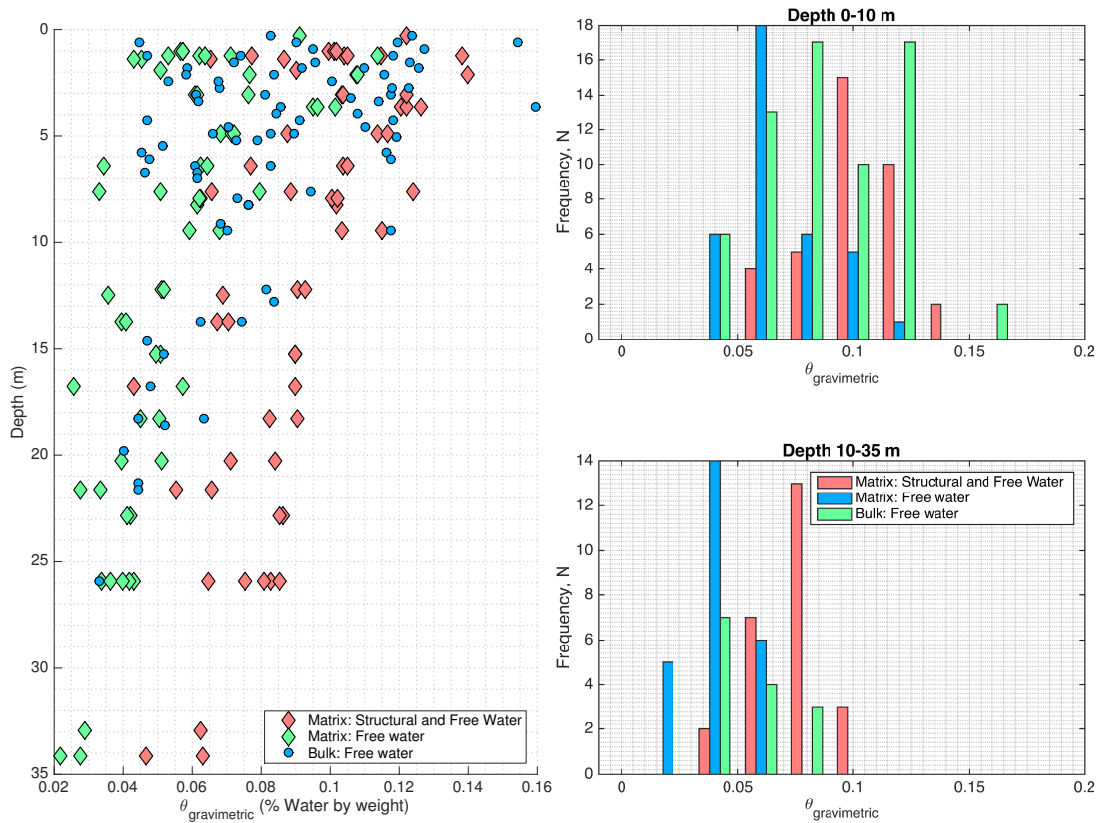
Figure B.15: Profile of structural and free water observed in samples of rock matrix (diamonds) and bulk (circles), where bulk samples were comprised of rock matrix and any particulates or soil like material between fractures. Free and total water (free plus structural) are shown for the rock matrix samples.
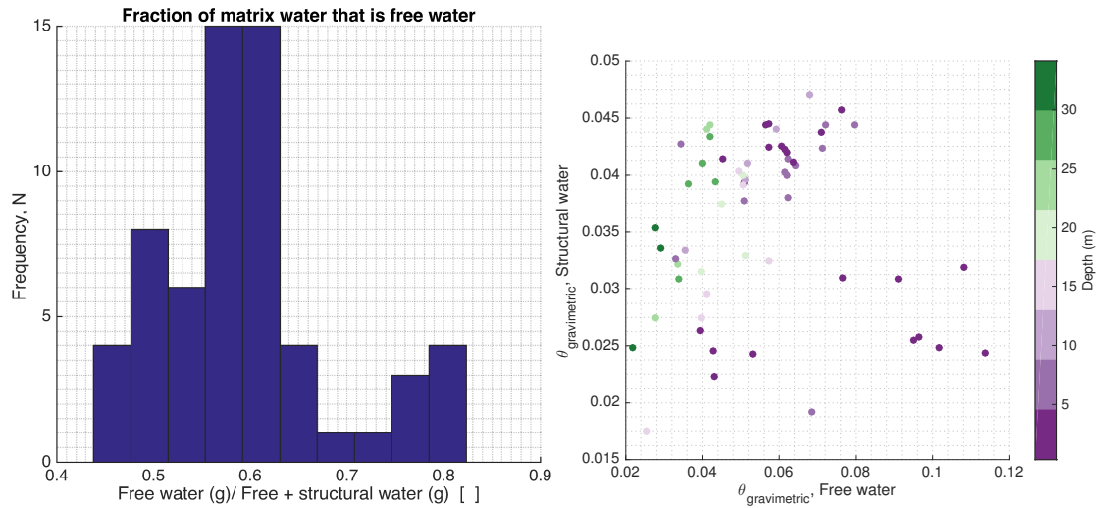
Figure B.16: The relationship between structural and free water within saturated matrix samples. (A) Of the water lost to heating at 500 C, the fraction of water that represents free water (lost at 105 C) comprises 45 to 80% of that total water leaving 20-55% of water as structural water. (B) There is no apparent relationship between the amount of water held as structural or free water in matrix samples.
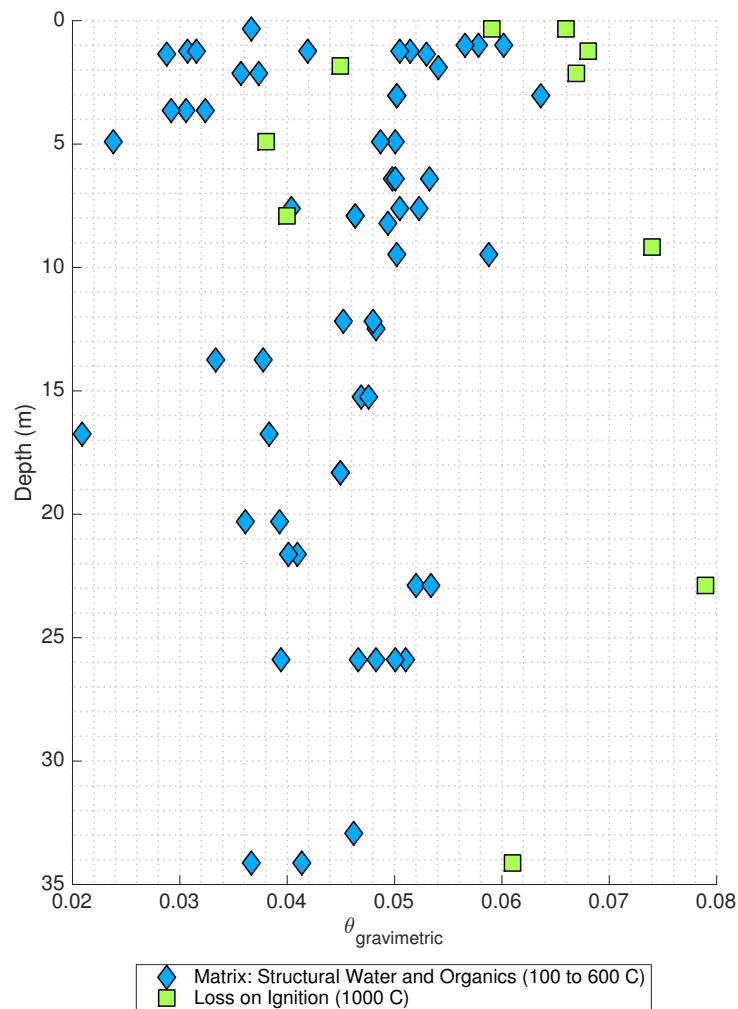
Figure B.17: Loss on ignition (expressed as a fraction) compared to mass lost due to heating associated with the loss of structural water and carbon in organic compounds. There is agreement among measurements at shallow depths while LOI is greater than mass lost at lower temperatures for samples from deeper depths suggesting that carbonate minerals may be abundant at greater depth within the weathering profile.
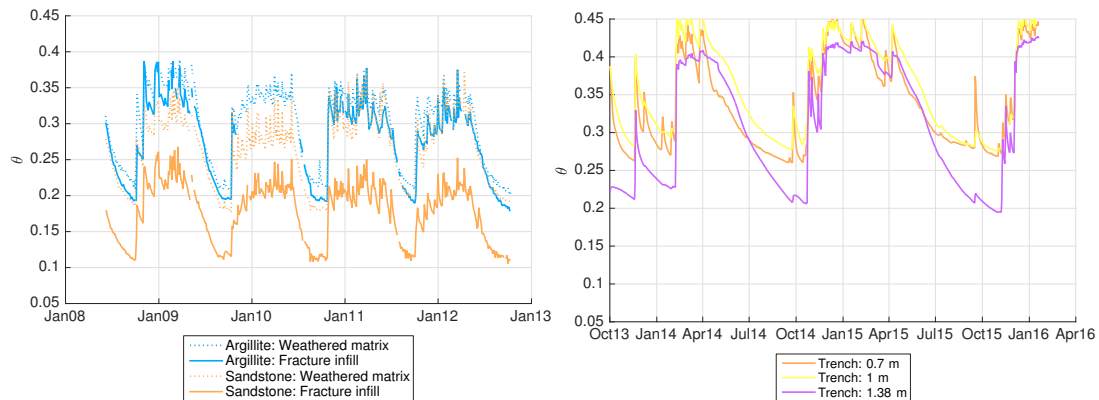
Figure B.18: Moisture content time series from TDR installed in weathered bedrock. Data on the left are derived from TDR installed by drilling holes for the TDR into the matrix of weathered rock in a trench face ("weathered matrix") and pressed into the space between fractures (see Salve and Rempe, 2013). Data on the right are from a deep trench located at the ridge top into which 30 cm long TDR rods were pressed into the trench face. The Topp equation (Topp et al., 1980) was used to convert dielectric to volumetric moisture content. The range of moisture contents observed within all probes is relatively narrow and <20%. Consistent annual minima are observed to occur for a short period in each probe.
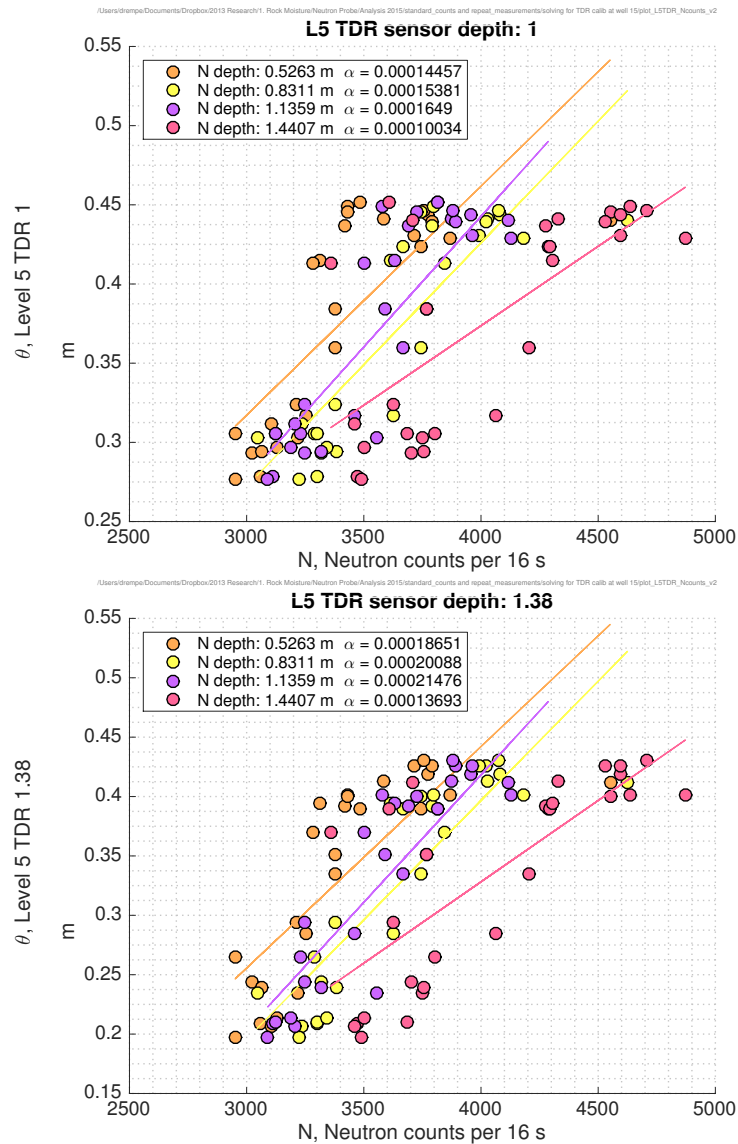
Figure B.19: TDR installed in weathered bedrock and saprolite (TDR_L5_1 and TDR_L5_1.38) compared to nearby neutron probe measurements in Well 15. Neutron counts are compared to moisture content measured at a nearby TDR sensor to derive a relationship between volumetric moisture content and neutron count. Several depths surveyed with the neutron probe are comapred to each figure (represented by different colors) and the slopes of a (poor) linear fit(α) for each depth are shown.
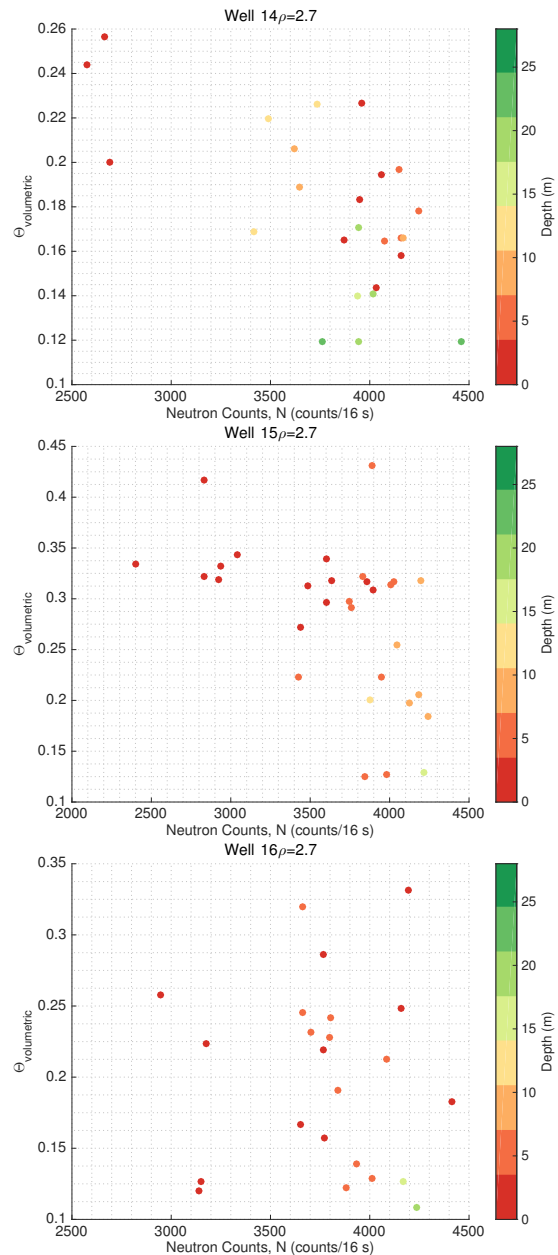
Figure B.20: Comparison of neutron probe data in cased boreholes shortly after drilling (Nov 2010) with volumetric moisture content of gravimetric samples extracted during drilling, where $\theta_{volumetric}$ was caclulated as $\rho * \theta_{gravimetric}$ where $\theta_{gravimetric}$ is the weight of water lost to 105 C over the dry weight of the sample. Note that the shallowest samples in Wells 14 and 15 are coarser grained than other samples.
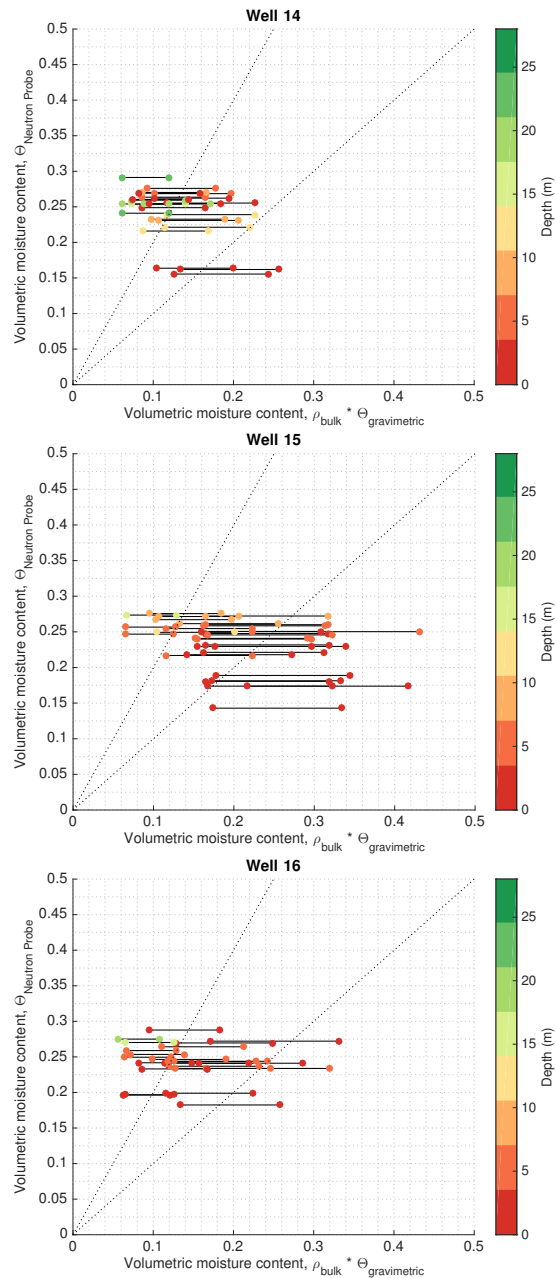
Figure B.21: Comparison of volumetric content derived from neutron probe measurements with samples analyzed for gravimetric moisture content. Gravimetric moisture content was converted to volumetric moisture content by multiplying $\theta_{gravimetric}$ by a range of bulk densities ρ_{bulk} from 1.4 - 2.7 g/cm^3 typical of shale saprolite and matrix. Neutron counts, N, were converted to volumetric moisture content using the calibration equation established for sand in a 3 inch slotted PVC borehole (Table B.4). Dashed lines are 1:1 and 1:2 lines to demonstrate how structural water, may influence θ. .
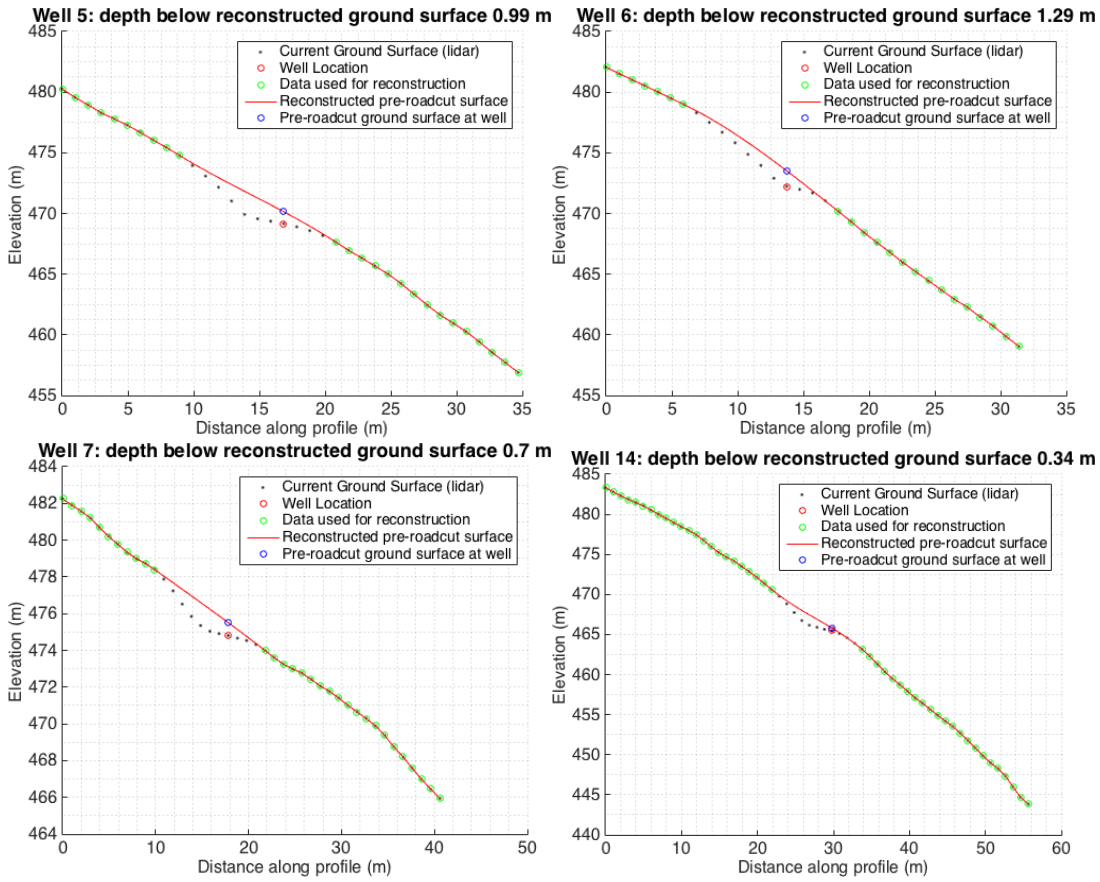
Figure B.22: Reconstruction of groundsurface above wells located along road cut gives depth of the current ground surface within the original weathering profile.

Bibliography

[1] S.P. Anderson, W.E. Dietrich, and G.H. Brimhall. Weathering profiles, mass-balance analysis, and rates of solute loss: Linkages between weathering and erosion in a small, steep catchment. *Geological Society of America Bulletin*, 114(9):1143, 2002.

[2] Suzanne Prestrud Anderson, William E Dietrich, David R Montgomery, et al. Subsurface flow paths in a steep, unchanneled catchment. *Water Resources Research*, 33(12):2637–2653, 1997.

[3] Yuko Asano, Taro Uchida, and Nobuhito Ohte. Residence times and flow paths of water in steep unchannelled catchments, Tanakami, Japan. *Journal of Hydrology*, 261(1):173–192, 2002.

[4] E.W. Banks, C.T. Simmons, A.J. Love, et al. Fractured bedrock and saprolite hydrogeologic controls on groundwater/surface-water interaction: a conceptual model (Australia). *Hydrogeology Journal*, 17(8):1969–1989, 2009.

[5] M Blumstock, D Tetzlaff, IA Malcolm, G Nuetzmann, and C Soulsby. Baseflow dynamics: Multi-tracer surveys to assess variable groundwater contributions to montane streams under low flows. *Journal of Hydrology*, 527:1021–1033, 2015.

[6] Michael Bonell. Progress in the understanding of runoff generation dynamics in forests. *Journal of Hydrology*, 150(2-4):217–275, 1993.

[7] Susan L Brantley, Molly E Holleran, Lixin Jin, and Ekaterina Bazilevskaya. Probing deep weathering in the Shale Hills Critical Zone Observatory, Pennsylvania (USA): the hypothesis of nested chemical reaction fronts in the subsurface. *Earth Surface Processes and Landforms*, 38(11):1280–1298, 2013.

[8] J. Büdel. Double surfaces of leveling in the humid tropics. *Zeitschrift für Geomorphologie*, 1:223–225, 1957.

[9] J St Clair, S Moon, WS Holbrook, et al. Geophysical imaging reveals topographic stress control of bedrock weathering. *Science*, 350(6260):534–538, 2015.

[10] B.A. Ebel, K. Loague, D.R. Montgomery, and W.E. Dietrich. Physics-based continuous simulation of long-term near-surface hydrologic response for the Coos Bay experimental catchment. *Water Resources Research*, 44(7):W07417, 2008.

[11] National Science Foundation. National Science Foundation, Program solicitation 12-575. 2012.

[12] Marty D Frisbee, Fred M Phillips, Andrew R Campbell, Fengjing Liu, and Steve A Sanchez. Streamflow generation in a large, alpine watershed in the southern Rocky Mountains of Colorado: Is streamflow generation simply the aggregation of hillslope runoff responses? *Water Resources Research*, 47(6), 2011.

[13] V Cody Hale, Jeffrey J McDonnell, Michael K Stewart, et al. Effect of bedrock permeability on stream base flow mean transit time scaling relationships: 2. Process study of storage and release. *Water Resources Research*, 2016.

[14] Atul H Haria and Paul Shand. Evidence for deep sub-surface flow routing in forested upland Wales: implications for contaminant transport and stream flow generation. *Hydrology and Earth System Sciences Discussions*, 8(3):334–344, 2004.

[15] Shin'ya Katsura, Ken'ichirou Kosugi, Tasuku Mizutani, Suemi Okunaka, and Takahisa Mizuyama. Effects of bedrock groundwater on spatial and temporal variations in soil mantle groundwater in a steep granitic headwater catchment. *Water Resources Research*, 44(9):n/a–n/a, September 2008.

[16] M Katsuyama, M Tani, and S Nishimoto. Connection between streamwater mean residence time and bedrock groundwater recharge/discharge dynamics in weathered granite catchments. *Hydrological Processes*, 24(16):2287–2299, 2010.

[17] K Kosugi, M Fujimoto, S Katsura, and H Kato. Localized bedrock aquifer distribution explains discharge from a headwater catchment. *Water Resources ...*, 2011.

[18] Ken'ichirou Kosugi, Shin'ya Katsura, Masanori Katsuyama, and Takahisa Mizuyama. Water flow processes in weathered granitic bedrock and their effects on runoff generation in a small headwater catchment. *Water Resources Research*, 42(2):n/a–n/a, February 2006.

[19] Cédric Legout, Jérome Molenat, Luc Aquilina, et al. Solute transfer in the unsaturated zone-groundwater continuum of a headwater catchment. *Journal of Hydrology*, 332(3):427–441, 2007.

[20] Andrew H Manning and Jonathan Saul Caine. Groundwater noble gas, age, and temperature signatures in an Alpine watershed: Valuable tools in conceptual model development. *Water resources research*, 43(4), 2007.

[21] Jean-Christophe Maréchal, Murari RR Varma, Jean Riotte, et al. Indirect and direct recharges in a tropical forested watershed: Mule Hole, India. *Journal of Hydrology*, 364(3):272–284, 2009.

[22] MJ Pavich. Regolith residence time and the concept of surface age of the Piedmont "peneplain". *Geomorphology*, 2(1):181–196, 1989.

[23] Shengwen Qi, Zhong Qi Yue, Faquan Wu, and Zhonghua Chang. Deep weathering of a group of thick argillaceous limestone rocks near Three Gorges Reservoir, Central China. *International Journal of Rock Mechanics and Mining Sciences*, 46(5):929–939, 2009.

[24] Laura K Rademacher, Jordan F Clark, David W Clow, and G Bryant Hudson. Old groundwater influence on stream hydrochemistry and catchment response times in a small Sierra Nevada catchment: Sagehen Creek, California. *Water resources research*, 41(2), 2005.

[25] Craig Rasmussen, Peter A Troch, Jon Chorover, et al. An open system framework for integrating critical zone structure and function. *Biogeochemistry*, 102(1-3):15–29, 2011.

[26] Daniella M Rempe and William E Dietrich. A bottom-up control on fresh-bedrock topography under landscapes. *Proceedings of the National Academy of Sciences*, 111(18):6576–6581, 2014.

[27] B.P. Ruxton and L. Berry. Weathering of granite and associated erosional features in Hong Kong. *Geological Society of America Bulletin*, 68(10):1263–1292, 1957.

[28] C Soulsby, D Tetzlaff, N Van den Bedem, et al. Inferring groundwater influences on surface water in montane catchments from hydrochemical surveys of springs and streamwaters. *Journal of Hydrology*, 333(2):199–213, 2007.

[29] Peter Troch, Emiel Van Loon, and Arno Hilberts. Analytical solutions to a hillslope-storage kinematic wave equation for subsurface flow. *Advances in Water Resources*, 25(6):637–649, 2002.

[30] Peter A Troch, Claudio Paniconi, and E Emiel van Loon. Hillslope-storage Boussinesq model for subsurface flow and variable source areas along complex hillslopes: 1. Formulation and characteristic response. *Water Resources Research*, 39(11), 2003.

[31] CJ Wilson and WE Dietrich. The contribution of bedrock groundwater flow to storm runoff and high pore pressure development in hollows. *IAHS-AISH publication*, (165):49–59, 1987.